Assessment and development of membrane materials and chemistries for the iron-chromium redox flow battery

JP du Toit

orcid.org/ 0000-0003-1979-2004

Thesis accepted in fulfilment of the requirements for the degree *Doctor of Philosophy in Science with Chemistry* at the North-West University

Promoter: Prof HM Krieg

Graduation: May 2026

RESEARCH CONTRIBUTIONS

Article publications in peer reviewed journals

1. J.P. du Toit[1], H.M. Krieg[1*] (2025). The feasibility of microporous separators in iron-chromium flow batteries. **In: Journal of Energy Storage** https://doi.org/10.1016/j.est.2024.115008

To be submitted:

2. J.P. du Toit[1], M. Wagner[2], V. Atanasov[3], J. Kerres[4], H. Cho[3], H.M. Krieg[1*]. Polybenzimidazole anion-exchange membranes for the iron-chromium redox flow battery.
3. J.P. du Toit[1], M. Wagner[2], V. Atanasov[3], J. Kerres[4], H. Cho[3], H.M. Krieg[1*]. Screening and development of cation-exchange membrane materials for the iron-chromium redox flow battery.

[1]*Chemical Resource Beneficiation, North-West University, Potchefstroom, South Africa*

[2]*Fraunhofer Institute for Ceramic Technologies and Systems IKTS, Forchheim 91301, Germany*

[3]*Institute of Chemical Process Engineering, University of Stuttgart, Stuttgart, Germany*

[4]*Forschungszentrum Jülich GmbH, Helmholtz-Institut Erlangen-Nürnberg (IET-2), Polymer Membrane Synthesis Team, Erlangen, Germany*

International conference outputs

1. J.P. du Toit[1], H.M. Krieg[1*] (2024). Performance and feasibility of porous separators in iron-chromium flow batteries. **Poster nr. 34** at the International Flow Battery Forum (IFBF®) Summer conference, 25–27 June (2024), Glasgow, Scotland.
2. J.P. du Toit, M. Wagner, V. Atanasov, J. Kerres, H. Cho, H.M. Krieg (2025). Ionically cross-linked highly sulfonated polyether ether ketone membranes for iron-chromium flow batteries. **Conference paper (ISBN: 978-1-9162004-5-6)** and **Poster nr. 49** at the International Flow Battery Forum (IFBF®) Summer conference, 24–26 June (2025), Vienna, Austria.

This thesis was also presented orally at the NWU postgraduate competition finals, where 2nd place was awarded for the Three Minute Thesis category.

ABSTRACT

The mitigation of climate change demands large-scale energy storage solutions (LSESSs) that can integrate electrical grids with renewable energy sources, such as solar and wind. Flow batteries (FBs) have been identified as promising LSESSs due to their high safety and scalable capacity, which is coupled to their electrolyte volumes. While the vanadium flow battery (VFB) is considered the most developed FB, the high cost of electrolyte remains the most significant barrier when competing with lithium-ion (Li-ion) batteries. The electrolyte of the iron-chromium flow battery (ICFB) is made from cheaper and more abundant metals, which would enable a more cost-effective up scaling. Additionally, the large ferrochrome ore reserves of South Africa, coupled with its low population density and high annual solar irradiance, gives the technology a unique opportunity to benefit the country by storing renewable solar energy, thereby reducing CO_2 and pollutant emissions by replacing coal plants.

To feasibly reach grid-scale development, flow batteries need to be low maintenance, safe, highly cost-effective, environmentally benign, while having recyclable active materials, long cycling life and high efficiencies. The high cost of the benchmark membrane used in the ICFB (perfluorinated sulfonic acid (PFSA)) is the biggest challenge towards commercialisation of the technology, however, there is limited literature focussing on alternative suitable membrane materials. While these PFSA membranes are highly chemically stable, they also exhibit a low metallic-ion selectivity with severe electro-osmotic crossover of iron-chrome electrolyte volumes. To address this research gap, various membrane materials and chemistries were assessed and developed in this study.

After construction and optimisation of a lab-scale ICFB test station, the first materials tested were simple and low-cost commercial hydrocarbon-based microporous separators (MPSs) that had been developed for the lithium-ion and lead-acid battery industries. Despite low air-permeabilities and relatively equalised differential pressures, most of the tested MPSs displayed high crossover rates resulting in reduced energy efficiency (EE) values and self-discharge times (4.3% and 40.5% below the benchmark cation exchange Nafion-212 (N-212) membrane, respectively), where 6 of the 10 MPSs were suitable for short-term cycling (10 cycles). The dynamic behaviour of the asymmetrical electrolyte viscosities, linked to the state of charge, led to changes in the differential pressures across MPSs which worsened convection. Despite pulse dampening and asymmetrical pumping, which reduced the convection and capacity decay, MPSs should be further optimised specifically for the ICFB. Further research should focus on MPS thickness and wettability, since they were shown to have the largest impact on the performance of an ICFB.

Since anion exchange membranes (AEMs) have the potential for a high cation selectivity with no published successful cycling in an ICFB to date, a range of AEMs

were manufactured and tested. Most of the AEMs failed to discharge the electrolyte due to membrane fouling by ferric chlorides, where adding sulfates (as sulfuric acid) only worsened the measured resistance due to sluggish anion migration. However, one cross-linked AEM consisting of *m*-polybenzimidazole (*m*-PBI) and phosphonated poly(pentafluorostyrene) was able to charge and discharge the ICFB electrolyte without electro-osmosis, yielding a 4.9% higher 30-cycle average coulombic efficiency (CE = 96.7%) and 1.3% higher EE (76.1%) than the N-212 cation exchange membrane (CEM). The successful application of *m*PBI was attributed to the high degree of swelling, due to the protonation of the imidazolium groups, that likely enabled proton migration through enlarged molecular spaces and electrolyte channels.

Finally, a wide variety (nanofibre reinforced, phosphonated, sulfonated, blends, ionically cross-linked and ionically-covalently cross-linked blends) of cation exchange membranes (CEMs) were manufactured and tested in the ICFB. Initial screening results showed an inherent incompatibility between phosphonic acid-based ionomers and the ICFB electrolyte. Accordingly, sulfonated ionomers were developed further. A low-cost and highly sulfonated poly(ether ether ketone) SPEEK was cross-linked with a diphenylether-containing PBI (OPBI) and optimised for the ICFB in terms of conductivity and selectivity by varying the acid-base blend ratios. A 55 µm CEM with a SPEEK-95 to OPBI blend ratio of 89:11 obtained a 3.3% lower EE than N-212 and 1.7% higher CE, while reducing the benchmark 30-cycle electrolyte imbalance levels from 33% to 4%. A novel sulfonated ionomer, SFS, was ionically and covalently ([1,1'-biphenyl]-4,4'-dithiol) cross-linked with OPBI and optimised, yielding an IEC of 1.54 mmol g^{-1}, outperforming the benchmark N-212 with an EE of 1.4% (76.2%) with no electro-osmotic crossover.

Various membrane types (MPSs, AEMs and CEMs) of cost-effective materials that have not previously been considered for the ICFB were sourced and manufactured in this study. The ICFB feasibility of these PFSA alternative materials, including hydrocarbon-based separators, polybenzimidazoles and various other aromatic polymers, were demonstrated on lab-scale. The AA900 MPS, the MIG-15 AEM and three OPBI containing CEMs (SPEEK-OPBI 89:11, SFS-OPBI 84:16 and SFS-OPBI (I+C)) all had comparable efficiencies, but significantly lower electro-osmosis, than N-212. Combining the different advantages of the ion-selective AEMs, conductive CEMs and low-cost porous hydrocarbon separators could further improve their ICFB performance. Longer term studies (multiple years of cycling) should also be considered to further validate the promising alternative materials. This would however require a capacity rebalancer, as well as the development of an ICFB electrolyte containing anionic ligands, alternative to Cl^- and H_2O, to ensure a sustained discharge capacity and Cr couple redox activity.

Key words: Iron-chrome redox flow battery, renewable energy storage, novel membrane development, porous separators, ion exchange, acid-base cross-linking, electro-osmosis, polybenzimidazole

PREFACE

The philosophy behind this thesis was not only to do scientific research or for myself to gain knowledge in membrane and polymer science, which I am passionate about, but to advance a technology that can realistically be implemented on a large scale someday. While studies showing high efficiency numbers coupled to headings with buzzwords can make good impressions on non-experts, in a given field of research, the real-life contributions are often questionable when having all the experimental context. It is therefore important to be honest with oneself and strive to find relevant solutions. Technological advancement can be favoured when there is a balance between the scientist who curiously searches for answers, especially for the things that do not work, and the industry that wants to sell something, not necessarily bothered by the things that do not work.

Acknowledgements

This work received funding from the DFG's Flow Battery Research and Innovation programme (GZ: KE 673/18-1 and AT 290/1-1), and Tharisa Minerals (Pty) Ltd.

I would like to thank my study leader, mentor and friend, Prof. Krieg, for believing in me and all my ideas. This thesis would literally not have been possible without his extensive support and motivation. This work was also made possible through the insightful collaboration with Jochen Kerres, Vladimir Atanasov and their research groups. I would also like to thank Dr. Anine Jordaan for her expertise and assistance regarding electron microscopy.

I also want to thank God for blessing me with resilience, wisdom and this opportunity. Lastly, I would like to thank my wife, family, friends and colleagues for their motivation after being held hostage to listen to hundreds of my challenges and ideas.

THESIS TABLE OF CONTENTS

LIST OF FIGURES

INTRODUCTION

LITERATURE REVIEW

CHAPTER 3

CHAPTER 4

CHAPTER 5

CHAPTER 6

APPENDIX A

APPENDIX B

LIST OF TABLES

LITERATURE REVIEW

CHAPTER 3

CHAPTER 4

CHAPTER 5

CHAPTER 6

APPENDIX B

NOMENCLATURE AND SYMBOLS

Symbol/term/abbreviation	Description	Unit
A	Ampere	A
AC	Alternating current	--
AEM	Anion-exchange membrane	
AH_E	Area of H_E peaks in H^1-NMR spectra	
Anolyte	Negative electrolyte	
ASR	Area specific resistance	Ω cm^2
BPP	Bipolar plate	--
CAES	Compressed air energy storage	
Cap. decay	Discharge capacity decay	% and % h^{-1}
$Cap_{(Discharge)}$	Discharge capacity	Ah L^{-1}
CAPEX	Capital expenditures	--
Catholyte	Positive electrolyte	
CCV	Continuing calibration verification	
CE	Coulombic efficiency	%
CEM	Cation exchange membrane	--
CFD	Computational fluid dynamics	
Current density	Current through a specified area	mA cm^{-2}
DC	Direct current	--
DI water	Ultra-purified deionised water	
DMAc	Dimethylacetamide (solvent)	
DMSO	Dimethyl sulfoxide (solvent)	
EDX	Energy dispersive X-ray	
EE	Energy efficiency	%
Electrolyte	Conductive solution containing active redox species used by a flow battery	--
Energy density	Energy storage capacity by volume	watt h L^{-1}
F_6PBI	Hexafluoroisopropylidene-containing polybenzimidazole	--
FB	Redox flow battery/Flow battery	
GWh	Gigawatt hour	10^9 watts
HDPE	High density polyethylene	--
HER	Hydrogen evolution reaction	
ICFB	Iron-chromium flow battery	
ICP-OES	Inductively coupled plasma - optical emission spectroscopy	
IEC	Ion exchange capacity	mmol g^{-1}
IEM	Ion exchange membrane	--
Ionomer	Ion-containing polymer	
KWh	Kilowatt hour	10^3 watts
LESS	Large-scale energy storage solution	--
LiB	Lithium-ion battery	
M	Molarity	mol L^{-1}
m_d	Weight of dried membrane	g

MEA	Membrane electrode assembly	--
$M_{mol\ L\text{-}1\ NaOH}$	Molarity of sodium hydroxide titrant	mol L^{-1}
*m*PBI	Poly[2,2-(m-phenylene)-5,5-bibenzimidazole]	--
MPS	Microporous separator	
m_w	Weight of wetted membrane	
MWh	Megawatt hour	10^6 watts
N-212	Nafion® 212	--
NASA	National aeronautics and space administration	
NWU	North-West University	
OCV	Open-circuit cell voltage	V
OPBI	Diphenylether-containing PBI	--
PA	Phosphoric acid	
PAN	polyacrylonitrile	
PBI	Polybenzimidazole	
PBIOO	Poly[6-((1H-benzo[*d*]imidazol-6-yl)oxy)-2-(4-phenoxyphenyl)-1H-benzo[*d*]imidazole]	
Permeability	Flow rate per unit area, normalized by membrane thickness and driving force	$m^3\ m\ m^{-2}\ s^{-1}\ Pa^{-1}$
PES	Poly(ether sulfone)	--
PEM	Proton exchange membrane	
PEMFC	Proton exchange membrane fuel cell	
PFAS	Perfluorinated alkyl substance	
PFSA	Perfluorinated sulfonic acid	
PGM	Platinum-group metals	
pH	Potential hydrogen	
PHES	Pumped hydroelectric energy storage	
PP	Poly(propylene)	
PPFS	Poly(pentafluorostyrene)	
ppm	Parts per million	mg L^{-1}
PSUOH	Partially sulfonated poly(arylene ether sulfone)	--
PVDF	Poly(vinylidene fluoride)	
PWN	Phosphonated poly(pentafluorostyrene)	
Self-Disch.	Self-discharge rate	mV h^{-1}
SEM	Scanning electron microscopy	--
SOC	State of charge	%
SPEEK	Sulfonated poly(ether ether ketone)	--
TEA	Triethanolamine	
Tensile strength	Membrane tearing resistance	MPa
TMImQPS	Tetramethylimidazolium-quaternised polystyrene	--
TWh	Terawatt hour	10^{12} watts

V	Voltage	V
VE	Voltage efficiency	%
VFB	Vanadium flow battery	--
$V_{mL\ NaOH}$	Volume of sodium hydroxide titrant	mL
WU	Water uptake	%
V_i	Initial electrolyte volume	mL
V_f	Final electrolyte volume	mL
ΔP	Differential pressure across membrane	Pa
$	United states dollar	USD
ρ	Density of fluid	g cm^{-3}
δ_{H2O}	Density of water	1 g cm^{-3}
η	Dynamic viscosity	Pa s

NORTH-WEST UNIVERSITY
NOORDWES-UNIVERSITEIT
YUNIBESITI YA BOKONE-BOPHIRIMA

Private Bag X1290, Potchefstroom
South Africa 2520

Tel: 018 299-1111/2222
Fax: 018 299-4910
Web: http://www.nwu.ac.za

Senate Committee for Research Ethics
Tel: 0169103446
Email: Feziwe.Mseleni@nwu.ac.za

ETHICS APPROVAL LETTER OF STUDY

Based on the review by the Faculty of Natural and Agricultural Sciences Ethics Committee (FNASREC), the Committee hereby clears your study as no ethical risk. This implies that the FNASREC grants permission that, provided the general conditions specified below are met, the study may be initiated, using the ethics number below.

Study title: Assessment and development of membrane materials and chemistries for the iron-chromium redox flow battery
Study Leader/Supervisor: Prof H Krieg
Student: Mr Johannes Petrus du Toit

Ethics number:

N	W	U	-	0	1	2	7	4	-	2	3	-	A	9
Institution				Study Number						Year			Status	

Status: S = Submission; R = Re-Submission; P = Provisional Authorisation; A = Authorisation

Application Type: Single
Commencement date: 2023-05-25
Expiry date: 2026-07-15

Risk Category: No risk

General conditions:
The following general terms and conditions apply:
- *The commencement date indicates the date when the study may be started.*
- *In the interest of ethical responsibility, the NWU-SCRE and FNASREC reserves the right to:*
  - *request access to any information or data at any time during the course or after completion of the study;*
  - *to ask further questions, seek additional information, require further modification or monitor the conduct of your research or the informed consent process;*
  - *withdraw or postpone approval if:*
    - *any unethical principles or practices of the study are revealed or suspected;*
    - *it becomes apparent that any relevant information was withheld from the FNASREC or that information has been false or misrepresented;*

    - *submission of the annual (or otherwise stipulated) monitoring report, the required amendments, or reporting of adverse events or incidents was not done in a timely manner and*

    accurately; and / or
    - *new institutional rules, national legislation or international conventions deem it necessary.*
- *FNASREC can be contacted for further information or any report templates via Nomali.Ngobese@nwu.ac.za*

The FNASREC would like to remain at your service as scientist and researcher, and wishes you well with your study. Please do not hesitate to contact the FNASREC or the NWU-SCRE for any further enquiries or requests for assistance.

Yours sincerely

Prof Nomali Ngobese
Chairperson Faculty of Natural and Agricultural Sciences Ethics Committee (FNAS-REC)

Generative AI statement:

The author hereby declares that generative AI was not used to generate or process any ideas, data, figures, writing, paraphrasing or for language editing of this thesis.

CHAPTER 1: Introduction

Chapter table of contents

1.1 Background

The world functions on the use and transformation of energy, with the combined consumption of coal, gas and oil having steadily increased over the last 59 years from 40.5 TWh in 1965 TWh to 142.4 TWh in 2024.[1] While estimating the date of global fossil fuel depletion is inherently complex and remains unclear, current reserves appear sufficient to meet the short-term increasing demand as the resources are abundant, while the primary difficulty lies in their discovery.[2] Apart from the time at which fossil fuels might deplete, the United Nations announced that the emission of global warming gases such as CO_2 needs to be reduced to an insignificant amount by 2050 if temperature increases compared to pre-industrial levels want to be kept below 1.5 °C.[2, 3] As a result, there is an increasing effort toward the global transition to renewable energy and reducing CO_2 emissions, where large-scale energy storage will be required as a buffer for the mismatch between human demand and renewable energy generation, e.g., solar and wind (see **Figure 1.1**).

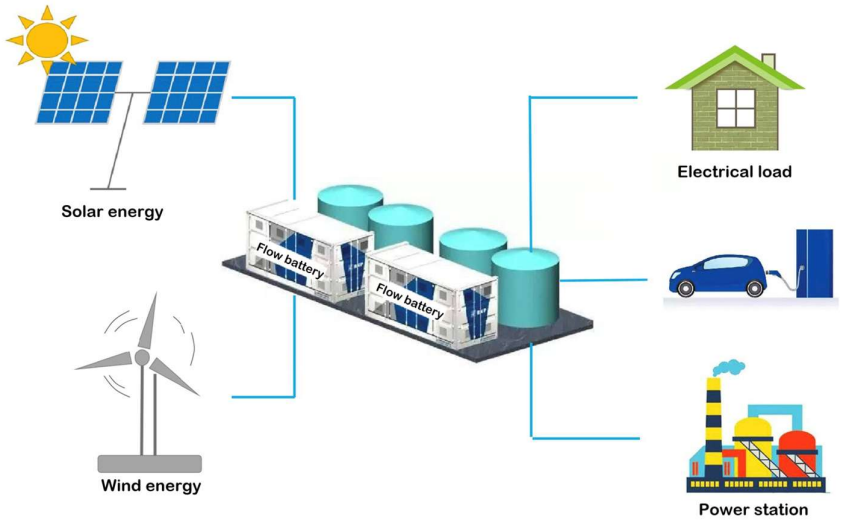

Figure 1.1: Integration of large-scale electrochemical energy storage into the electrical grid with solar and wind energy.[4]

One of the most promising solutions to supply stationary energy storage at this scale is energy storage using flow batteries (FBs), owing to their higher life time, scalable capacity via tank size, more abundant battery metals and energy to power flexibility compared to Lithium-based storage.[4-10] FBs differ from other energy storage technologies by electrochemically storing and releasing energy through redox reactions in an electrolyte fluid that is pumped through a battery stack, enabling full removal, purification and re-use of active battery components.[11] Compared to large-scale mechanical energy storage like pumped hydroelectric energy storage (PHES) and compressed air energy storage (CAES), FBs have the advantages of having fast response times and not being geographically restricted.[11, 12] Unfortunately,

depending on the type of chemistry, water-based FBs generally have low energy densities and encounter membrane oxidation, active specie degradation through parasitic side-reactions, corrosion of electrodes and other metal components from acidic environments, round-trip efficiency losses from auxiliary parts like pumps, and crossover of metal species and water that require remixing of electrolyte or crossover mitigation.[13-17] Although the energy density of FBs are considered low, large storage tanks can be used as they are not intended for mobile applications that have weight and space restrictions.[18] The challenges faced by FBs are continuously being addressed by interdisciplinary research on membrane polymers, materials science, electrochemistry, analytical chemistry, computational modelling and chemical and mechanical engineering.

The multiple advantages of the FB concept, combined with the urgency of the global transition to renewable energy requiring large-scale energy storage, has brought about a continuous growth in FB research. **Figure 1.2** illustrates this by showing how the number of published academic articles, conference papers and book chapters about FBs has increased annually since the conceptualisation of redox couples for FBs in the 1970s, with exponential growth in the last two decades.

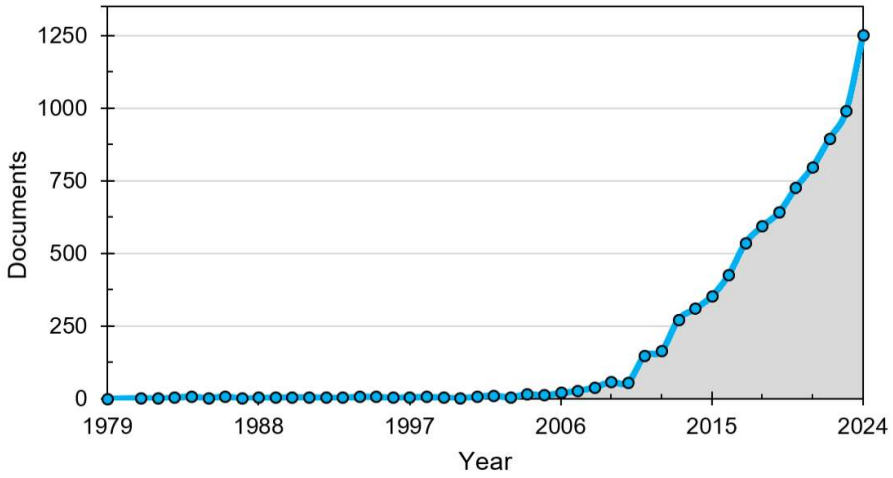

Figure 1.2: Annually increasing publications that include “flow battery” in the title (articles, reviews, conference papers and book chapters) on the Scopus database (accessed 2025-08).

The all-vanadium FB (VFB) is the most developed FB; however, its commercial competitiveness is still hindered by the cost and high purity requirements of vanadium for the electrolyte, membrane cost and membrane water transfer.[19-21] While developmental efforts have aided the VFBs penetration into the commercial market, the iron-chromium FB (ICFB) has comparatively inexpensive electrolyte components, but its overall development is still limited.[21-24] Additionally, the ICFB operates with an increased efficiency at elevated temperatures up to 65 °C, potentially giving it the

advantage of suitability in warm climates by requiring less/no heat dissipating efforts.[23] The ICFB has seen a notable increase in research efforts during the last decade due to having multiple advantageous features, resulting in an increased performance through electrode and electrolyte developments aimed at improving capacity decay, redox activity and overall efficiency.[25-36] Other than the limited cation exchange membrane (CEM) materials reported by literature [37, 38], there is also a lack of exploration into different materials and chemistries for membrane advancement. As a result, perfluorinated sulfonated membranes such as Nafion® (see **Figure 1.3**) remain the most widely applied material in the ICFB.[23, 37]

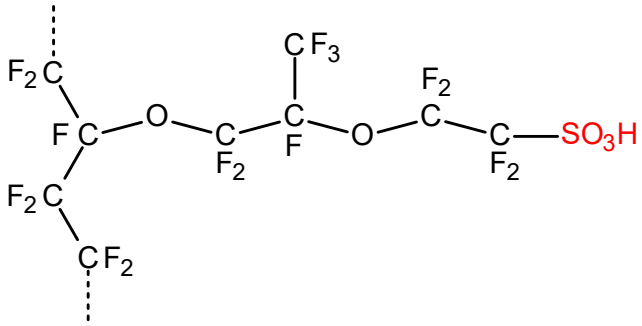

Figure 1.3: Molecular structure of the Nafion® molecule with a perfluorinated backbone and a sidechain containing sulfonic acid as functional group.

1.2 Problem statement

Among electrochemical energy storage technologies, the ICFB has many favourable traits, i.e. low-cost of abundant electrolyte materials [21, 36, 39], low environmental toxicity [40, 41] and a limited risk of thermal runaway from being water based [9, 42] that contributes towards its feasibility for up-scaling. However, with the current benchmark Nafion-212 membrane, the elevated CAPEX cost, environmental concern of perfluorinated alkyl polymers and electro-osmotic crossover rates of electrolyte restricts its maturation toward commercial viability.[37, 43-45] Compared to the VFB [22, 24, 46, 47] and FC [48-51] technologies that have received ample research efforts into low-cost membrane materials and achieved a certain degree of production at commercial stage, there is a significant research gap regarding the development of alternative materials for membranes in the ICFB. Other than commercial perfluorinated membranes, a select few membranes have been developed for the ICFB. Materials and chemistries reported include one porous polyethylene separator, one commercial anion exchange membrane, pristine SPEEK membrane and a sulfonated PBI membrane, with no feasibility of porous of anion exchange materials.[23, 37, 38, 43, 45]. As a result, scale-up consideration for the ICFB is left with limited knowledge on non-perfluorinated sulfonic acid (PFSA), cost-effective materials.

1.3 Aim and objectives

The overall aim of this study is therefore to advance ICFB technology by developing membrane alternatives to Nafion. These alternatives should advance the commercialisation and scale-up of the ICFB by reducing or eliminating the use of polyfluoroalkyl substances (PFAS), being cost-effective and having comparable or improved performance to the current benchmark Nafion-212 cation exchange membrane. Performance of various materials and chemistries were measured in terms of efficiency, selectivity and chemical stability, while prioritising the reduction of operational electrolyte imbalance. The subsequent objectives provide a framework of how the overall aim was achieved:

Objective 1: FB test station

Membrane development for an electrochemical energy storage technology such as the ICFB requires chemical compatibility and overall performance feedback, which in turn require repeatable testing of membranes. Apart from the membrane, the composition of the electrolyte and electrodes affects overall performance.[23] In order to benchmark performance and keep these variables constant, a test station needed to be constructed and optimised to a certain degree. Objective 1 was to:

i. Construct a lab-scale ICFB test station to screen and benchmark membranes.
ii. Optimise various parameters of the test station that affect performance, i.e. electrolyte, electrolyte flow rate and electrodes.
iii. Ensure repeatability by controlling environmental effects such as temperature and oxygen intrusion.

Objective 2: MPS feasibility

The most economical approach towards membrane alternatives, which has shown promise for the V and Fe/V FBs [47, 52-54], is using hydrocarbon-based microporous separators (MPSs). These MPSs have the potential to reduce the membrane contribution to the CAPEX cost of an ICFB by 99%, especially when considering the materials that are already available commercially for other technologies like lead-acid or lithium-ion batteries.[6, 21] However, challenges related to selectivity are expected when introducing pores in-between the redox couples, especially when applying materials that are optimised for other technologies. Objective 2 was thus to:

i. Test feasibility of commercially available MPSs and benchmark them against N-212.
ii. Identify key challenges of commercial MPSs in the ICFB.
iii. Address identified challenges of commercial MPSs.
iv. Identify key parameters that need to be optimised to provide direction for developing MPSs specifically catered to the ICFB.

Objective 3: AEM feasibility

The current benchmark Nafion CEM has a high ionic conductivity; however, crossover rates of metal cations are high, also leading to electro-osmotic crossover of the supporting electrolyte.[37, 38, 45, 55] Cost-effective anion exchange membranes (AEMs) can address this issue, since they are well known for their ionic selectivity through repelling metallic cations.[56-58] However, investigation of limited AEM materials in the ICFB have shown membrane fouling from ferric chloride anion complexes that congest ion-exchange sites, making them incompatible with the ICFB chemistry.[43, 59] Functional group interaction with electrolyte and feasibility of other AEM chemistries, i.e. imidazolium, pyrrolidinium, pyridinium and piperidinium, which show promise for the VFB, have not been investigated for the ICFB.[24, 60-63] Therefore, Objective 3 was to:

i. Test compatibility of novel AEM chemistries developed for the VFB.
ii. Investigate AEM inability to charge and/or discharge, further elucidating the effects of AEM incompatibility.
iii. Develop AEM with comparable performance to benchmark N-212 with higher selectivity.

Objective 4: CEM development

While the N-212 CEM currently offers the best trade-off between conductivity and selectivity for the ICFB, the cost and separation efficiency restricts commercialisation. Development of VFB and FC CEM materials in the recent years has delivered partially fluorinated, non-fluorinated, aromatic, sulfonated and phosphonated alternatives to Nafion.[64-70] These materials should be screened for their chemical compatibility and cycling performance in the ICFB, possibly enabling optimisation. Of these materials, highly aromatic fluorine-free CEM materials, namely pristine SPEEK and sulfonated PBI have received ICFB optimisation efforts, however, membranes need to be thin (≤ 30 μm) due to the smaller hydrophilic channels that restrict ionic conductivity.[67, 71, 72] There is room for optimisation, since thin membranes carry puncture risks and the reported capacity decay rates were high when using a traditional electrolyte of 1.0 M Fe/Cr in 3.0 M HCl. Objective 4 was to

i. Further develop and optimise SPEEK for the 1.3 M Fe/Cr in 1.0 M HCl electrolyte configuration.
ii. Screen various polymer materials, adopted from VFB and FC literature, that have not yet been assessed in the ICFB, including different cation exchange groups.
iii. Identify materials that are compatible and show promise.
iv. If any incompatible materials are found, investigate if the incompatibility can be resolved.
v. Develop promising and perfluorinated alkyl-free materials further and benchmark against N-212, identifying alternative materials/material combinations better suited for ICFB up-scaling and long-term cycling.

1.4 Layout of thesis

After the thesis introduction given by Chapter 1, Chapter 2 gives a literature overview of the ICFB and its developments, followed by promising membrane materials, membrane casting methods and characterisation techniques used or developed for the VFB and FC that can be adopted for the ICFB. Conforming to the objectives discussed in Section 1.3, in conjunction with published and planned publications, this membrane-focussed thesis is structured as a series of articles, with each article forming a chapter. In accordance with this structure, Objective 1 is addressed throughout the experimental work in Chapters 3 and 4, whereas Chapter 3 specifically addresses Objective 2, Chapter 4 addresses Objective 3, and Chapter 5 Objective 4. Chapter 6 summarises and concludes this thesis, while evaluating it in terms of the overall aim of advancing the ICFB through developing membrane alternatives to PFSA.

References

[1] Fossil fuels, 2024/01, https://ourworldindata.org/fossil-fuels (accessed: 2025/10/07).

[2] M. Kelkar, Demise of fossil fuels part I: Supply and demand, Heliyon, 10 (2024) e39200. https://doi.org/10.1016/j.heliyon.2024.e39200.

[3] D. Welsby, J. Price, S. Pye, P. Ekins, Unextractable fossil fuels in a 1.5 °C world, Nature, 597 (2021) 230-234. 10.1038/s41586-021-03821-8.

[4] H. Zhang, C. Sun, Cost-effective iron-based aqueous redox flow batteries for large-scale energy storage application: A review, Journal of Power Sources, 493 (2021) 229445. https://doi.org/10.1016/j.jpowsour.2020.229445.

[5] M. Resch, J. Bühler, B. Schachler, R. Kunert, A. Meier, A. Sumper, Technical and economic comparison of grid supportive vanadium redox flow batteries for primary control reserve and community electricity storage in Germany, International Journal of Energy Research, 43 (2019) 337-357. https://doi.org/10.1002/er.4269.

[6] S. Ha, K.G. Gallagher, Estimating the system price of redox flow batteries for grid storage, Journal of Power Sources, 296 (2015) 122-132. https://doi.org/10.1016/j.jpowsour.2015.07.004.

[7] H. Ibrahim, A. Ilinca, J. Perron, Energy storage systems—Characteristics and comparisons, Renewable and Sustainable Energy Reviews, 12 (2008) 1221-1250. https://doi.org/10.1016/j.rser.2007.01.023.

[8] C. Wadia, P. Albertus, V. Srinivasan, Resource constraints on the battery energy storage potential for grid and transportation applications, Journal of Power Sources, 196 (2011) 1593-1598. https://doi.org/10.1016/j.jpowsour.2010.08.056.

[9] S. Zhang, S. Gao, Y. Zhang, Y. Song, I.R. Gentle, L. Wang, B. Luo, All-soluble all-iron aqueous redox flow batteries: Towards sustainable energy storage, Energy Storage Materials, 75 (2025) 104004. https://doi.org/10.1016/j.ensm.2025.104004.

[10] F. Xie, X. Zhang, Z. Pan, Electrochemical systems for renewable energy conversion and storage: Focus on flow batteries and regenerative fuel cells, Current Opinion in Electrochemistry, 48 (2024) 101596. https://doi.org/10.1016/j.coelec.2024.101596.

[11] C. Roth, J. Noack, M. Skyllas-Kazacos, Flow Batteries: From Fundamentals to Applications, John Wiley & Sons, 2022.

[12] D.A. Elalfy, E. Gouda, M.F. Kotb, V. Bureš, B.E. Sedhom, Comprehensive review of energy storage systems technologies, objectives, challenges, and future trends, Energy Strategy Reviews, 54 (2024) 101482. https://doi.org/10.1016/j.esr.2024.101482.

[13] F. Lulay, C. Weidlich, M. Valtiner, C.M. Pichler, Membrane degradation in redox flow batteries, Green Chemistry Letters and Reviews, 16 (2023) 2274529. 10.1080/17518253.2023.2274529.

[14] K. Lourenssen, J. Williams, F. Ahmadpour, R. Clemmer, S. Tasnim, Vanadium redox flow batteries: A comprehensive review, Journal of Energy Storage, 25 (2019) 100844. https://doi.org/10.1016/j.est.2019.100844.

[15] Q. Ye, J. Hu, P. Cheng, Z. Ma, Design trade-offs among shunt current, pumping loss and compactness in the piping system of a multi-stack vanadium flow battery, Journal of Power Sources, 296 (2015) 352-364.
[16] A. Bhattarai, P.C. Ghimire, A. Whitehead, R. Schweiss, G.G. Scherer, N. Wai, H.H. Hng, Novel Approaches for Solving the Capacity Fade Problem during Operation of a Vanadium Redox Flow Battery, Batteries, 4 (2018). 10.3390/batteries4040048.
[17] S.N. Oreiro, A. Bentien, J. Sloth, M. Rahimi, M.B. Madsen, T. Drechsler, Crossover analysis in a commercial 6 kW/43kAh vanadium redox flow battery utilizing anion exchange membrane, Chem. Eng. J., 490 (2024) 151947. https://doi.org/10.1016/j.cej.2024.151947.
[18] G.L. Soloveichik, Flow Batteries: Current Status and Trends, Chemical Reviews, 115 (2015) 11533-11558. 10.1021/cr500720t.
[19] H. Choi, D. Mandal, H. Kim, Synthesis of a Low-Cost V3.5+ Electrolyte for Vanadium Redox Flow Batteries through the Catalytic Reduction of V2O5, ACS Sustainable Chemistry & Engineering, 10 (2022) 17143-17150. 10.1021/acssuschemeng.2c04632.
[20] M. Skyllas-Kazacos, L. Cao, M. Kazacos, N. Kausar, A. Mousa, Vanadium Electrolyte Studies for the Vanadium Redox Battery—A Review, ChemSusChem, 9 (2016) 1521-1543. https://doi.org/10.1002/cssc.201600102.
[21] Y.K. Zeng, T.S. Zhao, L. An, X.L. Zhou, L. Wei, A comparative study of all-vanadium and iron-chromium redox flow batteries for large-scale energy storage, Journal of Power Sources, 300 (2015) 438-443. https://doi.org/10.1016/j.jpowsour.2015.09.100.
[22] M. Kapoor, A. Verma, Technical benchmarking and challenges of kilowatt scale vanadium redox flow battery, WIREs Energy and Environment, 11 (2022) e439. https://doi.org/10.1002/wene.439.
[23] C. Sun, H. Zhang, Review of the Development of First-Generation Redox Flow Batteries: Iron-Chromium System, ChemSusChem, 15 (2021) 15. 10.1002/cssc.202101798.
[24] B.G. Thiam, S. Vaudreuil, Review—Recent Membranes for Vanadium Redox Flow Batteries, Journal of The Electrochemical Society, 168 (2021) 070553. 10.1149/1945-7111/ac163c.
[25] N. Mans, H.M. Krieg, D.J. van der Westhuizen, The Effect of Electrolyte Composition on the Performance of a Single-Cell Iron–Chromium Flow Battery, Advanced Energy and Sustainability Research, 5 (2024) 2300238. https://doi.org/10.1002/aesr.202300238.
[26] N. Mans, D.J. van der Westhuizen, H.M. Krieg, The Effect of Bismuth on the Performance of a Single-Cell Iron–Chromium Redox Flow Battery, Advanced Energy and Sustainability Research, 5 (2024) 2400113. https://doi.org/10.1002/aesr.202400113.
[27] Y. Niu, S. Zeng, G. Wu, Q. Gao, R. Zhou, C. Li, Y. Zhou, Q. Xu, Preparation of N-B doped composite electrode for iron-chromium redox flow battery, Green Energy and Intelligent Transportation, 3 (2024) 100158. https://doi.org/10.1016/j.geits.2024.100158.
[28] J.P. du Toit, H.M. Krieg, N. Mans, D.J. van der Westhuizen, UV–Vis spectrophotometric analytical technique for monitoring Fe2+ in the positive electrolyte of an ICRFB, Journal of Power Sources, 553 (2023) 232178. https://doi.org/10.1016/j.jpowsour.2022.232178.
[29] T. Herbert, N. Mans, D.J. van der Westhuizen, H.M. Krieg, Investigation of ICRFB hybrid rebalancing systems, Journal of Power Sources, 594 (2024) 234029. https://doi.org/10.1016/j.jpowsour.2023.234029.
[30] Y.K. Zeng, T.S. Zhao, X.L. Zhou, L. Zeng, L. Wei, The effects of design parameters on the charge-discharge performance of iron-chromium redox flow batteries, Applied Energy, 182 (2016) 204-209. https://doi.org/10.1016/j.apenergy.2016.08.135.
[31] Y.K. Zeng, X.L. Zhou, L. An, L. Wei, T.S. Zhao, A high-performance flow-field structured iron-chromium redox flow battery, Journal of Power Sources, 324 (2016) 738-744. https://doi.org/10.1016/j.jpowsour.2016.05.138.
[32] H. Zhang, Y. Tan, J. Li, B. Xue, Studies on properties of rayon- and polyacrylonitrile-based graphite felt electrodes affecting Fe/Cr redox flow battery performance, Electrochimica Acta, 248 (2017) 603-613. https://doi.org/10.1016/j.electacta.2017.08.016.
[33] Y. Liu, Y. Niu, C. Guo, F. Qu, Z. Liu, X. Zhou, W. Guo, C. Xu, Q. Xu, Nitrogen-Doped Bismuth Oxide-Modified Carbon Cloth as a Bifunctional Electrocatalyst for Iron–Chromium Redox Flow Batteries, Energy & Fuels, 38 (2024) 12202-12211. 10.1021/acs.energyfuels.4c01739.
[34] M. Wu, M. Nan, S. Liu, C. Zhong, L. Qiao, H. Zhang, X. Ma, Multi-dimensional Bi@C electrocatalyst for Cr3+/Cr2+ redox reaction boosting high-performance iron-chromium flow batteries, Science China Chemistry, 68 (2025) 2735-2743. 10.1007/s11426-024-2375-6.
[35] Y. Ye, M. Wu, M. Nan, M. Fang, M. Yang, L. Qiao, X. Ma, The Influence of Inorganic Salt Additives in the Electrolyte on Iron–Chromium Flow Batteries at Room Temperature, ACS Applied Energy Materials, 7 (2024) 4200-4206. 10.1021/acsaem.4c00542.

[36] M. Wu, M. Nan, Y. Ye, M. Yang, L. Qiao, H. Zhang, X. Ma, A highly active electrolyte for high-capacity iron-chromium flow batteries, Applied Energy, 358 (2024) 122534. https://doi.org/10.1016/j.apenergy.2023.122534.
[37] E. Bai, H. Zhu, C. Sun, G. Liu, X. Xie, C. Xu, S. Wu, A Comparative Study of Nafion 212 and Sulfonated Poly(Ether Ether Ketone) Membranes with Different Degrees of Sulfonation on the Performance of Iron-Chromium Redox Flow Battery, Journal, 13 (2023). 10.3390/membranes13100820.
[38] Y. Wang, K. Geng, Q. Tan, T. Guo, X. Hu, H. Tang, L. Liu, N. Li, Highly Ion Selective Proton Exchange Membrane Based on Sulfonated Polybenzimidazoles for Iron–Chromium Redox Flow Battery, ACS Applied Energy Materials, 5 (2022) 15918-15927. 10.1021/acsaem.2c03471.
[39] S. Belongia, X. Wang, X. Zhang, Progresses and Perspectives of All-Iron Aqueous Redox Flow Batteries, Advanced Functional Materials, 34 (2024) 2302077. https://doi.org/10.1002/adfm.202302077.
[40] Iron Chromium Flow Batteries (ICB), 2021, Energy Storage Association Archive https://energystorageassociationarchive.org/why-energy-storage/technologies/iron-chromium-icb-flow-batteries/ (accessed: 2025/10).
[41] M.M. Petrov, A.D. Modestov, D.V. Konev, A.E. Antipov, P.A. Loktionov, R.D. Pichugov, N.V. Kartashova, A.T. Glazkov, L.Z. Abunaeva, V.N. Andreev, Redox flow batteries: Role in modern electric power industry and comparative characteristics of the main types, Russian Chemical Reviews, 90 (2021) 677.
[42] S. Netherlands Institute for Public, Exploration of Future Battery Types and Safety, (2023).
[43] N. Mans, D.J. van der Westhuizen, H.M. Krieg, Membrane Screening for Iron–Chrome Redox Flow Batteries, Advanced Energy and Sustainability Research, 5 (2024) 2300195. https://doi.org/10.1002/aesr.202300195.
[44] Y. Zhou, L. Yu, J. Wang, L. Liu, F. Liang, J. Xi, Rational use and reuse of Nafion 212 membrane in vanadium flow batteries, RSC Advances, 7 (2017) 19425-19433. 10.1039/C7RA00294G.
[45] Y.S. Kim, S.H. Oh, E. Kim, D. Kim, S. Kim, C.H. Chu, K. Park, Iron-chrome crossover through nafion membrane in iron-chrome redox flow battery, Korean Chemical Engineering Research, 56 (2018) 24-28. 10.9713/kcer.2018.56.1.24.
[46] Y. Li, D. Kienbaum, T. Lüth, M. Skyllas-Kazacos, Long term performance evaluation of a commercial vanadium flow battery system, Journal of Energy Storage, 90 (2024) 111790. https://doi.org/10.1016/j.est.2024.111790.
[47] D. Düerkop, H. Widdecke, C. Schilde, U. Kunz, A. Schmiemann, Polymer membranes for all-vanadium redox flow batteries: a review, Membranes, 11 (2021) 214.
[48] I. Sebbani, M.K. Ettouhami, M. Boulakhbar, Fuel cells: A technical, environmental, and economic outlook, Cleaner Energy Systems, 10 (2025) 100168. https://doi.org/10.1016/j.cles.2024.100168.
[49] S. Hemmer, M. Walters, S. Tinz, Scalable fuel cell systems for commercial vehicles, MTZ worldwide, 80 (2019) 64-71.
[50] S.S. Araya, F. Zhou, V. Liso, S.L. Sahlin, J.R. Vang, S. Thomas, X. Gao, C. Jeppesen, S.K. Kær, A comprehensive review of PBI-based high temperature PEM fuel cells, International Journal of Hydrogen Energy, 41 (2016) 21310-21344. https://doi.org/10.1016/j.ijhydene.2016.09.024.
[51] N. Esmaeili, E.M. Gray, C.J. Webb, Non-Fluorinated Polymer Composite Proton Exchange Membranes for Fuel Cell Applications – A Review, ChemPhysChem, 20 (2019) 2016-2053. https://doi.org/10.1002/cphc.201900191.
[52] I.S. Chae, T. Luo, G.H. Moon, W. Ogieglo, Y.S. Kang, M. Wessling, Ultra-High Proton/Vanadium Selectivity for Hydrophobic Polymer Membranes with Intrinsic Nanopores for Redox Flow Battery, Advanced Energy Materials, 6 (2016) 1600517. https://doi.org/10.1002/aenm.201600517.
[53] H.-Y. Jung, G.-O. Moon, T. Sadhasivam, C.-S. Jin, W.-S. Park, H.-T. Kim, S.-H. Roh, Ionic transportation and chemical stability of high-endurance porous polyethylene separator for vanadium redox flow batteries, Solid State Ionics, 327 (2018) 110-116. https://doi.org/10.1016/j.ssi.2018.10.019.
[54] X. Wei, L. Li, Q. Luo, Z. Nie, W. Wang, B. Li, G.-G. Xia, E. Miller, J. Chambers, Z. Yang, Microporous separators for Fe/V redox flow batteries, Journal of Power Sources, 218 (2012) 39-45. https://doi.org/10.1016/j.jpowsour.2012.06.073.
[55] K. Oh, M. Moazzam, G. Gwak, H. Ju, Water crossover phenomena in all-vanadium redox flow batteries, Electrochimica Acta, 297 (2019) 101-111. https://doi.org/10.1016/j.electacta.2018.11.151.
[56] S. Maurya, S.-H. Shin, Y. Kim, S.-H. Moon, A review on recent developments of anion exchange membranes for fuel cells and redox flow batteries, RSC Advances, 5 (2015) 37206-37230. 10.1039/C5RA04741B.

[57] D. Chen, M.A. Hickner, E. Agar, E.C. Kumbur, Selective anion exchange membranes for high coulombic efficiency vanadium redox flow batteries, Electrochemistry Communications, 26 (2013) 37-40. https://doi.org/10.1016/j.elecom.2012.10.007.
[58] P. Sharma, S. Kumar, M. Bhushan, V.K. Shahi, Ion selective redox active anion exchange membrane: improved performance of vanadium redox flow battery, Journal of Membrane Science, 637 (2021) 119626.
[59] J. S. Ling, J. Charleston, Advances in Membrane Technology for the NASA Redox Energy Storage System, (1980).
[60] L. Zeng, T.S. Zhao, L. Wei, H.R. Jiang, M.C. Wu, Anion exchange membranes for aqueous acid-based redox flow batteries: Current status and challenges, Applied Energy, 233-234 (2019) 622-643. https://doi.org/10.1016/j.apenergy.2018.10.063.
[61] M.R. Hibbs, M.A. Hickner, T.M. Alam, S.K. McIntyre, C.H. Fujimoto, C.J. Cornelius, Transport Properties of Hydroxide and Proton Conducting Membranes, Chem. Mater., 20 (2008) 2566-2573. 10.1021/cm703263n.
[62] C. Noh, M. Jung, D. Henkensmeier, S.W. Nam, Y. Kwon, Vanadium Redox Flow Batteries Using meta-Polybenzimidazole-Based Membranes of Different Thicknesses, ACS Applied Materials & Interfaces, 9 (2017) 36799-36809. 10.1021/acsami.7b10598.
[63] Y. Ahn, D. Kim, Anion exchange membrane prepared from imidazolium grafted poly(arylene ether ketone) with enhanced durability for vanadium redox flow battery, Journal of Industrial and Engineering Chemistry, 71 (2019) 361-368. https://doi.org/10.1016/j.jiec.2018.11.047.
[64] B.G. Thiam, A. El Magri, S. Vaudreuil, An overview on the progress and development of modified sulfonated polyether ether ketone membranes for vanadium redox flow battery applications, High Perform. Polym., 34 (2022) 131-148.
[65] L. Ding, X. Song, L. Wang, Z. Zhao, Enhancing proton conductivity of polybenzimidazole membranes by introducing sulfonate for vanadium redox flow batteries applications, Journal of Membrane Science, 578 (2019) 126-135.
[66] T.T. Bui, M. Shin, S. Abbas, M.M. Ikhsan, X.H. Do, A. Dayan, M.R. Almind, S. Park, D. Aili, J. Hjelm, Sulfonated para-polybenzimidazole membranes for use in vanadium redox flow batteries, Advanced Energy Materials, 15 (2025) 2401375.
[67] S. Ahmad, T. Nawaz, A. Ali, M.F. Orhan, A. Samreen, A.M. Kannan, An overview of proton exchange membranes for fuel cells: Materials and manufacturing, International Journal of Hydrogen Energy, 47 (2022) 19086-19131. https://doi.org/10.1016/j.ijhydene.2022.04.099.
[68] J. Escorihuela, J. Olvera-Mancilla, L. Alexandrova, L.F. del Castillo, V. Compañ, Recent Progress in the Development of Composite Membranes Based on Polybenzimidazole for High Temperature Proton Exchange Membrane (PEM) Fuel Cell Applications, Journal, 12 (2020). 10.3390/polym12091861.
[69] B. Maria Mahimai, G. Sivasubramanian, K. Sekar, D. Kannaiyan, P. Deivanayagam, Sulfonated poly(ether ether ketone): efficient ion-exchange polymer electrolytes for fuel cell applications–a versatile review, Materials Advances, 3 (2022) 6085-6095. 10.1039/D2MA00562J.
[70] C.H.L. Tempelman, J.F. Jacobs, R.M. Balzer, V. Degirmenci, Membranes for all vanadium redox flow batteries, Journal of Energy Storage, 32 (2020) 101754. https://doi.org/10.1016/j.est.2020.101754.
[71] J. Molina, J.J. de Pablo, J.P. Hernández-Ortiz, Structure and proton conduction in sulfonated poly(ether ether ketone) semi-permeable membranes: a multi-scale computational approach, Physical Chemistry Chemical Physics, 21 (2019) 9362-9375. 10.1039/C9CP00598F.
[72] J. Xu, H. Zhao, W. Li, P. Li, C. Chen, Z. Yue, L. Zou, H. Yang, Facile strategy for preparing a novel reinforced blend membrane with high cycling stability for vanadium redox flow batteries, Chem. Eng. J., 433 (2022) 133197. https://doi.org/10.1016/j.cej.2021.133197.

CHAPTER 2: Literature review

Chapter table of contents

2.1 Introduction

The global drive to transition to renewable energy also increases the demand for large-scale energy storage solutions (LSESSs) to store and mitigate intermittent and fluctuating electricity supply and demand.[1-3] The commercialisation and up-scaling of flow batteries (FBs) would contribute to meeting the growing demand for LSESSs.[4, 5] In order to feasibly achieve this, the FBs should not only to be cost-effective, but attain a level of technological development to deliver both sufficient performance and efficiency. This implies that the LSESS would have to be reliable as the scale and integration into the grid necessitates an infrastructure that is low-maintenance and stable over extended time periods.[6] While lithium-ion batteries (LiBs) are currently considered to be the most developed energy storage technology, poor recyclability, safety concerns, scaling cost and the growing demand for LiBs in small and medium-size applications support the development of FBs as more logical and feasible LSESSs.[4-7] The iron-chromium flow battery (ICFB) specifically uses abundant and environmentally benign metals in a recyclable, non-flammable and water-based liquid electrolyte to store energy as a fluid in tanks, making it an attractive option for grid-scale energy storage.[8, 9]

While FBs are still considered a new technology in terms of commercialisation, the number of international manufacturers and site installations continue to grow, which demonstrates the technological feasibility and progress in transitioning to the commercialisation stage.[3, 10] This is also confirmed by the exponentially increasing number of articles published in this field (Figure 1.1). It is well known that the all-vanadium flow battery (VFB) currently holds the highest level of development, with multiple running installations globally on small and large scale.[11, 12] One example of an international FB manufacturer is Rongke Power, who has constructed several large-scale VFB installations globally, totalling an operating storage capacity of 3.5 GWh of which 400 MWh is at a single installation completed in 2022 in Dalian, China.[13, 14] The similarity between the inner workings of the ICFB and VFB provides an advantage for the iron-chromium couple since most of the technological achievements of the VFB are cross-compatible; however, the ICFB operates with a significantly cheaper electrolyte than the VFB.[8]

After providing a general ICFB background highlighting the technological developments (Section 2.2), the focus, in line with the scope of this thesis, shifts towards the membranes used in FBs in terms of i) membrane materials, discussing both porous separators and ion-exchange membranes (Section 2.3), ii) different membrane casting techniques (Section 2.4) and finally, iii) both in-situ and ex-situ membrane characterisation techniques (Section 2.5).

2.2 ICFB

This section provides background (Section 2.2.1) on the research motivations and advantages of the iron-chromium-based energy storage technology, followed by a chronological overview of ICFB developments and developmental shortcomings (Section 2.2.2).

2.2.1 Background

The ICFB, considered by many as the first redox flow battery, was invented in the early 1970s by Dr. Lawrence H. Thaller's research group at the Lewis Research Center, which was established by the National Aeronautics and Space Administration (NASA).[9, 15] The decoupled capacity and geographical flexibility of the FB concept, with low cost of abundant electrolyte components compared to other energy storage solutions at the time, made this technology highly attractive for large-scale applications, which still holds against more developed systems today.[16-19] This becomes apparent when comparing the recent cost and abundance of metal components (**Figure 2.1)**, while the material costs do not accurately reflect the cost per kW storage (which is also influenced by the energy density of each system). The costs are influenced by the mining supply vs global demand and qualitatively illustrates that the material abundance and cost of the Fe- and Cr-based electrolyte favours the scaling of the ICFB vs the more developed LiB and VFB.[20-23] While lab-scale tests typically use dissolved ferrous and chromic chloride salts (in hydrated form) [9, 24, 25], ferrochrome alloy can readily be dissolved in HCl and used as electrolyte after an uncomplicated impurity removal, allowing further cost reduction during the large-scale production of the ICFB electrolyte.[26]

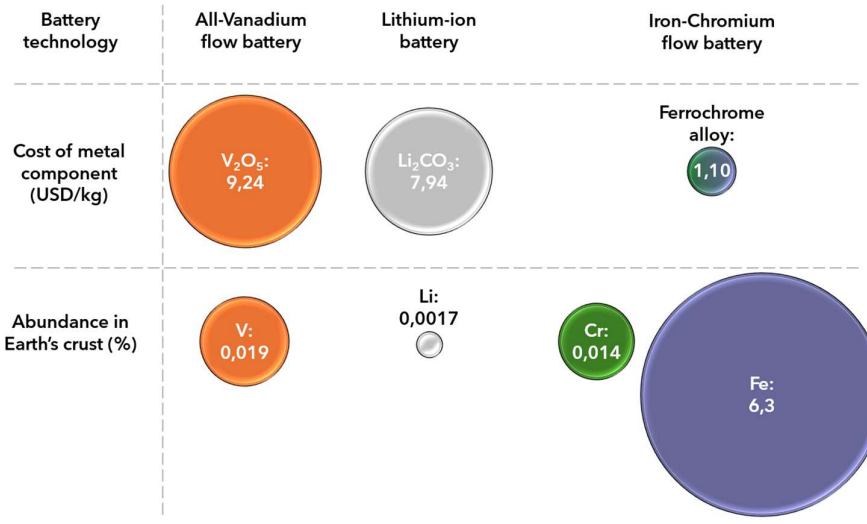

Figure 2.1: Comparison (VFB, LiB and ICFB) of cost and abundance of the battery metals used.

As illustrated in **Figure 2.2**, the ICFB uses tanks and pumped liquid electrolyte to electrochemically store and release energy using the Fe/Cr couple (see Equations 1.1–1.4). Electrodes allow the transfer of electrons to the outer circuit while charge carriers (e.g., protons) migrate through a selective membrane to maintain a balance of positive and negative charges. The battery components (membranes, electrolyte and electrodes) are discussed in more detail in Sections 2.3 and 2.5.1.1.

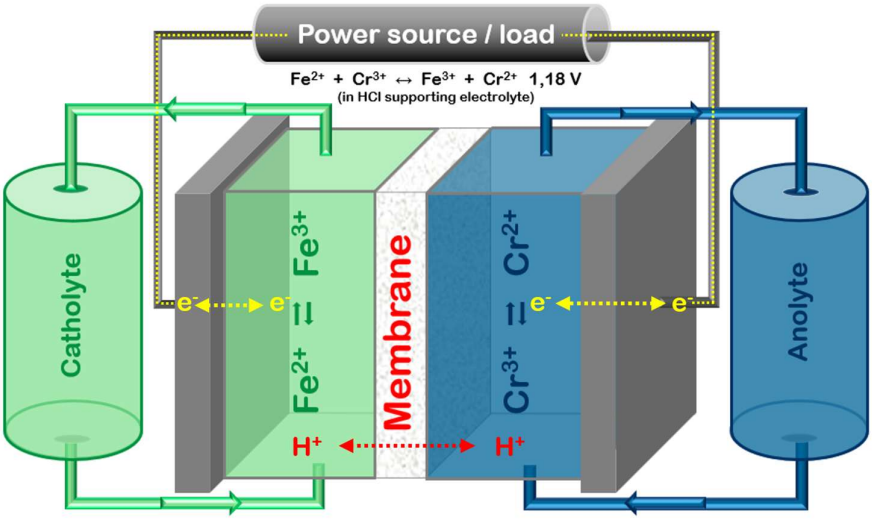

Figure 2.2: Illustration of an ICFB system.

Positive electrode reactions:

$$Fe^{2+} \rightleftharpoons Fe^{3+} + e^{-} \qquad +0.771\,V\ vs.SHE \qquad (1.1)$$

Negative electrode reactions:

$$Cr^{3+} + e^{-} \rightleftharpoons Cr^{2+} \qquad -0.408\,V\ vs.SHE \qquad (1.2)$$

Simplified Nernst equation [27]:

$$E_{cell} = E^{0}_{cell} - \frac{RT}{nF} ln\left\{\frac{[Oxidised]}{[Reduced]}\right\} \qquad (1.3)$$

Where E^0 is the standard electrode potential (V), R is the ideal gas constant 8.314 (J K^{-1} mol^{-1}), T is the temperature (K), n is the moles of electrons in the half-reaction and F is Faraday's constant (96485 C). The overall cell potential, where the oxidisable species (Fe^{2+} and Cr^{2+}) and reducible species (Fe^{2+} and Cr^{2+}) are at equal concentrations (50% state of charge) such that $ln\frac{[Oxidised]}{[Reduced]} = 0$ and E^0 = 1.179V.

$$Fe^{2+} + Cr^{3+} \rightleftharpoons Fe^{3+} + Cr^{2+} \qquad \Delta E^{0} = +1.179\,V \qquad (1.4)$$

Where the forward reaction in (1.4) describes the charging of an ICRFB, and the reverse describes discharging.

2.2.2 Development

Following it's conception in 1973, this FB technology has seen numerous developments at the Lewis Research Center where Thaller et al., Gann et al. and O'Donnel et al. published papers focussing on membrane screening, electrolyte compositions, the slow kinetics from the Cr^{2+}/Cr^{3+} couple, catalysts, and the need for a rebalancing system.[28-30] During this time, due to poor selectivity of commercially available membranes, Ionics Inc. was contracted to develop a membrane for the ICFB focussing on the screening and development of anion-exchange membranes (AEMs) with weak and strong base ion exchange functional groups such as primary, secondary and tertiary amines on styrene-divinylbenzene copolymers and PVC films.[31, 32] However, the generation of anionic ferric chlorides such as $FeCl_4^-$ in the catholyte side caused membrane fouling (depositing on ion exchange sites), resulting in a sharp increase in membrane resistance making discharging difficult.[33, 34] Nevertheless, further development delivered a balance between selectivity and conductivity using a cross-linked membrane (named CDIL-AA5-LC), resulting in lower resistances (2.6 Ω cm^2).[32]

Another major challenge was the kinetic constant of the Cr couple in HCl (2.5 $x10^{-3}$ cm s^{-1}), which was significantly lower than that of the Fe couple (up to 8.6 $x10^{-2}$ cm s^{-1}) [35, 36] which was attributed to the sluggish kinetics of Cr^{3+} as the $Cr(H_2O)_6^{3+}$ species is most prevalent in the ICFB electrolyte at room temperature. Operating the ICFB at elevated temperatures (65 °C) improved the kinetics by shifting the equilibrium more towards the redox active $Cr(H_2O)_5Cl^{2+}$ species.[37] However, the membranes at that time had a high degree of swelling at the elevated operating temperature, resulting in poor selectivity and hence increased diffusion rates resulting in high rates of metallic specie crossover. This was subsequently countered by switching to a mixed electrolyte configuration and opting for a low selectivity cation exchange membrane (CEM) named ML-21. This was the only membrane at that time that had been characterised for efficiencies using single cycles, where it obtained a CE of 92% and EE of 86% when charged to an upper voltage cutoff at ~1.12 V (corresponding to an OCV of ~1.07 V) using a 14.5 cm^2 cell, a current density of 43 mA cm^{-2}, and a mixed reactant electrolyte at 65 °C.[38]

After finding that the addition of a bismuth catalyst to the Cr electrode increased the kinetics of the system, N.H. Hagedorn reported the completion of the NASA development of the ICFB in 1984, concluding that the technology should be ready for scaling up and hence the commercial market.[32] However, the next phase, which was the scale-up of the ICFB, was hindered by the high amount of maintenance required to balance the electrolyte fluid levels resulting from electro-osmosis.[32, 38]

While few further developments for the ICFB were made after 1984 (see **Figure 2.3**), the technology has received a substantial increase in attention in the last decade, likely due to i) the general development in the field of membrane technology and ii) the increasing global demand for large-scale storage of renewable energy.[9]

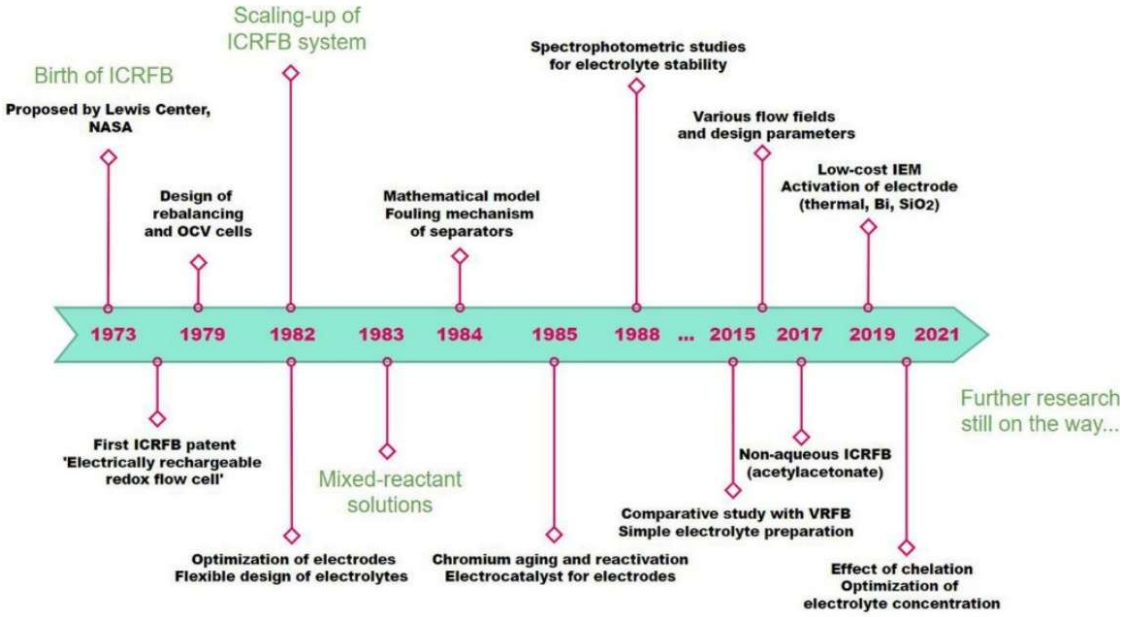

Figure 2.3: Timeline of developments for the ICFB (1973–2021).[9]

Recently, the performance was further improved by optimisation of the electrolyte composition. By i) lowering the acidity (from 3.0 M to 1.0 M HCl), ii) increasing the metallic-ion concentrations (from 1.0 M Fe/Cr to 1.3 M Fe, 1.4 M Cr) and iii) including a catalyst (5.0mM Bi_2O_3), a 40% higher storage capacity (from 8.75 Ah L^{-1} to 12.2 Ah L^{-1}) and a tenfold lower capacity decay rate (from 3.0% h^{-1} to 0.3% h^{-1}) were attained.[39] While the addition of bismuth oxide is known to improve performance by increasing the sluggish electrochemical activity of the Cr^{2+}/Cr^{3+} couple[40, 41], OCV measurements have confirmed that the presence of bismuth also promotes the undesired hydrogen evolution reaction (HER) when using the optimised electrolyte composition (1.3 M Fe, 1.4 M Cr in 1.0 M HCl) at 65 °C.[39] A further study on the influence of the presence of metallic impurities (Cu, Ni, Co, Mn, V, Ti, Mg, K, Na, Ca, and Al), has shown that Cu and Ni negatively impacts ICFB performance as Cu plating (negative electrode) could cause long-term operational issues and Ni decreased the overall EE and discharge capacity while decreasing the capacity decay.[42]

While the capacity decay from an ageing electrolyte and a buildup of Fe^{3+} resulting from oxygen intrusion and side reactions like the HER remain challenges, research into rectifying these losses shows that incorporating a rebalancing cell can restore the lost capacity.[43, 44] Accurate monitoring of imbalance and Fe^{3+} rebalancing recently became possible by deriving a near-infrared (NIR) light spectrum (UV–Vis spectrophotometry) function from Beer's law to approximate Fe^{2+} and Fe^{3+} concentrations in acidic aqueous solutions.[24, 45]

While numerous factors, including operating condition, electrolyte compositions, catalysts and electrodes, influence the performance of an ICFB [46-48], one of the

most important variables remains the membrane, which has seen limited new developments regarding materials and chemistries as alternatives for the current expensive and perfluorinated Nafion® standard.[9, 49] One polymer that has recently been evaluated in an ICFB is sulfonated poly(ether ether ketone) (SPEEK). Bai et al. found an optimal trade-off between selectivity and conductivity by casting SPEEK (degree of sulfonation – DS = 57%) to a very thin membrane (25 µm). They achieved energy efficiencies (EEs) of 77.7% – 87.5% at current densities of 40 – 120 mA cm^{-2}, which were up to 5% higher than the Nafion-212 (N-212) benchmark.[49] However, these membranes displayed relatively high capacity decays and have not yet been tested in modern electrolyte compositions, while using ultrathin membranes also poses a puncture risk in FBs that use compressed carbon fibre felts as electrodes.[50]

2.3 Membrane materials

The membrane of a FB is one of the most important components of the battery stack, significantly influencing efficiencies, cost and cycle life.[11, 51] Hence, as mentioned previously, research needs to focus on cost reduction and an increase in overall performance for the ICFB to reach commercialisation. While membranes with different versions of perfluorosulfonic acid (PFSA) ionomers are made by various manufacturers (see **Figure 2.4**), Nafion-212 (N-212) from Chemours (formerly DuPont) is currently the standard in research as it provides the highest conductivity and chemical stability in FBs.[52, 53] However, these perfluorinated CEMs have the disadvantage of high cost, low cation selectivity [54] and the uncertainty of future availability due the poor environmental compatibility and biodegradability of the perfluorinated alkyl polymer backbones.[9, 55, 56] As a result, the search for low-cost and chemically stable alternatives to perfluorinated CEMs with similar or better performance persists. For successful application in FBs, these alternative membranes need to have specific properties [57-59], including:

- High proton conductivity
- High ionic separation/selectivity
- Chemical stability
- Low degree of fluorinated alkyls
- Cost-effectiveness
- Low water drag during proton transfer

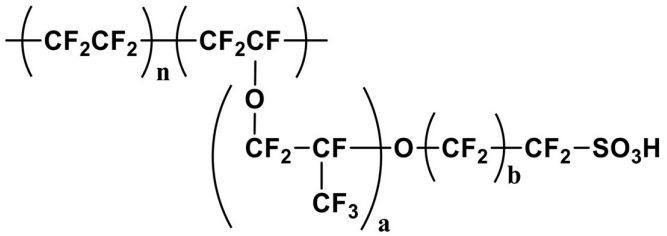

Figure 2.4: Generalised PFSA ionomer. Chemours Nafion® or Asahi ionomer (a = 1, b = 1), 3M ionomer (a = 0, b = 3), and Solvay Aquivion® ionomer (a = 0, b = 1).[60]

Since the membrane's cost, chemical stability, electrolyte crossover and self-discharge rates would arguably be more important for commercialisation than only the VEs for long term operations with a grid-coupled system (lower maintenance and less frequent electrolyte replacements outweighing higher voltage efficiencies), alternative membranes to the current benchmark are required to either reduce the capital expenditure (CAPEX) and/or improve the selectivity.[61, 62]

Due to the similar ion exchange requirements of FBs and fuel cells (FCs), most published works for alternative membrane materials to perfluorinated sulfonic acids (PFSAs) focus on porous hydrocarbon separators, CEMs based on sulfonic and phosphonic acid functional groups, and various novel chemistries for anion-exchange membranes (AEMs).[51, 63-68] Accordingly, this section briefly discusses the workings of porous separators (Section 2.3.1) and the ion exchange membranes (IEMs) which include both CEMs and AEMs (Section 2.3.2). In each section, a brief overview of ICFB membrane literature is given before discussing some of the chemistries and materials that have shown promise in FCs or VFBs. Lastly, Section 2.3.2.2.4 gives a more in-depth overview of SPEEK membrane material synthesis and current shortcomings, as a large part of this study focusses on the development of SPEEK-based membranes.

2.3.1 Porous separators

Porous separators, often referred to as microporous separators (MPSs), can have varying pore sizes (0.03–1 µm) and are widely used in lithium-ion and lead-acid batteries.[69-71] MPSs generally use embedded silica in hydrophobic polymers to absorb aqueous electrolyte inside pore channels facilitating the Grotthuss and the vehicular mechanism for migration (see **Figure 2.5** (a)) of charge carriers such as H_3O^+, $H_5O_2^+$, $H_9O_4^+$, OH^-, Cl^- and SO_4^- migrating through the surface pores and porous interior (see Figure 2.5 (b, c)).[64, 72] However, the porosity comes with an obvious drawback as convection crossover of the active redox couples and supporting electrolyte increases.[73] To separate the anolyte and catholyte, MPSs use both the pore size and pore lengths to exploit the different diffusion rates of large metallic cations and smaller charge carriers.[72, 73]

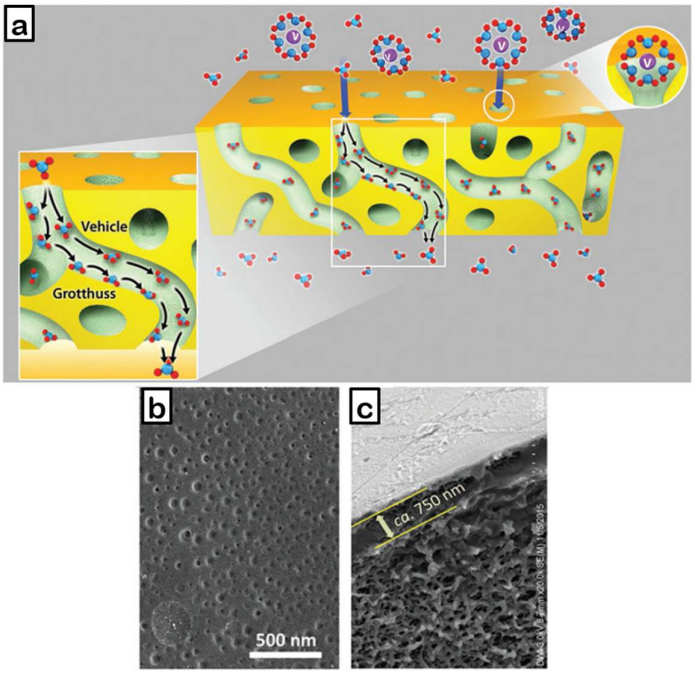

Figure 2.5: (a) Grotthuss and vehicular mechanism for proton migration through pores, and the blocking of metallic ions by a sub-nano sieving. (b) Surface and (c) cross-section morphology of a porous PIM-1/PAN VFB membrane.[74]

Membranes in an ICFB are exposed to a chemically more hospitable environment during operation (compared to the FC and VFB) due to the absence of OH^- radicals and strongly oxidising species like VO_2^+ in a 1 M HCl-containing ICFB electrolyte operated at a low cell voltage (below 1.25 V).[9, 49] MPSs have been extensively investigated for the VFB, with promising results in terms of conductivity, selectivity and stability.[64, 70, 75] In addition, the CAPEX cost of an ICFB can be reduced significantly (**Figure 2.6**) when switching from Nafion to porous separators, currently being produced at large scale for the LiB industry.[5] In Sections 2.3.1.1 and 2.3.1.2, the application of MPS in the ICFB and VFB are discussed, respectively.

	Nafion	MPS
Membrane cost ($ m^{-2})	500	5
Membrane contribution to total cost (%)	37	0,6
CAPEX cost ($ kWh^{-1})	194	123

Figure 2.6: ICFB cost comparison between Nafion and microporous hydrocarbon separators.[5, 8]

2.3.1.1 ICFB

Available literature on porous separators and related materials for the ICFB is considerably less abundant compared to that of the VFB. However, due to their successful application in VFBs and low cost, porous polyethylene (PE) separators were evaluated in the ICFB by Mans et al.[25] Due to the high rate of electrolyte crossover through the pores, a 200 µm porous PE separator embedded with silica yielded a 23% lower EE (54%) than the Fumatech FS-950 CEM during a 10-cycle ICFB test at a current density of 40 mA cm^{-2}. In another study, a porous PE separator (Daramic®) was modified with a Nafion dispersion (filling the pores) to lower crossover and yield a cost-effective composite membrane for the ICFB with a high chemical stability and conductivity.[76] By optimising the dispersion amount, an EE of 75.4% at a current density of 80 mA cm^{-2} was obtained.

2.3.1.2 VFB

As mentioned above, MPSs made from a wide variety of polymers have been investigated for the VFB application. Using various techniques including phase inversion, polymers such as poly(ether sulfone) (PES), poly(vinylidene fluoride) (PVDF), poly(tetrafluoroethylene) (PTFE) and polysulfone have been extensively modified and tested in the VFB.[64] During the last 5 years, these MPSs have improved significantly (see **Figure 2.7**), yielding EEs of > 90% at a current density of 80 mA cm^{-2} by 2016. Daramic separators have also been modified into low-cost composite membranes for the VFB.[77-79] Additionally, there are commercially available composites of porous separators, for example a thin Nafion-coated separator VANADion that was tested by Zhou et al., which yielded an EE of 76.2% at a current density of 240 mA cm^{-2} in a VFB.[80] However, it has been found that the oxidative environment of the VFB electrolyte (primarily from VO_2^+) causes degradation of simple hydrocarbon separators like PE, potentially limiting long-term applications in VFBs.[77, 81]

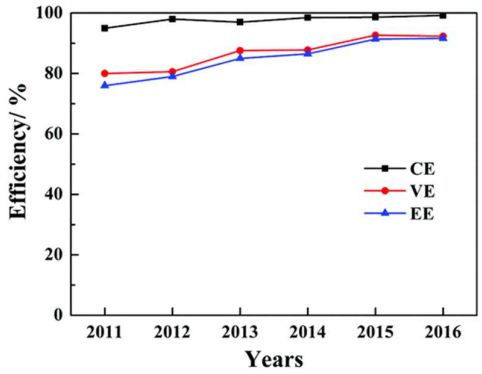

Figure 2.7: Performance parameters resulting from the development of MPSs for the VFB at 80 mA cm^{-2}.[64]

Due to the performance evident from developments made for the VFB and their potential to significantly reduce CAPEX costs, testing of more commercially available MPSs can be vital to understanding the direction of optimisations required for MPSs in the ICFB.

2.3.2 Ion-exchange membranes

The physical and chemical properties of ion exchange membranes (IEMs) largely determine the overall performance of a FB, where there is a typical trade-off between selectivity (separation efficiency) and conductivity.[82-84] Increasing the thickness of an IEM could reduce the coulombic efficiency (CE) by reducing undesired crossover of charged species, which in turn increases the path length of proton transport channels, effectively reducing conductivity and voltage efficiency (VE) by increasing resistance.[85-87] Whether a membrane facilitates the migration of anions (e.g., SO_4^{2-} and Cl^-) [32, 88] or cations (e.g., H^+, H_3O^+ etc) [72, 87], the main mechanism followed is the Grotthuss mechanism, which consists of ion hopping from functional groups. Considering the distance between functional groups in IEMs (~7–12 Å for Nafion) [89] and the presence of ion conducting channels (illustrated in **Figure 2.8**), the water and electrolyte absorbed into the membranes of a FB play a large role as an in-between step by aiding the migration of charge carriers.[72] In Sections 2.3.2.1 and 2.3.2.2, overviews of the literature for anion- and cation-exchange membranes are respectively discussed, focussing on both ICFB and VFB applications.

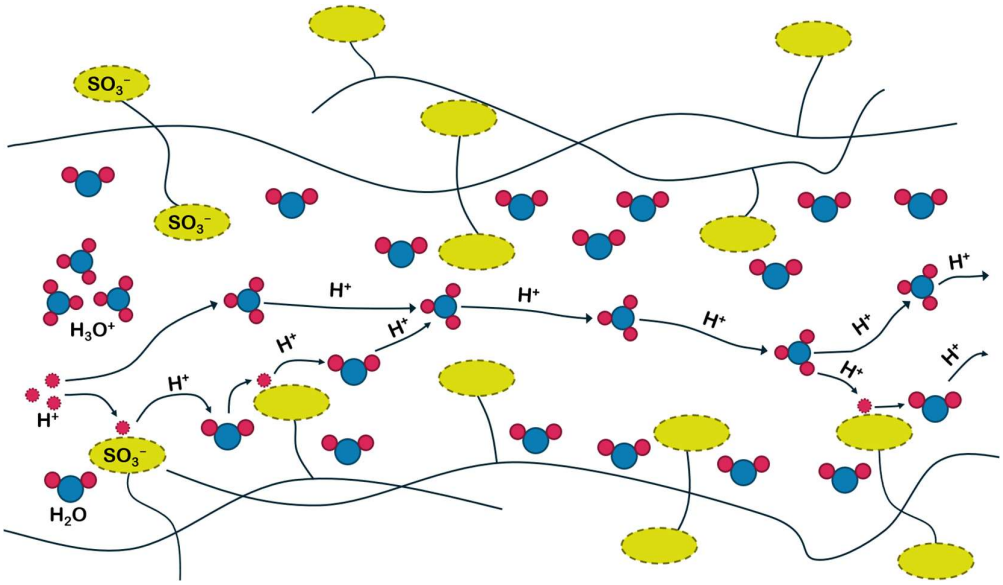

Figure 2.8: Mechanism of proton conduction through a membrane with sulfonic-acid functional group side chains.

2.3.2.1 Anion-exchange membranes (AEMs)

Since AEMs are used in alkaline and direct alcohol-based FCs, which are non-acidic, [90, 91] this section will focus on the literature of membrane materials developed for the acidic environment of the ICFB (Section 2.3.2.1.1), followed by a brief overview of VFB applications (Section 2.3.2.1.2).

2.3.2.1.1 ICFB

While both small- and large-scale applications are dominated by CEMs [92], novel AEMs have been shown to achieve charge balancing by permeating anions such as sulfates with high selectivity using functionalised cations.[51, 93] Using the Donnan exclusion principle, these membranes repel the redox-active metal cations that significantly increase selectivity, which increases both the CE and capacity retention; however, low anion conductivity is a well-known challenge.[51, 94] Despite the fouling of AEMs observed in ICFBs (discussed in Section 2.2.2), the Lewis research centre of NASA and Ionics Inc. initially conducted extensive research on AEM material selection and optimisation, proposing a vinylbenzyl chloride aminated with diethylenetriamine and dimethylaminoethyl methacrylate, which showed a high selectivity and chemical stability at a low ASR of 2.6 Ω cm^{-2}.[32] However, its application in large-scale systems was unsuccessful due to a buildup of electrolyte fluid level imbalance caused by electro-osmosis. Apart from the developments mentioned in Section 2.2.2, literature on the successful application of AEMs in an ICFB is lacking. The only study to date that had tested an AEM in the ICFB reported using a commercial 50 µm AEM (Fumatech FAP-450), which yielded a normal charge cycle followed by a rapid increase in ASR that inhibited any discharge of the charged electrolyte.[25] This was ascribed to the formation of $FeCl_4^-$ complexes that form with increasing concentration of ferric ions (charging) in the presence of chlorides, which congests the ion-conducting channels of the tested AEMs.[33]

2.3.2.1.2 VFB

There has been an increase in development of AEM materials in recent years, especially on nitrogen-based membranes, with ample literature on materials to reduce vanadium ion permeation and capacity retention in the VFB.[84, 93, 95, 96] Synthesis of quaternary nitrogen groups as positively charged anion-exchange functional groups has resulted in membranes with higher selectivity (see two examples in **Figure** 2.9 (a, b)) than the N-212 benchmark and adequate conductivity, resulting in higher overall EEs and capacity retentions.[97, 98] The potential for novel AEMs to deliver unmatched selectivity was demonstrated, for example, by Chen et al., who, when using a quaternary ammonium functionalised poly(fluorenyl ether) (QA-PFE), demonstrated a 100% CE and full capacity retention during short-term VFB tests (15 cycles) with 100 mL total electrolyte.[51]

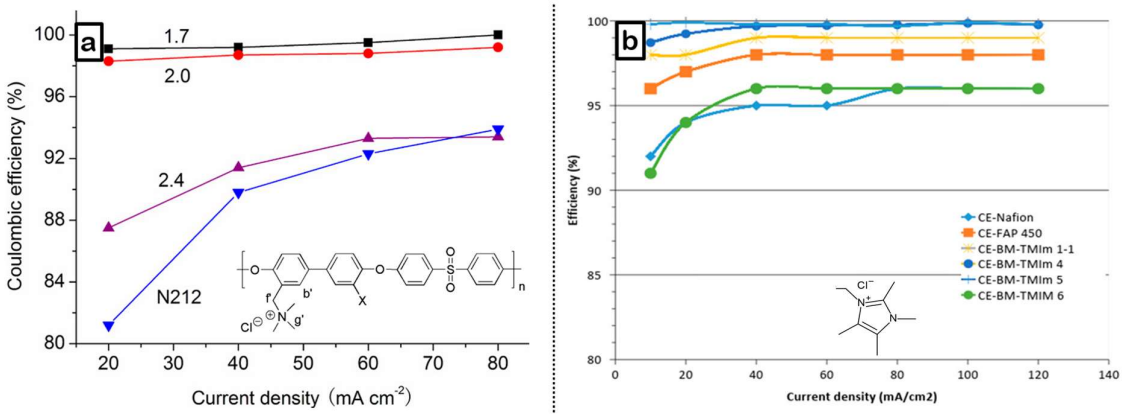

Figure 2.9: Coulombic efficiencies at varying current densities of N-212 compared to AEMs in VFBs with quaternary (a) ammonium (X = –H or quaternary ammonium side chains) as functionalized Radel membranes with ion exchange capacities 1.7 to 2.4 meq g^{-1} [97] and (b) imidazolium as tetramethylimidazolium-containing blended membranes with various amounts of Bromomethylated poly(2,6-dimethyl-1,4-phenylene oxide) and poly[(1-(4,4′-diphenylether)-5-oxybenzimidazole)-benzimidazole].[98]

(Reproduced with permission from [97, 98] under CC BY)

Investigations into the chemical stability of quaternary ammonium in the VFB have shown signs of degradation through oxidation by VO_2^+, leading to the development of more diverse and cyclic nitrogen-based anion-exchange functional groups.[62, 99-101]. Imidazolium-based membranes (as shown in Figure 2.9 (b)) have also been benchmarked against Nafion-117 (N-117), which is significantly thicker than N-212 (182 µm vs 58 µm), showing a high chemical stability with reported ion-exchange capacities (IECs) up to 1.43 meq g^{-1}.[96] With a lower thickness of 133 µm, the imidazolium-based membrane (PAEK-API 2.0) reported VO^{2+} crossover rates as low as 1.91 10^{-7} cm^2 min^{-1} (vs 20.28 10^{-7} cm^2 min^{-1} of Nafion-117) with a CE of 96.4% resulting in a 1.0% higher EE.

Functional groups with cyclic structures, such as pyrrolidinium, pyridinium and piperidinium, have been used with various polymer backbones such as low-cost polybenzimidazoles (PBIs), polysulfone, poly(arylene ether ketone) and poly(phenylene oxide).[84, 93, 102, 103] Since novel AEM materials show the potential to improve selectivity and CE for long-term cycling by being ion-selective and rejecting redox-active metal cations, it could be valuable to investigate novel AEM materials with a varying combination of materials/chemistries for the ICFB, especially considering the lack of recent ICFB literature.

2.3.2.2 Cation-exchange membranes (CEMs)

This section is divided into two parts. Firstly, membrane materials for three applications (ICFB, VFB and proton exchange membrane fuel cell (PEMFC): Section 2.3.2.2.1–

2.3.2.2.3) are discussed. The second part (Section 2.3.2.2.4) then elaborates on literature on specifically SPEEK in alignment with the objectives of this thesis.

2.3.2.2.1 ICFB

Literature on membrane materials for the ICFB other than per- and polyfluoroalkyl substances (PFAS) is scarce.[25] However, both PBI- and SPEEK-based membranes (low-cost, fluorine free and well-known for being more selective than PFSA membranes) that have been thoroughly investigated for VRBs and FCs, have recently been optimised for the ICFB.[19, 63, 104-106] Apart from the development of SPEEK that has been discussed in Section 2.2.2, PBI has also been modified to an optimal degree of sulfonation (DS) of 100% (see **Figure 2.10**) when seeking a low-cost alternative material to N-212 with a higher ionic selectivity. Wang et al. recently developed a thin (30 µm) sulfonated polybenzimidazole (PBI) for the ICFB that had an order of magnitude lower crossover of Fe^{3+} and Cr^{3+} species and obtained a capacity decay of 1.11% per cycle, coulombic efficiency (CE) of 98.2% and an EE of 83.2% at 80 mA cm^{-2}, with no observable chemical degradation (traditional electrolyte composition of 1.0 M Fe and 1.0 M Cr in 3.0 M HCl was used).[82]

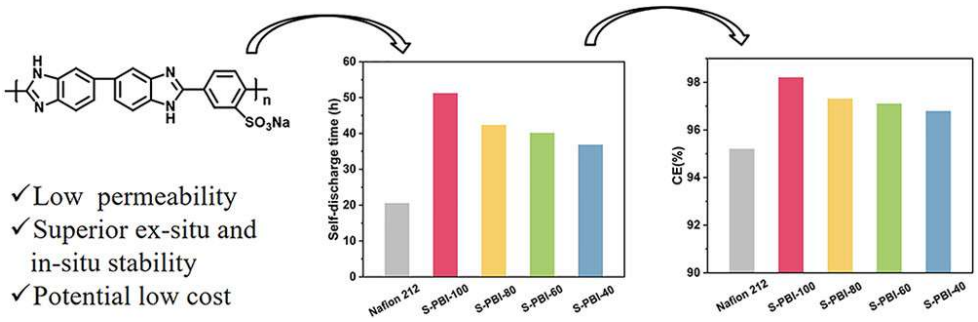

Figure 2.10: Graphical abstract of sulfonated PBI (S-PBI) structure, advantages and performance (self-discharge times and CE compared to N-212).[82]

2.3.2.2.2 VFB

For the VFB, various materials ranging in a degree of fluorination have been investigated for cross-linked and non-cross-linked polymer blends and non-blended membranes, varying in polymer backbones and acidic functional groups.[66, 67, 83, 99, 107] Within the frame of this study, this section will, however, focus mostly on SPEEK- and PBI-based polymers. Due to the ease and low cost of sulfonation, the VFB and PEMFC (Section 2.3.2.2.3) has seen ample developments, illustrating the suitability and potential for both SPEEK- and PBI-based membranes.[19, 63, 108-112]

While the aromaticity of these fluorine free polymers gives them chemical stability, the rigidity often carries the disadvantage of low ionic conductivity. Qian et al. for example, have shown that the narrower hydrophilic channels of a SPEEK membrane (80 µm

thickness and optimised DS of 63%) exhibit a 41.4% lower proton conductivity than N-212 (58 μm thickness).[107] However, Xi et al. demonstrated that the narrower channels also benefit ion selectivity, demonstrating a VO^{2+} permeability of 0.65×10^{-7} cm^2 min^{-1}, compared to 5.68×10^{-7} cm^2 min^{-1} of N-212, when using a 61% DS SPEEK membrane (70 μm thickness – at only 3.9% the manufacturing cost of Nafion (USD \$ m^{-2})).[113] The increased selectivity resulted in a higher overall EE of 85% at 30 °C compared to the 82% obtained when using N-212. However, during longer cycling tests, there have been reported cases of sudden battery failures, where pure SPEEK membranes either ruptured or a sudden and significant discharge capacity loss was observed.[114] It seems that this could have resulted from a degradation of the SPEEK (which is worsened with increasing DS), due to the high oxidation potential of the VO_2^+ ion.[114]

Blending of sulfonated ionomers have the unique advantage off allowing an IEC increase without increasing the degree of water swelling (retaining selectivity), thus providing a desired balance between selectivity and conductivity.[86, 115] Cross-linking acidic ionomers with basic polymers, such as PBIs, have yielded promising results for low-cost alternatives. For example, when using SPEEK-OPBI-based membranes that are mechanically strengthened with ionically cross-linked branches, EEs of 89.9% without signs of degradation after 350 cycles at a current density of 180 mA cm^{-2} have been obtained.[86] Similar to sulfonated materials, novel phosphonated poly(pentafluorostyrene) (PPFS) ionomers have also been cross-linked with PBI. After a high degree of phosphonation (74%, titrated IEC = 2.21 mmol g^{-1}) and cross-linking with hexafluoroisopropylidene-containing polybenzimidazole (F_6PBI), a 10-cycle CE of 99% and EE of 81% were obtained, with a 1600 cycle test showing only 30% capacity loss compared to the complete discharge capacity loss observed for N-212 before 100 cycles.[66]

2.3.2.2.3 PEMFC

Through studies on morphology, selection, alteration and combination of materials, membrane technology has delivered substantial advancements for FCs in recent years[63], with a significant focus on high temperature PEMFCs (HT-PEMFCs) which was driven by the accelerated reaction kinetics at higher temperatures combined with the thermal limitations of Nafion.[116] However, membrane challenges such as crossover, degradation and production cost still hinder market penetration, driving further research efforts.[117] While the use of non-fluorinated materials could significantly reduce production costs, their chemical stability often decreases due to the higher susceptibility to radical attacks and oxidation.[118, 119] Since aromaticity can offer chemical stability without fluorination, polymers with high aromaticity have been widely studied, focussing on their functionalisation (e.g., sulfonation for proton transport), modification or combination (with other materials) to improve flexibility and water uptake (WU).[116, 120-122]

While sulfonated polyimide (SPI)-based membranes, with or without blending with poly(ether sulfones) (PES) or poly(arylene ether sulfones), have shown excellent

proton conductivity, hydrolysis can occur at high temperatures.[123] Rigid polybenzimidazole (PBI)-based membranes, are widely used in PEMFCs due to their proton conductivity, low cost and high chemical and thermal stability (highly aromatic and rigid polymer backbone).[111] PBI flexibility is often improved by introducing a diphenyl ether group in the repeating chain to produce OPBIs, which, when doped with phosphoric acid (PA), have demonstrated a high conductivities and durability in HT-PEMFCs.[65, 124, 125]

2.3.2.2.4 SPEEK

One of the most promising alternatives to PFSAs are non-perfluorinated sulfonated aromatic polymers that are significantly cheaper to produce.[122, 126] Partially due to the ease of supply and availability of PEEK polymers, SPEEK is widely used and researched for proton exchange membranes (PEMs) in the field of PEMFCs and flow batteries.[63, 112] Compared to PFSAs, SPEEK is less acidic, has sulfonic groups with lower mobility, has higher thermal stability and has a more rigid backbone consisting of fluorine-free aromatic rings with ether and ketone groups, which also reduces cation conductivity by creating longer distances between proton exchange sites and thinner hydrophilic channels.[57, 63, 127] The crossover of cations is further reduced by the aromatic ring structures that advantageously introduce steric hindrance.[128] As discussed in Section 2.3.2.2.1, SPEEK is one of the few materials that have been considered and researched for ICFBs. In 2019, Sun et al. did a comparative study showing that SPEEK-based membranes not only bring down the CAPEX cost, elevated by the benchmark Nafion, but also reduce the metallic cation crossover rates when compared to Nafion (see **Figure 2.11** (a-c)).[129]

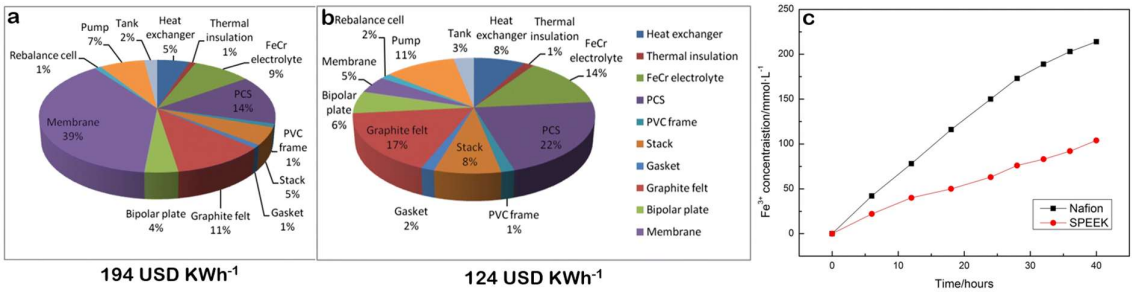

Figure 2.11: ICFB: (a) Nafion based CAPEX cost, (b) SPEEK based CAPEX cost and (c) metallic cation crossover rate comparison between Nafion and SPEEK.[129]

It is relatively easy to obtain the SPEEK ionomer free of by-products via sulfonation of commercially available PEEK powder with concentrated sulfuric acid (98%).[130] The sulfonation of PEEK is a second-order reaction, implying that the DS can be reasonably controlled by varying the reaction temperature and time, as shown in **Figure 2.12**.[131] Since the cell resistance is a function of the proton conductivity,

which is directly proportional to the IEC, high IECs in CEMs are desired.[132] However, the selectivity, influencing crossover, is negatively affected by an increasing IEC since swelling increases when increasing the hydrophilic component. As a result, accurately controlling the DS of SPEEK is crucial.[131, 133]

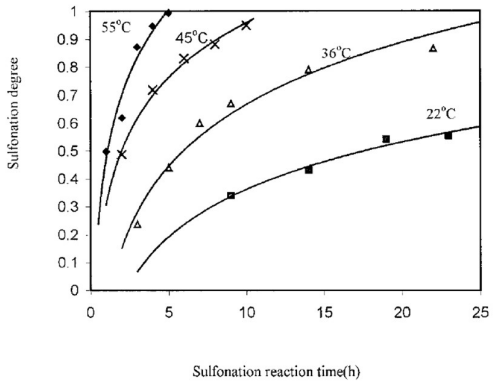

Figure 2.12: Second-order relationship between DS and sulfonation reaction time.[131]

If soluble, H-NMR spectroscopy can be used to characterise the synthesised SPEEK, where a sharp peak for the H_E proton appears due to the new $–SO_3H$ that introduces an asymmetric polar environment (see **Figure 2.13**).[104, 131]

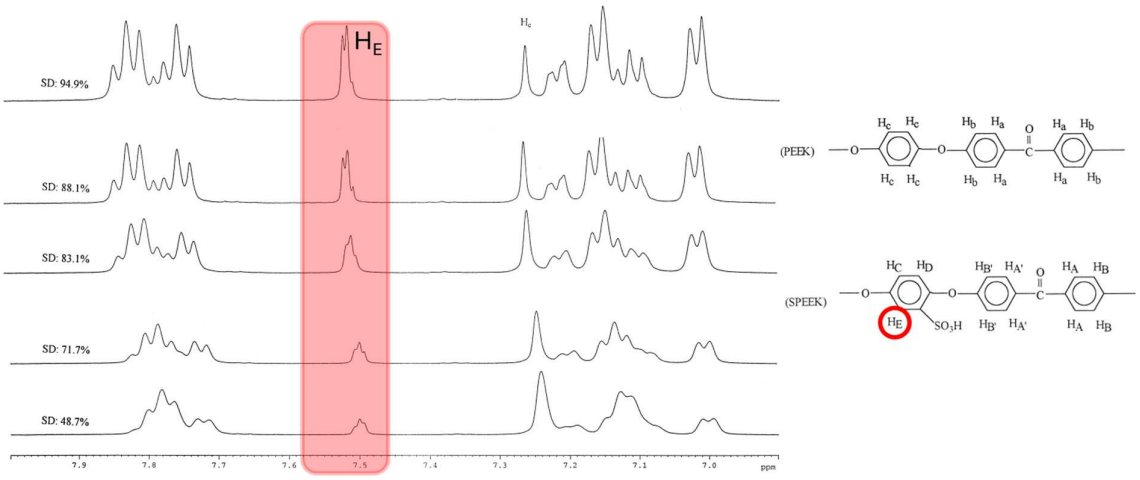

Figure 2.13: ^{1}H-NMR Spectra of SPEEK with various degrees of sulfonation.[131]

While the balance between proton conductivity and separation selectivity on overall performance highly depends on the application, the ideal DS reported is ~67% for VFBs, 70–75% for PEMFCs and 55–57% for ICFBs (dimensional stability must be

considered as SPEEK is water soluble at ambient temperatures at a DS > 80%).[49, 122, 129, 134, 135] The lower optimum DS in the ICFB results from the aqueous electrolyte and high operating temperature (65 °C), resulting in excessive swelling and dissolution of the highly polar SPEEK membranes. The optimal range of DS for the ICFB is also affected by the swelling ratio, which is proportional to the Cr^{3+} ion permeability.[49] The relatively high crystallinity of PEEK, which makes it highly resistant to most organic solvents, limits the casting solvents of low or 0% DS PEEK to either concentrated acids such as sulfuric acid (> 95%), which will heterogeneously alter the DS, or bulkier non-sulfonating acids such as methanesulfonic acid.[136, 137] Due to the heterogeneous sulfonation and the varying polarity of sulfonated PEEK molecules, the DS also affects the complexity of casting as molecules require a DS above 40% to be homogeneously soluble in polar organic solvents such as dimethylacetamide (DMAc), dimethylformamide (DMF), dimethyl sulfoxide (DMSO) and N-methyl-2-pyrrolidone (NMP).[112] As a result, it is crucial that the sulfonation is either carefully controlled at a lower DS, or a high enough DS is ensured to minimise the heterogeneity of the casting solution.

As mentioned in Section 2.2.2, the SPEEK-based membranes currently used for the ICFB are very thin (25 μm), which introduces the risk of puncture by the carbon felts. The casting of thicker membranes, however, is challenging due to the resulting high cell resistance stemming from the narrow ion-conducting channels of SPEEK.[49, 57] Apart from varying the thickness, the chemical stability, swelling, selectivity and mechanical properties can also be modified, for example by blending SPEEK with other polymers before casting.[129, 133] Adding polymers that are basic (e.g., PBI) can introduce ionic cross-linking while entanglement can be increased by adding inert polymers such as PEEK and poly(ether sulfone) (PES).[104] Blending acidic polymers such as SPEEK with basic polymers (e.g., PBI) is commonly used in membrane manufacture[138], to reduce excessive swelling, increase flexibility, reduce membrane cost and reduce electrolyte crossover, while retaining proton conductivity and allowing more variation in casting thickness.[67, 127, 133, 139] Blending of highly sulfonated SPEEK with PBI therefore offers dimensional stability in aqueous environments, while enhancing sulfonation for proton conducting channels, making it possible to optimise the conductivity and selectivity trade-off at any desired thickness and thus providing acid-base cross-linked membranes for FBs.[86, 140]

2.4 Membrane Casting

Since polymer/ionomer molecules of membranes typically have high molecular weights and chain lengths, colloidal solutions have long been used as the standard method of casting membrane films.[141] The formulation, casting and drying of a colloidal solution containing polymer/s and/or ionomer/s dissolved in suitable solvents (i.e., DMAc, DMF, DMSO or NMP) are crucial in the membrane development process as they influence properties such as thickness, uniformity, water uptake, matrix and surface morphology.[135, 142] Hence, this section provides a short overview of the

methods used in this study to prepare membranes, focussing on doctor blading (Section 2.4.1), spray coating (Section 2.4.2) and electrospinning (Section 2.4.3), before concluding with some other casting methods (Section 2.4.4).

2.4.1 Doctor blading

Doctor blade extrusion is one of the most common and well-established methods of membrane casting, where an elevated blade can be used to scrape a viscous colloidal solution to coat small or large areas in batches.[143] This method can be a low-cost manual method on lab scale to cast membranes on a glass plate, whereafter the solvent is evaporated by heating to leave behind a solid film, or adapted to industrial scale where membranes are manufactured in roll-to-roll processes (**Figure 2.14** (a, b)).

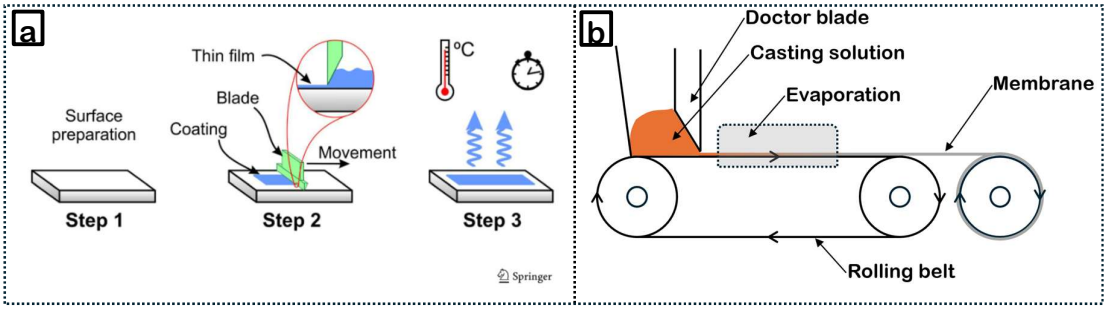

Figure 2.14: Illustration of doctor blade membrane casting method on a (a) batch and (b) roll-to-roll continuous scale.[144]

Doctor blading has multiple advantages, providing high accuracy and control over wet film thickness (uniform), being low in cost and complexity, and being suitable for a wide range of materials and a wide variety of applications.[145-147] However, this casting method has limitations since the polymer solution temperature is typically not controlled and high viscosities lower flow rates, requiring significant pressures for scraping which can lead to shearing forces and casting/coating defects.[148] Other disadvantages include the need for calibration (complexity depends on desired thickness) and limitations regarding casting of extremely thin films (< ~100 nm).[149]

2.4.2 Spray coating

Spray coating of solutions onto a surface is another conventional method to produce thin film membranes. It is widely used to produce dense ion-selective coatings on low-cost porous substrates, thereby producing multilayer composite membranes (see **Figure 2.15** (a, b)).[80, 138]

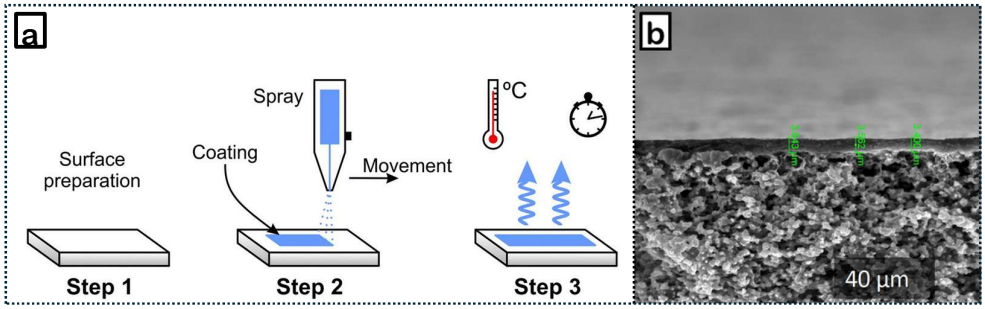

Figure 2.15: (a) Illustration of the spray coat membrane casting method [144] and (b) cross-section scanning electron microscopy (SEM) image of an ion-selective PBI layer on a porous PVDF support, manufactured by spray coating.[150]

While it is a slower method than doctor blading, spray coating is scalable and highly versatile, allowing membrane production from emulsions to solutions containing solid particles (e.g., catalysts for PEMFC applications), while membrane thickness can easily be controlled by the flow rate of the solution and the number of repeated passes.[151, 152] However, coating adhesion from poor polymer interaction often leads to delamination, while it can be difficult to control uniformity, which is influenced by solution viscosity, nozzle type, nozzle height and pressure.[153, 154]

2.4.3 Electrospinning

Electrospinning involves applying high voltage (kV-ranges) DC electricity between a target and a needle/nozzle, through which a polymer solution is forced at a certain flow rate to produce polymer nanofibres (see **Figure 2.16**).[155] This up-scalable method is mostly used in addition to other methods such as spray coating or printing to obtain advanced composite membranes that are reinforced by these fully connected fibre spun mats, showing longer membrane life-times than conventionally blended membranes.[156, 157] Another advantage is that blends of polymers with different polarity, i.e., SPEEK and PVDF, can be used to make fibre mat membranes, where fast vitrification inhibits the common issue of heterogeneous phase separation caused by the poor interaction of the blended polymers.[158]

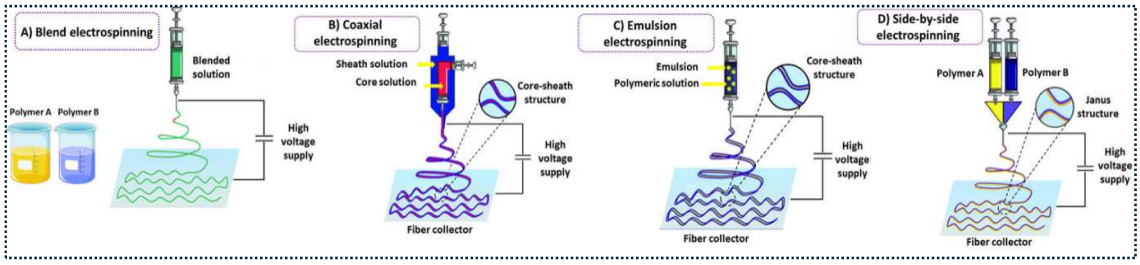

Figure 2.16: Schematic illustration of different conventional electrospinning methods.[159]

However, since only single strands of polymer can exit a nozzle during electrospinning, this process is a time-consuming membrane manufacturing method; for example, if the nozzle flow rate is 0.1 ml min^{-1}, only 1 g of membrane is deposited per hour using a 20 wt% spinning solution.[155, 158] Due to poor adhesion between fibres and supporting polymers, this method often requires the development and use of an additional heating press step to stabilise the mechanical strength of the membranes.[160] Due to the complexity required to obtain smooth operation by the range of optimisable variables (voltage, flow rate, nozzle diameter, viscosity and polymer concentrations), defects can also form when droplets form out of the spinning solution.[155]

2.4.4 Other casting methods

While the other membrane casting methods discussed in this subsection (slot die casting, printing and nip rolling) were not used in this study, they are worth mentioning as they are also used extensively both for research purposes and in industry.

2.4.4.1 Slot die casting

While similar to the doctor blade, the slot die favours up-scaling for continuous roll-to-roll casting and coating of polymer solutions, making it a common technique used for thin film casting in the polymer films industry.[148] Illustrated in **Figure 2.17** (a, b), a polymer solution is pumped into the slot die, depositing it on a glass plate or polymer substrate at a certain height from the die lip. However, smooth operation for defect free membranes requires a certain level of complexity, as film quality is influenced by various process parameters, including the solutions (temperature, flow rate and viscosity), substrates (velocity and wettability), and the slot die (inner width and height).[143, 148, 161]

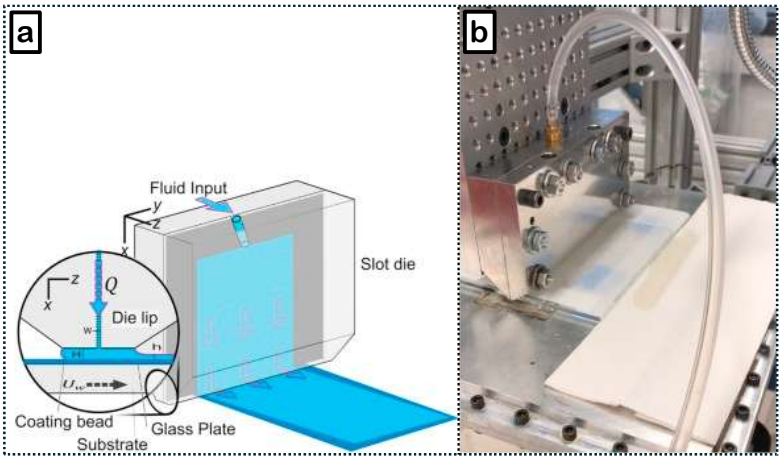

Figure 2.17: The lower section of a slot die coater: (a) schematic and (b) photographic image.[162]

2.4.4.2 Printing

The two different types of printing illustrated in **Figure 2.18** (a, b) that can be used to manufacture membrane films, electrospray and inkjet, have specifically been used in recent years to fabricate high-performance membrane electrode assemblies (MEAs) for FC applications.[156, 163] Inkjet printing, widely used in research using polymer solutions in commercial printers, can also be combined with other casting methods, such as electrospinning, to make advanced composite FC MEAs as illustrated in Figure 2.18 (c). Inkjet printing can be a cost-effective and accurate deposition method, since general inkjet printers can be used and chemical usage and waste is minimised, while allowing very precise solution deposition and control, resulting in the manufacture of ultrathin (< 10 nm) membrane and/or coating thicknesses.[164] Disadvantages include nozzle clogging from premature polymerisation and the need to fine-tune solution properties such as density and viscosity, which should be close to the properties of the water-based inks that the inkjet printers were initially designed for.

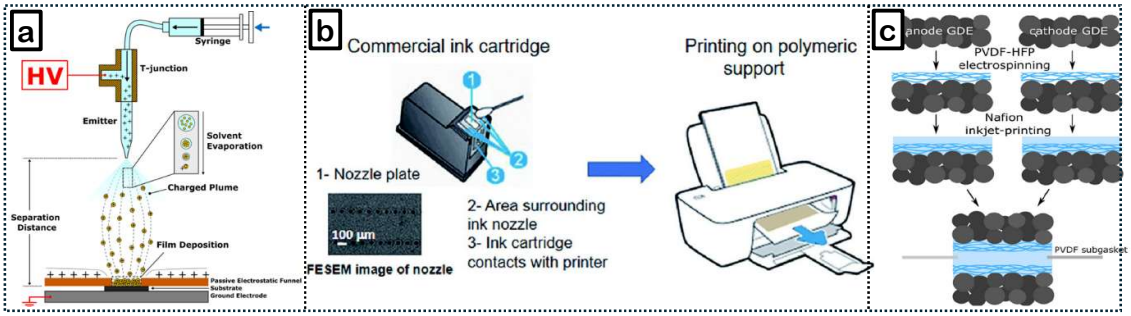

Figure 2.18: Illustration of (a) electrospray [165] and (b) inkjet printing.[164] (c) Composite sandwiched MEA with gas diffusion electrodes (GDEs) manufactured by combining electrospinning and inkjet printing of PVDF and Nafion polymer solutions.[157]

(Reproduced with permission from[157, 164, 165]. © 2021 American Chemical Society: 6093020724972, 2023 Elsevier: 6093050204867 and 2017 Elsevier: 6093040950848, respectively)

Electrospray polymer deposition is similar to spray coating, but on a significantly smaller scale with smaller aerosolised and ionised droplets that leave less defects and holes from having an enhanced interaction with the substrate acting as a counter electrode.[163] While it is also a low-cost method operating at ambient conditions, it naturally comes with a higher operating complexity introduced by a smaller coating area and more fine-tuneable variables than traditional spray coating.

2.4.4.3 Nip rolling

Nip roller extrusion is another industrial-scale technique that involves rolling a viscous polymer solution between two nip rollers to cast films, while uniform film thickness is controlled by adjusting the gap between the rollers.[143] Due to solutions sticking to rollers, barrier films are often required on which the membranes can be stored

afterwards. However, since this technique can generate pointed edges on the membrane surface and non-uniform thicknesses from solutions sticking to barrier films or rollers, its use is not reported as much in literature as the previously mentioned methods of solution casting.

2.5 Membrane Characterisation

Since both electrochemical performance and physico-chemical properties are crucial when determining the suitability and optimisation requirements of a membrane, this section will briefly discuss methods of membrane characterisation used in this study: flow battery performance (Section 2.5.1), scanning electron microscopy (SEM) (Section 2.5.2), ion exchange capacity (IEC) (Section 2.5.3), nuclear magnetic resonance (NMR) (Section 2.5.4), air permeance as Gurley number (Section 2.5.5) and tensile strength (Section 2.5.6).

2.5.1 Flow battery performance

For FB membrane development, the feedback and relevant adjustments to materials, apart from the chemical compatibility, are primarily driven by the FB performance compared to a benchmark value, which requires fair and repeatable testing of materials. Apart from the membranes, the system components with the most significant influence on FB performance are the electrolytes and electrodes.[9] Therefore, the testing environment should, where possible, be optimised in a simplistic and unbiased manner, such that the electrolyte and the electrodes can be kept as constant variables while focussing on the changes introduced by the different membrane materials. This section, therefore, firstly explores (Section 2.5.1.1.) possible optimisations for a lab-scale test station of the two most important variables (electrolyte and electrodes) influencing the performance, before discussing the ICFB performance parameters (Section 2.5.1.2) that could be used to evaluate the performance of both membranes and membrane materials.

2.5.1.1 Variables influencing performance

2.5.1.1.1 Electrolyte

In recent developments (see Section 2.2.2), the electrolyte composition for the ICFB was optimised at 1.3 M Fe(II)Cl_2 and 1.4 M Cr(III)Cl_3 dissolved in 1 M HCl, in the absence of a Bi catalyst, operated at 65 °C (to increase redox-active Cr complex concentration and minimise ohmic losses) [48] in an inert N_2 environment to inhibit oxygen intrusion.[39] Crossover rates, which are notably higher (~20 times using N-212) for the ICFB than the VFB, of the different metallic cations with varying cationic strengths, may differ for different membrane types.[54, 82] Since such crossover rates and directional changes would result in varying capacity decay rates and ASRs (due to the Nernst relationship), an equimolar composition of 1.3 M Fe/Cr (with optimal

capacity utilisation and VE as shown in **Figure 2.19**) would aid in promoting impartial performance measurements.[39]

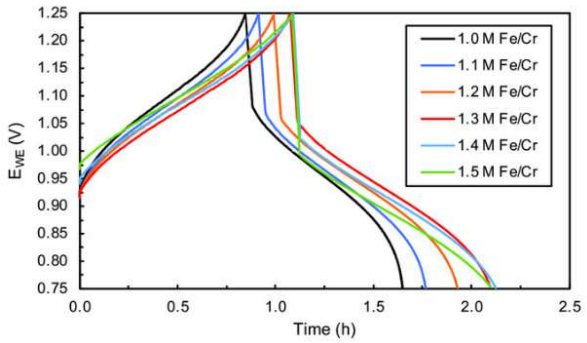

Figure 2.19: Charge and discharge curves with various equimolar Fe/Cr ratios in 1 M HCl.[39]

(Reproduced with permission from [39] under CC BY)

While literature is limited on the effects of electrolyte impurities in the ICFB, it is known that trace amounts of Cu and Ni negatively impact EE and capacity retention by depositing on the electrode and catalysing the HER.[42, 166] Due to possible impurities and precise equimolar concentration requirements of redox-active metals, the electrolyte used for this study was synthesised from salts of high chemical purity rather than using ferrochrome ore-derived electrolyte. Using a synthetic electrolyte ensures consistent results when evaluating membranes on lab scale.

2.5.1.1.2 Electrodes

The electrode assembly in FBs generally uses carbon cloth or felt as the electrode material, which is pressed against a conductive metal current collector, with a chemically inert conductive barrier between these two layers to separate the corrosive acidic environment from the current collector (see **Figure 2.20** (a)).[167] The most commonly used and commercially available material for chemically inert barriers are bipolar plates (BPPs), which conduct electricity through the high amount of graphite (~80%) [168] processed into polymer binders such as PE, polypropylene (PP), fluoroelastomers, poly(phenylene sulfide), nylon, epoxy or phenolic resins.[48, 167, 169] The high surface area carbon felt is placed inside the flow of the electrolyte (to distribute reactants onto the electrode surfaces) and pressed against the BPP. Since improving the distribution of electrolyte increases the EE while allowing a higher current density, designing different flow fields into BPPs (as shown in Figure 2.20 (b)) has received significant attention.[53, 170] However, a FB cell with no flow field in a flow-through cell configuration has the advantage of lower pumping losses and cost, while retaining simplicity and commercial availability, which arguably also favours consistent lab-scale cell design for membrane performance testing.

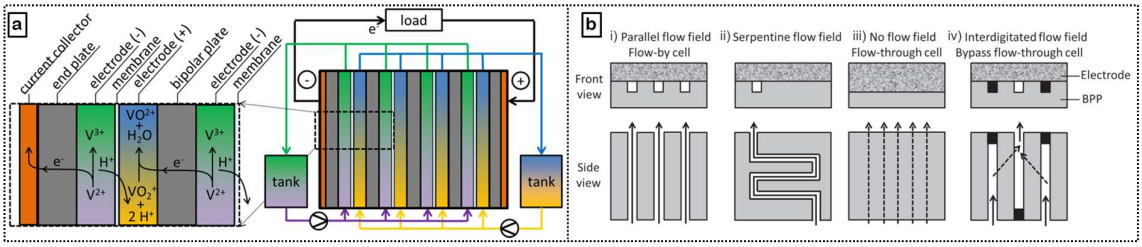

Figure 2.20: (a) Schematic overview of a VFB stack (discharging) with an enlarged view of the migration of protons through a membrane and electrons through BPP (in-between electrode and current collector). (b) Front and side view of different BPP designs on carbon felt.[167]

While the ICFB has seen some promising developments in enhancing electrode materials in recent years [40, 171, 172], the VFB has seen significantly more developments over the past three decades in carbon-based electrode material development to improve physico-chemical properties, including thermal and chemical treatments, loading of nanomaterials, heteroatom doping and metal loading.[173-177] Due to the similar operation and acidic aqueous environments of the ICFB and VFB, electrode developments and optimisations for the VFB could be adopted for the ICFB.[8] One of the simplest and most cost-effective modifications of commercially available electrode materials entails a simple thermal treatment of the carbon felt in ambient air, which increases i) the porosity, ii) the amount of oxygen/hydroxyl functional groups through partial oxidation of the carbon (**Figure 2.21** (b+c)), iii) the hydrophilicity, iv) the surface area and v) the reaction kinetics.[178, 179] Additionally, ASR data at different felt compression ratios in a single-cell VFB setup revealed that polyacrylonitrile (PAN) precursor felts at a compression ratio of 30% (Figure 2.21 (a)) outperformed (treatment time, pore size, mass reduction and oxygen content) rayon felts when using an optimised thermal treatment of 600 °C for 30 minutes.[178, 179]

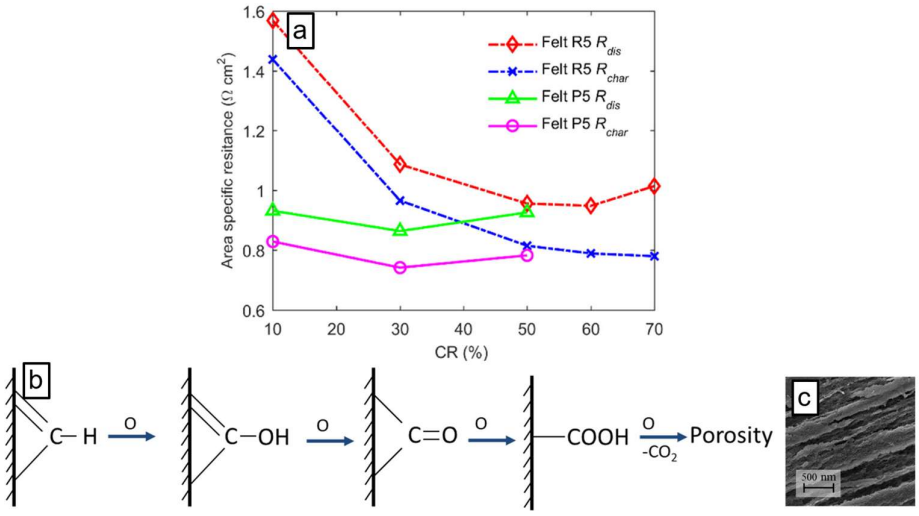

Figure 2.21: (a) ASRs of different carbon felts [178] vs various compression ratios in a VFB cell. (b) Illustration and (c) SEM imaging of oxidation of the carbon strand surface.[179]

Seeing that thermally treated PAN felts can achieve > 80% EE at 200 mA cm^{-2} in a VFB without requiring additional chemicals, gasses, special equipment or materials such as nanoparticles [178], the simplicity allows the repeatable screening and development of different membrane materials where felts can be exchanged regularly.

2.5.1.2 Performance parameters

By charging and discharging a flow battery electrolyte at a constant current, the performance parameters for different membranes, i.e. coulombic efficiency (CE), voltage efficiency (VE), capacities and ASR can be calculated (see **Table 2.1**) from the measured voltage response.[48, 180, 181] These measurements, in conjunction with crossover and self-discharge measurements, can then be used as primary indicators for further optimisation of membrane parameters such as material composition, casting process, thickness and IEC, since the CE and VE indicate a membrane's ionic selectivity and conductivity (see Section 2.3.2), respectively.[19, 49, 85, 139, 182, 183]

Table 2.1: List of ICFB performance parameter equations.

Parameter	Equation	#
Coulombic Efficiency (%)	$CE = \frac{A \times h_{(Discharge)}}{A \times h_{(Charge)}} \times 100\%$	(2.1)
A = current (A) and h = time of each charge or discharge cycle (h)		
Voltage Efficiency (%)	$VE = \frac{\bar{V}_{(Discharge)}}{\bar{V}_{(Charge)}} \times 100\%$	(2.2)
$\bar{V}$ = average voltage (V) calculated for the charge or discharge cycle		
Energy Efficiency (%)	$EE = CE \times VE$	(2.3)
Discharge Capacity (A h L^{-1})	$Cap_{(Discharge)} = \frac{A \times h_{(Discharge)}}{L}$	(2.4)
A = discharging current (A), h = time of a discharge cycle (h) and L = volume of total electrolyte (L)		
Capacity decay (% $cycle^{-1}$)	$\frac{\left\lvert Cap_{(Discharge)}(n) - Cap_{(Discharge)}(n+1)\right\rvert}{Cap_{(Discharge)}(n)} \times 100\%$	(2.5)
n = the cycle number		
Area Specific Resistance (Ω cm^2)	$ASR = \left(\frac{\bar{V}_{(Charge)} - \bar{V}_{(Discharge)}}{2}\right) \times \frac{1}{Current\ density}$	(2.6)
Current density expressed in A cm^{-2}		

2.5.2 SEM

SEM is commonly used to characterise surface and cross-section morphologies of porous and dense membranes, specifically before and after battery testing, to investigate visible degradation in their respective chemical environments.[184-187] SEMs with an integrated energy dispersive X-ray (EDX) detector can use the X-rays generated by the sample to combine microscope images with surface elemental mapping to investigate elemental distribution, which can provide more information for membrane synthesis and optimisation (see **Figure 2.22**).[188]

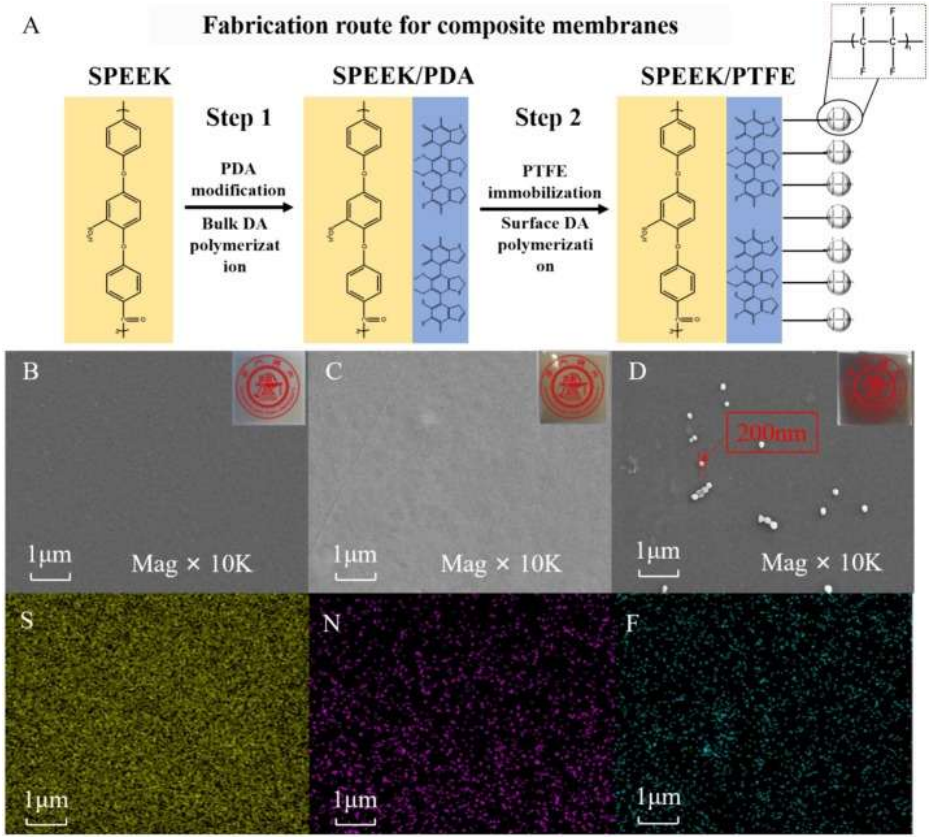

Figure 2.22: (A) The schematic diagram of the fabrication route for a SPEEK/PTFE composite membrane. SEM imaging of (B) SPEEK, (C) SPEEK/PDA and (D) SPEEK/PTFE membranes. EDX elemental mapping of S, N and F of the SPEEK/PTFE membrane.[181]

2.5.3 IEC

Measuring the IEC of membranes helps quantify the number of functional groups on the polymer/s available to facilitate ion exchange, measured in the amount of moles per gram of dry membrane material (mmol g^{-1}). As discussed in Section 2.3.2.2.4, higher IECs reduce resistances, since polymers with a higher concentration of polar functional groups have larger ionic clusters, which in turn increase water uptake (WU), swelling and unwanted hydraulic crossover.[189] Tracking changes in IEC values of membranes used in flow batteries can also indicate losses, or permanent occupation of functional groups, indicating degradation or chemical incompatibilities with the electrical and chemical environment that they are exposed to.[62, 190] Since the IEC can be correlated to the chemical compatibility and performance, the accurate determination of a membrane's IEC is essential to provide feedback for further material optimisation and developments.

The standard method for IEC determination involves protonation of a membrane sample in an acid (in the case of CEMs), followed by titration (using a pH probe and

adequate stirring) with a dilute basic solution (typically NaOH) to a pH of ~7.[191] Since acidic functional groups (i.e., $–SO_3$-H and $–PO_3$-H_2) are enclosed within the polymer matrix, diffusion rates can be slow during titration and affect the accuracy of measurements. Therefore, protons need to be extracted before titration by exchanging with Na^+ using a saturated NaCl solution. Finally, the IEC of membrane samples are determined using the volume of NaOH consumed and the dry membrane weight using Equation 2.7.[191]

$$IEC = mmol\ H^+\ or\ g^{-1}\ or\ meq\ H^+ g^{-1} = \frac{V_{mL\ NaOH} \times M_{mol\ L^{-1} NaOH}}{Weight_{g\ (dry\ membrane)}} \qquad (2.7)$$

2.5.4 NMR

If a high molecular weight polymer can be dissolved in a suitable deuterated solvent, liquid-state NMR can be a useful tool to determine the DS of a CEM as mentioned in Section 2.3.2.2.4 and illustrated in Figure 2.13.[192] Both H^1 and C^{13} NMR have been used to characterise membrane syntheses and degradations (for FCs and FBs), where the spectra can provide both molecular and atomic information of the polymer backbones, sidechains and functional groups.[184, 193] The analytical technique has potential drawbacks, however, as interpretation of peaks and chemical shifts for structure elucidation can be complex, often requiring in-depth knowledge on a specific polymer, or additional analytical information.[194] Since equipment with a high resolution and low noise require a cryogenically cooled superconducting magnet, this analytical technique is often highly specialised and expensive, which could limit accessibility.[195, 196]

2.5.5 Air permeance

This analytical tool is suitable for membranes that are porous throughout. As MPSs typically do not contain functional groups, their corresponding battery performance is largely determined by their permeability and physical morphology. The Gurley number of an MPS, expressed as Gurley seconds, which was originally developed for quality control in the paper industry, is commonly used today for LiBs and some FB separators where the electrochemical performance is determined by the ion permeability (illustrated in **Figure 2.23**).[197-200] According to the JIS (Japanese Industrial Standards)-P8117, the air permeance is defined as the time it takes for a constant air volume (100 mL) to pass through a 1 in^2 (6.45 cm^2) membrane specimen at a transmembrane pressure of 1.22 kPa.[201]

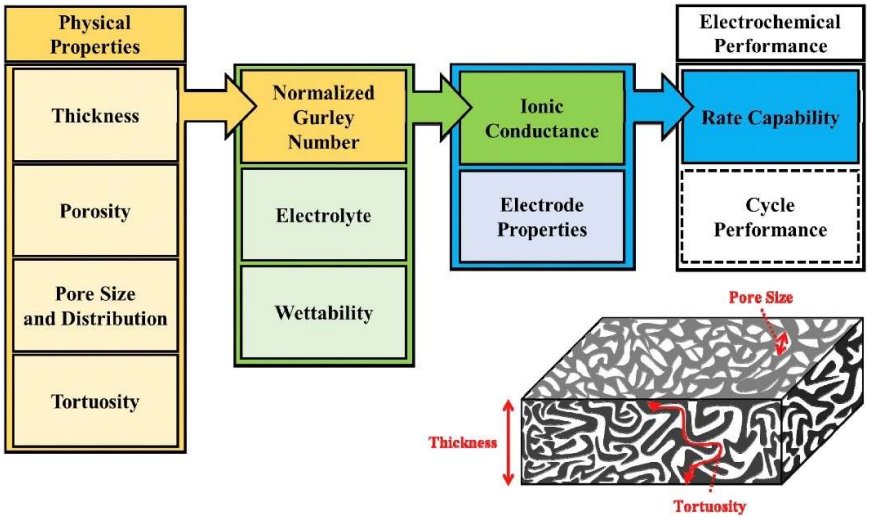

Figure 2.23: Correlation between physical properties and electrochemical performance.

(Reprint with permission from[198]. © 2016 Elsevier, License ID: 6100760621679)

Considering the limited knowledge on the application of MPSs in the ICFB, it can be useful to measure the air permeance (Gurley seconds) of both commercial and novel MPSs. Values could be compared and correlated with the ICFB performance to determine whether an ideal range of Gurley seconds exists for a separator for sufficient ICFB functionality.

2.5.6 Tensile strength

Since IEMs must provide continuous ion exchange functionality in FC or FB systems for long-term operation, the mechanical strength of a membrane can provide a measure of its long-term chemical stability and resistance against carbon felt puncture or pressure-induced rupturing.[19, 63, 127] The most common and straightforward method entails measuring both the maximum stress before breaking (tensile strength in MPa) and amount of elongation at breaking point.[202] With more advanced automated instruments, multiple data points for stress can be plotted against elongation (see **Figure 2.24**), which can also be used to calculate the Young's Modulus (which quantifies elasticity).[203] Since polymer backbone degradation, or changes in a matrix, can be investigated and compared using simple tensile strengths tests of membrane materials before and after electrolyte exposure, this measurement is regarded as a useful tool for membrane characterisation.[204]

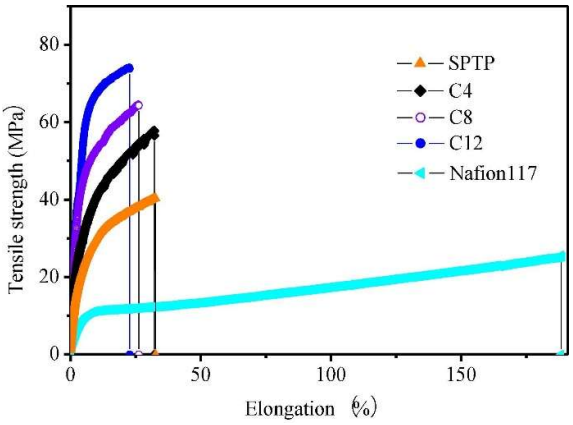

Figure 2.24: Mechanical properties of sulfonated poly(terphenylene) (SPTP), Nafion117, and SPTP/PBI acid-base blend membranes with blend ratios of 100:4 (C4), 100:8 (C8), and 100:12 (C12).[127]

2.6. Conclusion

Despite the advancements of the more established VFB and FC, and various initial challenges experienced with the ICFB, research on the ICFB has increased in the last decade due to its low cost (abundant Fe and Cr) and the concurrent improvement of membrane materials. Focussing on alternatives to perfluorinated polymers, VFB and FC research has delivered a variety of high-performance porous and non-porous environmentally benign, cost-effective and chemically stable membranes, including highly conductive sulfonic- and phosphonic-acid-based CEMs that have been shown to outperform Nafion. For the ICFB, literature on membrane development remains limited, mainly focussing on thin SPEEK and PBI based CEMs. Further research should focus on increasing the thickness and conductivity of SPEEK-based membranes (with DS limitations), or cross-linking (to overcome DS limitations and reduce puncture risks), while other PBI polymers that have been successfully used in FC and VFB applications should be evaluated in the ICFB. The limited literature on MPSs and current unsuitability of AEMs in the ICFB also warrant further investigations.

After developing a polymer, choosing an appropriate casting technique is important, where doctor blading provides a simple and accurate lab-scale method for a range of materials and membrane thicknesses (25–70 µm). Both in-situ and ex-situ characterisation aid in evaluating the synthesised membranes. After optimising the electrode/electrode (thermally treated PAN) and electrolyte (equimolar 1.3 M Fe/Cr dissolved in 1.0 M HCl) compositions, the membrane performance in the ICFB can be assessed using efficiencies as performance parameters (CE, VE, EE), discharge capacity, capacity decay and ASR data. Other analytical techniques that can aid in test-station performance correlation include SEM imaging, IEC titration, NMR spectroscopy, ion-permeability measurements and tensile strength testing, where IEC and NMR data provide information on the DS, which affects the selectivity and conductivity of CEMs. Simple and cost-effective Gurley measurements can be useful to relate physical properties to electrochemical performance when investigating MPSs.

References

[1] M. Gasser, S. Pezzutto, W. Sparber, E. Wilczynski, Public Research and Development Funding for Renewable Energy Technologies in Europe: A Cross-Country Analysis, Journal, 14 (2022). 10.3390/su14095557.

[2] K. Menyah, Y. Wolde-Rufael, CO2 emissions, nuclear energy, renewable energy and economic growth in the US, Energy Policy, 38 (2010) 2911-2915. https://doi.org/10.1016/j.enpol.2010.01.024.

[3] N. Blume, M. Neidhart, P. Mardilovich, C. Minke, Life cycle assessment of a vanadium flow battery based on manufacturer data, Procedia CIRP, 116 (2023) 648-653. https://doi.org/10.1016/j.procir.2023.02.109.

[4] Y. Huang, J. Li, Key Challenges for Grid-Scale Lithium-Ion Battery Energy Storage, Advanced Energy Materials, 12 (2022) 2202197. https://doi.org/10.1002/aenm.202202197.

[5] S. Ha, K.G. Gallagher, Estimating the system price of redox flow batteries for grid storage, Journal of Power Sources, 296 (2015) 122-132. https://doi.org/10.1016/j.jpowsour.2015.07.004.

[6] A.A. Kebede, T. Kalogiannis, J. Van Mierlo, M. Berecibar, A comprehensive review of stationary energy storage devices for large scale renewable energy sources grid integration, Renewable and Sustainable Energy Reviews, 159 (2022). 10.1016/j.rser.2022.112213.

[7] C.M. Costa, J.C. Barbosa, R. Gonçalves, H. Castro, F.J.D. Campo, S. Lanceros-Méndez, Recycling and environmental issues of lithium-ion batteries: Advances, challenges and opportunities, Energy Storage Materials, 37 (2021) 433-465. https://doi.org/10.1016/j.ensm.2021.02.032.

[8] Y.K. Zeng, T.S. Zhao, L. An, X.L. Zhou, L. Wei, A comparative study of all-vanadium and iron-chromium redox flow batteries for large-scale energy storage, Journal of Power Sources, 300 (2015) 438-443. https://doi.org/10.1016/j.jpowsour.2015.09.100.

[9] C. Sun, H. Zhang, Review of the Development of First-Generation Redox Flow Batteries: Iron-Chromium System, ChemSusChem, 15 (2021) 15. 10.1002/cssc.202101798.

[10] J. Noack, Standards for Flow Batteries, in: Flow Batteries, 2023, pp. 155-174. https://doi.org/10.1002/9783527832767.ch7.

[11] K. Lourenssen, J. Williams, F. Ahmadpour, R. Clemmer, S. Tasnim, Vanadium redox flow batteries: A comprehensive review, Journal of Energy Storage, 25 (2019) 100844. https://doi.org/10.1016/j.est.2019.100844.

[12] Z. Huang, A. Mu, Research and analysis of performance improvement of vanadium redox flow battery in microgrid: A technology review, International Journal of Energy Research, 45 (2021) 14170–14193. 10.1002/er.6716.

[13] M. Han, K. Zheng, H. Hu, J. Liu, Z. Zou, F. Yu, Y. Mu, W. Li, L. Wei, L. Zeng, Long-duration energy-storage technologies: A stabilizer for new power systems, The Innovation Energy, 2 (2025) 100077.

[14] Rongke Power Commissions Another 100MW/400MWh Vanadium Flow Battery Project in Northwest China, Surpassing 3.5 GWh in Global Installations, RKP © 2025 https://rkpstorage.com/?p=5187 (accessed: 2025/08).

[15] M. Bartolozzi, Development of redox flow batteries. A historical bibliography, Journal of Power Sources, 27 (1989) 219-234. https://doi.org/10.1016/0378-7753(89)80037-0.

[16] M. Warshay, L.O. Wright, L.R. Center, Cost and Size Estimates for an Electrochemical Bulk Energy Storage Concept, National Aeronautics and Space Administration, 1975.

[17] J. Walther, C. Greco, R. Rusinko, A. Wadsworth III, Study to establish cost projections for production of Redox chemicals, (1982).

[18] M. Wu, M. Nan, Y. Ye, M. Yang, L. Qiao, H. Zhang, X. Ma, A highly active electrolyte for high-capacity iron-chromium flow batteries, Applied Energy, 358 (2024) 122534. https://doi.org/10.1016/j.apenergy.2023.122534.

[19] C.H.L. Tempelman, J.F. Jacobs, R.M. Balzer, V. Degirmenci, Membranes for all vanadium redox flow batteries, Journal of Energy Storage, 32 (2020) 101754. https://doi.org/10.1016/j.est.2020.101754.

[20] V2O5 Vanadium Pentoxide Flake 98% Price, Vanadium Price Workflow Co.,Ltd. https://vanadiumprice.com/ (accessed: 2025/08).

[21] Lithium carbonate min 99.5% cif China prices USD/kg, Argus Media group https://www.argusmedia.com/metals-platform/price/assessment/lithium-carbonate-min-99-5--cif-china-prices-PA00233610000 (accessed: 2025/08).

[22] South African High-carbon Ferrochrome Price, USD/50referenceton, 2025 SMM Information & Technology Co., Ltd. https://www.metal.com/en/prices/202412310001 (accessed: 2025/08).

[23] Abundance in Earth's Crust of the elements, data provided by Mathematica's ElementData function from Wolfram Research, Inc., https://periodictable.com/Properties/A/CrustAbundance.an.html (accessed: 2025/08).
[24] J.P. du Toit, H.M. Krieg, N. Mans, D.J. van der Westhuizen, UV–Vis spectrophotometric analytical technique for monitoring Fe2+ in the positive electrolyte of an ICRFB, Journal of Power Sources, 553 (2023) 232178. https://doi.org/10.1016/j.jpowsour.2022.232178.
[25] N. Mans, D.J. van der Westhuizen, H.M. Krieg, Membrane Screening for Iron–Chrome Redox Flow Batteries, Advanced Energy and Sustainability Research, 5 (2024) 2300195. https://doi.org/10.1002/aesr.202300195.
[26] P.M. Chennels, S. Roopa, J.F. Bijzet, O.S.L. Bruinsma, (2025). *IRON CHROMIUM ELECTROLYTES* (WO/2025/008718). E.P. Office.
[27] A.Z. Weber, M.M. Mench, J.P. Meyers, P.N. Ross, J.T. Gostick, Q. Liu, Redox flow batteries: a review, Journal of Applied Electrochemistry, 41 (2011) 1137-1164. 10.1007/s10800-011-0348-2.
[28] L.H. Thaller, Recent advances in Redox Flow Cell Storage Systems, (1979).
[29] P. Odonnell, R.F. Gahn, in: Photovoltaic Specialist Conf., 1976.
[30] R.F. Gann, N.H. Hagedorn, J.A. Johnson, Cycling Performance of the Iron-Chromium Redox Energy Storage System, (1985).
[31] S.S. Alexander, R.R. Geoffroy, R.B. Hodgdon, Anion selective membrane, (1975).
[32] N.H. Hagedorn, NASA Redox Storage System Development Project. Final Report, (1984).
[33] J.S. Ling, J. Charleston, Advances in Membrane Technology for the NASA Redox Energy Storage System, (1980).
[34] R. Assink, Fouling mechanism of separator membranes for the iron/chromium redox battery, Journal of membrane science, 17 (1984) 205-217.
[35] G. Codina, A. Aldaz, Scale-up studies of an Fe/Cr redox flow battery based on shunt current analysis, Journal of Applied Electrochemistry, 22 (1992) 668-674. 10.1007/BF01092617.
[36] E. Hollax, D.S. Cheng, The influence of oxidative pretreatment of graphite electrodes on the catalysis of the Cr3+ Cr2+ and Fe3+ Fe2+ redox reactions, Carbon, 23 (1985) 655-664.
[37] D.A. Johnson, M.A. Reid, Chemical and Electrochemical Behavior of the Cr(III)/Cr(II) Half-Cell in the Iron-Chromium Redox Energy Storage System, Journal of The Electrochemical Society, 132 (1985) 1058-1062. 10.1149/1.2114015.
[38] R.F. Gann, N.H. Hagedorn, J.S. Ling, Single Cell Performance Studies on the Fe/Cr Redox Energy Storage System Using Mixed Reactant Solutions at Elevated Temperature, (1983).
[39] N. Mans, H.M. Krieg, D.J. van der Westhuizen, The Effect of Electrolyte Composition on the Performance of a Single-Cell Iron–Chromium Flow Battery, Advanced Energy and Sustainability Research, 5 (2024) 2300238. https://doi.org/10.1002/aesr.202300238.
[40] M. Wu, M. Nan, S. Liu, C. Zhong, L. Qiao, H. Zhang, X. Ma, Multi-dimensional Bi@C electrocatalyst for Cr3+/Cr2+ redox reaction boosting high-performance iron-chromium flow batteries, Science China Chemistry, 68 (2025) 2735-2743. 10.1007/s11426-024-2375-6.
[41] Y. Liu, Y. Niu, C. Guo, F. Qu, Z. Liu, X. Zhou, W. Guo, C. Xu, Q. Xu, Nitrogen-Doped Bismuth Oxide-Modified Carbon Cloth as a Bifunctional Electrocatalyst for Iron–Chromium Redox Flow Batteries, Energy & Fuels, 38 (2024) 12202-12211. 10.1021/acs.energyfuels.4c01739.
[42] N. Mans, D.J. van der Westhuizen, H.M. Krieg, The effect of common metallic impurities on the performance of a single-cell iron-chromium redox flow battery, Electrochimica Acta, 526 (2025) 146167. https://doi.org/10.1016/j.electacta.2025.146167.
[43] Y.K. Zeng, T.S. Zhao, X.L. Zhou, J. Zou, Y.X. Ren, A hydrogen-ferric ion rebalance cell operating at low hydrogen concentrations for capacity restoration of iron-chromium redox flow batteries, Journal of Power Sources, 352 (2017) 77-82. https://doi.org/10.1016/j.jpowsour.2017.03.125.
[44] T. Herbert, N. Mans, D.J. van der Westhuizen, H.M. Krieg, Investigation of ICRFB hybrid rebalancing systems, Journal of Power Sources, 594 (2024) 234029. https://doi.org/10.1016/j.jpowsour.2023.234029.
[45] J.P. du Toit, H. Krieg, N. Mans, D.J. van der Westhuizen, Purification and analysis of ferrous chloride for an Fe/Cr flow battery application, Masters Dissertation (2022).
[46] C.T.C. Wan, R.R. Jacquemond, Y.M. Chiang, K. Nijmeijer, F.R. Brushett, A. Forner-Cuenca, Non-Solvent Induced Phase Separation Enables Designer Redox Flow Battery Electrodes, Adv. Mater., 33 (2021) 2006716. 10.1002/adma.202006716.
[47] X. Zhang, D. Zhang, Z. Xu, K. Zhang, Y. Zhang, M. Jing, L. Liu, Z. Zhang, N. Pu, J. Liu, C. Yan, A pioneering melamine foam-based electrode via facile synthesis as prospective direction for vanadium redox flow batteries, Chem. Eng. J., 439 (2022) 135718. https://doi.org/10.1016/j.cej.2022.135718.

[48] Y.K. Zeng, T.S. Zhao, X.L. Zhou, L. Zeng, L. Wei, The effects of design parameters on the charge-discharge performance of iron-chromium redox flow batteries, Applied Energy, 182 (2016) 204-209. https://doi.org/10.1016/j.apenergy.2016.08.135.
[49] E. Bai, H. Zhu, C. Sun, G. Liu, X. Xie, C. Xu, S. Wu, A Comparative Study of Nafion 212 and Sulfonated Poly(Ether Ether Ketone) Membranes with Different Degrees of Sulfonation on the Performance of Iron-Chromium Redox Flow Battery, Journal, 13 (2023). 10.3390/membranes13100820.
[50] M. Jung, W. Lee, N. Nambi Krishnan, S. Kim, G. Gupta, L. Komsiyska, C. Harms, Y. Kwon, D. Henkensmeier, Porous-Nafion/PBI composite membranes and Nafion/PBI blend membranes for vanadium redox flow batteries, Appl. Surf. Sci., 450 (2018) 301-311. https://doi.org/10.1016/j.apsusc.2018.04.198.
[51] D. Chen, M.A. Hickner, E. Agar, E.C. Kumbur, Selective anion exchange membranes for high coulombic efficiency vanadium redox flow batteries, Electrochemistry Communications, 26 (2013) 37-40. https://doi.org/10.1016/j.elecom.2012.10.007.
[52] N. Lingappan, W. Lee, S. Passerini, M. Pecht, A comprehensive review of separator membranes in lithium-ion batteries, Renewable and Sustainable Energy Reviews, 187 (2023) 113726. https://doi.org/10.1016/j.rser.2023.113726.
[53] Y.K. Zeng, X.L. Zhou, L. An, L. Wei, T.S. Zhao, A high-performance flow-field structured iron-chromium redox flow battery, Journal of Power Sources, 324 (2016) 738-744. https://doi.org/10.1016/j.jpowsour.2016.05.138.
[54] Y.S. Kim, S.H. Oh, E. Kim, D. Kim, S. Kim, C.H. Chu, K. Park, Iron-chrome crossover through nafion membrane in iron-chrome redox flow battery, Korean Chemical Engineering Research, 56 (2018) 24-28. 10.9713/kcer.2018.56.1.24.
[55] K. Miyatake, Membrane Electrolytesmembraneelectrolytes, from Perfluoro Sulfonic Acid (PFSA) to Hydrocarbon Ionomers, in: R.A. Meyers (Ed.) Encyclopedia of Sustainability Science and Technology, Springer New York, New York, NY, 2012, pp. 6538-6565. 10.1007/978-1-4419-0851-3_146.
[56] R.-S. Yu, H.-C. Yu, Y.-F. Yang, S. Singh, A Global Overview of Per- and Polyfluoroalkyl Substance Regulatory Strategies and Their Environmental Impact, Journal, 13 (2025). 10.3390/toxics13040251.
[57] J. Molina, J.J. de Pablo, J.P. Hernández-Ortiz, Structure and proton conduction in sulfonated poly(ether ether ketone) semi-permeable membranes: a multi-scale computational approach, Physical Chemistry Chemical Physics, 21 (2019) 9362-9375. 10.1039/C9CP00598F.
[58] P. Sheth, D. Patil, B. Kandasubramanian, N. Mayilswamy, Advancements in chitosan membranes for promising secondary batteries, Polym. Bull., 81 (2024) 15319-15348. 10.1007/s00289-024-05448-x.
[59] H.-L. Wu, C.-C.M. Ma, C.-H. Li, C.-Y. Chen, Swelling behavior and solubility parameter of sulfonated poly(ether ether ketone), Journal of Polymer Science Part B: Polymer Physics, 44 (2006) 3128-3134. https://doi.org/10.1002/polb.20964.
[60] M.A. Yandrasits, M.J. Lindell, S.J. Hamrock, New directions in perfluoroalkyl sulfonic acid–based proton-exchange membranes, Current Opinion in Electrochemistry, 18 (2019) 90-98. https://doi.org/10.1016/j.coelec.2019.10.012.
[61] W. Wei, L. Qingtao, L. Bin, W. Xiaoliang, L. Liyu, Y. Zhenguo, Recent Progress in Redox Flow Battery Research and Development, Advanced Functional Materials, 23 (2013) 970-986. https://doi.org/10.1002/adfm.201200694.
[62] F. Lulay, C. Weidlich, M. Valtiner, C.M. Pichler, Membrane degradation in redox flow batteries, Green Chemistry Letters and Reviews, 16 (2023) 2274529. 10.1080/17518253.2023.2274529.
[63] S. Ahmad, T. Nawaz, A. Ali, M.F. Orhan, A. Samreen, A.M. Kannan, An overview of proton exchange membranes for fuel cells: Materials and manufacturing, International Journal of Hydrogen Energy, 47 (2022) 19086-19131. https://doi.org/10.1016/j.ijhydene.2022.04.099.
[64] W. Lu, Z. Yuan, Y. Zhao, H. Zhang, H. Zhang, X. Li, Porous membranes in secondary battery technologies, Chemical Society Reviews, 46 (2017) 2199-2236. 10.1039/C6CS00823B.
[65] V. Atanasov, A.S. Lee, E.J. Park, S. Maurya, E.D. Baca, C. Fujimoto, M. Hibbs, I. Matanovic, J. Kerres, Y.S. Kim, Synergistically integrated phosphonated poly(pentafluorostyrene) for fuel cells, Nature Materials, 20 (2021) 370-377. 10.1038/s41563-020-00841-z.
[66] E. Bülbül, V. Atanasov, M. Mehlhorn, M. Bürger, A. Chromik, T. Häring, J. Kerres, Highly phosphonated polypentafluorostyrene blended with polybenzimidazole: Application in vanadium redox flow battery, Journal of Membrane Science, 570-571 (2019) 194-203. https://doi.org/10.1016/j.memsci.2018.10.027.

[67] A. Chromik, A.R. dos Santos, T. Turek, U. Kunz, T. Häring, J. Kerres, Stability of acid-excess acid–base blend membranes in all-vanadium redox-flow batteries, Journal of Membrane Science, 476 (2015) 148-155. https://doi.org/10.1016/j.memsci.2014.11.036.
[68] C.G. Morandi, R. Peach, H.M. Krieg, J. Kerres, Novel imidazolium-functionalized anion-exchange polymer PBI blend membranes, Journal of Membrane Science, 476 (2015) 256-263. https://doi.org/10.1016/j.memsci.2014.11.049.
[69] G. Venugopal, J. Moore, J. Howard, S. Pendalwar, Characterization of microporous separators for lithium-ion batteries, Journal of Power Sources, 77 (1999) 34-41. https://doi.org/10.1016/S0378-7753(98)00168-2.
[70] R. Tan, A. Wang, R. Malpass-Evans, R. Williams, E.W. Zhao, T. Liu, C. Ye, X. Zhou, B.P. Darwich, Z. Fan, L. Turcani, E. Jackson, L. Chen, S.Y. Chong, T. Li, K.E. Jelfs, A.I. Cooper, N.P. Brandon, C.P. Grey, N.B. McKeown, Q. Song, Hydrophilic microporous membranes for selective ion separation and flow-battery energy storage, Nature Materials, 19 (2020) 195-202. 10.1038/s41563-019-0536-8.
[71] D.R. Rajagopalan Kannan, P.K. Terala, P.L. Moss, M.H. Weatherspoon, Analysis of the Separator Thickness and Porosity on the Performance of Lithium-Ion Batteries, International Journal of Electrochemistry, 2018 (2018) 1925708. https://doi.org/10.1155/2018/1925708.
[72] M. Eikerling, Y. Kornyshev, A.M. Kuznetsov, J. Ulstrup, S. Walbran, Mechanisms of Proton Conductance in Polymer Electrolyte Membranes, Journal of Physical Chemistry B, 105 (2001). 10.1021/jp003182s.
[73] X. Wei, L. Li, Q. Luo, Z. Nie, W. Wang, B. Li, G.-G. Xia, E. Miller, J. Chambers, Z. Yang, Microporous separators for Fe/V redox flow batteries, Journal of Power Sources, 218 (2012) 39-45. https://doi.org/10.1016/j.jpowsour.2012.06.073.
[74] I.S. Chae, T. Luo, G.H. Moon, W. Ogieglo, Y.S. Kang, M. Wessling, Ultra-High Proton/Vanadium Selectivity for Hydrophobic Polymer Membranes with Intrinsic Nanopores for Redox Flow Battery, Advanced Energy Materials, 6 (2016) 1600517. https://doi.org/10.1002/aenm.201600517.
[75] H.-Y. Jung, G.-O. Moon, T. Sadhasivam, C.-S. Jin, W.-S. Park, H.-T. Kim, S.-H. Roh, Ionic transportation and chemical stability of high-endurance porous polyethylene separator for vanadium redox flow batteries, Solid State Ionics, 327 (2018) 110-116. https://doi.org/10.1016/j.ssi.2018.10.019.
[76] L. Qiao, S. Liu, M. Fang, M. Yang, X. Ma, A Composite Membrane with High Stability and Low Cost Specifically for Iron–Chromium Flow Battery, Journal, 14 (2022). 10.3390/polym14112245.
[77] S.C. Chieng, M. Kazacos, M. Skyllas-Kazacos, Modification of Daramic, microporous separator, for redox flow battery applications, Journal of Membrane Science, 75 (1992) 81-91. https://doi.org/10.1016/0376-7388(92)80008-8.
[78] B. Tian, C.W. Yan, F.H. Wang, Proton conducting composite membrane from Daramic/Nafion for vanadium redox flow battery, Journal of Membrane Science, 234 (2004) 51-54. https://doi.org/10.1016/j.memsci.2004.01.012.
[79] T. Mohammadi, M. Skyllas-Kazacos, Preparation of sulfonated composite membrane for vanadium redox flow battery applications, Journal of Membrane Science, 107 (1995) 35-45.
[80] X.L. Zhou, T.S. Zhao, L. An, Y.K. Zeng, X.B. Zhu, Performance of a vanadium redox flow battery with a VANADion membrane, Applied Energy, 180 (2016) 353-359. https://doi.org/10.1016/j.apenergy.2016.08.001.
[81] X. Wei, B. Li, W. Wang, Porous polymeric composite separators for redox flow batteries, Polymer Reviews, 55 (2015) 247-272. 10.1080/15583724.2015.1011276.
[82] Y. Wang, K. Geng, Q. Tan, T. Guo, X. Hu, H. Tang, L. Liu, N. Li, Highly Ion Selective Proton Exchange Membrane Based on Sulfonated Polybenzimidazoles for Iron–Chromium Redox Flow Battery, ACS Applied Energy Materials, 5 (2022) 15918-15927. 10.1021/acsaem.2c03471.
[83] Y. Yang, Q. Wang, S. Xiong, Z. Song, Research progress on optimized membranes for vanadium redox flow batteries, Inorganic Chemistry Frontiers, 11 (2024) 4049-4079. 10.1039/D4QI00520A.
[84] B.G. Thiam, S. Vaudreuil, Review—Recent Membranes for Vanadium Redox Flow Batteries, Journal of The Electrochemical Society, 168 (2021) 070553. 10.1149/1945-7111/ac163c.
[85] D. Chen, M.A. Hickner, E. Agar, E.C. Kumbur, Optimizing membrane thickness for vanadium redox flow batteries, Journal of Membrane Science, 437 (2013) 108-113. https://doi.org/10.1016/j.memsci.2013.02.007.
[86] D. Chen, X. Chen, L. Ding, X. Li, Advanced acid-base blend ion exchange membranes with high performance for vanadium flow battery application, Journal of Membrane Science, 553 (2018) 25-31. https://doi.org/10.1016/j.memsci.2018.02.039.

[87] K. Schafner, M. Becker, T. Turek, Membrane resistance of different separator materials in a vanadium redox flow battery, Journal of Membrane Science, 586 (2019) 106-114. https://doi.org/10.1016/j.memsci.2019.05.054.
[88] Z. Wang, J. Ren, J. Sun, Y. Li, Z. Guo, B. Liu, X. Fan, T. Zhao, The anion conductivity of acid-doped polybenzimidazole membrane and utilization in mitigating the capacity decay of vanadium redox flow battery stacks, Chem. Eng. J., 474 (2023) 145621. https://doi.org/10.1016/j.cej.2023.145621.
[89] T.D. Gierke, G.E. Munn, F.C. Wilson, The morphology in nafion perfluorinated membrane products, as determined by wide- and small-angle x-ray studies, Journal of Polymer Science: Polymer Physics Edition, 19 (1981) 1687-1704. https://doi.org/10.1002/pol.1981.180191103.
[90] E. Berretti, L. Osmieri, V. Baglio, H.A. Miller, J. Filippi, F. Vizza, M. Santamaria, S. Specchia, C. Santoro, A. Lavacchi, Direct alcohol fuel cells: a comparative review of acidic and alkaline systems, Electrochemical Energy Reviews, 6 (2023) 30.
[91] S. Willdorf-Cohen, A. Zhegur-Khais, J. Ponce-González, S. Bsoul-Haj, J.R. Varcoe, C.E. Diesendruck, D.R. Dekel, Alkaline Stability of Anion-Exchange Membranes, ACS Applied Energy Materials, 6 (2023) 1085-1092. 10.1021/acsaem.2c03689.
[92] S.N. Oreiro, A. Bentien, J. Sloth, M. Rahimi, M.B. Madsen, T. Drechsler, Crossover analysis in a commercial 6 kW/43kAh vanadium redox flow battery utilizing anion exchange membrane, Chem. Eng. J., 490 (2024) 151947. https://doi.org/10.1016/j.cej.2024.151947.
[93] L. Zeng, T.S. Zhao, L. Wei, H.R. Jiang, M.C. Wu, Anion exchange membranes for aqueous acid-based redox flow batteries: Current status and challenges, Applied Energy, 233-234 (2019) 622-643. https://doi.org/10.1016/j.apenergy.2018.10.063.
[94] T. Wang, J.Y. Jeon, J. Han, J.H. Kim, C. Bae, S. Kim, Poly(terphenylene) anion exchange membranes with high conductivity and low vanadium permeability for vanadium redox flow batteries (VRFBs), Journal of Membrane Science, 598 (2020) 117665. https://doi.org/10.1016/j.memsci.2019.117665.
[95] D. Düerkop, H. Widdecke, C. Schilde, U. Kunz, A. Schmiemann, Polymer membranes for all-vanadium redox flow batteries: a review, Membranes, 11 (2021) 214.
[96] Y. Ahn, D. Kim, Anion exchange membrane prepared from imidazolium grafted poly(arylene ether ketone) with enhanced durability for vanadium redox flow battery, Journal of Industrial and Engineering Chemistry, 71 (2019) 361-368. https://doi.org/10.1016/j.jiec.2018.11.047.
[97] D. Chen, M.A. Hickner, E. Agar, E.C. Kumbur, Optimized Anion Exchange Membranes for Vanadium Redox Flow Batteries, ACS Applied Materials & Interfaces, 5 (2013) 7559-7566. 10.1021/am401858r.
[98] H. Cho, H.M. Krieg, J.A. Kerres, Application of Novel Anion-Exchange Blend Membranes (AEBMs) to Vanadium Redox Flow Batteries, Journal, 8 (2018). 10.3390/membranes8020033.
[99] T.N.L. Doan, T.K.A. Hoang, P. Chen, Recent development of polymer membranes as separators for all-vanadium redox flow batteries, RSC Advances, 5 (2015) 72805-72815. 10.1039/C5RA05914C.
[100] X. Hao, N. Chen, Y. Chen, D. Chen, Accelerated degradation of quaternary ammonium functionalized anion exchange membrane in catholyte of vanadium redox flow battery, Polym. Degrad. Stab., 197 (2022) 109864. https://doi.org/10.1016/j.polymdegradstab.2022.109864.
[101] J.J. Min-suk, J. Parrondo, C.G. Arges, V. Ramani, Polysulfone-based anion exchange membranes demonstrate excellent chemical stability and performance for the all-vanadium redox flow battery, Journal of Materials Chemistry A, 1 (2013) 10458-10464.
[102] M.R. Hibbs, M.A. Hickner, T.M. Alam, S.K. McIntyre, C.H. Fujimoto, C.J. Cornelius, Transport Properties of Hydroxide and Proton Conducting Membranes, Chem. Mater., 20 (2008) 2566-2573. 10.1021/cm703263n.
[103] C. Noh, M. Jung, D. Henkensmeier, S.W. Nam, Y. Kwon, Vanadium Redox Flow Batteries Using meta-Polybenzimidazole-Based Membranes of Different Thicknesses, ACS Applied Materials & Interfaces, 9 (2017) 36799-36809. 10.1021/acsami.7b10598.
[104] S.N.S.S. Daud, M.N.A.M. Norddin, J. Jaafar, R. Sudirman, M.H.D. Othman, A.F. Ismail, Highly Sulfonated Poly(Ether Ether Ketone) Blend with Hydrophobic Polyether Sulfone as an Alternative Electrolyte for Proton Exchange Membrane Fuel Cell, Arabian Journal for Science and Engineering, 46 (2021) 6189-6205. 10.1007/s13369-020-04898-5.
[105] S.S. Araya, F. Zhou, V. Liso, S.L. Sahlin, J.R. Vang, S. Thomas, X. Gao, C. Jeppesen, S.K. Kær, A comprehensive review of PBI-based high temperature PEM fuel cells, International Journal of Hydrogen Energy, 41 (2016) 21310-21344. https://doi.org/10.1016/j.ijhydene.2016.09.024.
[106] L. Ding, X. Song, L. Wang, Z. Zhao, G. He, Preparation of dense polybenzimidazole proton exchange membranes with different basicity and flexibility for vanadium redox flow battery

applications, Electrochimica Acta, 292 (2018) 10-19. https://doi.org/10.1016/j.electacta.2018.08.128.
[107] P. Qian, H. Wang, L. Zhang, Y. Zhou, H. Shi, An enhanced stability and efficiency of SPEEK-based composite membrane influenced by amphoteric side-chain polymer for vanadium redox flow battery, Journal of Membrane Science, 643 (2022) 120011. https://doi.org/10.1016/j.memsci.2021.120011.
[108] B.G. Thiam, A. El Magri, S. Vaudreuil, An overview on the progress and development of modified sulfonated polyether ether ketone membranes for vanadium redox flow battery applications, High Perform. Polym., 34 (2022) 131-148.
[109] L. Ding, X. Song, L. Wang, Z. Zhao, Enhancing proton conductivity of polybenzimidazole membranes by introducing sulfonate for vanadium redox flow batteries applications, Journal of Membrane Science, 578 (2019) 126-135.
[110] T.T. Bui, M. Shin, S. Abbas, M.M. Ikhsan, X.H. Do, A. Dayan, M.R. Almind, S. Park, D. Aili, J. Hjelm, Sulfonated para-polybenzimidazole membranes for use in vanadium redox flow batteries, Advanced Energy Materials, 15 (2025) 2401375.
[111] J. Escorihuela, J. Olvera-Mancilla, L. Alexandrova, L.F. del Castillo, V. Compañ, Recent Progress in the Development of Composite Membranes Based on Polybenzimidazole for High Temperature Proton Exchange Membrane (PEM) Fuel Cell Applications, Journal, 12 (2020). 10.3390/polym12091861.
[112] B. Maria Mahimai, G. Sivasubramanian, K. Sekar, D. Kannaiyan, P. Deivanayagam, Sulfonated poly(ether ether ketone): efficient ion-exchange polymer electrolytes for fuel cell applications–a versatile review, Materials Advances, 3 (2022) 6085-6095. 10.1039/D2MA00562J.
[113] J. Xi, B. Jiang, L. Yu, L. Liu, Membrane evaluation for vanadium flow batteries in a temperature range of −20–50°C, Journal of Membrane Science, 522 (2017) 45-55. https://doi.org/10.1016/j.memsci.2016.09.012.
[114] Z. Yuan, X. Li, J. Hu, W. Xu, J. Cao, H. Zhang, Degradation mechanism of sulfonated poly(ether ether ketone) (SPEEK) ion exchange membranes under vanadium flow battery medium, Physical Chemistry Chemical Physics, 16 (2014) 19841-19847. 10.1039/C4CP03329A.
[115] J. Li, J. Liu, W. Xu, J. Long, W. Huang, Y. Zhang, L. Chu, Highly ion-selective sulfonated polyimide membranes with covalent self-crosslinking and branching structures for vanadium redox flow battery, Chem. Eng. J., 437 (2022) 135414. https://doi.org/10.1016/j.cej.2022.135414.
[116] R. Haider, Y. Wen, Z.-F. Ma, D.P. Wilkinson, L. Zhang, X. Yuan, S. Song, J. Zhang, High temperature proton exchange membrane fuel cells: progress in advanced materials and key technologies, Chemical Society Reviews, 50 (2021) 1138-1187. 10.1039/D0CS00296H.
[117] J. Wang, H. Wang, Y. Fan, Techno-Economic Challenges of Fuel Cell Commercialization, Engineering, 4 (2018) 352-360. https://doi.org/10.1016/j.eng.2018.05.007.
[118] E. Ogungbemi, O. Ijaodola, F.N. Khatib, T. Wilberforce, Z. El Hassan, J. Thompson, M. Ramadan, A.G. Olabi, Fuel cell membranes – Pros and cons, Energy, 172 (2019) 155-172. https://doi.org/10.1016/j.energy.2019.01.034.
[119] M. Chatenet, S. Berthon-Fabry, Y. Ahmad, K. Guérin, M. Colin, H. Farhat, L. Frezet, G. Zhang, M. Dubois, Fluorination and its Effects on Electrocatalysts for Low-Temperature Fuel Cells, Advanced Energy Materials, 13 (2023) 2204304. https://doi.org/10.1002/aenm.202204304.
[120] N. Esmaeili, E.M. Gray, C.J. Webb, Non-Fluorinated Polymer Composite Proton Exchange Membranes for Fuel Cell Applications – A Review, ChemPhysChem, 20 (2019) 2016-2053. https://doi.org/10.1002/cphc.201900191.
[121] L. Brinke, M. Wagner, S. Thiele, J. Kerres, Sulfonamide-Sulfonimide Copolymers as Novel, Fluorine-Lean Type of Proton Exchange Membranes for Fuel Cell Application, Chemistry – A European Journal, 30 (2024) e202402025. https://doi.org/10.1002/chem.202402025.
[122] J. Li, N. Cui, D. Liu, Z. Zhao, F. Yang, J. Zhong, J. Pang, SPEEK-co-PEK-x proton exchange membranes with controllable sulfonation degree for proton exchange membrane fuel cells, International Journal of Hydrogen Energy, 50 (2024) 606-617. https://doi.org/10.1016/j.ijhydene.2023.08.334.
[123] L. Wang, B.L. Yi, H.M. Zhang, D.M. Xing, Characteristics of Polyethersulfone/Sulfonated Polyimide Blend Membrane for Proton Exchange Membrane Fuel Cell, The Journal of Physical Chemistry B, 112 (2008) 4270-4275. 10.1021/jp710704v.
[124] J. Kerres, V. Atanasov, Cross-linked PBI-based high-temperature membranes: Stability, conductivity and fuel cell performance, International Journal of Hydrogen Energy, 40 (2015) 14723-14735. https://doi.org/10.1016/j.ijhydene.2015.08.054.
[125] J. Chen, L. Wang, L. Wang, Highly Conductive Polybenzimidazole Membranes at Low Phosphoric Acid Uptake with Excellent Fuel Cell Performances by Constructing Long-Range

Continuous Proton Transport Channels Using a Metal–Organic Framework (UIO-66), ACS Applied Materials & Interfaces, 12 (2020) 41350-41358. 10.1021/acsami.0c10527.
[126] Z. Zhang, J. Ren, M. Ju, X. Chen, J. Xu, Z. Wang, L. Meng, P. Zhao, H. Wang, Construction of new alternative transmission sites by incorporating structure-defect metal-organic framework into sulfonated poly(arylene ether ketone sulfone)s, International Journal of Hydrogen Energy, 46 (2021) 27193-27206. https://doi.org/10.1016/j.ijhydene.2021.05.167.
[127] J. Xu, H. Zhao, W. Li, P. Li, C. Chen, Z. Yue, L. Zou, H. Yang, Facile strategy for preparing a novel reinforced blend membrane with high cycling stability for vanadium redox flow batteries, Chem. Eng. J., 433 (2022) 133197. https://doi.org/10.1016/j.cej.2021.133197.
[128] Z. Li, L. Liu, L. Yu, L. Wang, J. Xi, X. Qiu, L. Chen, Characterization of sulfonated poly(ether ether ketone)/poly(vinylidene fluoride-co-hexafluoropropylene) composite membrane for vanadium redox flow battery application, Journal of Power Sources, 272 (2014) 427-435. https://doi.org/10.1016/j.jpowsour.2014.08.101.
[129] C. Sun, Z. Huan, X.-D. Luo, N. Chen, A comparative study of Nafion and sulfonated poly(ether ether ketone) membrane performance for iron-chromium redox flow battery, Ionics, 25 (2019). 10.1007/s11581-019-02971-0.
[130] R.T.S. Muthu Lakshmi, V. Choudhary, I.K. Varma, Sulphonated poly(ether ether ketone): Synthesis and characterisation, Journal of Materials Science, 40 (2005) 629-636. 10.1007/s10853-005-6300-2.
[131] R.Y.M. Huang, P. Shao, C.M. Burns, X. Feng, Sulfonation of poly(ether ether ketone)(PEEK): Kinetic study and characterization, Journal of Applied Polymer Science, 82 (2001) 2651-2660. https://doi.org/10.1002/app.2118.
[132] Y. Wang, J. Xu, H. Zang, Z. Wang, Synthesis and properties of sulfonated poly(arylene ether ketone sulfone) containing amino groups/functional titania inorganic particles hybrid membranes for fuel cells, International Journal of Hydrogen Energy, 44 (2019) 6136-6147. https://doi.org/10.1016/j.ijhydene.2019.01.035.
[133] K.D. Kreuer, On the development of proton conducting polymer membranes for hydrogen and methanol fuel cells, Journal of Membrane Science, 185 (2001) 29-39. https://doi.org/10.1016/S0376-7388(00)00632-3.
[134] S. Swaby, D. Monzón, N. Ureña, J. Vivo Vilches, J.-Y. Sanchez, C. Iojoiu, A. Várez, M.T. Pérez-Prior, B. Levenfeld, Block Copolymer-Based Membranes for Vanadium Redox Flow Batteries: Synthesis, Characterization, and Performance, ACS Applied Polymer Materials, 6 (2024) 8966-8976. 10.1021/acsapm.4c01262.
[135] J. Xi, Z. Li, L. Yu, B. Yin, L. Wang, L. Liu, X. Qiu, L. Chen, Effect of degree of sulfonation and casting solvent on sulfonated poly (ether ether ketone) membrane for vanadium redox flow battery, Journal of Power Sources, 285 (2015) 195-204.
[136] J. Xu, Z. Zhang, X. Xiong, H. Zeng, A new solvent for poly(ether ether ketone), Polymer, 33 (1992) 4432-4434. https://doi.org/10.1016/0032-3861(92)90293-6.
[137] C. Zimmerer, M. Schwind, S. Putzke, R. Frenzel, A. Drechsler, F. Simon, Surface functionalization of poly(ether ether ketone) by wet-chemical modification with carboxylic acids and diamine, Journal of Adhesion Science and Technology, 38 (2024) 139-162. 10.1080/01694243.2023.2223334.
[138] F. Niccolai, E. Guazzelli, Z. El Koura, I. Pucher, E. Martinelli, A Critical Update on the Design of Dense Ion-Conducting Membranes for Redox Flow Batteries, Advanced Sustainable Systems, 9 (2025) 2400661. https://doi.org/10.1002/adsu.202400661.
[139] S. Auffarth, W. Dafinger, J. Mehler, V. Ardizzon, P. Preuster, P. Wasserscheid, S. Thiele, J. Kerres, Cross-linked proton-exchange membranes with strongly reduced fuel crossover and increased chemical stability for direct-isopropanol fuel cells, Journal of Materials Chemistry A, 10 (2022) 17208-17216. 10.1039/D2TA03832C.
[140] O.D. Thomas, T.J. Peckham, U. Thanganathan, Y. Yang, S. Holdcroft, Sulfonated polybenzimidazoles: Proton conduction and acid–base crosslinking, J. Polym. Sci., Part A: Polym. Chem., 48 (2010) 3640-3650. https://doi.org/10.1002/pola.24147.
[141] D.E. Curtin, M.A. Watkins, in: 2002 Fuel Cell Seminar, Palm Springs (November 2002), 2002.
[142] Y. Luan, H. Zhang, Y. Zhang, L. Li, H. Li, Y. Liu, Study on structural evolution of perfluorosulfonic ionomer from concentrated DMF-based solution to membranes, Journal of Membrane Science, 319 (2008) 91-101. https://doi.org/10.1016/j.memsci.2008.03.054.
[143] T.A.L. Harris, D.F. Walczyk, Development of a Casting Technique for Membrane Material Used in High-Temperature PEM Fuel Cells, Journal of Manufacturing Processes, 8 (2006) 8-20. https://doi.org/10.1016/S1526-6125(06)70097-4.

[144] D. Frederichi, M. Scaliante, R. Bergamasco, Structured photocatalytic systems: photocatalytic coatings on low-cost structures for treatment of water contaminated with micropollutants—a short review, Environmental Science and Pollution Research, 28 (2021). 10.1007/s11356-020-10022-9.
[145] A.M. LaChance, Z. Hou, M.M. Farooqui, S.A. Carr, J.M. Serrano, C.E. Odendahl, M.E. Hurley, T.E. Morrison, J.L. Kubachka, N.T. Samuels, A.T. Barrett, Y. Zhao, A.M. DeGennaro, L. Sun, M.T. Shaw, Doctor-Blade-Assisted Casting for Forming Thin Composite Coatings of Montmorillonite and Poly(vinyl alcohol), Industrial & Engineering Chemistry Research, 61 (2022) 3766-3774. 10.1021/acs.iecr.1c04381.
[146] J.C. Williams, Doctor-Blade Process, in: F.F.Y. Wang (Ed.) Treatise on Materials Science & Technology, Elsevier, 1976, pp. 173-198. https://doi.org/10.1016/B978-0-12-341809-8.50016-4.
[147] H. Yang, P. Jiang, Large-Scale Colloidal Self-Assembly by Doctor Blade Coating, Langmuir, 26 (2010) 13173-13182. 10.1021/la101721v.
[148] S. Chede, P. Griffiths, I.C. Escobar, T.A.L. Harris, Does casting method matter in filtration membranes? A comparison in performance between doctor blade and slot-die extruded polymeric membranes, Journal of Applied Polymer Science, 135 (2018) 45563. https://doi.org/10.1002/app.45563.
[149] O. Kwon, Y. Choi, E. Choi, M. Kim, Y.C. Woo, D.W. Kim, Fabrication Techniques for Graphene Oxide-Based Molecular Separation Membranes: Towards Industrial Application, Nanomaterials, 11 (2021) 757.
[150] W. Lee, M. Jung, D. Serhiichuk, C. Noh, G. Gupta, C. Harms, Y. Kwon, D. Henkensmeier, Layered composite membranes based on porous PVDF coated with a thin, dense PBI layer for vanadium redox flow batteries, Journal of Membrane Science, 591 (2019) 117333. https://doi.org/10.1016/j.memsci.2019.117333.
[151] J. Lin, F. Lin, R. Liu, P. Li, S. Fang, W. Ye, S. Zhao, Scalable fabrication of robust superhydrophobic membranes by one-step spray-coating for gravitational water-in-oil emulsion separation, Sep. Purif. Technol., 231 (2020) 115898. https://doi.org/10.1016/j.seppur.2019.115898.
[152] Manufacturing of membranes and electrodes, 2022/07, Helmholtz Institute Erlangen-Nürnberg for Renewable Energy https://www.hi-ern.de/en/research/electrocatalytic-interface-engineering-1/composite-membrane-analysis-and-design/manufacturing-of-membranes-and-electrodes (accessed: 2025/08).
[153] A. Ilyas, D. Madhav, I. Nulens, K.V. Agrawal, C. Van Goethem, I.F.J. Vankelecom, Influence of micro-patterned support properties and interfacial polymerization conditions on performance of patterned thin-film composite membranes, Journal of Membrane Science, 700 (2024) 122721. https://doi.org/10.1016/j.memsci.2024.122721.
[154] G. Zhao, W. Han, L. Dong, H. Fan, Z. Qu, J. Gu, H. Meng, Sprayed separation membranes: A systematic review and prospective opportunities, Green Energy & Environment, 7 (2022) 1143-1160. https://doi.org/10.1016/j.gee.2022.04.001.
[155] J.H. Wendorff, S. Agarwal, A. Greiner, Electrospinning: materials, processing, and applications, John Wiley & Sons, 2012.
[156] C. Klose, M. Breitwieser, S. Vierrath, M. Klingele, H. Cho, A. Büchler, J. Kerres, S. Thiele, Electrospun sulfonated poly(ether ketone) nanofibers as proton conductive reinforcement for durable Nafion composite membranes, Journal of Power Sources, 361 (2017) 237-242. https://doi.org/10.1016/j.jpowsour.2017.06.080.
[157] M. Breitwieser, C. Klose, M. Klingele, A. Hartmann, J. Erben, H. Cho, J. Kerres, R. Zengerle, S. Thiele, Simple fabrication of 12 µm thin nanocomposite fuel cell membranes by direct electrospinning and printing, Journal of Power Sources, 337 (2017) 137-144. https://doi.org/10.1016/j.jpowsour.2016.10.094.
[158] S. Abbasi, A. Forner-Cuenca, W. Kout, K. Nijmeijer, Z. Borneman, Low-cost wire-electrospun sulfonated poly(ether ether ketone)/poly(vinylidene fluoride) blend membranes for hydrogen-bromine flow batteries, Journal of Membrane Science, 628 (2021) 119258. https://doi.org/10.1016/j.memsci.2021.119258.
[159] B. Abadi, N. Goshtasbi, S. Bolourian, J. Tahsili, M. Adeli-Sardou, H. Forootanfar, Electrospun hybrid nanofibers: Fabrication, characterization, and biomedical applications, Frontiers in Bioengineering and Biotechnology, Volume 10 - 2022 (2022). 10.3389/fbioe.2022.986975.
[160] H.S. Bang, D. Kim, S.S. Hwang, J. Won, Surface-modified porous membranes with electrospun Nafion/PVA fibres for non-aqueous redox flow battery, Journal of Membrane Science, 514 (2016) 186-194. https://doi.org/10.1016/j.memsci.2016.04.068.

[161] N.K. Shrivastava, A. Chatterjee, T. A. L. Harris, Manufacturing defects in slot die coated polymer electrolyte membrane for fuel cell application, Chem. Eng. Sci., 280 (2023) 119051. https://doi.org/10.1016/j.ces.2023.119051.
[162] X. Dong, T.J. Jeong, E. Kline, L. Banks, E. Grulke, T. Harris, I.C. Escobar, Eco-friendly solvents and their mixture for the fabrication of polysulfone ultrafiltration membranes: An investigation of doctor blade and slot die casting methods, Journal of Membrane Science, 614 (2020) 118510. https://doi.org/10.1016/j.memsci.2020.118510.
[163] J.J. Conde, P. Ferreira-Aparicio, A.M. Chaparro, Electrospray Deposition: A Breakthrough Technique for Proton Exchange Membrane Fuel Cell Catalyst Layer Fabrication, ACS Applied Energy Materials, 4 (2021) 7394-7404. 10.1021/acsaem.1c01445.
[164] C. Wang, M.J. Park, Y.W. Choo, Y. Huang, S. Phuntsho, H.K. Shon, Inkjet printing technique for membrane fabrication and modification: A review, Desalination, 565 (2023) 116841. https://doi.org/10.1016/j.desal.2023.116841.
[165] B.J. Kingsley, E.E. Pawliczak, T.R. Hurley, P.R. Chiarot, Electrospray Printing of Polyimide Films Using Passive Material Focusing, ACS Applied Polymer Materials, 3 (2021) 6274-6284. 10.1021/acsapm.1c01073.
[166] L. Cao, M. Skyllas-Kazacos, C. Menictas, J. Noack, A review of electrolyte additives and impurities in vanadium redox flow batteries, Journal of Energy Chemistry, 27 (2018) 1269-1291. https://doi.org/10.1016/j.jechem.2018.04.007.
[167] M.C.L. de Oliveira, R.A. Antunes, Bipolar Plates in Redox Flow Batteries, Fuel Cells and Electrolyzers, in: Reference Module in Earth Systems and Environmental Sciences, Elsevier, 2021. https://doi.org/10.1016/B978-0-12-819723-3.00051-2.
[168] C. Minke, T. Hickmann, A.R. dos Santos, U. Kunz, T. Turek, Cost and performance prospects for composite bipolar plates in fuel cells and redox flow batteries, Journal of Power Sources, 305 (2016) 182-190.
[169] B. Satola, Review—Bipolar Plates for the Vanadium Redox Flow Battery, Journal of The Electrochemical Society, 168 (2021) 060503. 10.1149/1945-7111/ac0177.
[170] S. Kumar, S. Jayanti, Effect of flow field on the performance of an all-vanadium redox flow battery, Journal of Power Sources, 307 (2016) 782-787. https://doi.org/10.1016/j.jpowsour.2016.01.048.
[171] H. Zhang, Y. Tan, J. Li, B. Xue, Studies on properties of rayon- and polyacrylonitrile-based graphite felt electrodes affecting Fe/Cr redox flow battery performance, Electrochimica Acta, 248 (2017) 603-613. https://doi.org/10.1016/j.electacta.2017.08.016.
[172] Y. Niu, S. Zeng, G. Wu, Q. Gao, R. Zhou, C. Li, Y. Zhou, Q. Xu, Preparation of N-B doped composite electrode for iron-chromium redox flow battery, Green Energy and Intelligent Transportation, 3 (2024) 100158. https://doi.org/10.1016/j.geits.2024.100158.
[173] B. Sun, M. Skyllas-Kazacos, Modification of graphite electrode materials for vanadium redox flow battery application—I. Thermal treatment, Electrochimica acta, 37 (1992) 1253-1260.
[174] B. Sun, M. Skyllas-Kazacos, Chemical modification of graphite electrode materials for vanadium redox flow battery application—part II. Acid treatments, Electrochimica Acta, 37 (1992) 2459-2465.
[175] B. Li, M. Gu, Z. Nie, Y. Shao, Q. Luo, X. Wei, X. Li, J. Xiao, C. Wang, V. Sprenkle, Bismuth nanoparticle decorating graphite felt as a high-performance electrode for an all-vanadium redox flow battery, Nano Lett., 13 (2013) 1330-1335.
[176] P. Huang, W. Ling, H. Sheng, Y. Zhou, X. Wu, X.-X. Zeng, X. Wu, Y.-G. Guo, Heteroatom-doped electrodes for all-vanadium redox flow batteries with ultralong lifespan, Journal of Materials Chemistry A, 6 (2018) 41-44.
[177] K. Kim, M.-S. Park, Y. Kim, J.H. Kim, S. Dou, M. Skyllas-Kazacos, A technology review of electrodes and reaction mechanisms in vanadium redox flow batteries, Journal of Materials Chemistry A, (2015).
[178] J. Charvát, P. Mazúr, J. Dundálek, J. Pocedič, J. Vrána, J. Mrlík, J. Kosek, S. Dinter, Performance enhancement of vanadium redox flow battery by optimized electrode compression and operational conditions, Journal of Energy Storage, 30 (2020) 101468. https://doi.org/10.1016/j.est.2020.101468.
[179] A. Kaur, K. Il Jeong, S. Su Kim, J. Woo Lim, Optimization of thermal treatment of carbon felt electrode based on the mechanical properties for high-efficiency vanadium redox flow batteries, Composite Structures, 290 (2022) 115546. https://doi.org/10.1016/j.compstruct.2022.115546.
[180] M.T. Tsehaye, G. Mourouga, T.J. Schmidt, J.O. Schumacher, S. Velizarov, B. Van der Bruggen, F. Alloin, C. Iojoiu, Towards optimized membranes for aqueous organic redox flow batteries: Correlation between membrane properties and cell performance, Renewable and Sustainable Energy Reviews, 173 (2023) 113059. https://doi.org/10.1016/j.rser.2022.113059.

[181] T. Wang, Y. Cai, J. Ma, Z. Han, S. Rong, Q. Ye, Y. Ji, High-performance SPEEK membrane with polydopamine-bridged PTFE nanoparticles for vanadium redox flow batteries, Journal of Energy Storage, 99 (2024) 113318. https://doi.org/10.1016/j.est.2024.113318.
[182] K. Oh, M. Moazzam, G. Gwak, H. Ju, Water crossover phenomena in all-vanadium redox flow batteries, Electrochimica Acta, 297 (2019) 101-111. https://doi.org/10.1016/j.electacta.2018.11.151.
[183] Z. Tang, R. Keith, D.S. Aaron, J.S. Lawton, A.P. Papandrew, T.A. Zawodzinski, Proton Exchange Membrane Performance Characterization in VRFB, ECS Transactions, 41 (2012) 25. 10.1149/1.3697451.
[184] Z. Yuan, X. Li, Y. Duan, Y. Zhao, H. Zhang, Application and degradation mechanism of polyoxadiazole based membrane for vanadium flow batteries, Journal of Membrane Science, 488 (2015) 194-202. https://doi.org/10.1016/j.memsci.2015.04.019.
[185] X. Huang, Y. Pu, Y. Zhou, Y. Zhang, H. Zhang, In-situ and ex-situ degradation of sulfonated polyimide membrane for vanadium redox flow battery application, Journal of Membrane Science, 526 (2017) 281-292. https://doi.org/10.1016/j.memsci.2016.09.053.
[186] X.-Z. Yuan, S. Zhang, S. Ban, C. Huang, H. Wang, V. Singara, M. Fowler, M. Schulze, A. Haug, K. Andreas Friedrich, R. Hiesgen, Degradation of a PEM fuel cell stack with Nafion® membranes of different thicknesses. Part II: Ex situ diagnosis, Journal of Power Sources, 205 (2012) 324-334. https://doi.org/10.1016/j.jpowsour.2012.01.074.
[187] T. Ous, C. Arcoumanis, Degradation aspects of water formation and transport in Proton Exchange Membrane Fuel Cell: A review, Journal of Power Sources, 240 (2013) 558-582. https://doi.org/10.1016/j.jpowsour.2013.04.044.
[188] K. Divya, D. Rana, M.S. Sri Abirami Saraswathi, A. Nagendran, Custom-made sulfonated poly (vinylidene fluoride-co-hexafluoropropylene) nanocomposite membranes for vanadium redox flow battery applications, Polym. Test., 90 (2020) 106685. https://doi.org/10.1016/j.polymertesting.2020.106685.
[189] X. Luo, S. Holdcroft, A. Mani, Y. Zhang, Z. Shi, Water, proton, and oxygen transport in high IEC, short side chain PFSA ionomer membranes: consequences of a frustrated network, Physical Chemistry Chemical Physics, 13 (2011) 18055-18062.
[190] G.H.A. Wijaya, K.S. Im, S.Y. Nam, Advancements in commercial anion exchange membranes: A review of membrane properties in water electrolysis applications, Desalination and Water Treatment, 320 (2024) 100605. https://doi.org/10.1016/j.dwt.2024.100605.
[191] S.M. MacKinnon, T.J. Fuller, F.D. Coms, M.R. Schoeneweiss, C. Gittleman, Y.-H. Lai, R. Jiang, A.M. Brenner, Fuel Cells - Proton-Exchange Membrane Fuel Cells | Membranes: Design and Characterization, in, 2009, pp. 741-754. 10.1016/B978-044452745-5.00905-9.
[192] A.W.T. King, V. Mäkelä, S.A. Kedzior, T. Laaksonen, G.J. Partl, S. Heikkinen, H. Koskela, H.A. Heikkinen, A.J. Holding, E.D. Cranston, I. Kilpeläinen, Liquid-State NMR Analysis of Nanocelluloses, Biomacromolecules, 19 (2018) 2708-2720. 10.1021/acs.biomac.8b00295.
[193] T.H. Pham, J.S. Olsson, P. Jannasch, N-Spirocyclic Quaternary Ammonium Ionenes for Anion-Exchange Membranes, Journal of the American Chemical Society, 139 (2017) 2888-2891. 10.1021/jacs.6b12944.
[194] K. Saalwächter, Applications of NMR in Polymer Characterization – An Introduction, in: R. Zhang, T. Miyoshi, P. Sun (Eds.) NMR Methods for Characterization of Synthetic and Natural Polymers, The Royal Society of Chemistry, 2019, pp. 0. 10.1039/9781788016483-00001.
[195] H.N. Cheng, T. Asakura, K. Suganuma, J.M. Lagaron, B. Melendez-Rodriguez, A. Biswas, NMR Analyses and Statistical Modeling of Biobased Polymer Microstructures—A Selected Review, Journal, 16 (2024). 10.3390/polym16050620.
[196] Z. Zhou, J.C. Stevens, J. Klosin, R. Kümmerle, X. Qiu, D. Redwine, R. Cong, A. Taha, J. Mason, B. Winniford, P. Chauvel, N. Montañez, NMR Study of Isolated 2,1-Inverse Insertion in Isotactic Polypropylene, Macromolecules, 42 (2009) 2291-2294. 10.1021/ma802770f.
[197] C. Fellers, Paper physics, Pulp and Paper Chemistry and Technology: Paper Products Physics and Technology, 4 (2009) 25-67.
[198] Y. Lee, J. Park, H. Jeon, D. Yeon, B.-H. Kim, K.Y. Cho, M.-H. Ryou, Y.M. Lee, In-depth correlation of separator pore structure and electrochemical performance in lithium-ion batteries, Journal of Power Sources, 325 (2016) 732-738. https://doi.org/10.1016/j.jpowsour.2016.06.094.
[199] K.K. Jana, S.J. Lue, A. Huang, J.F. Soesanto, K.-L. Tung, Separator Membranes for High Energy-Density Batteries, ChemBioEng Reviews, 5 (2018) 346-371. https://doi.org/10.1002/cben.201800014.
[200] P.T. Nonjola, N. Mutangwa, H. Luo, Membrane Separators for Electrochemical Energy Storage Technologies, in: K.I. Ozoemena, S. Chen (Eds.) Nanomaterials in Advanced Batteries and

Supercapacitors, Springer International Publishing, Cham, 2016, pp. 417-462. 10.1007/978-3-319-26082-2_12.
[201] in, TAPPI, Air resistance of paper (Gurley method) (Revision of T 460 om-02), 2006/06.
[202] T.T.K. Huynh, T. Yang, P.S. Nayanthara, Y. Yang, J. Ye, H. Wang, Construction of High-Performance Membranes for Vanadium Redox Flow Batteries: Challenges, Development, and Perspectives, Nano-Micro Letters, 17 (2025) 260. 10.1007/s40820-025-01736-x.
[203] X.H. Do, S. Abbas, M.M. Ikhsan, S.-Y. Choi, H.Y. Ha, K. Azizi, H.A. Hjuler, D. Henkensmeier, Membrane Assemblies with Soft Protective Layers: Dense and Gel-Type Polybenzimidazole Membranes and Their Use in Vanadium Redox Flow Batteries, Small, 18 (2022) 2206284. https://doi.org/10.1002/smll.202206284.
[204] N. Zhao, H. Riley, C. Song, Z. Jiang, K.-C. Tsay, R. Neagu, Z. Shi, Ex-Situ Evaluation of Commercial Polymer Membranes for Vanadium Redox Flow Batteries (VRFBs), Journal, 13 (2021). 10.3390/polym13060926.

CHAPTER 3: The feasibility of microporous separators in the iron-chromium redox flow battery

Chapter table of contents

3.1 Introduction

Large-scale energy storage systems, required for renewable energy applications, must be feasible in terms of the cost of materials involved in upscaling, while remaining reliable, durable, and able to operate at high efficiencies with a rapid response to input and output demands.[1, 2] Flow batteries (FBs) have long been considered suitable candidates for such storage systems, meeting the essential requirements for such large-scale operations.[3]

While the iron-chrome FB (ICFB) has a significantly lower electrolyte cost than the well-developed and commercially available all vanadium FB (VFB), it is still expensive due to the high cost of the Nafion® cation-exchange membranes (CEMs), which are widely used as the standard in FB research and application.[4-6] Selectivity of Nafion® is also currently too low to achieve realistic long-term cycling, as the crossover rate of metallic ions is ~20 times higher than that of VFB when using the relatively thin (25 µm) Nafion® 211 variant.[7] The Fe^{2+} and Cr^{3+} required for ICFB electrolyte cost approximately 9.4 USD KWh^{-1}, which has a much lower contribution to CAPEX cost compared to the ~500 USD m^{-2} cost of Nafion® membranes (illustrated in **Figure 3.1** (b)), posing an economic hinderance for large-scale commercialisation.[8-10] In comparison, the highly developed Li-ion battery industry's scale of production enables the cost of porous separators and current collectors to be a fraction of the price (~5 USD m^{-2}).[11] Hence, advancing the ICFB towards large-scale application will require a reduction in membrane/separator cost.

CEMs such as Nafion®, which are perfluorinated sulfonic acid membranes (PFSAs), are sought after largely due to their i) long-term chemical stability, ii) proton conductivity (through a combination of the Grotthuss and vehicular mechanisms) facilitating charge balancing during charge and discharge cycles (Figure 3.1 (a)), and iii) ability to reject the active materials of the redox couples (Fe and Cr in the case of the ICFB).[12, 13]

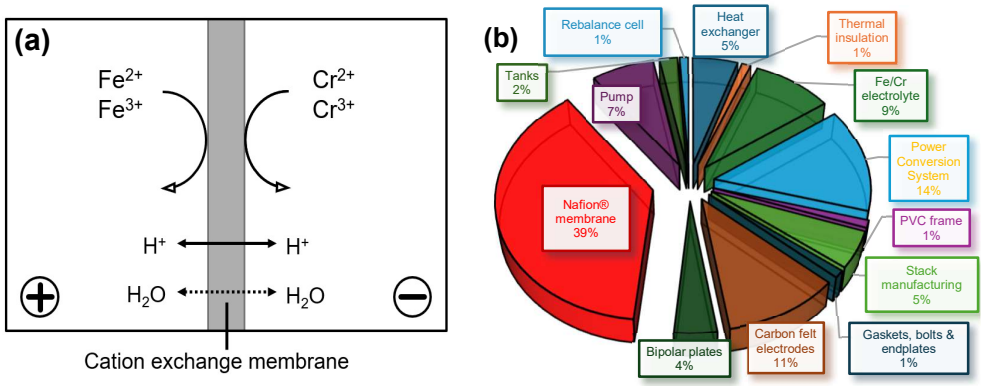

Figure 3.1: a) Basic working principle of a CEM in an ICFB and b) CAPEX cost of ICFB (194 USD kWh^{-1}).

To improve the cycling performance of FBs, various separators have been tested in the past, although the amount tested and published for the ICFB is very limited. While the focus has generally been on Nafion® CEM variants, the performance of anion exchange membranes (AEMs) and sulfonated poly(ether ether ketone) (SPEEK) membranes has also been investigated. AEMs were found unsuitable for the ICFB due to their inability to discharge, caused by a substantial increase in area specific resistance (ASR) from a mechanism that remains to be fully understood.[14] Results from SPEEK membrane testing with conventional electrolyte configuration (1.0 M $Fe(II)Cl_2 \cdot 4H_2O$ + 1.0 M $Cr(III)Cl_3 \cdot 6H_2O$ in 3.0 M HCl) show an energy efficiency (EE) of 79.1%, 3.2% lower than their N-115 benchmark, while exhibiting lower metallic-ion crossover and with the potential to reduce the CAPEX cost of the ICFB down 36% to 124 USD KWh^{-1}.[15] The long-term stability of non-fluorinated SPEEK remains to be investigated, since oxygen in the ether positions aggravate membrane degradation in strong acidic solutions and elevated temperatures.[16]

While other ion exchange membrane options exist and are currently being investigated for FBs, including fluorinated, sulfonated and phosphonated polymers, which could lead to improved efficiencies or reduction in the m^2 cost in stack production, their long-term stability requires further investigation.[6, 8, 17] Nonetheless, the search for finding a suitable separator for upscaling ICFB technology remains. Low-cost alternative options to CEMs that have been investigated for VFBs are microporous separators (MPSs) that, for example, consist of hydrocarbons embedded with hydrophilic materials such as Si.[6, 18] At a current density of 50 mA cm^{-1}, Wei *et al*. obtained an VFB EE of 81%, which was 5% lower than that of Nafion® 115 when using a 600 µm MPS consisting of PTFE and embedded Si.[19] Composite materials, such as MPSs with dense top layer or thin CEM coatings (reduced cost from CEM thickness using phase inversion) on low costing porous materials have not been investigated for ICFB, however, Zhou *et al*. investigated the feasibility for VFBs and yielded an EE of 76.2%, 4.9% higher than their benchmark N115. While MPSs have not been thoroughly tested in ICFBs, the lower acid concentration and energy density of an ICFB (1 M HCl and 10.5 Wh L^{-1}, lab-scale results) compared to a VFB (3 M H_2SO_4 and 25 Wh L^{-1}), does provide a less aggressive environment. [19-21] In addition, the Fe/Cr redox couple (Fe^{3+}: 0.771 V & Cr^{3+}: −0.408 V) used in the ICFB is less oxidative than specifically the V^{5+} (1.00 V) species in the VFB, which allows the use of a wider variety of basic and non-fluorinated hydrocarbons, such as polyethylene.[10, 18, 22] Manufacturing MPSs from simple hydrocarbon polymers such as polyethylene (PE) (with current collectors) at the mature and developed scale of the lithium-ion industry in 2015 cost only ~5 USD m^{-2}, which is 1% of the current ~500 USD m^{-2} of the benchmark for the ICFB and the VFB.[11] Subsequently, the ICFB could benefit substantially from a wide variety of low-costing separator materials, especially on grid-scale implementation, while limited research has been done on their feasibility in any other flow battery technology than the VFB.[23]

Rather than using static ion exchange functional groups in a non-porous CEM, transport through the pores of an MPS mostly follows the vehicular mechanism

(migration) of ion transport, where the charge carriers (HCl, H_3O^+, $H_5O_2^+$ and $H_9O_4^+$) in the electrolyte can transfer protons through direct contact and migration through the pores.[13] However, such pores also allow more crossover of the active redox couples and solvent than a CEM. Using the different transport and diffusion rates of larger (redox couple) and smaller (protons) ions in electrolytes, the transport of the active metal species with a larger Stokes radius can possibly be controlled by varying the pore size and pore length.[10]

The crossover (flux) of different chemical species, which is complex and driven by multiple factors, can generally be divided into 3 main mechanisms: diffusion, migration and convection.[6, 19] Diffusion, which is concentration-driven and a passive effect, is combated in an ICFB using an equimolar and mixed electrolyte system. The migration of metal species, which is caused by the potential gradient within the separator/membrane, is proportional to the state of charge (SOC) of the electrolyte as well as the current density at which the system operates.[6] Finally, convection, which is driven by possible pressure differences across the separator, causes the electrolyte bulk to cross the separator. Since the micro- and nano-range-sized pores in MPSs are large enough for dissolved active redox species and supporting electrolyte to move through, convection plays a larger role in an MPS than a CEM.[19]

While much research, characterisation and development efforts have been done for MPSs in the last few decades, the focus was mostly on lithium-ion battery applications.[24-26] However, due to the cost and material availability of separator materials, the VFB has also seen significant research efforts with porous separators, where optimisation of materials from 2011 to 2016 led to significant increases in performance, for example attaining an EE of 91% at 80 mA cm^{-2}.[23, 27] The purpose of this study was to evaluate the suitability of various developed and commercial MPSs in an ICFB. Currently, most commercially available MPSs are highly optimised for lithium-ion and lead-acid battery technologies, not only in terms of performance for specific chemistries, but also in production cost at large-scale. Evaluating commercial separators has the advantage of greatly reducing the time that it would take to optimise manufacturing and synthesis of these MPSs. Furthermore, since these MPSs are not produced costly and batch-wise on small scale, such as in a research lab, upscaling of the technology is accelerated since any suitable candidates will be readily available for large-scale implementation. Apart from determining the battery performance, the MPSs were characterised in terms of permeabilities, porosities and thicknesses, to provide data on the behaviour of an ICFB when using MPSs while also providing insight into the parameters requiring optimisation to achieve feasibility.

3.2 Experimentation

The MPS preparation and characterisation is presented in Section 2.1, whereas the ICFB setup and application is discussed in Section 2.2.

3.2.1 MPS preparation & characterisation

Ten commercial MPSs were evaluated in this study (**Table 3.1**). The MPSs were cut into 13.5 cm x 6.5 cm pieces, cleaned (submerged in 65°C DI for 24 hours) and photographed (see Appendix A – **Figure A1**) before being characterised as follows:

1. Weight and thickness: Mitutoyo 293-340-30 Digital Micrometer. All samples were measured at 4 random locations before calculating an average value.
2. Density: MPS thickness and the sample size (13.5 cm x 6.5 cm) were used to calculate volumes, which were used in conjunction with the dry weights to obtain the densities.
3. H_2O uptake: The water uptake was determined by weighing the MPSs before submerging and shaking each 13.5 cm x 6.5 cm piece in 250 mL DI water at room temperature for 10 minutes, before lightly pressing both sides for 2 seconds with a paper towel to remove any residual surface droplets. A v/v% of water uptake (% of void space) was calculated from the MPS volumes and wet and dry weights. While the accuracy would have been influenced by the compressibility of the MPS during thickness measurements, all the MPSs used in this study (excluding the asymmetric C-5550 containing compressible loose fibres on its rough side (see **Figure A2**) and the ribbed Breathtech) were rigid.
4. Air permeance: A GENUINE GURLEY 4340 Automatic Densometer calibrated with 3.2% deviation was used to measure the Gurley number, referring to the JIS (Japanese Industrial Standards)-P8117. The Gurley numbers (in seconds) were obtained by measuring the time it took for 100 mL of synthetic air to pass through a clean and dry circular piece of MPS (with an area of 1.0 square inch or 6.45 cm^2) at a pressure of 1.2156 kPa.
5. SEM imaging & EDX analysis: A 2 cm x 2 cm sample of each MPS was analysed before and after FB cycling using an FEI Quanta 250 FEG SEM (Czech Republic). For coating samples, an Emscope TB 500 Carbon evaporator and an Eiko IB-2 to sputter carbon or gold and palladium, respectively.
6. Chemical stability: The chemical stability was tested during preconditioning, where the MPSs were sealed in an ICFB electrolyte at 65 °C for 24 hours. After cleaning with 0.25 M HCl and DI water, samples were weighed, thickness changes measured and photographed again. Samples that were hydrophilic and chemically stable were tested in the FB.

Table 3.1: Supplier of the MPSs characterised and tested.

No	MPS	Supplier
1	EW-200	ENTEK
2	EW-200 Gen 2.2	ENTEK
3	C-5550	Celgard
4	C-3401	Celgard
5	C-2340	Celgard
6	Breathtech	----
7	DARAK 2000	Daramic
8	VANADion-20	DuPont
9	AA175	Daramic
10	AA900	Daramic

The Fe and Cr cation concentrations in the electrolyte were analysed using ICP-OES (Agilent Technologies 5800). The following standard solutions used during the analysis had been provided by Ultraspec®: 1 000 ± 3 µg mL^{-1} Fe + Cr (99.999%) in 5% HNO_3 and 10 000 ± 30 µg mL^{-1} Fe + Cr (99.999%) in 5% HNO_3 for QC.

3.2.2 ICFB

The ICFB electrolyte preparation is described in Section 2.2.1. Subsequently, the single-cell ICFB test station and the ICFB performance experiments are described in Sections 2.2.2. and 2.2.3, respectively.

3.2.2.1 Electrolyte preparation

For the electrolyte, (purity > 98%) $Fe(II)Cl_2 \cdot 4H_2O$ and $Cr(III)Cl_3 \cdot 6H_2O$ from Sigma-Aldrich (Merck) were dissolved in HCl (32%) from Labchem diluted with DI water (0.055 µS cm^{-1}). Each experiment in this study used 50 mL of a mixed 1.3 M $Fe(II)Cl_2 \cdot 4H_2O$ and $Cr(III)Cl_3 \cdot 6H_2O$ in 1.0 M HCl electrolyte in each electrolyte tank, totalling 100 mL. The electrolyte was bubbled with N_2 (while simultaneously flushing the entire system) for 15 minutes before sealing and heating the system for battery cycling. Consequently, the inert environment isolated the electrolyte from oxygen and any fluctuations in humidity.

3.2.2.2 Single-cell ICFB test station

The laboratory-scale single-cell ICFB test station constructed and used in this study is shown in Appendix A – **Figure A3** (a, b).

Cycling and data collection during all experiments were obtained with a Gamry (Interface 5000E) potentiostat using a constant current of 1.120 A with charging and discharging cut-off potentials at 1.25 V and 0.75 V, respectively. After flushing the entire system with N_2, the electrolyte and FB cell were heated and kept at 65 °C during cycling using a hot plate (Eins-Sci M-S5AS-H3-P) and a temperature probe capable of self-adjusting output for accurate temperature control, as well as a water heating circulator (Julabo CORIO CD-BC4), parallel water pipes and double walled glass

electrolyte tanks sealed airtight with Viton™ O-ring-fitted caps. This ensured static and specific electrolyte and electrode (as well as other cell components) temperatures of 65 °C, isolated from any ambient temperature changes. The headspaces of electrolyte tanks were directly connected with a pipe to equalise cell-outlet hydraulic pressure by equalising any fluctuation in gas pressures from H_2 formation, evaporation and pulsing from the peristaltic pump. Electrolyte was circulated at 65 mL min^{-1} using a Watson Marlow 323S, equipped with 313X and 313D (3 Roller 1.6mm wall) pump heads and acid-compatible 3.2 mm bore Marprene® peristaltic tubing. The in-house constructed lab-scale cell had an active area of 6.9 cm x 4.0 cm, resulting in an operational current density of 40.6 mA cm^{-2}.

CT GF065 graphite felt (CeTech) was used as electrodes, which were enclosed in the cell with a compression ratio of 32.6% (improved cell performance due to increased electrode area and reduced ASR).[28] The felts were pretreated at 600 °C for 30 minutes to increase hydrophilicity and surface area, thereby generating hydrophilic and redox active sites.[29, 30] The thermal treatment resulted in an increased hydrophilicity (see **Figure A4**) with a contact angle (θ) of 126° and < 90° (no droplet visible) before and after treatment, respectively.

3.2.2.3 ICFB performance

The testing of each MPS consisted of three steps: i) polarisation curves (to determine the ASR), 10 charge/discharge cycles (to determine battery performance indicators), and iii) self-discharges (to determine the self-discharge times). For every dataset, the first cycle (cycle #0) was excluded due to charging from 0 V. Hence, in this paper, the second to eleventh cycles were referred to as the first and tenth cycles, respectively.

After charging (cycle 0), each separator was exposed to a varied current density discharge ranging from 0 mA cm^{-2} to 180 mA cm^{-2} using fresh electrolyte for each current density to obtain polarisation curves (see Section 3.2), of which the slopes were used to calculate the ASR (in V mA^{-1} cm^2 converted to Ω cm^2). Although the electrolytes could start at different SOCs for each separator (due to varying ASRs causing variation in the time taken to reach cut-off potentials), it did not affect the ASRs obtained by polarisation curves of each separator. This was useful because different ion exchange rates lead to different mass transfer limitations that determine resistances for each sample.[31] After completing the polarisation curves, 10 charge and discharge cycles were completed. Experiments had to be restricted to 10 cycles due to the significant amount of electrolyte crossover (convection) observed with MPSs, with extended 30-cycle testing for more selective separators. Finally, if any anolyte or catholyte were still present after 10 cycles, the system was charged once more before allowing a self-discharge, where the electrolyte was cycled with no applied current until a cell potential of 0.6 V had been reached. The performance parameters calculated for each separator are listed in Table 2.1 (see Section 2.5.1.2). Additional to the ASR from the polarisation curves, an ASR for each cycle was calculated from the average charge/discharge voltages and current density to obtain 10-cycle average ASR values. The CEM Nafion® 212 (N-212) was used as a

benchmark. Optimal experimental conditions for the lab-scale ICFB test station were used for the benchmark CEM and all MPSs with a non-conventional electrolyte configuration.[32]

3.2.2.4 Repeatability

Any performance variation between experiments originating from changing electrolyte (a fresh 100 mL batch for each experiment), carbon felt electrodes, different MPS pieces, ambient temperatures and all other experimental equipment was measured by repeating experiments. These repetitions consisted of single-cell tests for ASR and 10-cycle performance parameter values using 3 different samples (see **Figure A5** (a, c and e)) of Daramic AA900, while also including the results from **Figure 3.6** (a) (as sample 4), after cleaning and pretreatment in ICFB electrolyte at 65 °C for 24 hours. From these results, the 10-cycle average EEs ranged from 68.9% to 70.5% with a standard deviation of 0.71%, while ASR values ranged from 3.08 Ω cm² to 3.34 Ω cm² with a standard deviation of 0.119 Ω cm². The charge/discharge profiles appear indistinguishable between tests, as observed in Figure A5 (b, d and f).

3.2.2.5 Hydraulic balancing with EW-200

To determine the influence of pulse dampening, the existing ICFB setup was modified by adding an extra connection to each cell inlet, which allowed small amounts of electrolyte to flow upwards and compress N_2 in the headspace of the vertical pulse dampening pipes.

Before applying different flow rates (asymmetrical pumping), the change in viscosity of Fe^{2+}/Fe^{3+} in the catholyte was measured by dissolving 1.3 M solutions of either $Fe(II)Cl_2{\cdot}4H_2O$ or $Fe(III)Cl_3{\cdot}6H_2O$ and 1.3 M $CrCl_3{\cdot}6H_2O$ in 1.0 M HCl, thereby simulating catholytes with either 0 or 100% SOC at 20 °C. The viscosity was measured using a Technico BS/U-Tube Viscometer and calculated using Equation 3.1:

$$\eta_2 = \frac{\eta_1 \times \rho_2 \times t_2}{\rho_1 \times t_1} \quad (3.1)$$

Where η_1 is the viscosity of water (10^{-3} Pa s), t_1 the time for water to flow (s), ρ_1 the density of water (0.997 g cm^{-3}) and η_2, t_2 and ρ_2 the values for the measured liquid.

3.3 Results and Discussion

The characterisation (see Section 2.1) and ICFB performance (see Section 2.3) of the MPSs are presented in Sections 3.1 and 3.2, respectively. Appendix A contains graphs, figures, photographs and SEM images of the MPSs.

3.3.1 MPS preparation and characterisation

The measured physical and chemical properties of the ten commercial MPSs (Table 3.1) tested are presented in **Table 3.2**. The densities of the membranes were calculated from the weight and volume of the membranes, while the % water uptake was converted (δ_{H2O} = 1 g cm^{-3}) to a v/v ratio, which then equals the void volume %. This, however, only holds if the membranes are wettable (hydrophilic), as can be seen from the low % water uptake observed for the C-2340 (0%) and Breathtech (2%) MPS, showing that these membranes were hydrophobic. Due to their hydrophobicity, they were not evaluated further. Since no swelling was observed for all MPSs, the porosity is indicative of the functionality of the separator to transport charge carriers and protons.

Table 3.2: Thickness, density, air permeance (in Gurley seconds), % water uptake and chemical stability of MPSs tested.

MPS	Thickness (µm)	Density (g cm^{-3})	Gurley no. (s)	H_2O uptake (v/v%)	Chemical stability
EW-200	201	1.83	1135 ± 7	39	Yes
EW-200 Gen 2.2	240	2.43	NP	32	Yes
C-5550	75	2.75	1322 ± 12	30	*Yes
C-3401	25	1.56	15099 ±1 24	38	*Yes
C-2340	38	2.00	586 ± 6	0	Yes
Breathtech	275	1.38	3786 ± 45	2	Yes
DARAK 2000	456	2.30	111.4 ± 1	69	Yes
VANADion-20	243	1.60	NP	48	Yes
AA175	183	1.87	521.5 ± 5	63	Yes
AA900	884	2.22	3831 ± 41	50	Yes

NP = non-permeable

* loss of Si was observed (see discussion)

The MPSs varied significantly in thickness (25–884 µm), density (1.56 g cm^{-3} and 2.75 g cm^{-3}), Gurley number (111–15099 s) and water uptakes (32–69 v/v% when considering only the hydrophilic membranes). All polymers were chemically inert when initially exposed to the electrolyte (preconditioning), showing less than −6.96% (AA175) and 2.04% (DARAK 2000) change in weight and thickness, respectively, with no difference in appearance observed. The weight loss for the AA175 MPS was most likely caused by the removal of lubricants added during its manufacturing.[19] Apart from 30-cycle extended testing in the ICFB, no long-term chemical stability, correlating to years of cycling in large-scale applications, was conducted on any separator materials. Studies on the chemical stability of PE (Daramic® and Entek®) in highly

corrosive vanadium electrolytes have shown 27 times higher chemical stability than the N-212 benchmark and PP (Celgard®), which is widely used in bipolar plates for aqueous acidic flow batteries as carbon binding material, has shown minimal morphological changes when subjected to aggravated worst-case scenario testing in VFBs.[33, 34] Performance degradation from morphology changes during long-term operation of these unfunctionalised and inert materials, due to material degradation, would likely only develop from loss of hydrophilicity. As previously mentioned, these polymers are functional in aqueous systems only because of embedded Si. Hence, it is recommended that long-term testing of a suitably developed MPS should be conducted in an ICFB, paired with methods used in this study, e.g., SEM EDX, to ensure adequate Si retention.

3.3.2 ICFB performance

In this section, the ICFB performance (and SEM analysis where relevant) of the various membranes tested is discussed. Firstly (Section 3.2.1), the results obtained when using N-212, which was included as a benchmark, are presented, followed by an analysis of the 10 MPSs (Sections 3.2.2–3.2.9). Finally, an overview is presented in Section 3.2.10.

3.3.2.1 N-212

In **Figure 3.2** (a), the battery performance is presented as efficiencies (CE and VE that result in EE) on the left Y-axis, as well as the discharge capacity on the right Y-axis, for each of its 30 cycles. In Figure 3.2 (b), the first-cycle charge and discharge curves are presented. Figure 3.2 (c, d) represents the concentration changes of both Fe and Cr over the first 2 cycles. While the efficiencies (Figure 3.2 (a)) remained stable over 30 cycles (CE = 91.8%, VE = 81.5% and EE = 74.8% averages), it is interesting to note that the capacity remained near constant for the first seven cycles before decreasing reaching a near-linear capacity decay of 1.34% per cycle, which is notably lower than literature values (20 cycle average of 2.3%) where Nafion® was used with higher HCl concentrations in an ICFB.[35] Assuming that this reduced initial decay could have been the result of active specie crossover, the concentrations of Fe and Cr in both anolyte and catholyte were determined i) before cycling, ii) after one cycle and iii) after charge and discharge of the second cycle (Figure 3.2 (c) – Fe & (d) – Cr). Only two cycles were used due to volume changes resulting in increasing concentration shifts, which due to accumulation (due to electro-osmosis and osmotic drag) leads to increased inaccuracies over time when using a highly conductive CEM such as N-212 (@ 51µm). However, while only the short-term crossover behaviour could be investigated, it is presumed that metal concentration shifts would be highest at the early stages of cycling, i.e., before equilibrium had been reached. This implies that 10-cycle testing with CEMs in flow batteries is inadequate since capacity retention could be overestimated for membranes with specific metallic-ion crossover behaviour, which is linked to the desired equilibrium between the CEM and electrolyte concentrations, in particular mixed electrolyte configurations. Due to this finding, we suggest using equimolar mixed electrolyte configurations when screening membrane

performance to mitigate metallic-ion crossover-driven discharge capacity inaccuracies since different membranes could selectively facilitate either Fe or Cr crossover and donate capacity to the anolyte or catholyte.

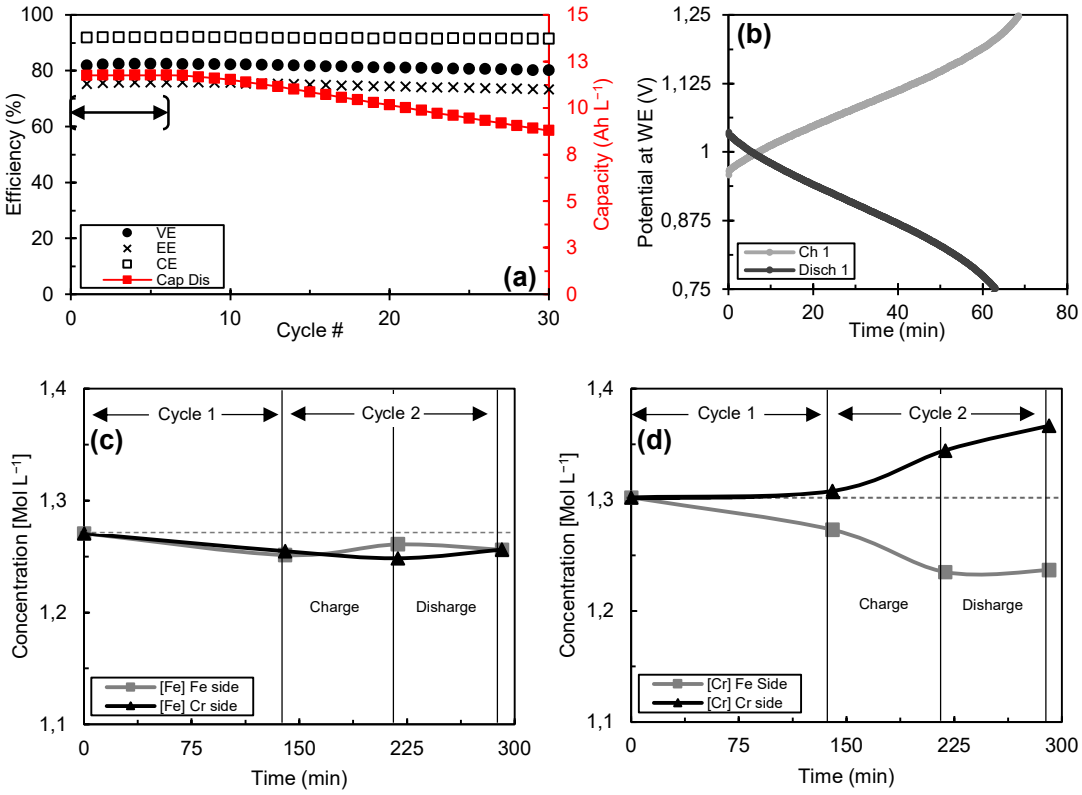

Figure 3.2: N-212: (a) ICFB performance parameters for 30 cycles and (b) 1st charge/discharge cycle. Cation concentrations in ICFB catholyte and anolyte of (c) total $Fe^{2+/3+}$ and (d) total $Cr^{2+/3+}$.

According to the results, the Fe concentrations remained the same (Figure 3.2 (c)), while Cr migrated from the Fe-side to the Cr-side (Figure 3.2 (d)), i.e., from the catholyte to the anolyte. This suggests that during charging, when using N-212, the applied potential facilitates the transport of Cr to the anolyte through large enough cation-conducting channels that result in Cr^{3+} acting as a charge balancer. Since the ICFB is operated at 65 °C to shift the Cr chemical equilibrium from the redox-inactive $Cr(H_2O)_6^{3+}$ to the more active $Cr(H_2O)_5Cl^{2+}$ species, it can be assumed that Cr is the limiting factor in an equimolar electrolyte, which would help explain the initial capacity gain when Cr crosses to the anolyte.[36] While the capacity gain during the first 10 cycles was significantly smaller than the crossover effects seen in the MPS studies, this effect should be considered when comparing the capacity retention of membranes, as it might lead to inaccurate interpretations. Accordingly, only the 10-cycle average decay from cycle 11–20 (1.25%) was used as the benchmark when comparing the various separators (Section 3.2.10).

3.3.2.2 EW-200

As mentioned previously, only 10 ICFB cycles were measured due to often excessive electrolyte convection during cycling of MPSs. According to **Figure 3.3** (a), a stable 10-cycle average VE of 80.8% was obtained with this 201 µm thick PE separator, which was 1.1% lower than the average obtained with the thinner (57.8 µm, wetted) N-212. The 20.8% lower average CE of this MPS (71.0%) compared to N-212's (91.8%) was a result of a higher self-discharge rate due to convection, as displayed in Figure 3.3 (b) showing the proportionally longer charge cycles compared to the discharge cycles. During cycling, ~50% of the electrolyte had migrated to the anolyte side after 10 cycles. This suggests that the Cr^{2+} and Fe^{3+} discharge through direct contact in the solution rather than through the external circuit, resulting in significant efficiency losses (EE = 57.3%). While there is limited data on performance parameters using MPSs in an ICFB, Mans *et al.* obtained an EE of 54% for the same MPS when using a slightly different electrolyte composition (1.3 M Fe and 1.4 M Cr) and a 23% lower electrolyte flow rate (50 mL min^{-1}).[14] The 7.86% per cycle capacity decay was mainly attributed to the high rate of convection.

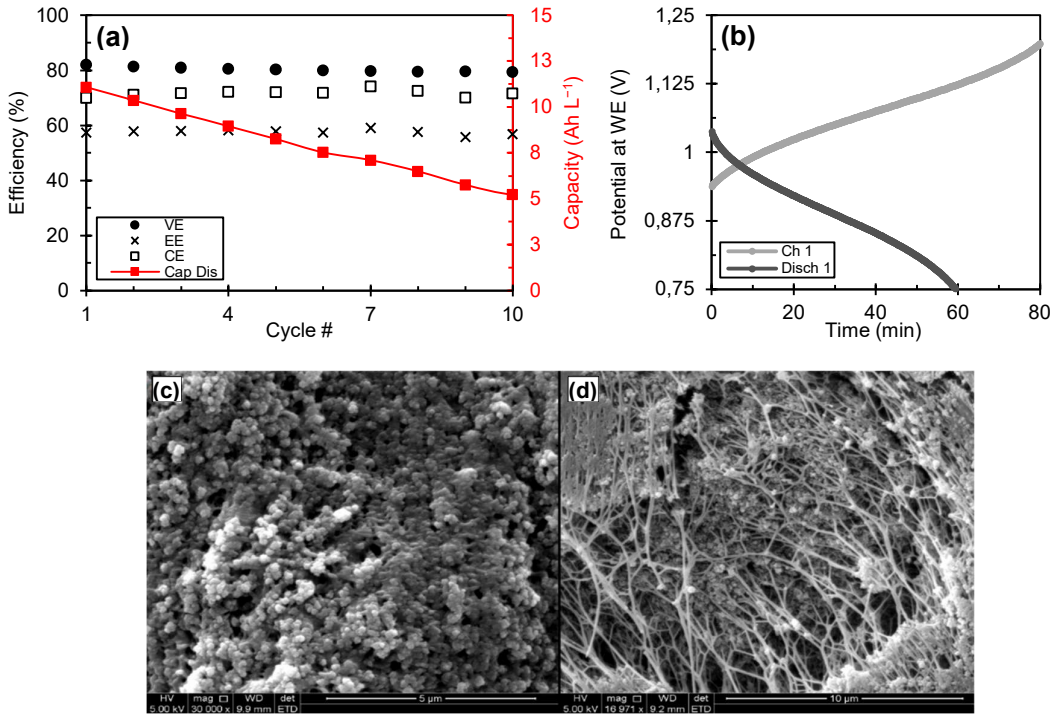

Figure 3.3: EW-200: (a) 10 cycle performance, (b) first-cycle charge and discharge curves and (c, d) SEM imaging of surface (at 30 000x), and cross-section at (16 971x), respectively.

A SEM image of the surface and cross-section of EW-200 is shown in Figure 3.3 (c, d), respectively. According to the EDX analysis of these surfaces, EW-200 had a Si to other element ratio of 25.5%, where the remaining composition consisted of carbon (40.6%), most likely from PE and oxygen (31.5%) from the embedded Si. The polymer

strands, which are in the nanometre range Figure 3.3 (d)), seem to hold together a matrix of Si particles in a highly amorphous structure, providing pore sizes in the range of 0.5–1.0 µm.

3.3.2.3 EW-200 Gen 2.2

In an attempt to reduce convection, an asymmetric coated variant of the EW-200, the Gen 2.2, was evaluated. As seen in Table 3.2, the coating was not air permeable, although the porous section still allowed 32% (v/v) water uptake. No chemical degradation, colour change or weight loss was observed by exposure to electrolyte.

When using the EW-200 Gen 2.2, gas bubbles were observed in the anolyte's outlet pipe. Furthermore, no performance parameters could be obtained due to excessive resistances resulting in failure to cycle. The large gap between the charge and discharge cycles (**Figure A6** (a)) confirms a very high cell resistance, with the anomaly on the first charge cycle resulting from a buildup and release of large gas pockets that fluctuate and decrease the electrode surface area, thereby increasing the ASR. From the inspection after ICFB testing, which included attempting to wet the separator, it was clear that the porous section of the MPS was hydrophilic, while the coating was hydrophobic (see Figure A6 (b)), which would explain the gas pockets and high resistance due to the lack of charge carriers in the coating. This confirmed that this separator was not suitable for an ICFB due to its hydrophobic coating.

3.3.2.4 C-5550

The cycling results of the 75 µm C-5550 asymmetric MPS are shown in **Figure A7** (a). The discharge capacity remained low, starting with only 4.2 Ah L^{-1} in the first cycle before reaching an equilibrium at ~3 Ah L^{-1} between cycles 2 and 10. This can be ascribed to the significant convection and subsequent decrease of electrolyte in the catholyte tank. Excluding cycle 0, (see Section 2.2.3), when using highly permeable and/or thin separators (high convection rates), resulted in very low discharge capacities due to the rapid convection of anolyte or catholyte (dependent on direction of pressure difference) from significant volume changes in both anolyte and catholyte tanks, as was observed in varying degrees for most of the MPSs tested. The separator not only lost 4.2% weight after preconditioning, but had also lost its hydrophilicity after cycling. According to the SEM EDX, the ratio of Si to other elements during cycling decreased from 0.81% to 0%, confirming a loss of detectable surface Si, which in turn explains the loss of hydrophilicity. From SEM imaging (Figure A7 (b)), it is possible that the porosity of this stretched PP MPS might have increased with the slight weight and Si loss. The increase in an already high electrolyte convection, the loss of hydrophilicity and the low performance made this separator unsuitable for an ICFB.

3.3.2.5 C-3401

While C-3401 had the lowest air permeance of all samples (Gurley number = 15099 s), making it more than 15 times less permeable than EW-200 despite being $1/8^{th}$ of its thickness, visibly all catholyte crossed over to the anolyte tank within 4 ICFB cycles.

Despite the convection, it was possible to obtain data for the 10 cycles with the residual catholyte (**Figure 3.4** (a)).

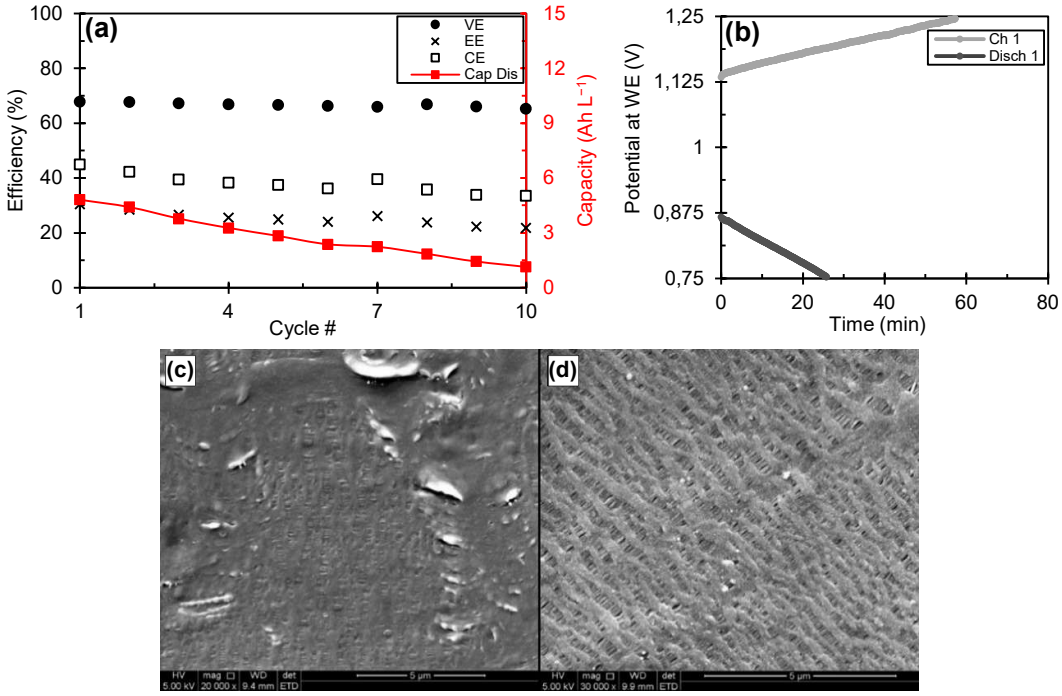

Figure 3.4: C-3401: (a) 10 cycle performance, (b) first-cycle charge and discharge curves and (c, d) SEM imaging of surface before (20 000x) and after cycling (at 30 000x), respectively.

This symmetrical PP separator has smooth surfaces, whereas C-5550 was asymmetric with a rough side that might have influenced convection through different surface pressures. When comparing the difference in Gurley seconds (Table 3.2) and pore sizes and porosity from SEM imaging (Figure 3.4 (c, d)) to the more amorphous structure and larger cavities in EW-200 (Figure 3.3 (c, d)), it seems that the air permeance (Gurley number) on its own is not an accurate depicter of a separator's ability to separate ICFB electrolytes and prevent them from mixing or crossing over due to convection, which confirms the lack of correlation observed for the data presented in Table 3.2. It is evident that i) the hydrophilicity (related to the Si content) and ii) the thickness (affecting the separation) also impacted performance.

According to EDX spectroscopy of the surfaces in Figure 3.4 (c, d) the surface ratio of Si to the rest decreased from 0.85% to 0% after cycling, which corresponds to the measured weight loss of 6.4%. Apart from the loss of embedded Si and hence wettability, the PP-based MPS was chemically stable. It was however too thin for ICFB application, with a high electrolyte convection resulting in a significant decrease in discharge capacity (from 4.8 Ah L^{-1} to 1.1 Ah L^{-1}) and a low average CE (38.1%). However, despite the low thickness (25 µm), a high ASR of 4.35 Ω cm^{-2} (**Table 3.3**) resulted in a low VE (66.6%).

3.3.2.6 DARAK 2000

The ICFB testing of the DARAK 2000 MPS had to be terminated due to leakage of electrolyte from the membrane protruding from the cell gasket. This was most likely caused by the high permeability and void space (v/v%) of this MPS (Table 3.2). As a result, the phenolic resin-based MPS was unsuitable for the ICFB, although it remained hydrophilic with no weight loss, which did confirm the material's stability in the electrolyte.

3.3.2.7 VANADion-20

To address the high convection and limited ion selectivity when using MPSs in FBs, porous separators have been coated with solid ion exchange layers.[19, 37] One such example is the VANADion-20 bilayer membrane, which has a 20 µm Nafion® coating. Using this membrane in an VFB, Zhou *et al*. reported a high performance (CE of as high as 95.3% and an EE of 76.2%) with a normalised capacity decay of only 0.33% when using a higher current density of 320 mA cm^{-2}.[37]

When using VANADion-20 in the ICFB with 40.6 mA cm^{-2}, electrolyte crossover was observed with more than 20% volume crossover to the anolyte after 10 cycles. Nonetheless, the separator performed well during short-term tests, yielding a capacity decay of 1.05% per cycle (**Figure 3.5** (a)). It is, however, likely that the capacity decay was lowered by the Cr crossover as discussed in Section 3.2.1. The ionomer layer seemed to be intact after cycling, therefore, as with N-212, electrolyte volume shifts were caused by water and HCl crossover due to i) electro-osmosis (water flux through a membrane as hydration spheres of cations), ii) different osmotic pressures on both sides of the separator, or iii) electro-osmotic drag (charge balancing ionic fluxes through a separator with trailing water molecules).[38, 39]

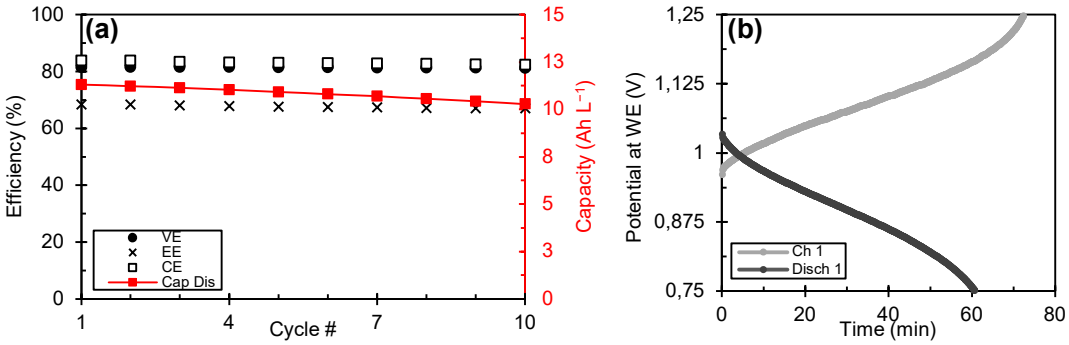

Figure 3.5: VANADion-20: (a) 10 cycle performance and (b) first-cycle charge and discharge curves.

The average CE (83.0%) over 10 cycles was 8.8% lower than N-212 but 12% higher than EW-200, which had a similar thickness but no coating. Additionally, this separator was able to obtain a 3x longer self-discharge time than EW-200 (18 h 40 min),

suggesting that the thin CEM coating resulted in an increased separation efficiency. However, the self-discharge time was significantly lower than the benchmark 46 h, which is a thicker CEM of the same (expensive) Nafion® ionomer coating. This implies that the coating might be too thin or not selective enough for the metallic cations of an ICFB, which could have been worsened by the permeable porous layer (~210 μm). Nonetheless, by significantly reducing pressure-driven capacity losses, this bilayer separator outperformed most of the uncoated MPSs (except for the 884 μm Daramic separator) in terms of EE, capacity retention and self-discharge time. Hence, while the addition of a non-porous coating can successfully increase the CE and the cycling life, the trade-off is an increase in ASR, cost and manufacturing complexity while introducing a possible proton exchange functional group as well as CEM backbone degradation. From these results, it might be worth coating different ionomers on porous MPSs (such as those used in this study) and comparing their short- and long-term performance in an ICFB.

3.3.2.8 AA175

Two similar Daramic MPSs (AA175 and AA900, Section 3.2.9) were tested with thicknesses of 183 μm and 884 μm, respectively. The 10-cycle performance of AA175 presented in **Figure A8** (a) showed a low average EE (43.1%), due to a high operational self-discharge where the charge cycles were twice as long as the discharge cycles Figure A8 (b), resulting in a low CE (56.3%). In addition, ~60% of the anolyte had migrated to the catholyte after 10 cycles. The 521 s (Gurley number) permeance of AA175, which is less than half of EW-200's (1135 s), despite the similar thicknesses (183 μm vs 201 μm), could have contributed to the high convection due to a higher porosity resulting in an inadequate separation efficiency.

In this study, it was observed that slight positional or mechanical changes in the tubing inside the clamps of the peristaltic pump during cycling led to hydraulic pressure differences that, although small, contributed to the increased electrolyte convection.[18] However, pressure differences can also be caused by viscosity differences in electrolytes during pumping. The capacity gain observed after cycle 6 was likely due to a directional change in the pressure difference, introducing electrolyte with Cr^{3+} back to the anolyte and increasing the charging capacity. This effect suggests that asymmetrical flow rates of electrolyte could regenerate discharge capacity by rebalancing electrolyte volumes without any additional hardware, with the same benefit of a hydraulic shunt.[40] The possible effect of pressure differences was further investigated and elucidated in Section 3.3.

3.3.2.9 AA900

According to Figure 3.6 (a), the first and last cycles' capacities of 11.6 Ah L^{-1} and 9.9 Ah L^{-1}, respectively, show a notably higher capacity retention than that of other MPSs, resulting in the lowest observed per-cycle capacity decay of 0.55%. Unlike most separators tested, the AA900, despite a Gurley number that was nearly four times less than that of C-3401 (which had shown severe convection), showed no

convection. After an additional test of 30 cycles followed by self-discharge, AA900 yielded only ~5% crossover in terms of change in fluid levels, compared to the ~30% observed when using N-212. This low crossover could have resulted from the significant thickness of this MPS (884 µm). This resulted in less operational self-discharge and a 10-cycle average CE of 91.4%, which was close to the N-212 benchmark while being 35.1% and 20.4% higher than the thinner AA175 (183 µm) and EW-200, respectively. The higher thickness also resulted in a longer path length for proton transport, resulting in a lower VE of 77.1% compared to the 80.8% of EW-200 and 81.7% of N-212. Although the thin and thick AA variants had the same average VE, the 183 µm separator had a higher initial VE of 78.4%, where the average was negatively affected by an increasing ASR due to the significant convection. The high thickness of this MPS resulted in an ASR of 3.08 Ω cm², illustrated by the prominent separation between the charge and discharge curves (Figure 3.6 (b)).

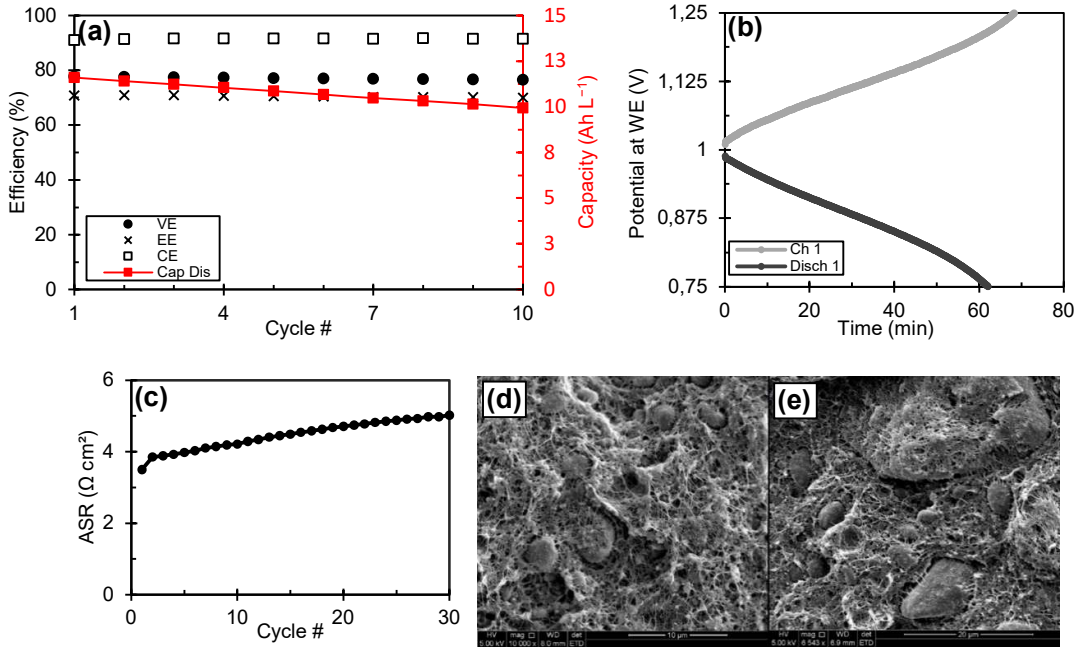

Figure 3.6: AA900: (a) 10 cycle performance, (b) first-cycle charge and discharge curves, (c) ASR of extended testing and (d, e) SEM imaging of freeze-snapped cross-section before (at 10 000x) and after cycling (at 6 543x), respectively.

Considering the adequate short-term performance of this MPS (Figure 3.6 (a, b)), extended testing was conducted (30 cycles), which showed an increasing ASR (Figure 3.6 (c)) that could have been caused by i) the migration of active species, ii) an unobservable mechanical change in the separator, or iii) the influence of diffusing residual lubricant from the extrusion process of this MPS. Further investigation into the high per-cycle ASR increase would need to be conducted before this separator could be deemed fit for realistic long-term cycling. No noticeable structural changes were observed with SEM imaging of the freeze-snapped cross-sectional samples before

and after cycling, as seen in Figure 3.6 (d, e), respectively (see also **Figure A9**). A Si content of 26.76% (before) and 26.45% (after) showed higher Si retention compared to the other MPSs evaluated.

3.3.2.10 Summary

In Table 3.3, a 10-cycle average summary of the performance indicators is presented for N-212 and the 10 MPSs tested, which were made of different materials and manufacturing techniques and had a wide variety of thicknesses, pore sizes and porosity. From the results, AA900 and VANADion-20 separators achieved the highest EEs of 70.5% and 67.7%, respectively, which was more than 4.5% below the N-212 benchmark.

Table 3.3: Performance parameters of various separators over 10 cycles.

Separator	Peak Cap Dis (Ah L^{-1})	Cap Decay (%)	CE (%)	VE (%)	EE (%)	avg. ASR (Ω cm^2)	ASR (Ω cm^2)
#N-212	11.8	*1.25/H0.54 h^{-1}	91.8	81.7	75.0	2.51	2.38
EW-200	11.9	*7.86/H2.74 h^{-1}	71.0	80.8	57.3	2.59	2.39
EW-200 Gen 2.2	X	X	X	X	X	X	X
C-5550	10.4	*4.27/H4.79 h^{-1}	53.4	72.2	38.5	3.95	3.65
C-3401	7.5	*14.61/H8.55 h^{-1}	38.1	66.6	25.4	5.00	4.35
C-2340	X	X	X	X	X	X	X
Breathtech	X	X	X	X	X	X	X
DARAK 2000	X	X	X	X	X	X	X
VANADion-20	11.6	*1.05/H0.43 h^{-1}	83.0	81.5	67.7	2.54	2.40
AA175	10.4	*2.19/H0.91 h^{-1}	56.3	77.1	43.1	3.21	2.82
AA900	11.6	*0.55/H0.71 h^{-1}	91.4	77.1	70.5	3.24	3.08

10-cycle average for cycles 11–20
* average capacity decay per cycle using charge/discharge average voltages
H hourly capacity decay (from electrolyte run time)
X MPS unsuitable for ICFB

Due to their porous nature, the self-discharge rates of all the MPSs were higher than that of N-212 (**Figure 3.7** (a)). The thicker AA900 and coated VANADion-20 separators achieved the highest self-discharge times (27 h 19 min and 18 h 45 min, respectively), which was significantly less than the 46 hours obtained when using N-212. These high self-discharge rates contributed significantly to the generally lower CE values obtained (Table 3.3). However, these self-discharge times had been obtained at the end of cycling, which often resulted in low electrolyte levels in the catholyte tank (apart from AA900 and VANADion-20), resulting in possibly reduced values.

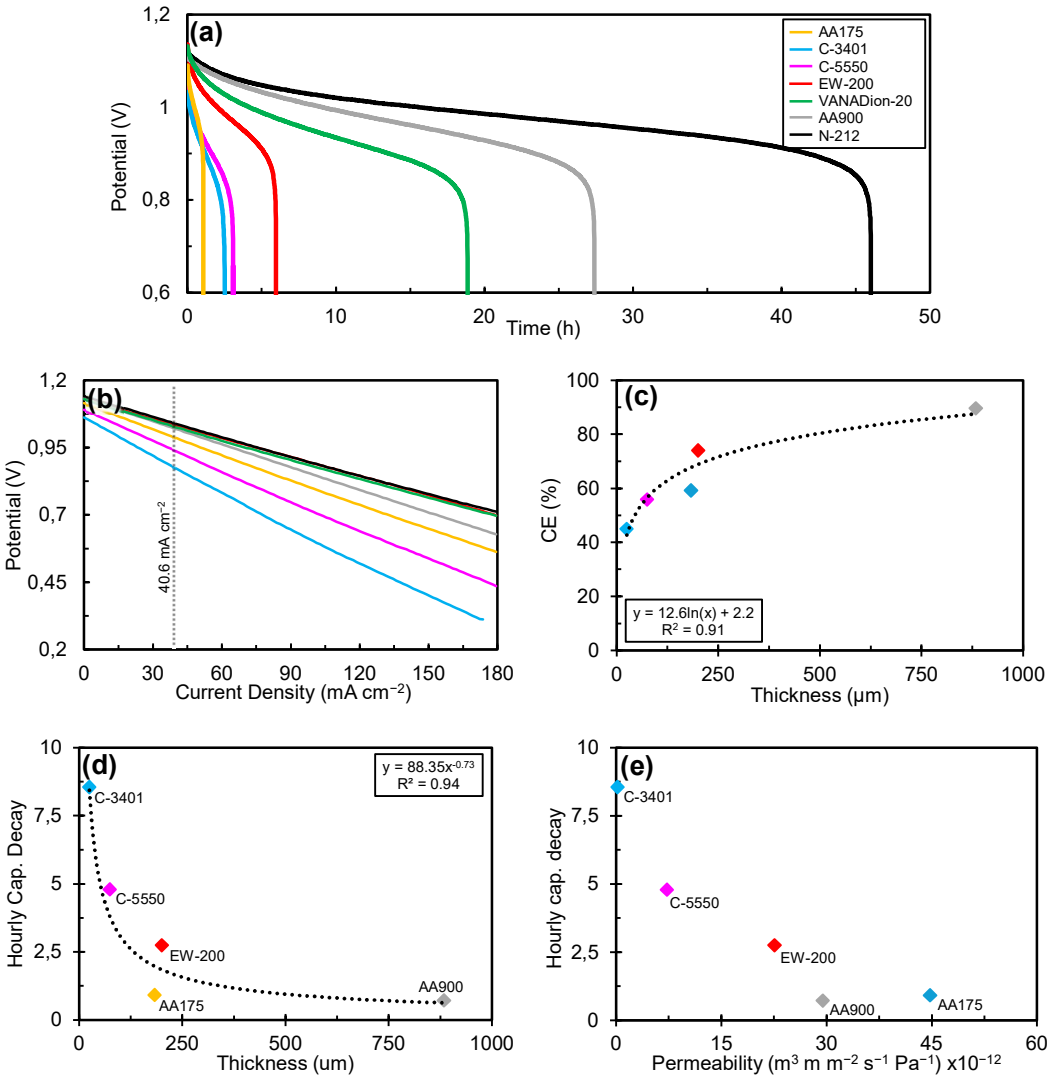

Figure 3.7: (a) Self-discharge curves, (b) discharge polarisation curves (up to 180 mA cm^{-2}), (c) CE as function of thickness for various separators, as well as hourly capacity decay as functions of (d) thickness and (e) permeability.

Seeing that the resistance against ion conduction across a separator relates to the overpotential required to balance electrical charge in a flow battery, the ASR is an important parameter that directly correlates to the VE, which in turn determines the EE. The ASRs as a function of the current density (0–180 mA cm^{-2}), as well as the 10-cycle average ASR at 40.6 mA cm^{-2}, presented in Table 3.3, were calculated using the polarisation curves obtained for the MPSs and N-212 (Figure 3.7 (b)). While the initial potentials of the polarisation curves were affected by different cell SOCs (see Section 2.2.3), the slopes were not. Since MPSs typically do not have ion exchange groups, the polarisation curves were predominantly determined by the facilitated ion transport of the electrolyte within the pores and the internal resistance related to the membrane thicknesses rather than by the IECs.[41] When correlating the data from Table 3.2 with

the ASRs results (Table 3.3), it seems that the ASRs had been affected by membrane thickness, void spaces and air permeance. The values obtained mostly correlated to the 10-cycle averages, however, due to convection, loss of hydrophilicity and imbalance from metal cation migration, the ASRs increased during cycling, negatively affecting the average ASR. The MPS with the lowest ASR was EW-200 (2.39 Ω cm²), which was comparable to that of N-212 (2.38 Ω cm²). Compared to the best-performing porous separator (AA900) in terms of EE, the EW-200 separator had a lower air permeance (1135 s vs 3831 s) while being more than 4 times thinner. However, these properties resulted in a lower selectivity and separation efficiency, evidenced by its low self-discharge time (6 hours), a CE of 71.0% and significant electrolyte volume changes. The resistance from MPSs with steeper slopes than -0.003 V mA^{-1} cm^2 most likely resulted from higher thicknesses or Gurley seconds. It is noteworthy that contradictory to what is observed with CEMs, the thinnest (25 µm) separator, C-3401, had the highest ASR, despite suffering from high convection, relating to still being easily permeable by electrolyte. Porous separators for nanofiltration could potentially use the size exclusion principle to obtain higher separation efficiency of metallic ions while still allowing charge carrier migration, where the optimal thickness range considering an increase in ASR should be investigated.

The crossover resulting in a lowered CE and increased capacity decay was the leading cause of the lacking ICFB performance observed for the MPSs. Therefore, the main source of performance degradation of the tested MPSs was electrolyte related. To further elucidate this, three relations between battery performance and physical properties are shown in Figure 3.7 (c) CE vs thickness, (d) capacity decay vs thickness and (e) capacity decay vs air permeance (calculated from the Gurley number in Table 3.2). Despite some fluctuations, it is still clear that an increase in thickness improved CE and decreased hourly capacity decay (Figure 3.7 (c, d)). The decreasing decay with increasing thickness is understandable considering that a thicker MPS would reduce crossover by increasing path lengths and possibly tortuosity, which correlates with an increasing CE. While Gurley number measurements (see Section 2.5.5) are only a substitute for liquid measurements, it provides correlations to the permeability of ions. While the air permeance (Figure 3.7 (e)) reflects the permeability (takes into account the separator thickness), it is not clear with the current amount of data what exact result it has on the hourly capacity decay; however, there is likely an area of permeability where the overall performance is ideal. Seeing that the commercial MPSs tested differed significantly in terms of physical and chemical properties, it was not possible to provide a clear relationship between the capacity decay and water uptake. However, it is known that the properties affecting water uptake, such as higher hydrophilicity, larger pores and more pore interconnectivity, generally increase ionic conductivity while decreasing selectivity.[27]

Manufacturing MPSs while varying only single parameters such as thickness, porosity, pore size and hydrophilicity at a time would provide a better understanding of these relationships, enabling the ideal physical MPS properties for an ICFB to be modelled.

The effects of single MPS parameters on the key challenge of convection could be explained by considering the Hagen-Poiseuille equation.[42]

$$J = \frac{\varepsilon r^2 \Delta P}{8\eta\tau\Delta x} \quad (2.2)$$

The rate and volume of electrolyte convection (Flux = *J*) increase with increasing porosity (ε), pore radius (r) and differential pressure across the separator (ΔP), while it decreases with increasing electrolyte viscosity (η), tortuosity ($\tau \approx$ pore path resistance) and MPS thickness (Δx). Omitting cation migration due to other crossover mechanisms, this relationship indicates that convection, i.e., electrolyte permeation, increases with increasing pore size, hydraulic pressure and decreasing pore length. Although tortuosity is difficult to control and quantify, it is affected by the void volume % and membrane thickness, and hence, will also influence electrolyte flux. While the results obtained broadly correlated with this trend, MPSs with the smallest pore sizes, such as C-3401 (Figure 3.4 (d)), however, had the highest rate of convection. When comparing this to that of AA900, which had no convection while having significantly larger pore sizes (Figure 3.6 (d, e)), it is clear, and a significant finding, that the membrane thickness as well as the hydraulic pressure difference has a more significant influence on the flux than the pore size. As a result, the main objective of developing MPSs with pore sizes large enough for metallic-ion crossover and convection in the µm range for the ICFB should be to maximise the thickness while considering the trade-offs with increasing ASR.

3.3.3 Hydraulic balancing with EW-200

As discussed in Section 3.2.8, small pressure differences (ΔP in Equation 3.2) across the MPS could increase the driving force for convection, which was found to be the dominant crossover mechanism when employing MPSs. Although MPS properties can be modified to mitigate convection, i.e., dense bilayer membranes, CEM coatings and increasing thickness (which was found to have a larger impact than reducing pore size), when considering low-cost alternatives and large-scale implementation, it is vital to investigate cost-effective mitigation techniques outside of the modification of MPS properties. To determine the influence of the hydraulic pumping pressure of the electrolyte on the performance of the ICFB, the experimental setup was modified to investigate the effect of pulse dampening and an asymmetrical pumping rate on capacity retention and convection. The EW-200 MPS was chosen for these tests seeing that it could obtain 10 cycles and had high convection rates.

3.3.3.1 Pulse dampening

With the initial setup, pressure peaks were observed both in the anolyte and catholyte outlet streams owing to the pulsing nature of the peristaltic pumps used. Decreasing each pulse with a dampener would scale down the magnitude of ΔP (illustrated in **Figure 3.8**) and create a more even flow of electrolyte over the MPS surface.

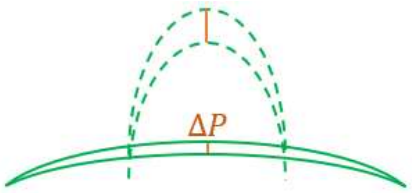

Figure 3.8: Illustration of pulse dampening and its effect on ΔP.

Adding an extra connection to each cell inlet using the compression of N_2 as a dampener (see Section 2.2.4) would provide a simple and low-cost lab-scale system that could be upscaled for industrial applications. Although centrifugal pumps are generally used at larger scale systems, small hydraulic pressure spikes can occur due to the nature of turbulent flow.[43] Accordingly, the capacity and performance with extended cycling of 30 cycles of EW-200 with and without dampening are shown in **Figure 3.9** (b, a), respectively. Without pulse dampening (Figure 3.9 (a)), the cycling stability was negatively affected, which resulted in increasingly unstable efficiencies close to catholyte depletion point. At the end of cycle 22, all catholyte from the electrolyte tank had migrated to the anolyte tank, with only the retained catholyte from the wetted felt in the cell, ceasing the normal cycling of the ICFB. Convection as the cause for capacity loss was supported by an 82% capacity recovery by remixing and redistribution of the electrolyte (cycles 23 and 24), similar to volume balancing of a hydraulic shunt.[40] Using a pulse dampener reduced the average catholyte crossover rate from 0.99 mL h^{-1} to 0.21 mL h^{-1}, which allowed cycling to be extended past 22 cycles. The mitigation of convection increased performance (Figure 3.9 (b)) by reducing the average per-cycle capacity decay from 7.8% to 3.0% and stabilising the 10-cycle average EE, increasing it by 5.2% (to 62.8%).

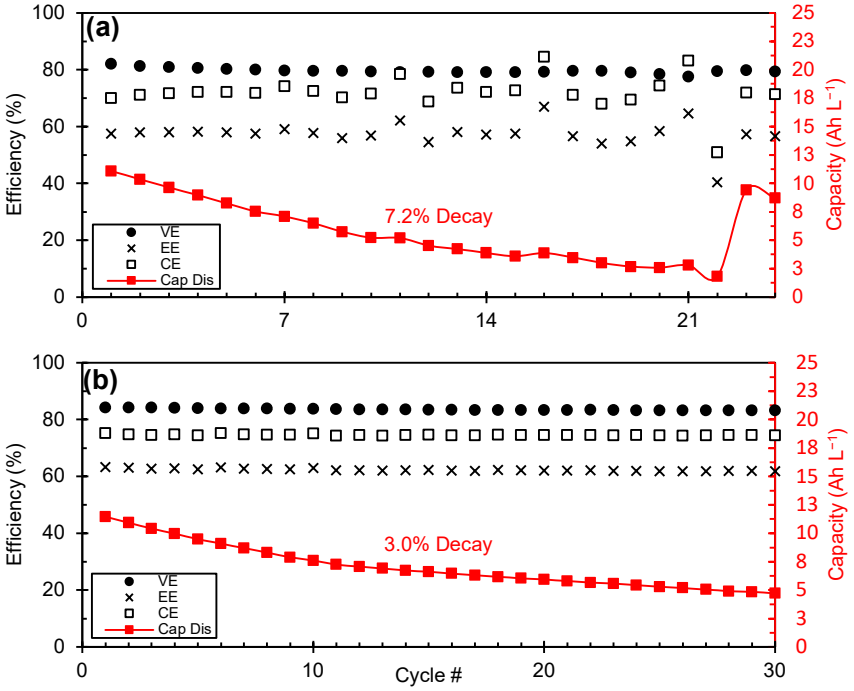

Figure 3.9: EW-200: Performance over 30 cycles using (a) normal experimental setup and (b) a pulse dampener.

3.3.3.2 Pulse dampening & asymmetrical pumping

During experiments, it was observed that Fe^{3+} solutions were more viscous than Fe^{2+} solutions. An elevated viscosity would increase the flow resistance through the electrode felts and pipes as Fe^{2+} in the catholyte is increasingly charged to Fe^{3+}, which could result in more convection during equal anolyte and catholyte pumping rates, especially when using positive displacement pumps. The kinematic viscosity measurements of a 0% and 100% synthetic SOC catholyte (Section 2.2.4), which were 2.1 $m^2\ s^{-1}\ x10^{-6}$ and 2.6 $m^2\ s^{-1}\ x10^{-6}$, respectively, confirmed that the viscosity of the catholyte will change during cycling with a maximum of 24% (at 20 °C). It is known that the anolyte is charged from Cr^{3+} to Cr^{2+} in the form of $Cr(H_2O)_5Cl^{2+}$ to $Cr(H_2O)_5Cl^{+}$ at 65 °C, and that lower ionic strength generally results in lower densities and viscosities as a result of less compaction and ionic interaction.[36, 44] Because of this and the challenges of preparing and isolating a readily oxidising Cr^{2+} solution, it was presumed that charging would result in a decrease in anolyte viscosity.

In consideration of the pressure increase at the catholyte side of the MPS from an increase in viscosity, a higher anolyte flow rate of 1.4–2.8% was used, thereby increasing its pressure. This was achieved by adjustment of the tubing clamps for the anolyte and catholyte to deliver electrolyte flow rates of 71.5± 0.5 mL min^{-1} and 70.0 ± 0.5 mL min^{-1} at 20 °C, respectively. During the following experiments, the ICFB was operated for only 10 cycles to obtain comparable self-discharge times and reduce the possibility of slight positional shifts of tubing likely to occur with longer duration tests,

which was observed to equalise the flow rate. The results with equal and asymmetrical flow rates, both of which had pulse dampeners fitted at the cell inlets, are shown in **Figure 3.10** (a, b), respectively. Using an asymmetrical flow rate in addition to pulse dampening eliminated any measurable catholyte crossover over a 39.2 h period (11 cycles + OCV rest periods + self-discharge), which resulted in a further decrease in the capacity decay from a 3.3% cycle average (Figure 3.10 (a)) to 0.44% (Figure 3.10 (b)), while also increasing the peak discharge capacity (from 11.8 Ah L^{-1} to 12.1 Ah L^{-1}).

From the results of the 10-cycle average performance of the standard setup compared to the system with pulse dampening, we show that the CE increased from 71.7% to 74.8% and the VE from 80.3% to 84.0%. However, the 10-cycle average efficiencies were not improved further by implementing an asymmetrical flow rate. Efficiencies of long-term cycling will likely benefit from further mitigation of convection, as ASR would increase less, and therefore, a sustained VE. A substantial improvement, however, was observed for the self-discharge rate. As shown in Figure 3.10 (c), the reduced convection-related crossover due to pulse dampening and asymmetrical pumping resulted in self-discharge rate reductions of 25% (pulse dampening) and 87.3% (pulse dampening and asymmetrical pumping), respectively.

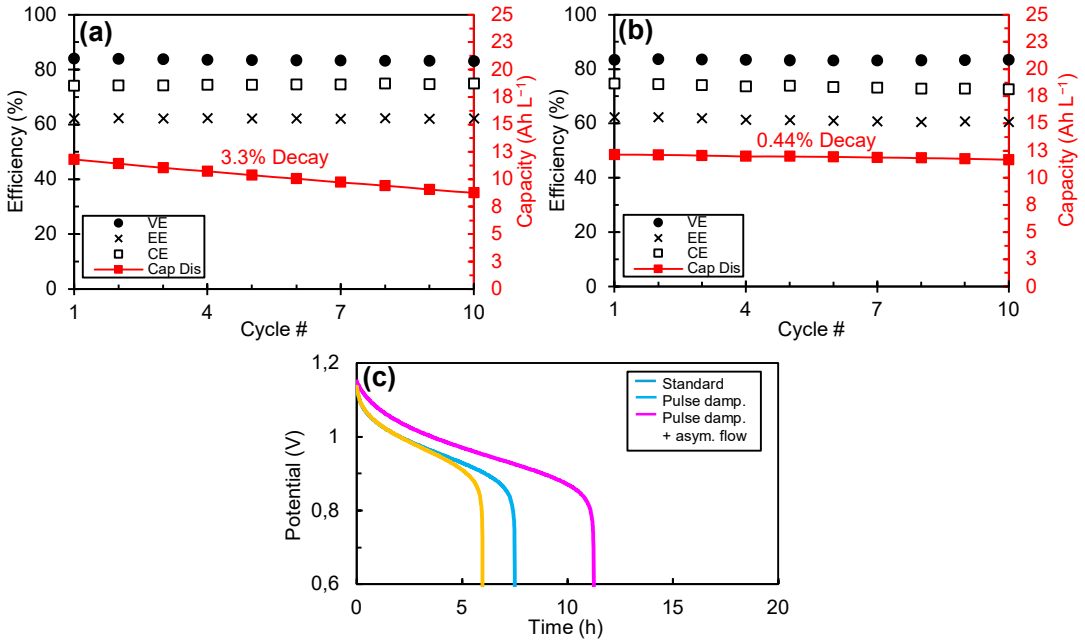

Figure 3.10: EW-200: Performance over 10 cycles using (a) a pulse dampener and (b) a pulse dampener with 1.4–2.8% increased anolyte flow. (c) Self-discharge curves comparing different pumping adaptations.

These results illustrate that viscosity differences between electrolytes can affect the capacity retention of separators that are susceptible to convection-related crossover from small pressure differences (such as MPSs) and that mitigation is achievable by

employing an asymmetrical flow rate. It could be beneficial to use lower electrolyte flow rates closer to the stoichiometric flow rate, as this would reduce pressure-driven convection (with the trade-off of increasing ASR), which is already a requirement on large-scale systems to minimise pumping losses. Considering this, different MPSs would have different optimal and asymmetric flow rates to find the best capacity retention and ASR, and optimal values should be determined for large-scale stacks after a suitable separator is found. As previously mentioned, the viscosities of electrolytes are dynamic and dependent on the SOC, therefore, further studies should be conducted to precisely measure the pressure differences at the cell inlets and outlets. Computational fluid dynamics (CFD) modelling studies would also benefit ICFB development, as it has the VFB, since pressures from various flow rates could be simulated at different points of permeable MPSs at single-cell level as well as multi-cell stacks.[45] Doing so would provide insight into balancing and minimising these pressures, which in large-scale applications would enable convection mitigation through straightforward pump RPM adjustments linked to SOC, which would not require any additional hardware or costs.

3.4 Conclusion

In this study, the suitability of 10 commercially available MPSs for the ICFB was evaluated. The MPSs tested, from materials such as PP and PE that are chemically inert in aqueous FB applications, did not show any degradation in weight loss or morphology changes after short-term tests. However, a decline in embedded Si was observed in stretched-type separators, contrary to those manufactured by extrusion. The best EEs (> 4.5% lower than N-212) were obtained with the relatively thick (884 µm) AA900 and Nafion®-coated composite VANADion-20, with hourly capacity decays of 0.71% and 0.43%, respectively. The electrolyte crossover observed for all uncoated MPSs (except AA900), primarily convection-related, resulted in performance degradation by substantially lowering capacities and coulombic efficiencies. Investigating the crossover with N-212, the benchmark non-porous CEM, revealed that a notable amount of Cr selectively migrated from the catholyte to the anolyte during the first 8 cycles while using a symmetrical mixed electrolyte configuration, which increased and masked the actual discharge capacity during short-term ICFB testing.

The most predominant properties affecting the electrolyte flux through the tested MPSs were i) void volume v/v%, ii) thickness (crucial for sustained cycling and should be at least four times thicker than the current CEMs and ten times thicker than Li-ion separators being used), iii) air permeance (as Gurley seconds) and iv) wettability, as H_2O uptake (v/v%) from Si and porous morphology, (recommended 39–50% with leakage challenges at > 50%). These properties, in turn, influenced the capacity retention and EE due to convection, cation migration and resistance through the path lengths for the charge carriers. In correlation with the Hagen-Poiseuille equation, highly permeable separators that were also thin seemed to suffer more from hydraulic

pressure and convection. Properties such as permeance, % void space, and pore size influence the performance of an MPS, where higher permeabilities and thicknesses reduce the hourly capacity decay rate and improve the CE.

Using the porous EW-200 (201 µm), it was shown that a simple pulse dampener and higher anolyte flow rate reduced both the per-cycle capacity decay (from 7.2% to 0.44%) and self-discharge rate (by 87.3%) while increasing its EE (from 57.3% to 62.3%). While pulse dampening and a static asymmetrical electrolyte flow rate improve the performance on lab-scale, further studies are required to accurately quantify the pressure changes associated with the SOC. An in-depth investigation into the dynamic range of asymmetrical electrolyte viscosity could be used to develop a cost-effective and simple employment strategy to use adaptive pump rpms, set up to marginally adjust according to the system's SOC estimation, at large-scale to mitigate capacity losses from convection. For large-scale employment of ICFB technology, the potential CAPEX cost reduction of 38.6% by using commercially manufactured MPSs and prolonged chemical stability should be considered against the reduced EE and discharge capacity challenges brought on by convection. With the currently available MPSs being unoptimised for the ICFB, the performance degradation is still too high for prolonged cycling, as small amounts of convection would accumulate and cause electrolyte imbalance.

Considering the low cost of electrolyte, lower capacities from imbalance could be combated by using larger amounts of electrolyte and more frequent maintenance. A substantial reduction in cost could enable market penetration while further development continues. Alternatively, an imbalance in electrolyte volume in large-scale systems can be rectified via cost-effective hydraulic shunts rather than periodic maintenance. Optimisation of MPS properties specifically for the ICFB has the potential to solve these challenges and should mainly focus on thickness while considering operational pressure controls for asymmetric electrolyte flow rates to minimise crossover and maximise the trade-offs between separation effectiveness, ASR and CE. From our findings, an optimal thickness for a feasible MPS will be found between 200 µm and 800 µm, for extruded separators with porosity comparable to those tested in this work, with the lower half of this range in favour of a high VE and the upper half CE. In addition to the demonstrated feasibility of MPSs in an ICFB, cost-effective CEM-type coatings and phase-inversion membranes can be used to further reduce electrolyte convection.

References

[1] A.Z. Weber, M.M. Mench, J.P. Meyers, P.N. Ross, J.T. Gostick, Q. Liu, Redox flow batteries: a review, Journal of Applied Electrochemistry, 41 (2011) 1137-1164. 10.1007/s10800-011-0348-2.

[2] EPRI-DOE Handbook of Energy Storage for Transmission & Distribution Applications, EPRI, Palo Alto, CA, and the U.S. Department of Energy, Washington, DC: 2003. 1001834.

[3] Z. Huang, A. Mu, Research and analysis of performance improvement of vanadium redox flow battery in microgrid: A technology review, International Journal of Energy Research, 45 (2021) 14170–14193. 10.1002/er.6716.

[4] Y.K. Zeng, X.L. Zhou, L. An, L. Wei, T.S. Zhao, A high-performance flow-field structured iron-chromium redox flow battery, Journal of Power Sources, 324 (2016) 738-744. https://doi.org/10.1016/j.jpowsour.2016.05.138.

[5] Z. Yang, Y. Wei, Y. Zeng, Y. Yuan, Effects of in-situ bismuth catalyst electrodeposition on performance of vanadium redox flow batteries, Journal of Power Sources, 506 (2021) 230238. https://doi.org/10.1016/j.jpowsour.2021.230238.

[6] L. Gubler, Membranes and separators for redox flow batteries, Current Opinion in Electrochemistry, 18 (2019) 31-36. https://doi.org/10.1016/j.coelec.2019.08.007.

[7] Y.S. Kim, S.H. Oh, E. Kim, D. Kim, S. Kim, C.H. Chu, K. Park, Iron-chrome crossover through nafion membrane in iron-chrome redox flow battery, Korean Chemical Engineering Research, 56 (2018) 24-28. 10.9713/kcer.2018.56.1.24.

[8] C. Sun, H. Zhang, Review of the Development of First-Generation Redox Flow Batteries: Iron-Chromium System, ChemSusChem, 15 (2021) 15. 10.1002/cssc.202101798.

[9] S. Ahmad, T. Nawaz, A. Ali, M.F. Orhan, A. Samreen, A.M. Kannan, An overview of proton exchange membranes for fuel cells: Materials and manufacturing, International Journal of Hydrogen Energy, 47 (2022) 19086-19131. https://doi.org/10.1016/j.ijhydene.2022.04.099.

[10] Y.K. Zeng, T.S. Zhao, L. An, X.L. Zhou, L. Wei, A comparative study of all-vanadium and iron-chromium redox flow batteries for large-scale energy storage, Journal of Power Sources, 300 (2015) 438-443. https://doi.org/10.1016/j.jpowsour.2015.09.100.

[11] S. Ha, K.G. Gallagher, Estimating the system price of redox flow batteries for grid storage, Journal of Power Sources, 296 (2015) 122-132. https://doi.org/10.1016/j.jpowsour.2015.07.004.

[12] M. Amjadi, S. Rowshanzamir, S.J. Peighambardoust, M.G. Hosseini, M.H. Eikani, Investigation of physical properties and cell performance of Nafion/TiO2 nanocomposite membranes for high temperature PEM fuel cells, International Journal of Hydrogen Energy, 35 (2010) 9252-9260. https://doi.org/10.1016/j.ijhydene.2010.01.005.

[13] M. Eikerling, Y. Kornyshev, A.M. Kuznetsov, J. Ulstrup, S. Walbran, Mechanisms of Proton Conductance in Polymer Electrolyte Membranes, Journal of Physical Chemistry B, 105 (2001). 10.1021/jp003182s.

[14] N. Mans, D.J. van der Westhuizen, H.M. Krieg, Membrane Screening for Iron–Chrome Redox Flow Batteries, Advanced Energy and Sustainability Research, 5 (2024) 2300195. https://doi.org/10.1002/aesr.202300195.

[15] C. Sun, Z. Huan, X.-D. Luo, N. Chen, A comparative study of Nafion and sulfonated poly(ether ether ketone) membrane performance for iron-chromium redox flow battery, Ionics, 25 (2019). 10.1007/s11581-019-02971-0.

[16] Z. Yuan, X. Li, J. Hu, W. Xu, J. Cao, H. Zhang, Degradation mechanism of sulfonated poly(ether ether ketone) (SPEEK) ion exchange membranes under vanadium flow battery medium, Physical Chemistry Chemical Physics, 16 (2014) 19841-19847. 10.1039/C4CP03329A.

[17] E. Bülbül, V. Atanasov, M. Mehlhorn, M. Bürger, A. Chromik, T. Häring, J. Kerres, Highly phosphonated polypentafluorostyrene blended with polybenzimidazole: Application in vanadium redox flow battery, Journal of Membrane Science, 570-571 (2019) 194-203. https://doi.org/10.1016/j.memsci.2018.10.027.

[18] X. Wei, L. Li, Q. Luo, Z. Nie, W. Wang, B. Li, G.-G. Xia, E. Miller, J. Chambers, Z. Yang, Microporous separators for Fe/V redox flow batteries, Journal of Power Sources, 218 (2012) 39-45. https://doi.org/10.1016/j.jpowsour.2012.06.073.

[19] X. Wei, B. Li, W. Wang, Porous polymeric composite separators for redox flow batteries, Polymer Reviews, 55 (2015) 247-272. 10.1080/15583724.2015.1011276.

[20] Y. Guo, J. Huang, J.-K. Feng, Research progress in preparation of electrolyte for all-vanadium redox flow battery, Journal of Industrial and Engineering Chemistry, 118 (2023) 33-43. https://doi.org/10.1016/j.jiec.2022.11.037.

[21] T. Puleston, A. Clemente, R. Costa-Castelló, M. Serra, Modelling and Estimation of Vanadium Redox Flow Batteries: A Review, Journal, 8 (2022). 10.3390/batteries8090121.

[22] D.A. Skoog, D.M. West, F.J. Holler, S.R. Crouch, Fundamentals of analytical chemistry, Ninth edition. ed., Brooks/Cole, Cengage Learning, Belmont, CA, 2014.
[23] W. Lu, Z. Yuan, Y. Zhao, H. Zhang, H. Zhang, X. Li, Porous membranes in secondary battery technologies, Chemical Society Reviews, 46 (2017) 2199-2236. 10.1039/C6CS00823B.
[24] G. Venugopal, J. Moore, J. Howard, S. Pendalwar, Characterization of microporous separators for lithium-ion batteries, Journal of Power Sources, 77 (1999) 34-41. https://doi.org/10.1016/S0378-7753(98)00168-2.
[25] Y. Lee, J. Park, H. Jeon, D. Yeon, B.-H. Kim, K.Y. Cho, M.-H. Ryou, Y.M. Lee, In-depth correlation of separator pore structure and electrochemical performance in lithium-ion batteries, Journal of Power Sources, 325 (2016) 732-738. https://doi.org/10.1016/j.jpowsour.2016.06.094.
[26] N. Lingappan, W. Lee, S. Passerini, M. Pecht, A comprehensive review of separator membranes in lithium-ion batteries, Renewable and Sustainable Energy Reviews, 187 (2023) 113726. https://doi.org/10.1016/j.rser.2023.113726.
[27] C.H.L. Tempelman, J.F. Jacobs, R.M. Balzer, V. Degirmenci, Membranes for all vanadium redox flow batteries, Journal of Energy Storage, 32 (2020) 101754. https://doi.org/10.1016/j.est.2020.101754.
[28] J. Charvát, P. Mazúr, J. Dundálek, J. Pocedič, J. Vrána, J. Mrlík, J. Kosek, S. Dinter, Performance enhancement of vanadium redox flow battery by optimized electrode compression and operational conditions, Journal of Energy Storage, 30 (2020) 101468. https://doi.org/10.1016/j.est.2020.101468.
[29] A. Kaur, K. Il Jeong, S. Su Kim, J. Woo Lim, Optimization of thermal treatment of carbon felt electrode based on the mechanical properties for high-efficiency vanadium redox flow batteries, Composite Structures, 290 (2022) 115546. https://doi.org/10.1016/j.compstruct.2022.115546.
[30] H. Zhang, Y. Tan, J. Li, B. Xue, Studies on properties of rayon- and polyacrylonitrile-based graphite felt electrodes affecting Fe/Cr redox flow battery performance, Electrochimica Acta, 248 (2017) 603-613. https://doi.org/10.1016/j.electacta.2017.08.016.
[31] K. Schafner, M. Becker, T. Turek, Membrane resistance of different separator materials in a vanadium redox flow battery, Journal of Membrane Science, 586 (2019) 106-114. https://doi.org/10.1016/j.memsci.2019.05.054.
[32] N. Mans, H.M. Krieg, D.J. van der Westhuizen, The Effect of Electrolyte Composition on the Performance of a Single-Cell Iron–Chromium Flow Battery, Advanced Energy and Sustainability Research, 5 (2024) 2300238. https://doi.org/10.1002/aesr.202300238.
[33] H.-Y. Jung, G.-O. Moon, T. Sadhasivam, C.-S. Jin, W.-S. Park, H.-T. Kim, S.-H. Roh, Ionic transportation and chemical stability of high-endurance porous polyethylene separator for vanadium redox flow batteries, Solid State Ionics, 327 (2018) 110-116. https://doi.org/10.1016/j.ssi.2018.10.019.
[34] B. Satola, Review—Bipolar Plates for the Vanadium Redox Flow Battery, Journal of The Electrochemical Society, 168 (2021) 060503. 10.1149/1945-7111/ac0177.
[35] E. Bai, H. Zhu, C. Sun, G. Liu, X. Xie, C. Xu, S. Wu, A Comparative Study of Nafion 212 and Sulfonated Poly(Ether Ether Ketone) Membranes with Different Degrees of Sulfonation on the Performance of Iron-Chromium Redox Flow Battery, Journal, 13 (2023). 10.3390/membranes13100820.
[36] D.A. Johnson, M.A. Reid, Chemical and Electrochemical Behavior of the Cr(III)/Cr(II) Half-Cell in the Iron-Chromium Redox Energy Storage System, Journal of The Electrochemical Society, 132 (1985) 1058-1062. 10.1149/1.2114015.
[37] X.L. Zhou, T.S. Zhao, L. An, Y.K. Zeng, X.B. Zhu, Performance of a vanadium redox flow battery with a VANADion membrane, Applied Energy, 180 (2016) 353-359. https://doi.org/10.1016/j.apenergy.2016.08.001.
[38] T. Sukkar, M. Skyllas-Kazacos, Water transfer behaviour across cation exchange membranes in the vanadium redox battery, Journal of Membrane Science, 222 (2003) 235-247. https://doi.org/10.1016/S0376-7388(03)00309-0.
[39] K. Oh, M. Moazzam, G. Gwak, H. Ju, Water crossover phenomena in all-vanadium redox flow batteries, Electrochimica Acta, 297 (2019) 101-111. https://doi.org/10.1016/j.electacta.2018.11.151.
[40] A. Bhattarai, P.C. Ghimire, A. Whitehead, R. Schweiss, G.G. Scherer, N. Wai, H.H. Hng, Novel Approaches for Solving the Capacity Fade Problem during Operation of a Vanadium Redox Flow Battery, Batteries, 4 (2018). 10.3390/batteries4040048.
[41] L. Liu, T. Liu, F. Ding, H. Zhang, J. Zheng, Y. Li, Exploration of the Polarization Curve for Proton-Exchange Membrane Fuel Cells, ACS Applied Materials & Interfaces, 13 (2021) 58838-58847. 10.1021/acsami.1c20289.

[42] M. Mulder, Basic Principles of Membrane Technology, 2nd ed., Kluwer Academic Publishers, Centre for Membrane Science and Technology, University of Twente, Enschede, The Netherlands, 1997.
[43] A. Trovò, F. Picano, M. Guarnieri, Comparison of energy losses in a 9 kW vanadium redox flow battery, Journal of Power Sources, 440 (2019) 227144. https://doi.org/10.1016/j.jpowsour.2019.227144.
[44] W.E. Waghorne, Viscosities of Electrolyte Solutions, Philosophical Transactions: Mathematical, Physical and Engineering Sciences, 359 (2001) 1529-1543.
[45] O.C. Esan, X. Shi, Z. Pan, X. Huo, L. An, T.S. Zhao, Modeling and Simulation of Flow Batteries, Advanced Energy Materials, 10 (2020) 2000758. https://doi.org/10.1002/aenm.202000758.

CHAPTER 4: Anion-exchange membranes for the iron-chromium redox flow battery

Chapter table of contents

4.1 Introduction

Owing to their high proton conductivity and chemical stability, cation exchange membranes (CEMs), predominantly from perfluorosulfonic acid (PFSA), are the most commonly used ion-exchange membranes in electrochemical energy storage technologies.[1-3] However, low ionic selectivity leads to operational challenges for aqueous flow batteries (FBs) due to the migration of active metallic cations and electro-osmotic crossover of water and supporting electrolyte.[1, 4, 5] Anion exchange membranes (AEMs) generally have higher ionic selectivity towards anions such as sulfates (SO_4^-), hydroxides (OH^-), bicarbonates (HCO_3^-) and chlorides (Cl^-) through the functionalised cations attached to the membrane polymer, making them suitable for various applications including flow batteries, alkaline fuel cells and electrolysers.[6, 7]

While AEMs have seen ample recent developments in vanadium flow batteries (VFBs), showing increased coulombic efficiencies CEs and capacity retentions through vanadium cation repulsion, the chemical stability and low anion conductivity are well-known challenges of AEMs in FBs.[1, 8-12] In addition, AEMs can also facilitate proton migration in acid-based FBs (influenced by swelling and molecular pore sizes), which further complicates the ionic conduction mechanisms.[6, 8] Still, novel anion exchange polymers are consistently being advanced, showing significant ionic selectivity increases in the VFB.[4, 8, 12-14] One example of such a polymer is quaternary ammonium functionalised poly(fluorenyl ether) (QA-PFE), which has shown a CE of 100% with short-term (15 cycles) VFB tests.[8] Since quaternary ammonium groups can be oxidised by the vanadium pentoxide in VFB electrolyte, functional groups such as quaternary benzyl trimethylammonium were investigated in a polysulfone-based AEM, resulting in a 96% CE with less than 4% loss of functional groups after 90-day electrolyte exposure testing.[15, 16] Other nitrogen-based cationic anion exchange functional groups that have been investigated include imidazolium, pyrrolidinium, pyridinium and piperidinium.[6, 17] To reduce the cost and use of the perfluorinated polymers in VFBs, alternative materials, for example aromatic hydrocarbon-based polymers including polybenzimidazole, polysulfone, poly(arylene ether ketone) and poly(phenylene oxide), have also been modified with anion-exchange functional groups.[6, 18] Since the iron-chromium flow battery (ICFB), which also suffers from a low ionic-selectivity, has a similar operation and aqueous chemistry as the VFB, the ICFB could benefit from the novel AEM materials developed for the VFB.

The wide development (apart from VFBs) of novel polymers and their synthesis methods over the last decade has resulted in further improvements of anion-exchange polymers, providing a wider variety of anion-exchange polymers and membrane types with increased stability, conductivity and performances in alkaline fuel cells and electrolysers.[19-23] For example, recently ionically cross-linked blend membranes from OPBI and polystyrene, with quaternary N-methyl piperidinium anion-exchange groups attached to hexyl side chains, displayed reduced swelling through the interactions of the deprotonated benzimidazole N^- and the piperidinium cation.[19]

These blend membranes showed excellent alkaline stability (after 1000 hrs of immersion in 1 M KOH at 85 °C, no conductivity decrease could be observed) with performances comparable to that of a commercial Aemion® membrane in an alkaline electrolyser. Anion-exchange polymers synthesised by polyhydroxyalkylation of biphenyl or terphenyl with 7-bromo-1,1,1-trifluoroheptan-2-one, which were quaternised after polymerisation with tetramethylimidazole, showed excellent chemical stability and performance in a seawater electrolyser free of platinum-group metal (PGM) catalysts.[20] Another recent novel material, polynorbornene, has been developed from 54 mol% (1R,4R)-5-((2-(2-bromoethoxy)ethoxy)methyl)bicyclo [2.2.1]hept-2-ene (abbreviated as EM) and 46 mol% (9R,10S,12S,13S,17R)-9,10-dihydro-9,10-[2]bicycloanthracene (abbreviated as AM) polymerised by ring-opening metathesis polymerisation (ROMP). This copolymer, which was hydrogenated, quaternised with trimethylamine and blended with polyisatine (synthesised via polyhydroxyalkylation), showed promising alkaline stability through controllable water uptake properties, able to deliver current densities of 2.0 A cm^{-2} without platinum group metal catalysts in an AEM water electrolyser.[21]

Compared to the more developed VFBs, fuel cells and electrolysers, there is currently no recent literature on the successful application or development of AEMs in the ICFB. Similarly the testing of commercially available, or novel AEM materials remains scarce, possibly also due to the observed inability to discharge when using an AEM in an ICFB.[3, 24] When charging the HCl-containing ICFB electrolyte, the increasing Fe^{3+} concentration results in the formation of anionic complexes (like $FeCl_4^-$) that seem to irreversibly congest ion-exchange channels, resulting in a rapid increase in area specific resistances (ASR) inhibiting electrolyte discharge.[3, 25] The only reports on the successful use of AEM materials (charging and discharging) in an ICFB, have resulted from the developments by Ionics Inc., which did extensive materials selection and optimisation work for the Lewis research centre of NASA over 40 years ago.[26, 27] By aminating a vinylbenzyl chloride with diethylenetriamine and dimethylaminoethyl methacrylate, a highly porous (lowering resistances) AEM was obtained. However, the AEM resulted in excessive operational electro-osmosis, curtailing long-term suitability.[28] While the mechanism of AEM fouling seems to exclude AEMs for the ICFB, the wide variety of novel AEM materials developed for ion-exchange in other applications warrants a further investigation into their possible suitability for an ICFB. Testing the effects of different AEM chemistries and material combinations in the ICFB could not only deliver more selective and cost-effective membranes than PFSAs, but also elucidate the high ASR observed during ICFB discharge.

4.2 Experimental

4.2.1 Membrane synthesis

All polymers and anion exchange membranes used in this study (see **Table 4.1** and **Table 4.2**), including pristine, blended and ionically cross-linked membranes, were synthesised and manufactured based on previous studies.[29-31] Membranes were provided by the groups of J. Kerres (HI-ERN, Germany) and V. Atanasov (University of Stuttgart, Germany).

Table 4.1: An overview of the names and molecular structures of polymers/ionomers present in the ion exchange membranes tested.

Name/description	Structure
TMImQPS Tetramethylimidazolium-quaternised polystyrene	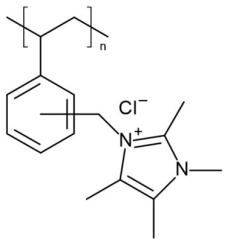
F_6PBI Poly[2-(4-(1,1,1,3,3,3-hexafluoro-2-phenylpropan-2-yl)phenyl)-3H,3′H-5,5′-bibenzo[*d*]imidazole]	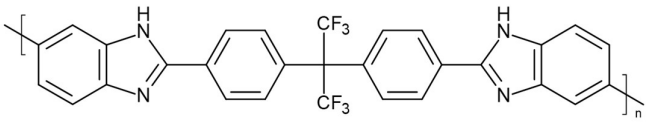
***m*PBI** Poly[2,2-(m-phenylene)-5,5-bibenzimidazole]	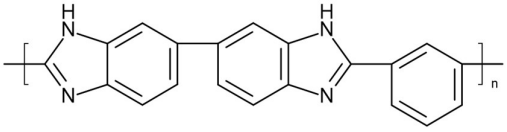
OPBI Poly(4,40-diphenylether-5,50-bibenzimidazole)	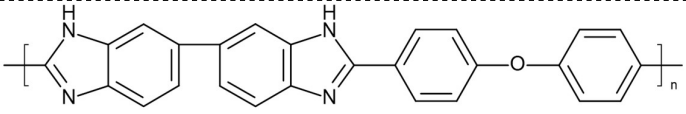
PWN (70) Phosphonated poly(pentafluorostyrene)	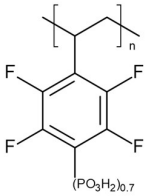
SPEEK Sulfonated poly(ether ether ketone)	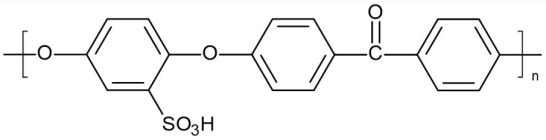

Table 4.2: Composition (wt.%) of membranes tested.

Membrane	Blend component 1	Blend component 2
HT-3	F_6PBI (70%)	TMImQPS (30%)
MIG-11	*m*PBI (98%)	PWN70 (2%)[cl]
MIG-15	*m*PBI (97%)	PWN70 (3%)[cl]
OPBI-P	OPBI (98%)	PWN72 (2%)[cl]
OPBI-S	OPBI (98%)	SPEEK (2%)[cl]
OPBI	OPBI (100%)	--

[cl] Cross-linker

4.2.2 Membrane characterisation

All membranes used in this study were washed once in 2.0 M H_2SO_4 (MINEMA Chemicals, 98%) and twice in deionised (DI) water (> 200 mL) at 65 °C for 24 h to remove any residual solvents (e.g., DMSO), while also protonating ion exchange sites and ensuring sufficient ionic cross-linking that can result in dimensional changes. Membranes were then cut into a 13.5 cm x 6.5 cm piece (87.75 cm^2) for the ICFB tests and a ~4 cm^2 sample for further characterisation. Before the ICFB membrane pieces were subjected to cycling tests (see Section 4.2.2.6), they were first preconditioned in 200 mL of the ICFB electrolyte (1.3 M Fe & Cr in 1.0 M HCl) at 65 °C for 24 h. The preconditioning i) served as a chemical stability screening as heated electrolyte would deteriorate any chemically incompatible membranes, while ii) conditioning the samples to ensure testing in an improved equilibrated chemical state compared to the freshly washed membranes filled with DI water. After the ICFB tests, the membranes were rinsed multiple times in dilute HCl (0.25 M) (Labchem, 32%), to inhibit any precipitation of absorbed Fe^{3+}, followed by rinsing with DI water. Finally, ~4 cm^2 samples were cut from the active area (pressed against the felt electrodes), for characterisations after cycling. During the abovementioned steps, membranes were photographed to log visual changes from electrolyte exposure and cycling.

4.2.2.1 Weight and thickness

To track any physical changes due to degradation from ICFB electrolyte interaction, the wet weight and average thickness (Mitutoyo 293-340-30 Digital Micrometer) of the 87 75 cm^2 ICFB membrane pieces were measured in triplicate for each membrane (before and after preconditioning and after ICFB operation). For each measurement, the average was taken for 4 points inside the active area of electrode contact. After adequate rinsing as previously mentioned, membranes were pressed carefully between paper towels to remove excess external water before being weighed.

4.2.2.2 Ion exchange capacity (IEC)

Proton IECs are usually measured for CEMs while the opposite, the hydroxide (OH^-) exchange capacity, is measured to quantify the available sites of anion exchange for AEMs. However, the PBI-based membranes evaluated in this study are all in protonated form when inside the acidic electrolyte of the ICFB. These protonated sites,

imidazolium groups, are responsible for water uptake and charge balancing Cl^- migration. Additionally, loss of these functional groups from before and after ICFB tests can be correlated to AEM degradation or permanent fouling. As a result, the traditional H^+ IEC procedure of CEMs was adopted to also measure degradation of AEMs.

To ensure identical preconditioning before analysis, the membrane samples (~4 cm^2) before and after cycling were washed by submerging them in 30 mL of 0.25 M HCl for 1h at 65 °C before rinsing them twice in DI water (0.055 µS cm^{-1}). Subsequently, the samples were dried at 65 °C for at least 4 h, before being transported to scales in closed hot containers (supress humidity absorption) and weighed (dry weight). Samples were then submerged in 40 mL of 2.0 M H_2SO_4 at 65 °C for 24 h (protonate acidic groups). To remove any residual acid trapped in the membranes that could affect titration values, the samples were then i) rinsed (lightly shaking) twice with DI water, ii) heated in DI water for 10 hours at 65 °C and iii) rinsed again.

To determine the IEC values, the ionically bonded protons were removed by submerging the samples in 40 ml of a 2.0 M NaCl (purity >99.0%, from Sigma-Aldrich (Merck)) solution for 24 h at 20–25 °C. The free acid was obtained by titrating (SI Analytics Titroline® 7000) with a 0.0100 M standardised (with ICP-OES) NaOH solution from Supelco®. Subsequently, the IEC of the membrane samples (before and after cycling) was determined using Equation 2.7 (see Literature review – Section 2.5.3).[32] Using four different N-212 samples (2 cm x 2 cm), the IEC method was validated, yielding an error margin (standard deviation from the average) of 1.5% (**Table 4.3**).

Table 4.3: IEC and water uptake (WU) method validation using N-212.

Membrane	IEC (mmol g^{-1})	WU (%)
N-212 A	0.980	16.98
N-212 B	0.946	15.70
N-212 C	0.959	16.85
N-212 D	0.979	17.45
Average	**0.966 ± 0.016**	**16.75 ± 0.65**

4.2.2.3 Water uptake

Water uptake (WU) values were used as an indication of dimensional swelling and to assess changes in hydrophilicity that both correlated to changes in battery performance, for example changes in overpotentials linked to ionic conductivity. The samples from before and after cycling (~4 cm^2) were protonated, rinsed and dried (as described previously) before being weighed. The wet and dry weights (m_w and m_d) were used to calculate the WU of the membranes in their protonated forms without titration according to Equation 4.1.[32, 33] According to Table 4.3, a 3.9% error margin was obtained for the WU method when using N-212.

$$WU\% = 100 \times \frac{m_w}{m_d} - 100 \quad (4.1)$$

4.2.2.4 Tensile strength

Membrane samples of before and after cycling were cut into dogbone-shaped pieces (~2 cm length & ~7 mm cross-section width), to ensure accurate and repeatable breaking at the narrow middle of the samples. After obtaining the thickness and width of the sample (Mitutoyo 293-340-30 Digital Micrometer), a manual force-measuring test stand (KERN TVL 500FHS71), equipped with a Sauter LB 500-2 digital calliper gauge, was carefully operated to stretch and break pieces in a controlled way. The maximum applied force before breakage was measured using the Sauter FH 500 digital force gauge installed onto the stand. The slightly higher standard deviation of 6% for tensile strength, which was determined during method validation using 5 arbitrary membrane samples of OPBI-P varying 3 µm in thickness (see **Table 4.4**), can be ascribed to the manual nature of measurements and variations in the matrix and thickness inhomogeneity from the blending and casting of the membranes. OPBI-P was chosen as it has a higher tensile strength and more thickness variation, from less precise casting, than the commercial reference N-212.

Table 4.4: Tensile strength method validation values using five OPBI-P membrane samples.

Thickness (µm)	Sample width (mm)	Elongation (mm)	Maximum force (N)	Tensile strength (MPa)
38	6.60	5.65	26.7	106
40	6.91	3.75	27.7	100
40	8.55	3.89	34.2	100
37	6.91	3.78	28.9	113
37	6.55	4.21	29.2	111
Average			**29.3 ± 2.9**	**106 ± 6**

4.2.2.5 SEM & EDX

For SEM imaging & EDX analysis, samples of roughly 1 cm x 1 cm were cut and washed in 0.25 M HCl, followed by protonation in 2.0 M H_2SO_4 (24 h at 65 °C) and multiple washes with DI water at 65 °C to remove any free acid. Samples were then dried and coated using an Emscope TB 500 Carbon evaporator (carbon) and an Eiko IB-2 (gold and palladium sputtering). Any surface morphology changes (e.g., pinhole formations) due to ICFB cycling where then investigated using an FEI Quanta 250 FEG SEM.

4.2.2.6 ICFB

All equipment, chemicals and materials (e.g., in-house manufactured flow-through single-cell FB, electrolyte and carbon felt electrodes) used in the test station, as well as calculations and repeatability of performance parameters, were used as discussed in Sections 3.2.2.1–3.2.2.4.[34, 35] It has been shown that extended short-term cycling (30 cycles) with CEMs are required for representative performance parameters when using 100 mL electrolyte, due to capacity gain from chromium crossover in the first 7 cycles.[34] For benchmarking the battery performance of the AEMs, N-212 was cycled for 30 cycles (excluding the first cycle required for discharge polarisation tests) using 100 mL of electrolyte (1.3 M $Fe(II)Cl_2 \cdot 4H_2O$ and $Cr(III)Cl_3 \cdot 6H_2O$, in 1.0 M HCl) in total (50 mL catholyte + 50 mL anolyte). Depending on the membrane evaluated, the total battery testing time per membrane, including the self-discharge tests, ranged from 3 to 7 days.

The self-discharge rate (mV h^{-1}) was used to determine membrane selectivity since it is directly proportional to the passive crossover rate of charged metallic-ion species.[36, 37] The self-discharge rate was measured at a midpoint of 50% SOC (**Figure 4.1**) where the electrolyte concentrations were balanced, since voltage losses over time in this region are the most linear. This region gave more representative measurements for each membrane, as opposed to lower or higher SOC values where the open circuit voltage (OCV) readings are non-linear due to i) the change in charge transfer kinetics, ii) the logarithmic aspect of the Nernst equation and iii) deviations in OCV readings of flow batteries vs the Nernst equation.[38]

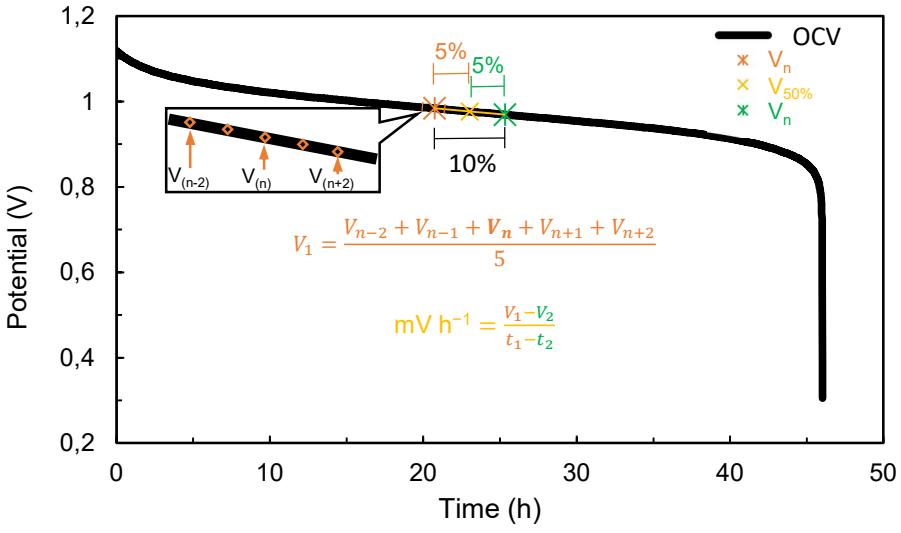

Figure 4.1: Illustration of self-discharge rate calculation using linear OCV region and 5-point averages.

The tested membranes yielded a wide range of self-discharge rates, where the high rates of some resulted in total capacity losses within 2 hours, convoluting accurate

calculations for impartial comparison. Subsequently, a data range of 5% in both directions ($V_{(n-2)} - V_{(n+2)}$) of the midpoint ($V_{(n)}$), obtained by extracting the middle of all logged data points, (10% total) was used, with 5-point averages calculated for each voltage and time value at 30-second intervals. Using this method and the equations developed (see Figure 4.1), more accurate and representable values for all membranes were obtained despite the total self-discharge times varying significantly (2–417 hours).

The electrolyte imbalance, which results from various and complex crossover mechanisms, including proton-trailing, electro-osmosis and diffusion, was hard to measure due to dynamic (fluctuating) electrolyte concentrations and cell potentials, as well as the directional changes of charge carrier migration.[34, 39, 40]. The supporting electrolyte crossover, which poses challenges in upscaled real-world applications [5, 28, 41], was quantified for each membrane by determining the anolyte and catholyte volumes ex-situ (electrolyte pumped from ICFB setup and measured using a volumetric cylinder) after cycling and the self-discharge test. After deducting the volume retained by the system, (e.g., felts, pipes, pumps, etc) the electrolyte imbalance (volume changes) was calculated, with an average deviation, for the catholyte and anolyte according to Equation (4.2).

$$Imbal. = \frac{\left|100 - 100 \times \frac{V_{f(+)}}{V_{i(+)}}\right| + \left|100 - 1 \times \frac{V_{f(-)}}{V_{i(-)}}\right|}{2} \pm 3\% \qquad (4.2)$$

where (V_i) and (V_f) are the initial and final electrolyte volumes (mL), respectively, for both catholyte (+) and anolyte (−). An error margin of 3% was extrapolated to account both for the ≤ 1 mL variation in electrolyte volumes after cycling and the general accuracy of measurements.

4.3 Results and Discussion

In this section, the physico-chemical properties, stabilities and ICFB performance of the AEMs that were used in this study are discussed. In the light of the importance of the membrane's feasibility for large-scale applications, osmotic transfer rates were considered equally important to efficiency parameters. The slopes from discharge polarisation curves (ASR) were used to measure membrane resistances [42-44], which were especially useful when testing membranes that do not discharge due to the fouling mentioned in Section 2.2.2. This allowed the measuring of possible changes in the overpotential required to facilitate ion migration during charge balancing as the electrons migrate between the catholyte to anolyte. The experimentally determined physical and chemical properties of the AEMs tested are presented in **Table 4.5**. While the only success for AEMs to date in an ICFB was reported by the Lewis Research Center of NASA [27], the only efficiencies that they

characterisation when adopting a mixed electrolyte configuration at an elevated temperature of 65 °C in 1983, was for a CEM (ML-21) that replaced their CDIL-AA5-LC AEM.[45] As a result, no cycling performance data currently exists for commercial or novel AEMs that could be used to benchmark the results obtained in this study. Accordingly, the cross-linked AEMs tested in this study were benchmarked against the commercial N-212 CEM. A detailed discussion of the results obtained when using F_6PBI (HT-3), *m*PBI (MIG-11, MIG-15) and OPBI (including OPBI-P and OPBI-S) are given in Sections 4.3.1, 4.3.2 and 4.3.3, respectively.

Table 4.5: Thickness, tensile strength and IEC (before and changes due to cycling), as well as WU of the AEMs tested.

Membrane	Thickness, 65 °C, wet (µm)	Δ Thickness (%)*	Tensile strength (MPa)	Δ Tensile strength (%)	H^+ IEC (mmol g^{-1}) ± 1.5%	Δ H^+ IEC (%)	WU (%) ± 3.3
N-212	58	3	23	−16	0.980	0	17.0
HT-3	39	7	110	−9	0.054	0	22.7
MIG-11	66	15	48	−8	0.394	25	36.0
MIG-15	46	14	47	3	0.407	28	35.5
OPBI-P	40	8	106	−10	0.097	13	28.5
OPBI-S	45	2	86	−1	0.098	12	27.8
OPBI	56	5	137	−5	0.105	0	28.6

*Wet thickness (65 °C)
Standard deviations are represented as % deviations were relevant

All 6 AEMs tested contained a PBI polymer (F_6PBI, *m*PBI or OPBI). The cation conduction capability of PBI membranes, which can attain proton conductivities of up to 0.217 S cm^{-1} at operating temperatures of 200 °C (typically as CEMs in HT-PEMFCs), stems from the doping with phosphoric acid (PA) to add biphosphates at the basic sites of the polymer.[2, 46, 47] Both biphosphates and absorbed PA are, however, easily washed out with hot water (during membrane preparation) or aqueous ICFB electrolyte, given the relatively weak interactions of these acids with the membrane's active sites. Furthermore, both strong (e.g., HCl) and weaker acids (e.g., methane sulfonic acid) protonate the imidazolium nitrogen atoms to create basic imidazolium anion exchange sites.[48, 49] Protons on these nitrogen groups do not dissociate as freely as when found on the acidic functional groups of CEMs, due to their significantly weaker pKa values.

In **Figure 4.2**, the titration and first derivative data (pH as function of volume NaOH) for OPBI are given. While the signal was relatively weak, the experimentally estimated pKa for OPBI ≈ 5 coincides with the literature for PBI ≈ 6 [50] and with the results of pKa calculations using ACD (Advanced Chemistry Development software) lying in the range of 4.1 – 5.3, showing the low potential for the Grotthuss mechanism via dissociation of H^+ compared to, for example, the −6 of N-212 [51]. Since these protonated groups generate a positively charged barrier when in an acidic medium

such as HCl, which repel cations and accept anionic counterions [49, 50], all the PBI-based membranes listed in Table 4.2 were classified as AEMs.

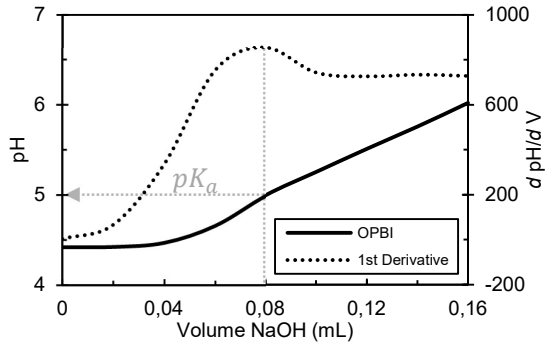

Figure 4.2: Titration curve for OPBI and the first derivative of pH over volume.

The N-212 CEM was used as a benchmark against AEMs. Accordingly, an overview of the battery performance data obtained for the six AEMs compared to N-212 is presented in **Table 4.6**, with membranes ordered in the chronological order of the development process. See Sections 4.3.1, 4.3.2 and 4.3.3. for a detailed discussion of the F_6PBI, *m*PBI and OPBI based membranes, respectively. The slope used for ASR determination during discharge polarisation was only calculated in the linear curve regions, since some membranes encountered mass transfer limitations, indicated by non-linearity, when discharging at current densities > 25 mA cm^{-2}.

Table 4.6: Summary of discharge capacity, capacity decay (per cycle (%) and normalised hourly (% h^{-1})), performance parameters, operational electrolyte imbalance and self-discharge values for the AEMs.

Membrane	Peak Dis Cap (Ah L^{-1})	Cap Decay (%, % h^{-1})	CE (%)	VE (%)	EE (%)	ASR (Ω cm^2)	Imbal. (%)	Self-Disch. (mV h^{-1})
N-212	11.8	*1.00/^{H}0.42	91.8	81.5	74.8	2.38	33	3.187
<u>F_6PBI (TMImQPS)</u>								
HT-3	0.47	--	--	--	--	9.93	0	0.515
<u>*m*PBI</u>								
MIG-11	12.28	*2.32/^{H}1.00	97.3	73.8	71.9	4.11	1	1.529
MIG-15	13.68	*2.80/^{H}1.09	96.7	78.6	76.1	3.45	4	2.907
<u>OPBI</u>								
OPBI-P	0.00	--	--	--	--	5.47$^{\#}$	1	0.589
OPBI-S	0.00	--	--	--	--	6.76$^{\#}$	1	0.398
OPBI	0.00	--	--	--	--	7.42$^{\#}$	0	0.236

$^{\#}$Initial ASR calculated at a current density ≤ 25 mA cm^{-2}

4.3.1 F_6PBI (HT-3)

Since AEMs with quaternised imidazolium groups have successfully been applied in FCs [52] and VFBs with a 2% higher EE than N-212 (at 40 mA cm^{-2}),[10] an AEM (HT-3) containing F_6PBI and a tetramethylimidazolium-quaternised polystyrene (TMImQPS) was prepared (70:30) to investigate the compatibility of this novel AEM material in an ICFB (discussed in Section 2.3.2.1.2). In addition, to determine the effect of the electrolyte counterion on the performance of HT-3, the influence of both an HCl (HT-3) and an HCl:H_2SO_4 (0.5 M:1.5 M) mixed electrolyte (HT-3 (sulfates)) was evaluated. Initial attempts at charging and discharging in the HCl electrolyte using this AEM failed, as the cut-off potentials at 1.25 V and 0.75 V, respectively, were reached as soon as a current was applied. When increasing the cut-off potential range to 1.45 V and 0.55 V, a higher overpotential allowed electrolytes to charge for 73 minutes outside of the normal operating range (see **Figure 4.3** (a) HT-3 Charge). However, a rapid decrease in the ionic conductivity while discharging resulted in a discharge time of only 2.5 minutes before reaching the lower cut-off. This suggested that the migration of anions (and/or protons) via anion-exchange moieties and absorbed electrolyte in the membrane only occurred when using an overpotential, despite being 33% thinner than N-212 and having a 4% higher WU value (see Table 4.5). While a significantly decreased current density could be applied to reduce the high membrane resistance, it would lead to unpractically long cycling times and a low power output.

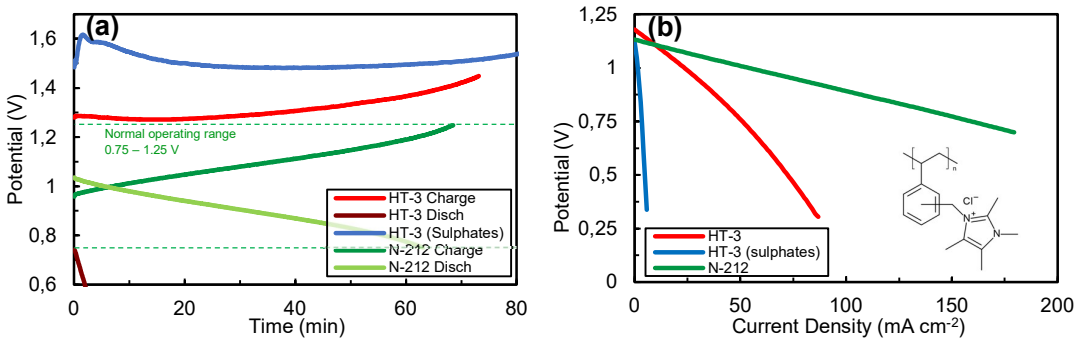

Figure 4.3: (a) Charge/discharge curves and (b) discharge polarisation curves of the HT-3 AEM with different electrolyte acids (HT-3 = HCl & HT-3 (sulfates) = HCl:H_2SO_4 (0.5 M:1.5 M)) and benchmark N-212.

Since it was possible to charge the electrolyte, the ionic selectivity that AEMs usually exhibit could be verified with both discharge polarisation and self-discharge tests. The cation repulsion of this AEM resulted in a self-discharge rate of 0.515 mV h^{-1} (see Table 4.6), which was 6 times lower than the benchmark CEM (N-212). The steep voltage drop and non-linear curve (~9.9 Ω CM^2) of HT-3 in Figure 4.3 (b) shows a high and increasing discharge resistance as the current is increased, suggesting mass transfer limitations.

Considering i) the high resistance observed when using chlorides in the ICFB and ii) the confirmed sulfate-facilitated ion transport of AEMs in VFBs[8, 53], the 1.0 M HCl

electrolyte was substituted with an electrolyte containing 0.5 M HCl and 1.5 M H_2SO_4 to investigate the possible effect of sulfates on the discharge resistance of this AEM. According to the charge/discharge results (Figure 4.3 (a) — HT-3 (sulfates)), the addition of sulfuric acid, introducing free sulfates for anion migration while reducing the free chlorides, resulted in a further increase of the charge and discharge resistances. This coincides with a study showing an increasing capacity decay with increasing sulfuric acid concentrations in the electrolyte when using N-212 in an ICFB.[35] Removing the chlorides from the electrolyte could theoretically eliminate membrane fouling by removing ferric chloride complex formation, believed to clog anion exchange channels.[25, 54] However, ICFB electrolyte without chlorides show extremely sluggish charge transfer kinetics for both chrome and iron (see cyclic voltammograms in **Figure 4.4** (a) compared to (b)) that would result in poor performance, making an H_2SO_4-based ICFB electrolyte unfeasible. Quaternised imidazolium-based membranes, hence, seem incompatible for the ICFB with the current electrolyte composition.

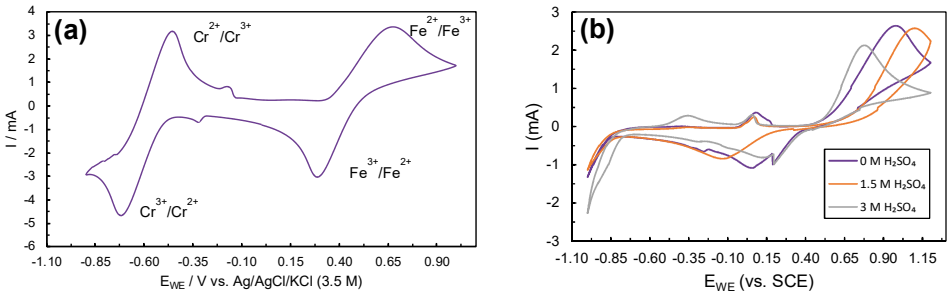

Figure 4.4: Cyclic voltammograms of a (a) conventional ICFB electrolyte containing 1.0 M $FeCl_2$, 1.0 M $CrCl_3$ and 3.0 M HCl and (b) sulfate-based electrolyte with 1.0 M $FeSO_4$, 1.0 M $Cr_2(SO_4)_3$ and 0.0–3.0 M H_2SO_4.

4.3.2 *m*PBI (MIG-11 & MIG-15)

The MIG-11 and MIG-15 membranes, containing *m*PBI and PWN70 (ratio of 98:2 and 97:3, respectively – see Table 4.2) were the only AEMs that achieved normal charge and discharge cycles for 30 cycles (see **Figure 4.5** and Appendix A – **Figure A10** (a–c)), albeit with relatively high ASRs (4.11 Ω cm² and 3.45 Ω cm², respectively − Table 4.6). According to Table 4.6, both AEMs exhibited a higher ionic selectivity than N-212, with self-discharge rates of 2.907 mV h^{-1} and 1.529 mV h^{-1} for MIG-11 and MIG-15 (vs 3.187 mV h^{-1} of N-212), respectively, which typically also increase the resistance (ASR).[55] However, the high ASR obtained by MIG-11 outweighed the benefits from selectivity gains, resulting in a 2.9% lower EE (71.9%) than N-212. The Donnan exclusion principle increases selectivity by introducing $Fe^{2+/3+}/Cr^{2+/3+}$ repulsion in MIG-11 and MIG-15 base-excess membranes, despite having pre-cycling WU values (36.0% and 35.5%, respectively) that are almost twice that of N-212 (17.0%).[56, 57] While the wetted MIG-15 membrane was 32% thinner than the MIG-11 membrane

(likely from casting), the 1% additional cross-linker in the MIG-15 membrane (compared to MIG-11) did not significantly affect the tensile strength, WU or IEC (Table 4.5). However, the reduced MIG-15 thickness resulted in the reduction in ASR and increase in VE to benefit the EE (76.1%). The higher CE of both MIG-11 (97.3%) and MIG-15 (96.7%) than N-212 (91.8%) over 30 cycles corresponds to the performance observed of PBI-based AEMs at the same current density in the VFB, where a slightly lower overall performance (EE = 65–73%) was reported.[11]

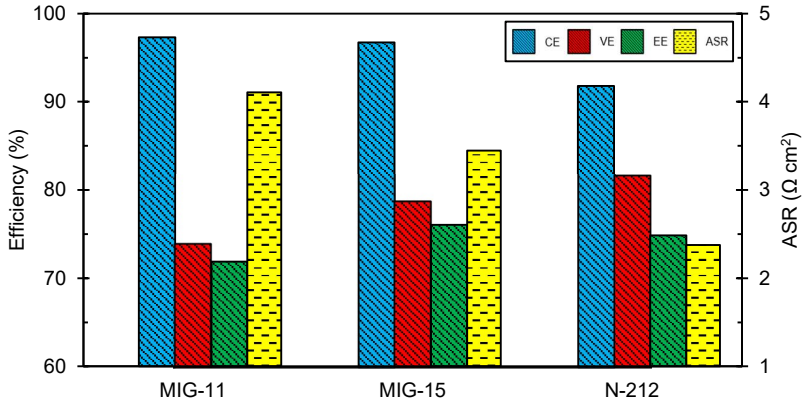

Figure 4.5: 30-Cycle average efficiencies and ASRs of *m*PBI based membranes (MIG-11 & MIG-15) and N-212.

The successful charging and discharging of these two AEMs, which are contrary to previous results reported on fouling of non-porous AEMs [3, 54], prompted further investigations. Seeing that anion permeation for charge balancing in an ICFB is a challenge due the high discharge resistance (from blockage of anion transfer channels), it is reasonable to assume the presence of cation migration. It is unlikely that these *m*PBI membranes had any cation exchange moieties, despite exhibiting a proton IEC value 8 times higher than that of F_6PBI in HT-3 (Table 4.5). These H^+ IEC values suggest protonation of nitrogen atoms for all PBI variants without sufficient CEM ionomers (base-excess blend membranes). Since the PWN CEM ionomer was present in such small quantities (2% and 3%) and ionically cross-linked to imidazole groups in the *m*PBI-based membranes, it would most likely not provide phosphonic acid channels, making the facilitation of cation migration highly unlikely. However, the type of polymer and/or the cross-linker could have other effects from ICFB electrolyte interaction. Interactions by the electrolyte were observable between new (cleaned) membranes vs right after cycling. There was abnormal gold coloration (see **Figure 4.6**), an increase in H^+ IEC and an increased thickness (14–15% increase in wet thickness comparing before and after cycling) compared to the other AEMs tested (see Δ Thickness − Table 4.3).

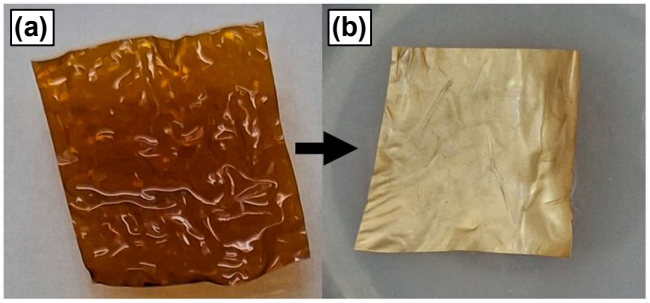

Figure 4.6: MIG-11 membranes (a) before and (b) after ICFB cycling.

To investigate the interaction of the electrolyte and the observed gold coloration, samples of MIG-11 from before and after cycling in the ICFB were washed in 0.25 M HCl to remove any remaining Fe and Cr (electrolyte), followed by protonation in 2 M H_2SO_4 before being repeatedly washed with DI water (24 hours at 65 °C) to remove any remaining acid. The acid removal did not affect the colour of the pristine sample while slightly intensifying the gold colour of the cycled sample, implying that the coloration is not reversible by free-acid cation exchange. The SEM and EDX imaging of both washed samples are shown in **Figure 4.7** ((a) – before and (b) – after cycling). While the surface morphology (SEM at 50 000x magnification) did not change during cycling, 0.89% Cr and 0.34% Fe was detected (EDX mapping) for the cycled sample. The presence of electrolytic metals, despite thorough washing, strongly suggests that the phosphonic acid on the PWN ionomer had formed irreversible complexes with the cationic Fe and Cr species.[58-60] While the additional hydrophilic complexes imbedded in the membrane could explain the previously mentioned increase in H^+ IEC after cycling, further investigation was required regarding the effects of ionic cross-linking (see Section 4.3.3). The EDX imaging showed a homogeneous distribution of P and F (from the PWN cross-linker), while also verifying the AEM nature of the protonated PBI membranes by the presence of Cl and S species (from the Cl^- and SO_4^{2-} counterions) after DI washing.

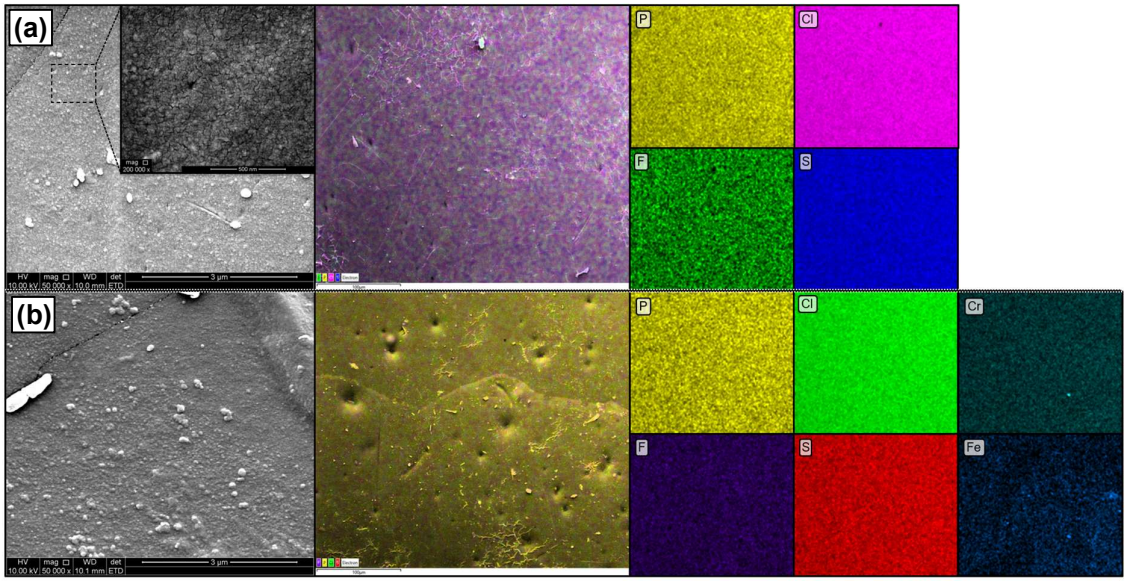

Figure 4.7: SEM imaging at 50 000x magnification and EDX mapping of MIG-11 membranes (a) before and (b) after cycling.

While small cracks and surface tears caused by the drying of swollen membranes can be difficult to distinguish from intrinsic porosity, the 200 000x magnification (Figure 4.7 (a)) of the surface could point to the formation of large molecular pores caused by the phase separation during the drying of the membrane casting solutions. However, porosity and pore size should be verified and quantified, for example using TEM imaging and staining of swollen samples, as understanding the exact mechanics of ion transport for these membranes in the ICFB could contribute to further optimisation.

It is important to understand why *m*PBI-based AEMs could cycle ICFB electrolyte, while the F_6PBI-based AEM (HT-3) could not discharge. As previously mentioned, electrolyte exposure increased the swelling of these membranes. However, the initial protonation and washing with DI water at 65 °C (see Section 2.2), could also have contributed to the final degree of swelling of *m*PBi vs F_6PBI, leading to a total increase in molecular pore sizes (due to polymer matrix expansion). The polymer backbone of *m*PBI, vs for example F_6PBIs, is polymerised on the meta position of the aromatic rings (see Table 4.1), which provides flexibility to the rigid polymer, resulting in a slightly more amorphous structure, which also increases its solubility in some polar solvents.[61] The free volume is further increased by the acidic protonation of the imidazolium nitrogen atoms that reduces the amount of hydrogen bonding between polymers, which has been reported by literature to enlarge water channels and produce a degree of porosity.[48, 62] All these factors contribute to the membranes' ability to swell in an acidic ICFB environment at an elevated temperature, which could enlarge molecular pores and hydrophilic channels, thereby preventing the possible blockages (that likely occurred with HT-3 that had 30% wt. TMImQPS) from deposits of larger anions such as $FeCl_4^-$.[6, 8, 25, 63]

While excessive swelling usually decreases the CE of CEMs by increasing supporting electrolyte and metal cation crossover, the anion exchange sites in the hydrophilic channels could theoretically still repel large metal cations via the Donnan exclusion effect as reported for the VFB.[8, 10, 11, 49] Although the expanded molecular pores and hydrophilic channels had a cation repulsive barrier, it is possible that they could have facilitated proton migration through the absorbed supporting electrolyte while still being small enough for effective rejection of larger metal cations as seen by their higher-than-benchmark CEs and lower self-discharge rates. While the use of fluorinated alkyls in FB membranes should be reduced/eliminated, investigating and comparing a pristine F_6PBI membrane in the ICFB would further elucidate the different behaviours of *m*PBI membranes vs HT-3.

Contrary to N-212, where a 33% electrolyte imbalance was observed after 30 cycles, no measurable electrolyte volume imbalance from electro-osmosis was observed after 30 cycles when using either of the MIG membranes, which would make such AEMs more feasible for large-scale and long duration applications.

4.3.3 OPBI (OPBI-P, OPBI-S & OPBI)

The only PBI-containing AEM with successful cycling thus far was the *m*PBI-based membranes with low (2–3%) cross-linker content. To investigate whether the type of acidic cross-linker had any significant effect on membrane resistance, three non-fluorinated OPBI membranes (Table 4.2), which differed in terms of the cross-linkers used (OPBI-P: PWN72 (2%), OPBI-S: SPEEK (2%) and OPBI: no cross-linker), were evaluated. A further objective was to test if the PWN72-containing OPBI (which has a more flexible backbone than PBI [64]), with a similar low amount of PWN cross-linker, would be able to discharge an ICFB.

While an initial charging of the electrolyte with the three membranes was possible (**Figure 4.8** (a)), a rapid increase in internal resistance when discharging was observed similar to the results obtained with the F_6PBI-containing AEM (Figure 4.3). Despite higher WU values (27.8–28.6%) of the three OPBI-containing membranes (Table 4.5) than HT-3 (22.7%) and N-212 (17.0%), with a higher degree of protonation than HT-3 (IEC = 0.097–0.105 mmol g^{-1}), electrolyte absorption was likely still too low, resulting in failure to discharge (within the normal voltage ranges), similarly to previous results on the use of AEMs in ICFBs.[3, 54] The discharge resistance of each was quantified by discharge polarisation curves, discharging with an increasing current density. According to Figure 4.8 (a, b) and Table 4.6, the pure OPBI displayed the highest charge resistance, with a theoretical charged capacity of only 7.70 Ah L^{-1}, when calculated with exclusion of the charge time extension effects from coulombic losses.

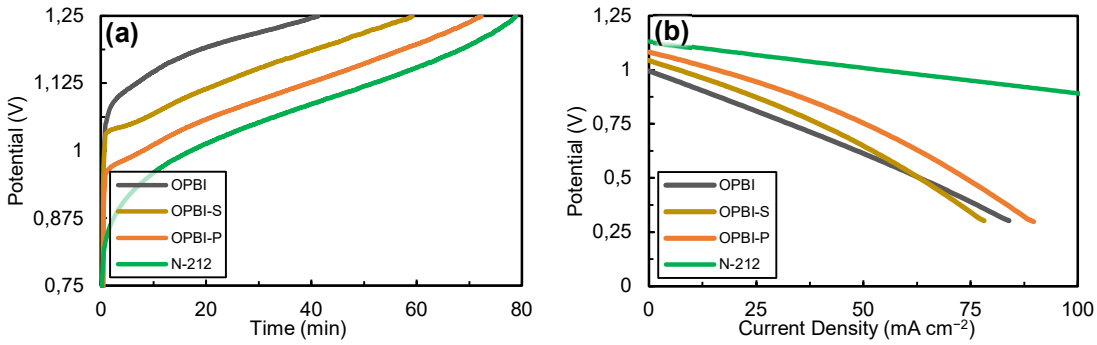

Figure 4.8: (a) First charge curves and (b) discharge polarisation curves of various OPBI membranes.

While all three OPBI membranes were casted with the same blade height to obtain similar thicknesses to N-212, the wet thicknesses were affected differently by different cross-linkers, as well as the change in thickness due to cycling (Table 4.5), where using the PWN cross-linker resulted in the thinnest membrane with the highest (8%) increase in thickness after cycling. While wet thicknesses varied, the significant reduction of overpotential in the charge curves of Figure 4.8 (a) shows that it is possible that the addition of a SPEEK and a PWN cross-linker could have decreased charge resistances. OPBI-P with the PWN cross-linker had the lowest resistance of the series and was able to achieve a charged capacity of 13.51 Ah L^{-1}, 8.2% lower when compared to the same first charge cycle of N-212 (14.72 Ah L^{-1}).

Only the OPBI membranes with cross-linkers showed an increase in protonation degree (Table 4.5) after cycling, similar to MIG membranes, but to a lower degree. These results suggest that electrolyte exposure and/or battery cycling breaks a certain number of ionic cross-links to expose additional imidazole, sulfonate and phosphonate groups to be protonated and titrated. Breakage and protonation of these groups would also explain the increased swelling (Δ thickness) observed for *m*PBI membranes. At a current density of 25 mA cm^{-1}, the internal resistance decreased in the order of OPBI>OPBI-S>OPBI-P, which held for both charging and discharging, where pure OPBI displayed a 241% higher ASR than N-212 during discharge polarisation tests. It is clear, however, from the discharge polarisation curves that the addition of cross-linkers affected the linearity of resistance. Different cross-linkers in small amounts (2%) did not significantly affect WU values. However, the same OPBI>OPBI-S>OPBI-P trend of decrease in resistance held for self-discharge rates. The reduction in self-discharge rate by polarisation of the pristine OPBI membrane significantly extended the self-discharge time, sustaining an OCV reading above 0.75 V for 417 hours compared to the 46 hours for N-212.

Successful application of an OPBI membrane has been reported for the VFB, obtaining a 90% EE at 40 mA cm^{-2} while also exhibiting a higher ASR (twice as much) than N-115 in the same system.[64] However, further in-depth investigation of the complex interactions with cross-linkers and AEMs, increased porosity and anion/cation

conduction mechanisms will be required before OPBI AEMs can be used in ICFBs. These results, however, confirm that the morphology of *m*PBI plays a larger role in the reduction of AEM discharge resistance in ICFBs than the PWN cross-linker, while using low amounts of PWN as cross-linker could reduce the overall resistance.

4.4 Conclusion

The cycling performance of AEM materials have not been published to date. Testing anion-exchange functional group tetramethylimidazolium resulted in high overpotentials during charging of the electrolyte and similar discharge challenges to commercial AEMs reported by literature. The failure of Cl^- counterions to permeate during discharge was investigated by introducing 1.5 M sulfates (see Section 4.3.1) as well as by using a sulfuric acid-based electrolyte, which only worsened the high internal resistance.

Successful cycling of an AEM was obtained using blended base-excess *m*PBI membranes with a low amount of PWN as a cross-linker. A 46 µm *m*PBI-based AEM was cycled for 30 cycles without measurable electrolyte imbalance due to electro-osmotic crossover, obtaining a CE of 96.7% and EE of 76.1%, outperforming the N-212 benchmark with an EE of 74.8% which had 33% electrolyte imbalance. Additionally, the Donnan exclusion effect contributed to lower self-discharge rates of 1.592 mV h^{-1} and 2.907 mV h^{-1} compared to the benchmark of 3.187 mV h^{-1}, despite higher WU values. Further investigation of different cross-linkers and a different PBI material confirmed that the type of cross-linker can affect membrane casting thickness, resistance and polarisation of membranes, while base-excess OPBI membranes failed to discharge electrolyte in an ICFB. While the charge-transfer mechanism is not fully understood, proton migration of *m*PBI was likely facilitated through absorbed acidic electrolyte in hydrophilic channels, which is supported by the degree of swelling, elevated resistance and high ionic selectivity.

References

[1] S. Maurya, S.-H. Shin, Y. Kim, S.-H. Moon, A review on recent developments of anion exchange membranes for fuel cells and redox flow batteries, RSC Advances, 5 (2015) 37206-37230. 10.1039/C5RA04741B.

[2] S. Ahmad, T. Nawaz, A. Ali, M.F. Orhan, A. Samreen, A.M. Kannan, An overview of proton exchange membranes for fuel cells: Materials and manufacturing, International Journal of Hydrogen Energy, 47 (2022) 19086-19131. https://doi.org/10.1016/j.ijhydene.2022.04.099.

[3] N. Mans, D.J. van der Westhuizen, H.M. Krieg, Membrane Screening for Iron–Chrome Redox Flow Batteries, Advanced Energy and Sustainability Research, 5 (2024) 2300195. https://doi.org/10.1002/aesr.202300195.

[4] W. Tang, T. Mu, X. Che, J. Dong, J. Yang, Highly Selective Anion Exchange Membrane Based on Quaternized Poly(triphenyl piperidine) for the Vanadium Redox Flow Battery, ACS Sustainable Chemistry & Engineering, 9 (2021) 14297-14306. 10.1021/acssuschemeng.1c05648.

[5] K. Oh, M. Moazzam, G. Gwak, H. Ju, Water crossover phenomena in all-vanadium redox flow batteries, Electrochimica Acta, 297 (2019) 101-111. https://doi.org/10.1016/j.electacta.2018.11.151.

[6] L. Zeng, T.S. Zhao, L. Wei, H.R. Jiang, M.C. Wu, Anion exchange membranes for aqueous acid-based redox flow batteries: Current status and challenges, Applied Energy, 233-234 (2019) 622-643. https://doi.org/10.1016/j.apenergy.2018.10.063.

[7] A. Amel, N. Gavish, L. Zhu, D.R. Dekel, M.A. Hickner, Y. Ein-Eli, Bicarbonate and chloride anion transport in anion exchange membranes, Journal of Membrane Science, 514 (2016) 125-134. https://doi.org/10.1016/j.memsci.2016.04.027.

[8] D. Chen, M.A. Hickner, E. Agar, E.C. Kumbur, Selective anion exchange membranes for high coulombic efficiency vanadium redox flow batteries, Electrochemistry Communications, 26 (2013) 37-40. https://doi.org/10.1016/j.elecom.2012.10.007.

[9] T. Wang, J.Y. Jeon, J. Han, J.H. Kim, C. Bae, S. Kim, Poly(terphenylene) anion exchange membranes with high conductivity and low vanadium permeability for vanadium redox flow batteries (VRFBs), Journal of Membrane Science, 598 (2020) 117665. https://doi.org/10.1016/j.memsci.2019.117665.

[10] H. Cho, H.M. Krieg, J.A. Kerres, Application of Novel Anion-Exchange Blend Membranes (AEBMs) to Vanadium Redox Flow Batteries, Journal, 8 (2018). 10.3390/membranes8020033.

[11] I. Strużyńska-Piron, M. Jung, A. Maljusch, O. Conradi, S. Kim, J.H. Jang, H.-J. Kim, Y. Kwon, S.W. Nam, D. Henkensmeier, Imidazole based ionenes, their blends with PBI-OO and applicability as membrane in a vanadium Redox flow battery, Eur. Polym. J., 96 (2017) 383-392. https://doi.org/10.1016/j.eurpolymj.2017.09.031.

[12] S. Sreenath, N. P S, M. Krebsz, J. Andrews, R.K. Nagarale, Ion Exchange Membranes: Latest Developments toward High-Performance Vanadium Redox Flow Batteries, ACS Applied Energy Materials, 7 (2024) 10846-10876. 10.1021/acsaem.4c01714.

[13] P. Sharma, S. Kumar, M. Bhushan, V.K. Shahi, Ion selective redox active anion exchange membrane: improved performance of vanadium redox flow battery, Journal of Membrane Science, 637 (2021) 119626.

[14] E. Lallo, A. Khataee, R.W. Lindström, Vanadium redox flow battery using aemion™ anion exchange membranes, Processes, 10 (2022) 270.

[15] X. Hao, N. Chen, Y. Chen, D. Chen, Accelerated degradation of quaternary ammonium functionalized anion exchange membrane in catholyte of vanadium redox flow battery, Polym. Degrad. Stab., 197 (2022) 109864. https://doi.org/10.1016/j.polymdegradstab.2022.109864.

[16] J.J. Min-suk, J. Parrondo, C.G. Arges, V. Ramani, Polysulfone-based anion exchange membranes demonstrate excellent chemical stability and performance for the all-vanadium redox flow battery, Journal of Materials Chemistry A, 1 (2013) 10458-10464.

[17] B.G. Thiam, S. Vaudreuil, Review—Recent Membranes for Vanadium Redox Flow Batteries, Journal of The Electrochemical Society, 168 (2021) 070553. 10.1149/1945-7111/ac163c.

[18] M.R. Hibbs, M.A. Hickner, T.M. Alam, S.K. McIntyre, C.H. Fujimoto, C.J. Cornelius, Transport Properties of Hydroxide and Proton Conducting Membranes, Chem. Mater., 20 (2008) 2566-2573. 10.1021/cm703263n.

[19] L. Hager, M. Hegelheimer, J. Stonawski, A.T.S. Freiberg, C. Jaramillo-Hernández, G. Abellán, A. Hutzler, T. Böhm, S. Thiele, J. Kerres, Novel side chain functionalized polystyrene/O-PBI blends with high alkaline stability for anion exchange membrane water electrolysis (AEMWE), Journal of Materials Chemistry A, 11 (2023) 22347-22359. 10.1039/D3TA02978F.

[20] M.L. Frisch, T.N. Thanh, A. Arinchtein, L. Hager, J. Schmidt, S. Brückner, J. Kerres, P. Strasser, Seawater Electrolysis Using All-PGM-Free Catalysts and Cell Components in an Asymmetric Feed, ACS Energy Letters, 8 (2023) 2387-2394. 10.1021/acsenergylett.3c00492.
[21] L. Hager, T. Maron, T.N. Thanh, J. Stonawski, A. Hutzler, T. Böhm, P. Strasser, S. Thiele, J. Kerres, Polynorbornene copolymers combining flexible ether side chains and rigid hydrophobic segments for AEMWE, Journal of Materials Chemistry A, 13 (2025) 8059-8074. 10.1039/D4TA07753A.
[22] S. Zhang, X. Zhu, C. Jin, Development of a high-performance anion exchange membrane using poly(isatin biphenylene) with flexible heterocyclic quaternary ammonium cations for alkaline fuel cells, Journal of Materials Chemistry A, 7 (2019) 6883-6893. 10.1039/C8TA11291F.
[23] F. Xu, Y. Li, J. Ding, B. Lin, Current Challenges on the Alkaline Stability of Anion Exchange Membranes for Fuel Cells, ChemElectroChem, 10 (2023) e202300445. https://doi.org/10.1002/celc.202300445.
[24] N. Sinclair, M. Vasil, C. Kellamis, E.A. Nagelli, J. Wainright, R. Savinell, G.E. Wnek, Membrane considerations for the all-iron hybrid flow battery, Journal of The Electrochemical Society, 170 (2023) 050516.
[25] J.S. Ling, J. Charleston, Advances in Membrane Technology for the NASA Redox Energy Storage System, (1980).
[26] L.H. Thaller, Recent advances in Redox Flow Cell Storage Systems, (1979).
[27] J. S. Ling, J. Charleston, Advances in Membrane Technology for the NASA Redox Energy Storage System, (1980).
[28] N.H. Hagedorn, NASA Redox Storage System Development Project. Final Report, (1984).
[29] H. Cho, J. Seiler, P. Atanasova, V. Atanasov, Ion-Pair Membrane Based on Imidazolium-Functionalized Poly(pentafluorostyrene) for High-Temperature Proton Exchange Membrane Fuel Cell Application, ACS Applied Energy Materials, 7 (2024) 1864-1872. 10.1021/acsaem.3c02854.
[30] V. Atanasov, M. Bürger, S. Lyonnard, L. Porcar, J. Kerres, Sulfonated poly(pentafluorostyrene): Synthesis & characterization, Solid State Ionics, 252 (2013) 75-83. https://doi.org/10.1016/j.ssi.2013.06.010.
[31] J.A. Kerres, H.M. Krieg, Poly(vinylbenzylchloride) Based Anion-Exchange Blend Membranes (AEBMs): Influence of PEG Additive on Conductivity and Stability, Journal, 7 (2017). 10.3390/membranes7020032.
[32] S.M. MacKinnon, T.J. Fuller, F.D. Coms, M.R. Schoeneweiss, C. Gittleman, Y.-H. Lai, R. Jiang, A.M. Brenner, Fuel Cells - Proton-Exchange Membrane Fuel Cells | Membranes: Design and Characterization, in, 2009, pp. 741-754. 10.1016/B978-044452745-5.00905-9.
[33] Z. Tang, R. Keith, D.S. Aaron, J.S. Lawton, A.P. Papandrew, T.A. Zawodzinski, Proton Exchange Membrane Performance Characterization in VRFB, ECS Transactions, 41 (2012) 25. 10.1149/1.3697451.
[34] J.P. du Toit, H.M. Krieg, The feasibility of microporous separators in iron-chromium flow batteries, Journal of Energy Storage, 107 (2025) 115008. https://doi.org/10.1016/j.est.2024.115008.
[35] N. Mans, H.M. Krieg, D.J. van der Westhuizen, The Effect of Electrolyte Composition on the Performance of a Single-Cell Iron–Chromium Flow Battery, Advanced Energy and Sustainability Research, 5 (2024) 2300238. https://doi.org/10.1002/aesr.202300238.
[36] J. Li, J. Liu, W. Xu, J. Long, W. Huang, Y. Zhang, L. Chu, Highly ion-selective sulfonated polyimide membranes with covalent self-crosslinking and branching structures for vanadium redox flow battery, Chem. Eng. J., 437 (2022) 135414. https://doi.org/10.1016/j.cej.2022.135414.
[37] E. Bülbül, V. Atanasov, M. Mehlhorn, M. Bürger, A. Chromik, T. Häring, J. Kerres, Highly phosphonated polypentafluorostyrene blended with polybenzimidazole: Application in vanadium redox flow battery, Journal of Membrane Science, 570-571 (2019) 194-203. https://doi.org/10.1016/j.memsci.2018.10.027.
[38] K.W. Knehr, E.C. Kumbur, Open circuit voltage of vanadium redox flow batteries: Discrepancy between models and experiments, Electrochemistry Communications, 13 (2011) 342-345. https://doi.org/10.1016/j.elecom.2011.01.020.
[39] L. Gubler, Membranes and separators for redox flow batteries, Current Opinion in Electrochemistry, 18 (2019) 31-36. https://doi.org/10.1016/j.coelec.2019.08.007.
[40] X. Wei, B. Li, W. Wang, Porous polymeric composite separators for redox flow batteries, Polymer Reviews, 55 (2015) 247-272. 10.1080/15583724.2015.1011276.
[41] A. Bhattarai, P.C. Ghimire, A. Whitehead, R. Schweiss, G.G. Scherer, N. Wai, H.H. Hng, Novel Approaches for Solving the Capacity Fade Problem during Operation of a Vanadium Redox Flow Battery, Batteries, 4 (2018). 10.3390/batteries4040048.

[42] M. Nourani, C.R. Dennison, X. Jin, F. Liu, E. Agar, Elucidating Effects of Faradaic Imbalance on Vanadium Redox Flow Battery Performance: Experimental Characterization, Journal of The Electrochemical Society, 166 (2019) A3844. 10.1149/2.0851915jes.
[43] G. Gonzalez, P. Peljo, Experimental Set-Up for Measurement of Half-Cell- and Over-Potentials of Flow Batteries During Operation, Batteries & Supercaps, 8 (2025) e202400394. https://doi.org/10.1002/batt.202400394.
[44] P.C. Ghimire, A. Bhattarai, T.M. Lim, N. Wai, M. Skyllas-Kazacos, Q. Yan, In-Situ Tools Used in Vanadium Redox Flow Battery Research—Review, Batteries, 7 (2021) 53.
[45] R.F. Gann, N.H. Hagedorn, J.S. Ling, Single Cell Performance Studies on the Fe/Cr Redox Energy Storage System Using Mixed Reactant Solutions at Elevated Temperature, (1983).
[46] X. Li, H. Ma, H. Wang, S. Zhang, Z. Jiang, B. Liu, M.D. Guiver, Novel PA-doped polybenzimidazole membranes with high doping level, high proton conductivity and high stability for HT-PEMFCs, RSC Advances, 5 (2015) 53870-53873. 10.1039/C5RA05953D.
[47] F. Mack, K. Aniol, C. Ellwein, J. Kerres, R. Zeis, Novel phosphoric acid-doped PBI-blends as membranes for high-temperature PEM fuel cells, Journal of Materials Chemistry A, 3 (2015) 10864-10874. 10.1039/C5TA01337B.
[48] L. Ding, Y. Wang, L. Wang, Z. Zhao, M. He, Y. Song, A simple and effective method of enhancing the proton conductivity of polybenzimidazole proton exchange membranes through protonated polymer during solvation, Journal of Power Sources, 455 (2020) 227965. https://doi.org/10.1016/j.jpowsour.2020.227965.
[49] O. Setiawan, Y.-H. Huang, Z.G. Abdi, W.-S. Hung, T.-S. Chung, pH-tunable and pH-responsive polybenzimidazole (PBI) nanofiltration membranes for Li+/Mg2+ separation, Journal of Membrane Science, 668 (2023) 121269. https://doi.org/10.1016/j.memsci.2022.121269.
[50] O.D. Thomas, T.J. Peckham, U. Thanganathan, Y. Yang, S. Holdcroft, Sulfonated polybenzimidazoles: Proton conduction and acid–base crosslinking, J. Polym. Sci., Part A: Polym. Chem., 48 (2010) 3640-3650. https://doi.org/10.1002/pola.24147.
[51] K.D. Kreuer, On the development of proton conducting polymer membranes for hydrogen and methanol fuel cells, Journal of Membrane Science, 185 (2001) 29-39. https://doi.org/10.1016/S0376-7388(00)00632-3.
[52] T.T. Letsau, P.P. Govender, P.F. Msomi, Imidazolium-Quaternized Poly(2,6-Dimethyl-1,4-Phenylene Oxide)/Zeolitic Imidazole Framework-8 Composite Membrane as Polymer Electrolyte for Fuel-Cell Application, Journal, 14 (2022). 10.3390/polym14030595.
[53] S.N. Oreiro, A. Bentien, J. Sloth, M. Rahimi, M.B. Madsen, T. Drechsler, Crossover analysis in a commercial 6 kW/43kAh vanadium redox flow battery utilizing anion exchange membrane, Chem. Eng. J., 490 (2024) 151947. https://doi.org/10.1016/j.cej.2024.151947.
[54] C. Arnold Jr, R.A. Assink, Structure–property relationships of anionic exchange membranes for Fe/Cr redox storage batteries, Journal of Applied Polymer Science, 29 (1984) 2317-2330. https://doi.org/10.1002/app.1984.070290708.
[55] K. Schafner, M. Becker, T. Turek, Membrane resistance of different separator materials in a vanadium redox flow battery, Journal of Membrane Science, 586 (2019) 106-114. https://doi.org/10.1016/j.memsci.2019.05.054.
[56] C. Noh, M. Jung, D. Henkensmeier, S.W. Nam, Y. Kwon, Vanadium Redox Flow Batteries Using meta-Polybenzimidazole-Based Membranes of Different Thicknesses, ACS Applied Materials & Interfaces, 9 (2017) 36799-36809. 10.1021/acsami.7b10598.
[57] S.M. Ahn, H.Y. Jeong, J.-K. Jang, J.Y. Lee, S. So, Y.J. Kim, Y.T. Hong, T.-H. Kim, Polybenzimidazole/Nafion hybrid membrane with improved chemical stability for vanadium redox flow battery application, RSC Advances, 8 (2018) 25304-25312. 10.1039/C8RA03921F.
[58] Chromium(III) phosphate, 2024/12, © 2023 ChemicalBook https://www.chemicalbook.com/ChemicalProductProperty_EN_CB0406705.htm (accessed: 2025/09).
[59] F. Al-Sogair, H.M. Marafie, N.M. Shuaib, H.B. Youngo, M.S. El-Ezaby, Interaction of Phosphate with Iron(III) in Acidic Medium, Equilibrium and Kinetic Studies, J. Coord. Chem., 55 (2002) 1097-1109. 10.1080/0095897021000010053.
[60] C. Xu, M. Zhang, Y. Liu, X. Peng, T. Li, W. Li, Z. Meng, G. Zhu, Y. Cui, X. Jiang, G. Sun, Construction of multidentate phosphonic acid ligand for targeted multi-metal extraction toward purification of wet-process phosphoric acid: mechanistic insights into Fe3+ chelation, Chem. Eng. J., 521 (2025) 166957. https://doi.org/10.1016/j.cej.2025.166957.
[61] S.S. Araya, F. Zhou, V. Liso, S.L. Sahlin, J.R. Vang, S. Thomas, X. Gao, C. Jeppesen, S.K. Kær, A comprehensive review of PBI-based high temperature PEM fuel cells, International Journal of Hydrogen Energy, 41 (2016) 21310-21344. https://doi.org/10.1016/j.ijhydene.2016.09.024.

[62] X.L. Zhou, T.S. Zhao, L. An, L. Wei, C. Zhang, The use of polybenzimidazole membranes in vanadium redox flow batteries leading to increased coulombic efficiency and cycling performance, Electrochimica Acta, 153 (2015) 492-498. https://doi.org/10.1016/j.electacta.2014.11.185.
[63] Y. Xing, L. Liu, C. Wang, N. Li, Side-chain-type anion exchange membranes for vanadium flow battery: properties and degradation mechanism, Journal of Materials Chemistry A, 6 (2018) 22778-22789. 10.1039/C8TA08813F.
[64] L. Ding, X. Song, L. Wang, Z. Zhao, G. He, Preparation of dense polybenzimidazole proton exchange membranes with different basicity and flexibility for vanadium redox flow battery applications, Electrochimica Acta, 292 (2018) 10-19. https://doi.org/10.1016/j.electacta.2018.08.128.

CHAPTER 5: Screening and development of cation-exchange membrane materials for the iron-chromium redox flow battery

Chapter table of contents

5.1 Introduction

The all-vanadium flow battery (VFB) and proton-exchange membrane fuel cell (PEMFC) have both seen extensive developments, specifically in membrane materials, unlike the iron-chromium flow battery (ICFB) that shows promise as a large-scale renewable energy storage technology due to the abundance and low cost of its electrolyte materials.[1-4] However, further reduction of the CAPEX cost and improvement of cycling performance are required to advance the technology towards global market penetration.[5-8] One key challenge is the high cost and potential environmental impact of the perfluorinated cation exchange membrane (CEM) Nafion® 212 (N-212), which is commonly used in the ICFB and VFB due to its excellent chemical stability and ionic conductivity.[8-12] Research efforts focussing on alternative CEMs for these energy storage technologies have been concentrated on low-cost aromatic polymers such as SPEEK (sulfonated poly(ether ether ketone)), SPI (sulfonated polyimide) and PBI (polybenzimidazole) for membranes, which often pose chemical stability and ionic conductivity challenges.[13-18]

Aromatic ring backbone membranes are stabilised by carbon atoms with little or no sp^3 orbitals due to the overlapping p orbitals forming low-energy conjugated sp^2 orbitals with π bonds.[19] As a result, even though these polymers are not perfluorinated, they can provide a chemically stable alternative, while reducing the CAPEX cost of the ICFB (from 194 US$ kWh^{-1} to 124 US$ kWh^{-1}).[19-21] To increase H^+ conductivity for higher voltage efficiencies (VEs) and lower resistances in FBs, the ion-exchange capacity (IEC) of these membranes can be increased. However, the additional swelling can decrease selectivity that worsens crossover of metallic ions and the supporting electrolyte which ultimately reduces the coulombic efficiency (CE).[22-24]

Within the large variety of materials investigated for fuel cell (FC) and VFB research that may be adopted in the ICFB, the degree of fluorination and the acidic functional group responsible for charge carrier migration can vary. Material compositions developed for VFBs and PEMFCs membranes vary between pristine [25, 26], blended [27], ionically cross-linked [28, 29] and covalently cross-linked [30], with different chemistries such as partially fluorinated sulfonated poly(arylene (sulfone) ethers) (SFS) [31, 32] or phosphonated poly(pentafluorostyrene) (PWN), to name a few.[33-37]

According to literature, substantially fewer materials have to date been developed for the ICFB. SPEEK membranes that have recently been optimised (57% degree of sulfonation (DS) and 25 μm thickness), with the traditional electrolyte configuration (1 M metal salts and 3 M HCl), reported a 5% higher energy efficiency (EE) than N-212.[17] However, the capacity retention remained low, losing 50% of discharge capacity within one day of cycling. A CEM of sulfonated polybenzimidazole (PBI) has also been optimised for the ICFB with a DS of 100%, showing comparable ionic conductivity and significantly lower Fe/Cr crossover than Nafion.[18] However, due to

the increased resistance from narrow cation conducting channels of aromatic ionomers, these membranes have to be thin (≤ 30 µm), making them more susceptible to carbon felt punctures that can lead to short-circuits.[38, 39] However, increasing the thickness would imbalance the current optimal trade-off between conductivity and selectivity, requiring an increase in water uptake by increasing the degree of sulfonation (DS), which will again lead to poor dimensional stability and water solubility.[40, 41]

Nonetheless, alternative chemistries than the sulfonic acid-based Nafion, SPEEK and sulfonated PBI have to date not been investigated nor optimised for the ICFB, providing scope for the development of for example alternative acids or PBI-based membranes. In the case of SPEEK and other sulfonated aromatic polyethers, using thicker and highly sulfonated (> 80% DS) CEMs may increase H^+ (H_3O^+, $H_5O_2^+$ and $H_9O_4^+$) [42] conduction, where ionic cross-linking with a basic polymer, e.g., PBI with increased flexibility from diphenyl ether groups (OPBI), could help retain the desired swelling levels (see **Figure 5.1**) and dimensional stability.[26, 28] To reduce the CAPEX cost and increase overall performance and separation efficiency for the ICFB, various VFB and FC CEM materials alternative to Nafion were screened for chemical compatibility and cycling performance. Identifying viable chemistries enabled optimisation and fine tuning of the conductivity and selectivity trade-off illustrated in Figure 5.1, specifically by modifying the degree of swelling for the 65 °C aqueous environment of the ICFB.[11, 43, 44]

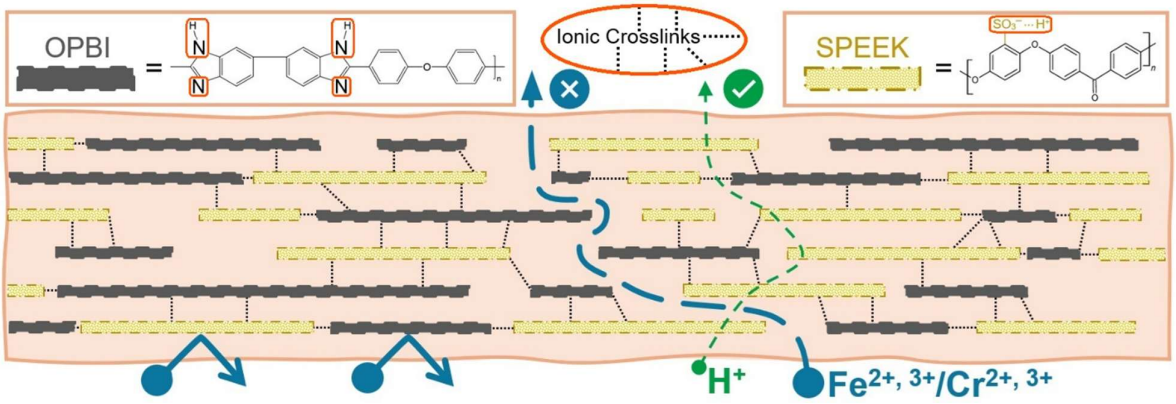

Figure 5.1: Illustration of conductivity vs selectivity of a SPEEK-OPBI cross-linked membrane in an ICFB.

5.2 Experimental

Performance parameters and physico-chemical properties for each CEM were obtained as described in the experimental sections of Chapters 3 (Section 3.2) and 4 (Section 4.2).

5.2.1 Membranes

The molecular structures of all the ionomers and polymers that were used are presented in **Table 5.1**. While most membranes were obtained (Section 5.2.1.1) from the groups of Kerres (HI-ERN, Germany) and Atanasov (University of Stuttgart, Germany), the SPEEK-57 and SPEEK-95-OPBI membranes were developed in-house (Section 5.2.1.2). Nafion-212 (N-212) was used as benchmark throughout.

Table 5.1: An overview of the names and molecular structures of polymers/ionomers present in ion exchange membranes tested.

Name/description	Structure
PBIOO Poly[6-((1H-benzo [*d*]imidazol-6-yl)oxy)-2-(4-phenoxyphenyl)-1H-benzo[*d*]imidazole]	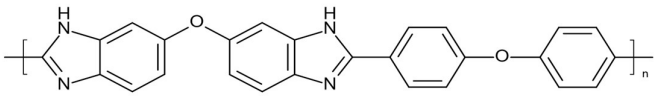
Phosphonated Terphenyl Poly(*p*-terphenyl perfluorophenyl)	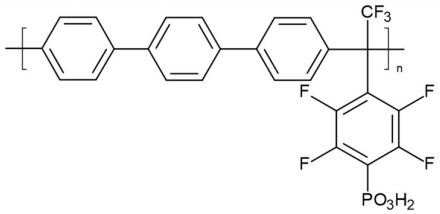
SFS 001 Partially fluorinated sulfonated polyether (Hereafter referred to as SFS)	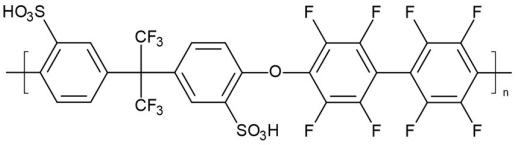
PSUOH Partially sulfonated poly(arylene ether sulfone)	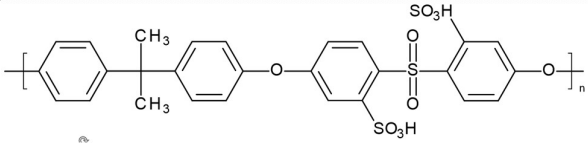
PVDF Polyvinylidene fluoride	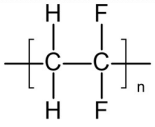
PWN (70) Phosphonated Poly(pentafluorostyrene)	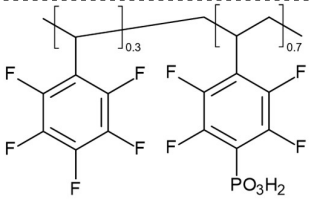

PPFS Poly(pentafluorostyrene)	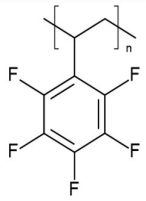
PPFS-Pip Piperidine functionalised PPFS	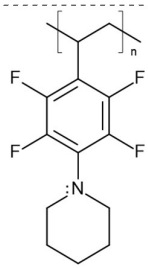
OPBI Poly(4,40-diphenylether-5,50-bibenzimidazole)	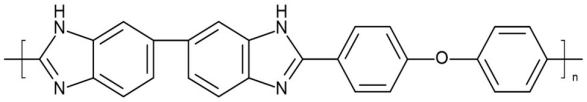
SPEEK Sulfonated poly(ether ether ketone)	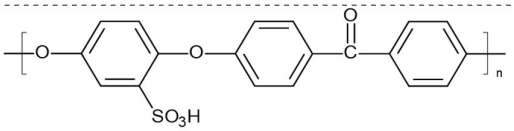

5.2.1.1 Membranes (Kerres & Atanasov)

The polymer synthesis and subsequent manufacture of the acquired CEMs used in this study, which included ionically cross-linked and ionically-covalently cross-linked membranes as well as nanofibre-reinforced composites, were based on literature.[30, 32, 36, 45-47] The compositions of the initially screened membranes, the results of which are discussed in Section 5.3.1, are given in **Table 5.2**. The composition of the membranes developed thereafter are presented and discussed in Section 5.3.2.

Table 5.2: Composition (wt.%) of initially screened membranes.

Membrane	Ionomer	Support Polymer/ Ionomer	Fibre mat
Blended membranes			
SPEEK-PBIOO-a*	SPEEK (83%)	PBIOO (17%)	--
SPEEK-PBIOO-b*	SPEEK (78%)	PBIOO (22%)	--
SA-99T-a	Phos. Terph. (100%)	--	--
SA-99T-ab	Phos. Terph. (60%)	SFS (40%)	--
SA-104-c	Phos. Terph. (40%)	PSUOH (60%)	--
PWN-PVDF	PWN 70 (60%)	PVDF (40%)	--
SFS-PVDF	SFS (80%)	PVDF (20%)	--
Nanofibre-reinforced composites			
PPFS-D	Nafion#	--	PPFS
PWN-D	Nafion#	--	PWN 70
PWN-OPBI	PWN 75#	--	OPBI
PWN-OPBI-D	Nafion#	--	OPBI, PWN 70
SFS-PVDF-D	Nafion#	--	SFS:PVDF (7:3)
PPFS-Pip-D	Nafion#	--	PPFS-Piperidine

* Ionically cross-linked
# Dispersion/pore-filler

5.2.1.2 Membrane synthesis (NWU)

The SPEEK-95-OPBI membranes made in view of development of SPEEK-based membranes needed to be compared to literature-reported pure SPEEK-57.[17] The synthesis and manufacturing of pure and blended membranes (carried out at the North-West University of SA) is described in-depth in this section.

i) SPEEK-57

Due to oversulfonation challenges experienced when attempting to replicate the synthesis of the 57% DS SPEEK CEMs from literature at elevated temperatures [17], the second-order sulfonation reaction [20, 48] was investigated by shaking (until thoroughly mixed) 1.0 g of dried PEEK powder (Victrex® grade, 50 µm mean particle size, Goodfellow) with 19.0 g 98% H_2SO_4 (Platinum Line, ACE Chemicals) to obtain a 5 wt.% polymer solution. The reaction was completed in a sealed container to inhibit atmospheric water absorption by H_2SO_4, which we found significantly lowered the reaction rate (by reducing H_2SO_4 concentration), promoting a heterogeneous sulfonation observed by cloudy casting solutions. The lowered reaction rates were confirmed by lower-than-expected DSs. During the magnetic stirring of the reaction mixture at decreased temperatures of 25 °C (for a more controlled reaction rate), 6 mL samples were taken at 20, 24 and 28 hours for their DS determination.

After precipitation in a deionised (DI) water ice bath, the residual acid was washed from the polymer strings in 250 mL DI water that was exchanged once after one hour and then every 24 hours (until reaching a pH of ~6). Samples were then dried at 70 °C for 24 hours in a convection oven and 2 hours at 120 °C at 5 mbar in a vacuum

oven before NMR analysis (see Section 5.2.2). The 57% DS SPEEK was obtained using a synthesis time of 20 hours and 51 minutes. After dissolving the SPEEK in dimethylacetamide (DMAc ≥ 99% purity, Sigma-Aldrich), a 12 wt.% solution was cast with a doctor blade at a height of 400 µm (to obtain a ~25 µm dry thickness). After casting, the membranes were dried for 24 hours at 65 °C in an air-extraction convection oven before being lifted from the glass surface by wetting with DI water.

ii) SPEEK-95-OPBI

The acid-excess acid-base cross-linked SPEEK-95-OPBI membranes, containing SPEEK with a DS of 95%, were manufactured according to the scheme illustrated in **Figure 5.2**. To obtain the highly sulfonated (95% DS) SPEEK, the PEEK was sulfonated at 65 °C for 4 hours. Due to the high DS, the resulting water-soluble polymer was washed in dialysis tubes (molecular cut-off weight of 14 000 Dalton), before drying and analysis. The SPEEK and OBPI (obtained from Fumatech GmbH) were weighed and blended in specific ratios while using 5 wt.% triethanolamine (≥ 99% purity, Sigma-Aldrich) to neutralise acidic sites and inhibit ionic cross-linking. The casting (DMAc solvent for a 10 wt.% casting solution) and drying methods were similar to the methods described above for the SPEEK-57 membrane. After determining the optimum swelling and water uptake of various SPEEK:OPBI blend ratios (see Figure 5.2 (d)), blend membranes with various ideal swelling ratios were prepared for ICFB testing (see Figure 5.2 (e)).

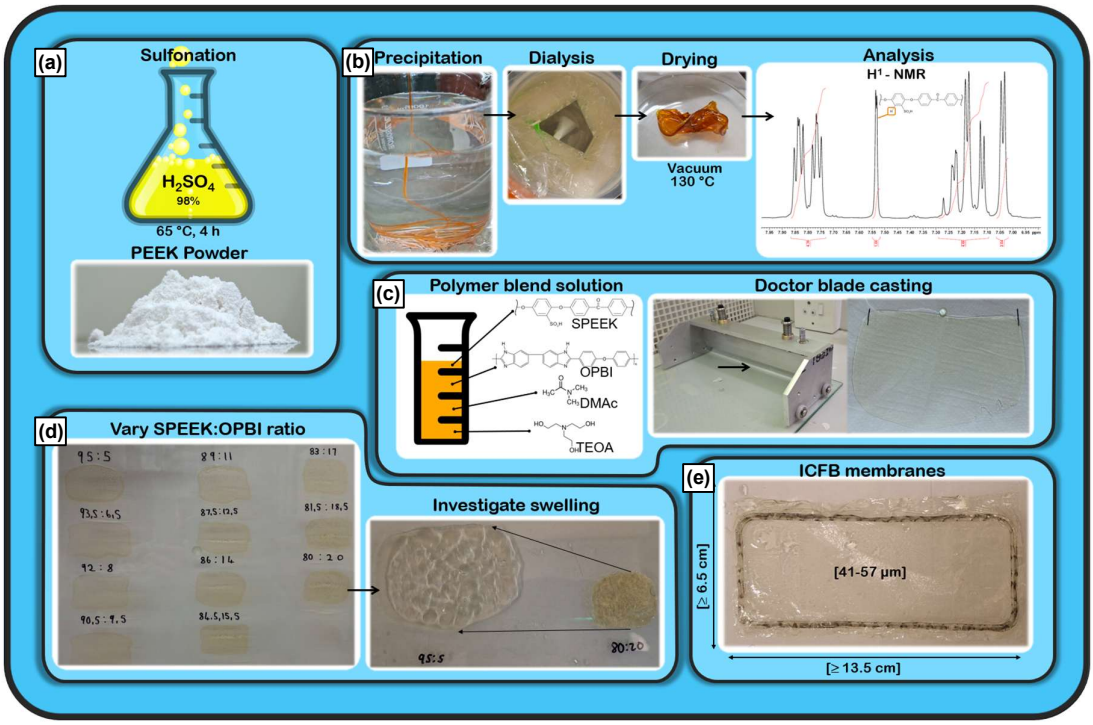

Figure 5.2: (a) Synthesis and (b) precipitation of highly sulfonated SPEEK-95. (c) Composition and casting technique of SPEEK-95-OPBI acid-base blends. (d) Eleven membranes with various blend ratios (SPEEK-95:OPBI = 95:5–80:20) to determine ideal swelling ranges before casting (e) membranes for lab-scale ICFB tests.

5.2.2 DS characterisation

The handling procedure and characterisations for all membranes were carried out as described in the AEM chapter (Section 4.2.2). In this section only the method that was developed to determine the DS of the SPEEK polymer for the in-house membrane synthesis is discussed.

The dried samples from 20, 24 and 28 hours sulfonation at 25 °C (see Section 5.2.1.2) were dissolved (15 mg) in D_6-DMSO (99.9 atom % D, 99% purity, Merck) using an ultrasonic bath at 80 °C before being analysed with a Bruker Avance NEO 600 MHz. After processing the H^1-NMR spectra (baseline and phase corrections), the areas of the peaks were obtained by integration with regards to the H_E proton neighbouring the newly introduced sulfonic acid (see Literature Review – Section 2.3.2.2.4).[48, 49] Equation (5.1) was used to calculate the DS.[48] Subsequently, a quadratic function (Equation (5.2)) was derived from the plotted results of time vs DS confirming a second-order reaction (see **Figure 5.3** and Appendix B – **Figure B1–3**).[50] The DS was determined for both the SPEEK-57 and SPEEK-95 polymers (see **Figure B4** and **B5**).

$$\frac{n}{12-n} = \frac{AH_E}{\sum AH_{A,A',B,B',C,D}} \quad (0 \leq n \leq 1) \tag{5.1}$$

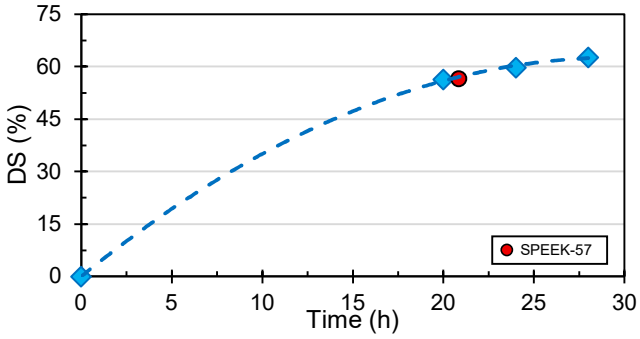

Figure 5.3: Degree of sulfonation at different reaction times for 5 wt.% PEEK in 98% H_2SO_4 at 25 °C with SPEEK-57 as verification of the DS equation (5.2).

$$DS_{25\,°C} = -0.0708t^2 + 4.21t, \quad 0 \leq t \leq 28 \tag{5.2}$$

5.3 Results and Discussion

In this section, the chemical stability performance and electrolyte volume imbalance, caused for example by diffusion and osmotic transfer, of various cation exchange materials and polymers in an ICFB were evaluated. Based on their suitability for other electrochemical systems, a variety of CEMs that might be suitable for the ICFB were initially screened (Section 5.3.1). Following from these results, both ionically and ionically-covalently cross-linked membranes were developed and evaluated (Section 5.3.2). All CEM results were benchmarked against N-212.

Research on the biodegradation of fluoroaromatic compounds in the natural environment are overlooked and very limited.[51, 52] Due to low reactivity of fluorinated alkyls, per- and polyfluoroalkyl substances (PFAS) such as N-212 do not degrade and has a negative impact on the environment [10, 12, 53]. It can be assumed that the versatile fluoroaromatic compounds investigated in this study are more easily biodegradable due to the higher reactivity of aromatic F−C bonds by aromatic substitution reactions of F by N, S or P nucleophiles (see **Figure 5.4**).[40, 54-58] Additionally, the treatment of F^- ion-containing waste water with aqueous calcium salt solutions is an established method for removal of fluoride ions.[59] Hence, F ions released by the nucleophilic substitution reactions should readily react with naturally available calcium ions to form calcium fluoride, thereby no longer posing any environmental hazard.

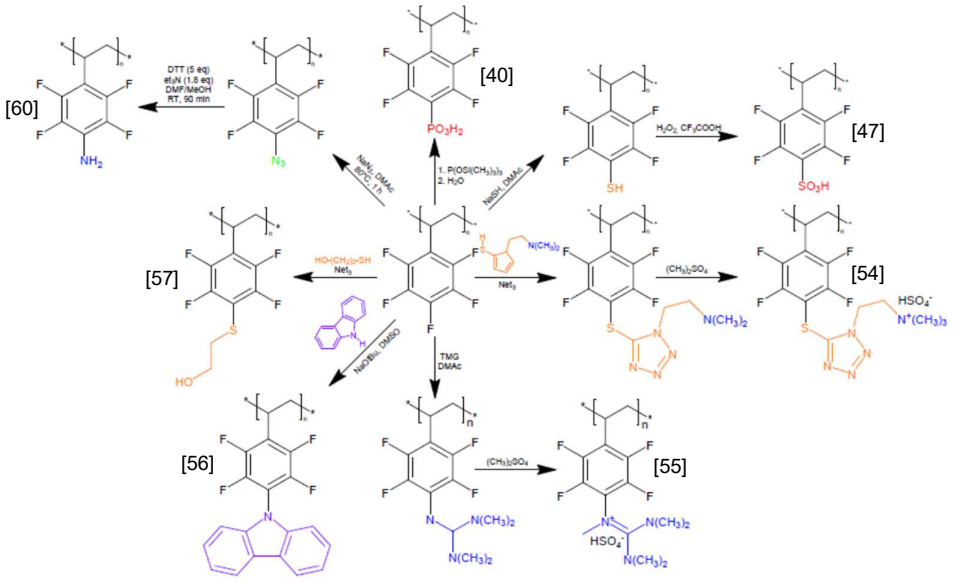

Figure 5.4: Substitution reaction pathways of aromatic F−C bonds.[40, 47, 54-57, 60]

5.3.1 Screening

Initially a variety of membranes (see Section 5.2.1.1) with either sulfonic or phosphonic ion-exchange functional groups were screened and modified according to performance and stability. The choice of membrane materials was based on previous demonstrations of suitability for other electrochemical applications including PEMFC [34, 46, 61, 62] and VFB [21, 25, 26, 31, 33, 63]. The SPEEK-PBIOO-based membranes are discussed in Section 5.3.1.1, followed by the phosphonated terphenyl-containing membranes (SA-99T-a, SA-99T-ab and SA-104-c) in Section 5.3.1.2 and finally the phosphonic and sulfonic acid-based PVDF blends (PWN-PVDF and SFS-PVDF) in Section 3.1.3. Due to the well-known chemical stability and ionic conductivity of the Nafion ionomer, Nafion was also combined with various materials to produce nanofibre-reinforced composites that were tested for selectivity improvements (Section 5.3.1.4). The physico-chemical properties of the blended membranes and the nanofibre-reinforced composites are given in **Table 5.3** and **Table 5.4** respectively (composition is given in Table 5.2), where the thickness, tensile strength, IEC and WU were measured before any electrolyte contact and after ICFB cycling.

Table 5.3: Physico-chemical properties of initially screened blended membranes.

Membrane	Thickness, wet (µm)	Tensile strength (MPa) ± 6%	IEC (mmol g^{-1}) ± 1.5%	WU (%) ± 3.3
N-212	58	23	0.980	17.0
SPEEK-PBIOO-a*	26	73	1.54	23.5
SPEEK-PBIOO-b*	36	67	1.06	21.1
SA-99T-a	52	n.m.	1.45	20.7
SA-99T-ab	36	38	2.02	35.3
SA-104-c	64	58	2.18	57.5
PWN-PVDF	65	17	2.12	93.4
SFS-PVDF	38	45	2.01	78.1

*Ionically cross-linked

5.3.1.1 SPEEK-PBIOO

The ICFB performance and stability of acid-excess SPEEK-PBIOO acid-base cross-linked membranes (provided by the group of Atanasov) were determined. After 24h of preconditioning in the ICFB electrolyte (see Section 3.2.2.1) and one cycle in the testing cell, both the SPEEK-PBIOO-a and -b (SPEEK/PBIOO ratio = 83/17 and 78/22, respectively) membranes showed slight decreases in IEC values (≤ 5.6%), while no loss in mechanical strength or discoloration was observed (see Appendix B – **Table B1** and **Figure B6**, respectively). However, the subsequent electrolyte charging failed as both membranes exhibited excessive cell potentials (> 1.25 V cut-off) when applying a current density of 40.6 mA cm^{-2}. While similarly blended SPEEK with OPBI (10–30%) membranes have successfully been applied in HT-PEMFCs with high proton conductivities (191 mS cm^{-1}), the key difference to an ICFB is that the membranes in an HT-PEMFC are not in contact with the pumped electrolyte and are doped with 98% phosphoric acid (PA) to increase water uptake and proton conductivity. It is thus likely that despite their low thicknesses (26 µm & 36 µm) and adequate H^+ IEC values (1.54 mmol g^{-1} & 1.04 mmol g^{-1}), the ion-conducting channels and sulfonic acid clusters of the SPEEK-PBIOO blended membranes without the PA-doping were too disconnected and narrow, resulting in a decreased ionic conductivity.[64] Enhancing the hydrophilic channels could be investigated by lowering the amount of cross-linker or increasing the DS of SPEEK.

5.3.1.2 Phosphonated terphenyl-containing membranes

The three membranes, SA-99T-a, SA-99T-ab and SA-104-c (provided by the group of Kerres) contain varying amounts of terphenyl polymer with phosphonic acid cation exchange groups (100%, 60% & 40%), with SA-99T-ab also containing 40% SFS and SA-104-c 60% PSUOH. When testing the phosphonic acid-containing CEMs, the only unblended membrane, SA-99T-a, failed after one short cycle yielding a poor discharge capacity of 3.03 Ah L^{-1} (**Figure 5.5**) and a high area specific resistance (ASR = 4.00 Ω cm^2), while the blended SA-99 T-ab completed cycling with a reduced resistance (3.50 Ω cm^2); however, with a substantial drop in capacity during operation (from 9.39 Ah L^{-1} to 2.6 Ah L^{-1} after 28 cycles). This implies that the ion conducting capabilities

of the phosphonated terphenyl membrane, in ICFB electrolyte, were improved by blending with a sulfonic acid ionomer (SFS). However, both SA-99T-a and SA-99T-ab were extremely brittle and glass-like after cycling tests with extensive IEC losses (58% & 38%). These factors contributed to an elevated resistance, as evident in the separation of charge and discharge curves in Figure 5.5, yielding a VE of 66.1% for SA-99T-a and a 28-cycle average VE of 68.8% for SA-99 T-ab.

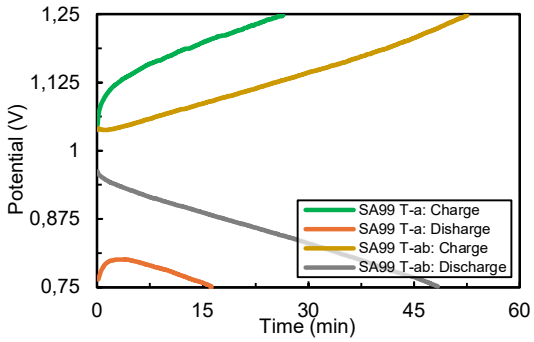

Figure 5.5: Charge and discharge curves of the only cycle (# 1) when using SA-99 T-a and cycle (#1) using SA-99 T-ab.

It was clear that adding and blending 40 wt.% of a sulfonated aromatic main-chain polyether polymer (SFS – see Table 5.1) to phosphonated terphenyl (SA-99T-ab) resulted in a decreased resistance and increased chemical stability. Hence, a blended CEM containing a higher amount (60 wt.%) of a similar sulfonated polymer, poly-(ether sulfone) (PSUOH), which i) has an added SO_2 in the backbone, ii) is non-fluorinated and iii) has a slightly different placement of the sulfonic acid moieties, was manufactured (SA-104-c) and tested in the ICFB.[65]

The lengthening and closer placement of the 1st charge and discharge curves (**Figure 5.6** (a)) confirm that the higher sulfonated ionomer content reduced the resistance (3.20 Ω cm^2) and improved the discharge capacities. The increase in conductivity resulted in a 30-cycle (Figure 5.6 (b)) average discharge capacity increase (from 4.5 Ah L^{-1} to 8.4 Ah L^{-1}) and a higher VE of 73.3%, compared to the 68.8% obtained for SA-99T-ab (Table B1). The conductivity increase, however, also resulted in an increased self-discharge rate from 3.11 mV h^{-1} (SA-99T-ab) to 6.27 mV h^{-1}. While a higher sulfonic acid content increased the stability and conductivity of the phosphonated terphenyl membranes, the irreversible green staining (see Figure 5.6 (c, d)), fragility (brittleness) and lacking capacity retention due an operational increase in resistance indicated that the chemical compatibility remained a challenge. When attempting to dissolve the pristine and stained samples from before and after cycling (to investigate degradation using NMR), the stained samples remained insoluble in DMSO, despite prolonged heating and sonication, which strongly implied the presence of cross-linking.

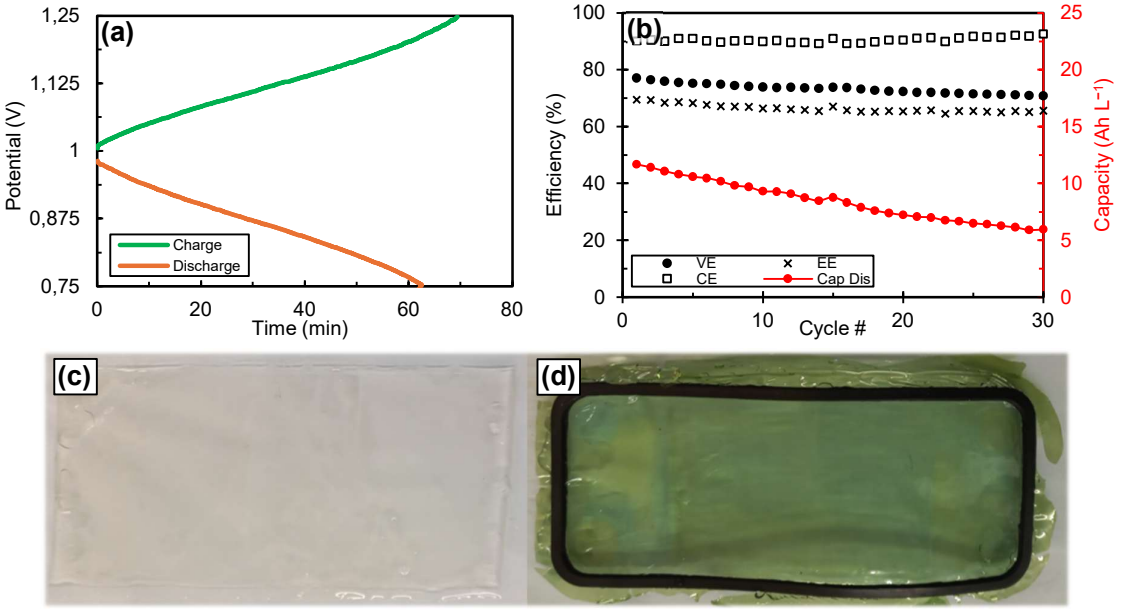

Figure 5.6: (a) Cycle #1 charge and discharge curves, (b) 30-cycle performance parameters and (c, d) photographic images before and after 30 cycles of SA-104-c, respectively.

Polysulfones like PSUOH, without any blend component such as phosphonated terphenyl, have been used as a CEM in the VFB at an optimised DS of 62% and WU of 24.5%.[66] Although chemical degradation (oxidation by VO_2^+) in the form of chain breakage was reported, no brittleness was observed.

5.3.1.3 Phosphonic and sulfonic acid-based PVDF blends

In this section a phosphonic acid (PWN-PVDF) and a sulfonic acid-based (SFS-PVDF) PVDF blended membrane was screened.

i) PWN-PVDF

To further investigate the poor chemical compatibility of phosphonic acid-based membranes, a CEM was prepared (group of Kerres) by blending a phosphonated PPFS (PWN-70), which has previously demonstrated excellent stability in fuel cell applications [34], with the low-cost and relatively chemically inert PVDF polymer in a 6:4 blend ratio (Table 5.2).[4] Preconditioning of the PWN-PVDF membrane in the electrolyte solution, however, quickly resulted in a similar green discoloration (see **Figure B7** (a, c) before and (b, d) after preconditioning) and a reduction in WU% (93.4% vs 21.6%), while the high fragility (low mechanical strength) prevented battery testing by tearing repeatedly during handling.

After repeatedly observing the green discolouration and brittleness, it was hypothesised that the green electrolyte component Cr^{3+} could have attached to the phosphonic acid sites, given the insolubility of Cr(III) phosphates even in acidic environments [67], essentially cross-linking the cation exchange groups (see Figure

B7 (h)). To confirm this, a stained piece of membrane (1 cm x 3 cm) was thoroughly washed in 1 M HCl, followed by washing in a 1 M solution of Al^{3+} and finally in a 2 M V^{5+} solution to determine if the visible staining can be reversed by replacing the Cr^{3+} with cations that have different cationic strengths. The persistence of green staining (Figure B7 (e–g)), further supports that Cr^{3+} was strongly ionically bonded to the active membrane sites. SEM-EDX imaging was used to compare elemental mapping of an unstained and stained membrane (**Figure 5.7** (a, b)) that had both been repeatedly washed in 1 M HCl, 65 °C for 24 h, which confirmed the presence of the Cr cations after washing.

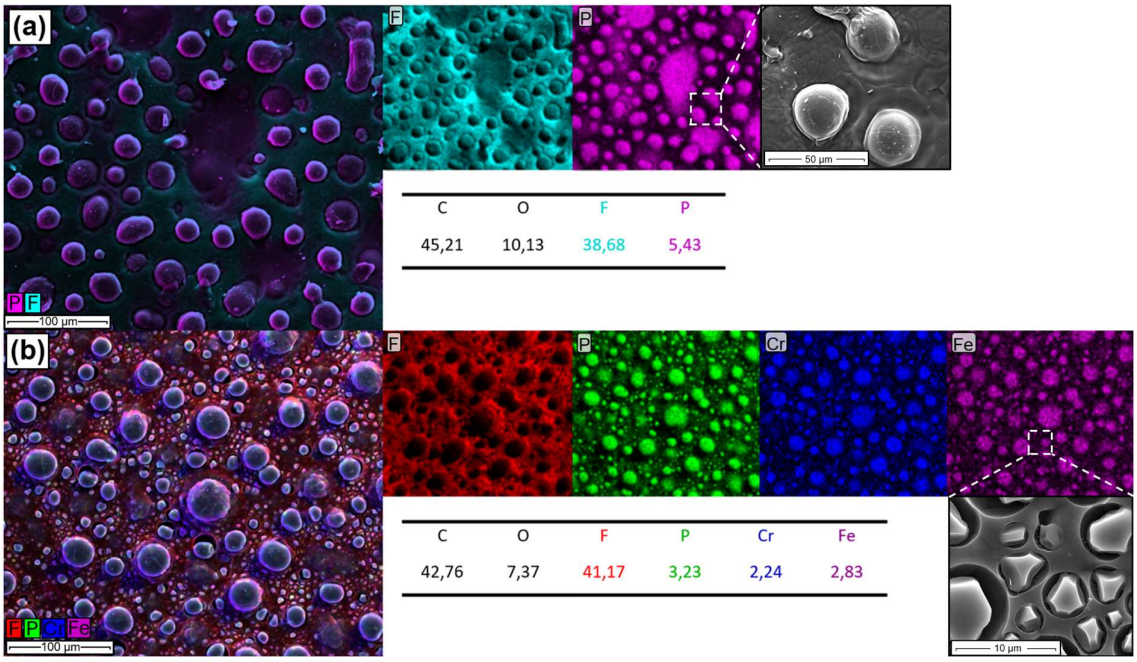

Figure 5.7: Surface SEM imaging and EDX elemental mapping of the PWN-PVDF blend membrane (a) pristine and (b) stained by ICFB electrolyte.

The SEM imaging of the surface showed distinctly heterogeneous F and P regions, which indicates that microphase separation between the PVDF and PWN had occurred. The cluster formation likely occurred during the membrane casting process due to the difference in polymer polarity which leads to incompatibility and thus microphase separation between the two blend components.[27, 68] While using two samples make it unclear if the staining from ICFB electrolyte reduced the dimensions of PWN clusters, the cluster diameter for the stained sample ranged between 2 µm and 42 µm while only large clusters were visibly present in the pristine sample (10–36 µm). The presence of both Cr and Fe, in a relatively similar amount to P specifically in the PWN region, could also imply a bimetal complex bonded on or between the $–PO_3^{2-}$ sites. The PWN ionomer, which is present as spherical formations on the surface, also appears to be partially broken off from the membrane surface after electrolyte contact.

When examining the change in tensile strength before and after cycling of the sulfonated (SPEEK-PBIOO-a and SPEEK-PBIOO-b) and phosphonated (SA-99T-a, SA-99T-ab, SA-104-c and PWN-PVDF) membranes (see Table B1), all the phosphonic acid-based membranes displayed substantial deterioration in mechanical strength ranging between 64% (for SA-104-c) and 80% (SA-99T-ab), while the glass-like properties of the pure SA-99T-a prevented tensile strength measurements. Both SPEEK-PBIOO membranes had a slightly increased tensile strength, which was likely due to the compression of the polymer lattice, considering the measured reduction in thickness of up to 14.7% for SPEEK-PBIOO-b. However, despite the sufficient chemical stability of the SPEEK membranes in electrolyte, their conductivity was insufficient for any ICFB cycling. The study on the phosphonic acid-based membranes and their interaction with electrolyte has shown severe chemical instability with irreversibly strong ionic bonding from cationic Cr, and likely Fe.

ii) SFS-PVDF

It was shown that the addition of sulfonated ionomers (SFS and PSUOH) improved the chemical stability and cycling performance of phosphonated terphenyl membranes. Additionally, partial F substitution provides improved chemical inertness (C-F bonds in SFS stronger than C-H in PSUOH) [21, 69] and an increased acidity from the electron withdrawing and strong inductive (−I) effect.[70] Accordingly, for the last membrane in this screening series, SFS was blended with inert PVDF before investigating the membrane conductivity and chemical compatibility in an ICFB.

According to **Figure 5.8** (c, d), the sulfonic acid-based CEM underwent no visual or mechanical changes from preconditioning or cycling, which was also confirmed by the insignificant changes in tensile strength (45 MPa vs 44 MPa) and WU (78.1% vs 77.3%) values. The CEM was able to charge and discharge ICFB electrolyte (Figure 5.8 (a)), while demonstrating an enhanced conductivity, resulting in an ASR (obtained from discharge polarisation curves) of 1.90 Ω cm² (Table B1) and a VE of 80.7% over 20 cycles (Figure 5.8 (b)). However, the elevated conductivity negatively impacted selectivity, yielding a CE of only 57.4% at a high self-discharge rate of 63.50 mV h^{-1}. Poor selectivity, i.e. high crossover, from the high IEC and excessive WU (78.1% compared to 17.0% measured for N-212), ultimately resulted in the termination of testing after 20 cycles due to a total imbalance of electrolyte volumes.

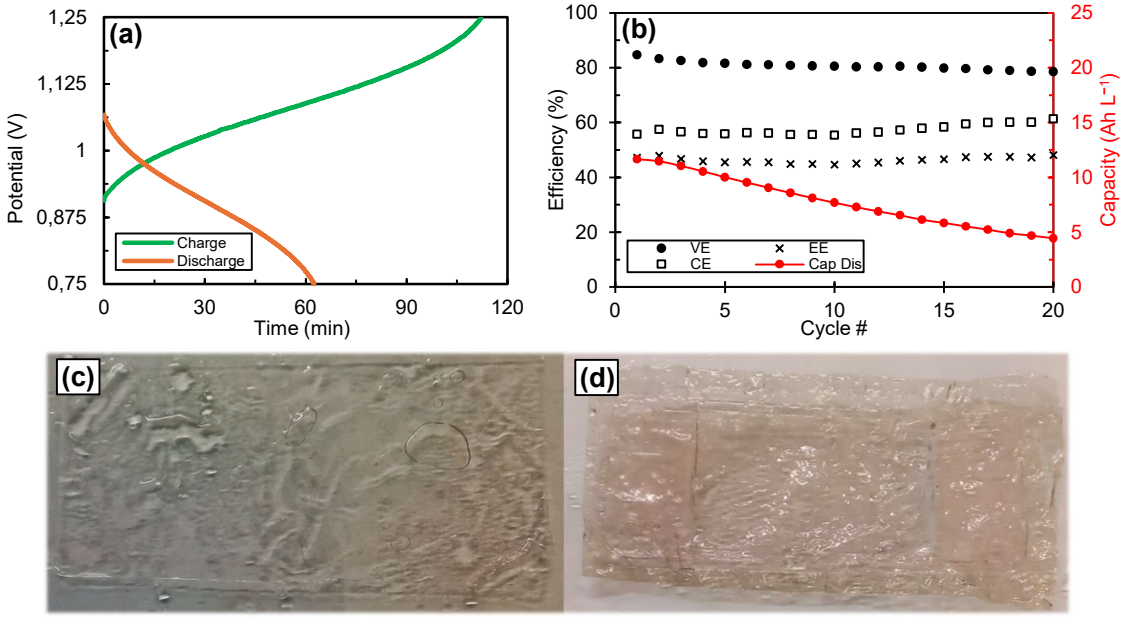

Figure 5.8: (a) Cycle #1 charge and discharge curves, (b) 20-cycle performance parameters and (c, d) photographic images before and after cycling of SFS-PVDF, respectively.

5.3.1.4 Nanofibre-reinforced composites

Nafion, being the current benchmark for this study, is known not only for its stability, performance and wide use, but also its high cost and low selectivity in the ICFB.[18, 46, 71] The conductivity, however, cannot be enhanced without increasing the current rate of self-discharge and operational electrolyte volume imbalances from electro-osmotic drag. Using a reduced amount of PFSA in combination with a more selective material in a reinforced composite membrane could reduce membrane cost and improve selectivity.

Composite membranes were manufactured by the group of Kerres with various chemistries using electrospinning to deposit a mat of nanofibres which was then spray-coated with Nafion or PWN ionomer dispersions to fill all voids (see Table 5.2). The summary of the physico-chemical properties of the six membranes tested are presented in Table 5.4 (see Table 5.2 for the composition).

Table 5.4: Physico-chemical properties of nanofibre-reinforced composites.

Membrane	Thickness, wet (µm)	Tensile strength (MPa) ± 6%	IEC (mmol g^{-1}) ± 1.5%	WU (%) ± 3.9
PPFS-D	54	17	1.19	24.3
PWN-D	n.m.	--	--	--
PWN-OPBI	n.m.	--	--	--
PWN-OPBI-D	58	15	1.07	60.5
SFS-PVDF-D	66	15	2.01	112.6
PPFS-Pip-D	62	16	1.08	26.3

The electrolyte incompatibility and adverse effects of Fe/Cr cations on phosphonated ionomers observed previously (Sections 5.3.1.2 and 5.3.1.3) resulted in an inability to measure the mechanical stability of the phosphonic acid-containing fibre spun composites PWN-D and PWN-OPBI. These membranes could also not be tested in the ICFB. The 30-cycle efficiencies and self-discharge of the four remaining composites are compared to N-212 in **Figure 5.9** (electrolyte imbalance and other performance parameters are shown in Appendix B – Table B1).

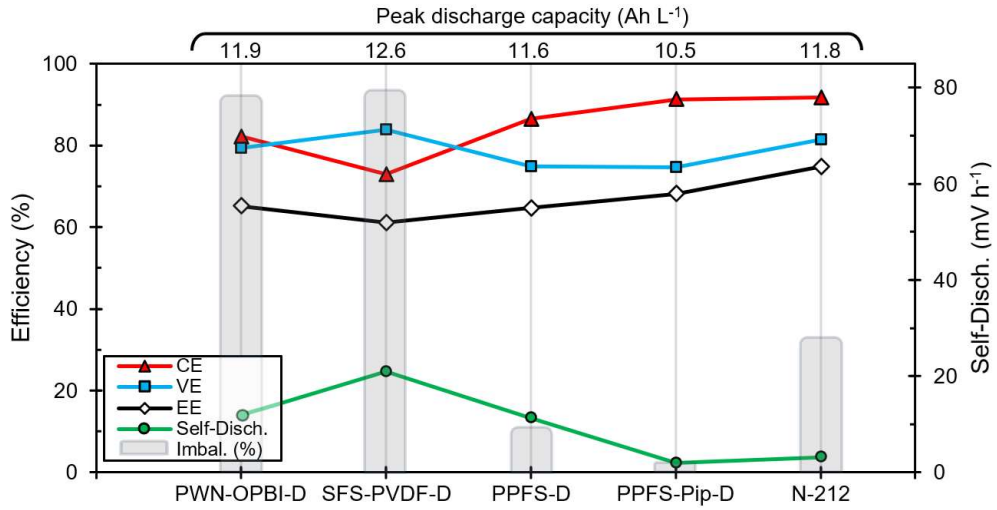

Figure 5.9: Discharge capacities, self-discharge rates, electrolyte imbalance and 30-cycle avg. efficiencies of various Nafion composite membranes compared to N-212.

Unlike the screened PWN-PVDF blend membrane, PWN-D and PWN-OPBI, the acid-base interaction of the pore-filling-Nafion and base-excess cross-linked PWN-OPBI fibre mat membrane (PWN-OPBI-D) provided adequate mechanical stability to measure cycling performance. However, the electrolyte imbalance level was high (93%) after cycling. The EE of the SFS-PVDF blend (see Section 5.3.1.3) was improved (from 47.1% to 61.2%) by using the blend as nanofibres with a Nafion dispersion and changing the blend ratio from 8:2 to 7:3 SFS:PVDF (SFS-PVDF-D).

This performance increase was the result of a slight decrease in swelling and the additional use of Nafion for cation exchange, which increased the CE. However, the swelling was still too high with water uptake levels at 43.9%, resulting in poor selectivity and 96% electrolyte imbalance after cycling.

Compared to the benchmark N-212, a composite of Nafion with the non-polar polymer fibre mat of PPFS (PPFS-D) resulted a reduction in supporting electrolyte crossover, while the reduction in cation exchange material also reduced the VE. The lack of interaction between the Nafion and the PPFS polymer mat, however, led to visible delamination (see **Figure B8**) and a reduced CE (73.0%) compared to the benchmark (91.8%). For the last nanofibre-reinforced composite PPFS-Pip-D, a piperidine functional group was attached to the PPFS to prevent delamination by acting as a weak base, due to the −I effect from the aromatic F atoms of the tetrafluorophenyl groups, which can interact ionically with Nafion and be protonated in the acidic ICFB electrolyte to piperidinium.[32, 72] The positively charged fibre mat layer likely enhanced selectivity by cation repulsion via the Donnan exclusion principle, which allowed the PPFS-Pip-D membrane to obtain a reduced self-discharge value of 2.038 mV h^{-1} (vs 11.35 mV h^{-1} for PPFS-D and 3.187 mV h^{-1} for N-212), while also reducing electrolyte imbalance levels to 2% compared to the 11% of PPFS-D and 33% of N-212. Logically, the ionic conductivity was also decreased by this fibre mat layer as is evident from the separation of the 1st charge/discharge curve and the slope of the discharge polarisation curves of PPFS-Pip-D (see **Figure 5.10** (a, b)). No discoloration was observed after 30 cycles (Figure 5.10 (c, d)); however, the 10% tensile strength reduction (Table B1) could be indicative of degradation. Since the selectivity can be increased by the weak base, further development of PPFS-Pip with other CEM ionomers is recommended, including long-term chemical stability testing.

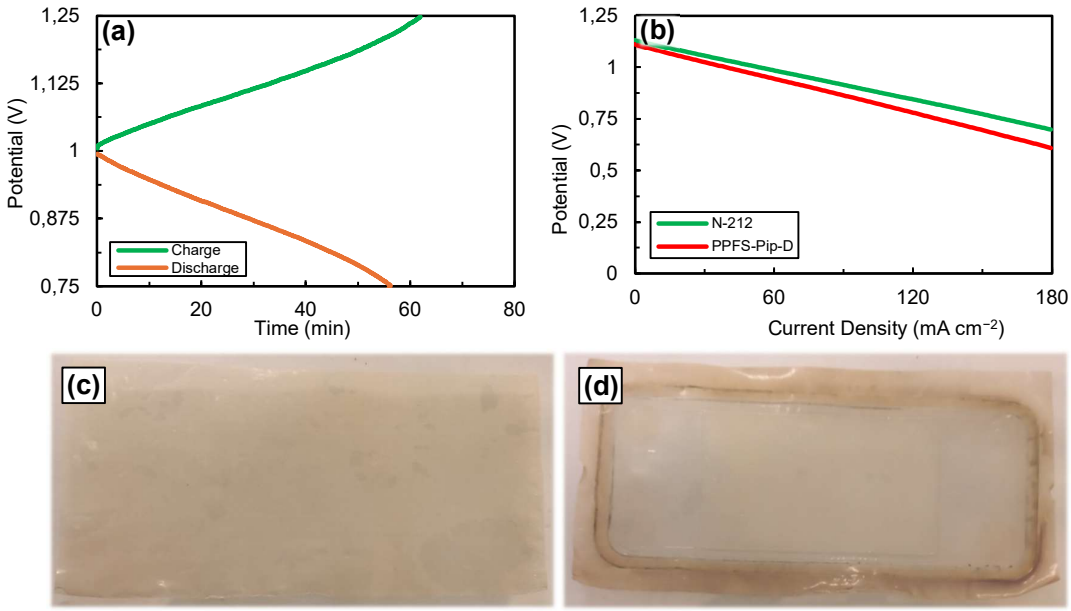

Figure 5.10: PPFS-Pip-D (a) Cycle #1 charge and discharge curves, (b) discharge polarisation curves compared to the benchmark and (c, d) photographic images before and after cycling.

5.3.2 Ionically (& covalently) cross-linked blends

Literature has reported the successful application of a thin (25 µm) SPEEK (DS = 55–57%) CEM in the ICFB with promising conductivity and selectivity.[17, 20] The low-cost and chemical stability of SPEEK warranted its further investigation. While a higher DS SPEEK would increase the size and interconnectivity of hydrophilic channels and sulfonic acid clusters, the excessive swelling and dimensional instability would have to be countered. OPBI has previously been used as a low-cost and chemically stable cross-linker to retain dimensional stability and modify the degree of swelling of highly sulfonated SPEEK (90% DS) in a VFB, obtaining an EE of 89.9% at 180 mA cm^{-2} with no signs of degradation.[28] Despite the electrolyte related challenges of AEMs in the ICFB, the results from Chapter 4 also confirmed that OPBI-based membranes were chemically compatible with the ICFB electrolyte (see Section 4.3.3). When combined with SPEEK, the preliminary testing of acid-excess SPEEK-PBIOO blends (Section 5.3.1.1) confirmed a chemical stability (no visible staining or tensile strength loss), but yielded a poor conductivity despite having IECs higher than that of N-212 (1.06–1.54 mmol g^{-1} vs 0.980 mmol g^{-1}), which was ascribed to the absence of PA doping and too much cross-linking restricting hydrophilic channels. Accordingly, highly sulfonated SPEEK-95 (DS = 95%) was ionically cross-linked with a reduced amount of basic OPBI polymer (acid-excess), in order to improve the dimensional stability, in various ratios (90:10 to 87:13) and tested in the ICFB (Section 5.3.2.1). These membranes were prepared in-house. The 57% DS SPEEK (SPEEK-57) from literature was also synthesised in-house and included to benchmark against the blended membranes.[17]

While the SFS ionomer has shown the potential for high ionic conductivity during screening (see Section 5.3.1.3), the accompanying swelling led to undesirable electro-osmosis and poor ionic selectivity. To reduce its swelling, the SFS was also ionically cross-linked with OPBI (SFS-OPBI) and blended in various ratios before testing in an ICFB (see Section 5.3.2.2). To further reduce swelling, ionically and covalently ([1,1'-biphenyl]-4,4'-dithiol (2%)) cross-linked SFS-OPBI (88:10) membranes with varying thicknesses were finally tested, the results of which are presented in Section 5.3.2.3. The SFS-OPBI blends presented in Sections 5.3.2.2 and 5.3.2.3 were prepared and provided by the group of Kerres. In **Table 5.5**, the physico-chemical properties and compositions of the ionically cross-linked SPEEK-95-OPBI and SFS-OPBI, as well as the covalently and ionically cross-linked SFS-OPBI, are presented.

Table 5.5: Physico-chemical properties and composition (wt.%) of ionically cross-linked blends.

Membrane	Thickness, wet (µm)	Tensile strength (MPa) ± 6%	IEC (mmol g^{-1}) ± 1.5%	WU (%) ± 3.3	Ionomer	Support Polymer/ Ionomer
N-212	58	23	0.980	17.0	Nafion®	--
SPEEK-57	26	58	1.62	56.9	SPEEK-57	--
Ionically cross-linked (SPEEK- & SFS-OPBI)						
SPEEK-95-OPBI 90:10	57	57	1.57	56.8	SPEEK-95 (90%)	OPBI (10%)
SPEEK-95-OPBI 89:11	55	60	1.55	35.2	SPEEK-95 (89%)	OPBI (11%)
SPEEK-95-OPBI 88:12	47	64	1.52	32.3	SPEEK-95 (88%)	OPBI (12%)
SPEEK-95-OPBI 87:13	41	72	1.40	28.8	SPEEK-95 (87%)	OPBI (13%)
SFS-OPBI 9:1	83	53	1.68	90.4	SFS (90%)	OPBI (10%)
SFS-OPBI 86:14 A	66	59	1.52	56.9	SFS (86%)	OPBI (14%)
SFS-OPBI 84:16 A	59	63	1.20	34.1	SFS (84%)	OPBI (16%)
SFS-OPBI 8:2	53	67	1.18	31.5	SFS (80%)	OPBI (20%)
Ionically & covalently cross-linked (SFS-OPBI)						
SA-210a[#]	26	66	1.54	42.5	SFS (88%)	OPBI (10%)
SA-210b[#]	50	53	1.54	42.6	SFS (88%)	OPBI (10%)
SA-262a-1100[#]	46	55	1.57	49.1	SFS (88%)	OPBI (10%)

[#]Ionically & covalently cross-linked with [1,1'-biphenyl]-4,4'-dithiol (2%)

5.3.2.1 Ionically cross-linked SPEEK-95-OPBI

Firstly, the degree of swelling of SPEEK-95-OPBI cross-linked membranes was investigated since the swelling strongly determines the selectivity and conductivity through the size of molecular pores retaining electrolyte, which can be exacerbated by the elevated temperature of ICFB operation. As mentioned in Section 5.2.1.2 (in-house membranes), this study firstly entailed a broad investigation to determine the effect of the amount of OPBI cross-linker on the swelling and the WU, providing an ideal region of blend ratios with a desired swelling degree. Based on these results, ratios were selected and cast as membranes that were tested in the ICFB.

According to the results from the first part of this study, it was found that SPEEK-95 on its own quickly dissolved in 65 °C water requiring ≥ 5% cross-linker (OPBI) before minimal dimensional stability was obtained. Hence, the swelling of cross-linked membranes with (5–20% OPBI) was investigated. **Figure 5.11** (a) visually shows the significant reduction in planar swelling by 1.5% incremental additions of OPBI from left to right. Figure 5.11 (b, c) show that limited swelling occurred above 13%, while the water uptake increased exponentially below 10%. Due to these findings, four membranes for ICFB testing were casted with a thickness of ~50 µm (twice as thick as the ultrathin SPEEK-57) with 10–13% OPBI content (highlighted area Figure 5.11 (b, c)) to relate the degree of swelling to the performance parameters and electrolyte volume imbalances.

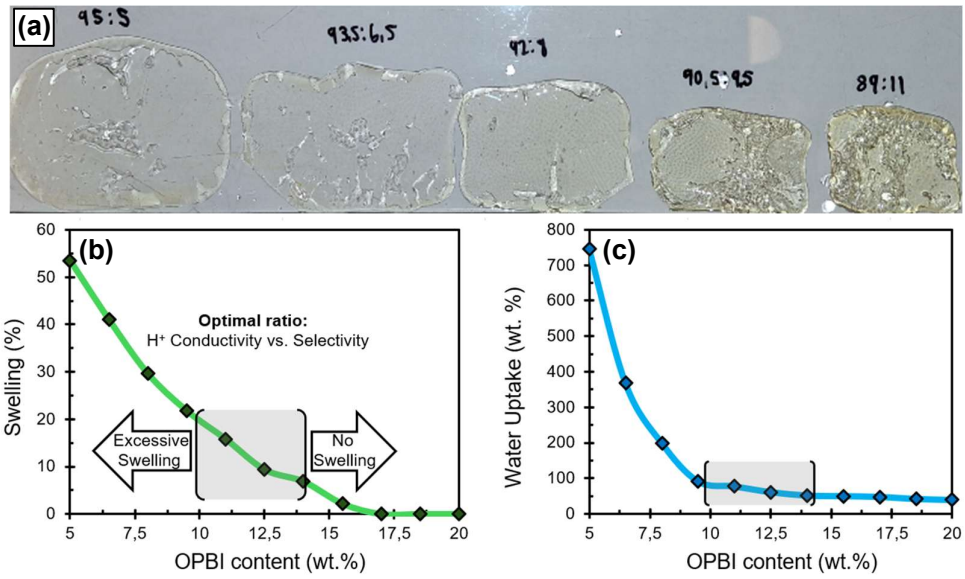

Figure 5.11: Dimensional swelling [a) photographic, b) thickness and c) water uptake - weight] of different SPEEK-95-OPBI blend ratios.

The physical properties and ICFB performances of the SPEEK-95-OPBI blends were compared to SPEEK-57 and N-212. According to Table 5.5, the tensile strengths of the SPEEK-95-OPBI membranes, which increased with increasing OPBI content, were approximately three times higher than N-212, but similar to the SPEEK-57. The calculated performance parameters (CE, VE, EE, self-discharge) after 30 cycles, as well as self-discharge rates and ASRs from discharge polarisation curves for the four SPEEK-95-OBI blends, SPEEK-57 and N-212, are presented in **Figure 5.12**. While no IEC losses (see Table B1) were measured, the thickness of the SPEEK-57/-95-OPBI membranes decreased during cycling, resulting in a higher operational increase in ASR compared to N-212. The observed shrinking resulted in increased tensile strengths and an increasing ASR that reduced VE with each cycle, causing a decline in capacity retention due to the 1.25 V cut-off shortening the charge cycles. The reduction in swelling (see wet thicknesses & WU in Table 5.5) with an increasing amount of OPBI cross-linker (Figure 5.11) correlated with the decrease in self-discharge rate and improvement in CE observed during cycling (Figure 5.12). The IEC was reduced by the incremental increases in OPBI that consumed sulfonic acid sites, resulting in a decrease in IECs and average VEs.

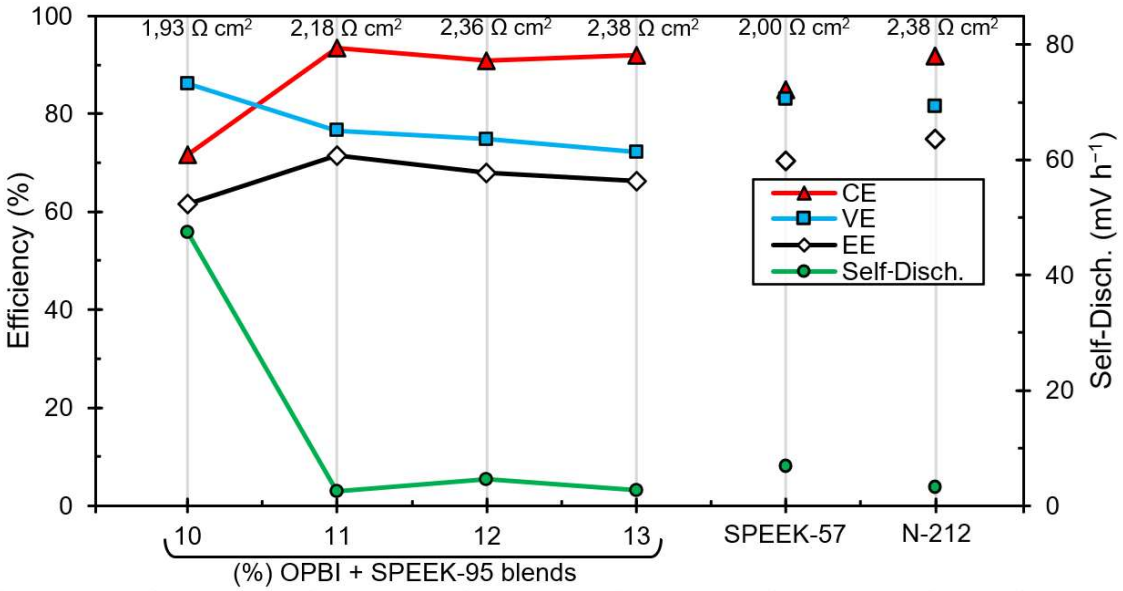

Figure 5.12: Efficiencies, self-discharge rates and ASRs of SPEEK-95-OPBI blends (40–55 µm), SPEEK-57 (26 µm) and N-212 (58 µm).

Literature comparing 57% DS SPEEK to N-212 in the ICFB (using an electrolyte composition of 1.0 M Fe & Cr in 3.0 M HCl) [17] reported a slightly higher IEC (1.72 mmol g^{-1} vs 1.62 mmol g^{-1}) than the SPEEK-57 used in this study, which is supported by the DS (57.4% vs 56.6%). The lower 30-cycle avg. EE (Table B1) compared to literature SPEEK-57 (70.4% at 40.6 mA cm^{-2} vs ~81% at 80 mA cm^{-2}) was likely due to the reduced resistance from experimental differences with this study. Differences include using a 3.0 M HCl electrolyte, a higher electrolyte pumping rate (115 mL min^{-1}

vs 65 mL min^{-1}) and reduced cut-off potentials (0.8–1.2 V vs 0.75–1.25 V). However, in line with literature findings [43], the reduced acidity of the 1.0 M electrolyte used in this study showed a significant reduction in capacity decay from ~3.4% h^{-1} to 0.7% h^{-1} when comparing the similar SPEEK membranes. Unfortunately, modern literature on ICFB membranes does not report on any measurement of imbalance from electro-osmotic solvent crossover, which is a well-known challenge for up-scaling and long term operation of FBs.[73-76].

When comparing the results of cross-linked and highly sulfonated SPEEK, SPEEK-95-OPBI 89:11 yielded the highest CE (93.5%), while the EE was 1.1% higher than the unblended SPEEK-57 and 3.3% lower than N-212. In terms of ionic selectivity and separation efficiency, the self-discharge rates of all membranes in Figure 5.12 were generally comparable, except for SPEEK-95-OPBI 90:10 that had an elevated WU. One critical finding is that the physico-chemical and performance results both show that decreasing the basic cross-linker, in an acid-base blend ratio, increases VE up to a threshold (< 11 wt.% OPBI specifically for SPEEK-95), whereafter selectivity exponentially decreases. The electrolyte imbalance from cycling differed significantly (Table B1), where SPEEK-95-OPBI (90:10) had ~80% electrolyte imbalance, SPEEK-57 ~50%, N-212 ~33% and SPEEK-95-OPBI (89:11) only ~4%. From these results, it is clear that the optimal trade-off between selectivity and conductivity for ionically cross-linked SPEEK-95-OPBI membranes, in the range of 50 µm thickness, is a SPEEK:OPBI blend ratio of 89:11.

5.3.2.2 Ionically cross-linked SFS-OPBI

While SFS-PBI blends have been investigated for other applications (SO_2/H_2SO_4 electrolysis, HT-PEMFC and direct isopropanol FC) [30, 77, 78], it is important to optimise the acid-base blend ratio in terms of the selectivity vs conductivity trade-off in an ICFB. Hence, in a first set of screening experiments, nine SFS:OPBI membranes (provided by the group of Kerres) with varying ratios (9:1, 8:2, …, 1:9) were casted (500 µm) and ionically cross-linked. The single-cell ICFB tests showed that all membranes with ≥ 30% OPBI yielded a high ASR and a low water uptake (< 13%) while failing to discharge the electrolyte, which aligns with the results presented on SPEEK-PBIOO (Section 5.3.1.1) and base-excess AEMs in Chapter 4 (see Section 4.3.1). This non-CEM functionality was ascribed to an inadequate amount of sulfonic acid sites available, most likely by being either consumed by cross-linking, or by blocking of the OPBI anion exchange imidazolium nitrogen by the $FeCl_4^-$ complexes formed during charging. While the 7:3 SFS-OPBI blend could not be discharged at 40.6 mA cm^{-2}, a discharge polarisation curve could be obtained, yielding an ASR of 8.28 Ω cm^2 with an especiallyry low self-discharge rate of 0.407 mV h^{-1}.

Based on the results of the nine membranes screened, only the 9:1 and 8:2 SFS-OPBI membranes yielded ICFB cycling results and were therefore included in Table 5.5 and Table B1. The first charge and discharge curves when using SFS-OPBI 9:1 and SFS-OPBI 8:2 are presented in **Figure 5.13** (a, b), respectively, illustrating the effects on CE, VE and discharge capacity. The high WU (90.4%) of the 9:1 SFS-OPBI blend

negatively affected the CE. The increased degree of cross-linking successfully reduced the WU of the 8:2 blend to 31.5%, leading to a subsequent increased 1st cycle CE (Figure 5.13 (b)) of 94.5%. However, the increased resistance from the 20% OPBI cross-linker reduced the VE to 77.9% and the discharge capacity from 11.6 Ah L^{-1} to 6.8 Ah L^{-1}. According to these results, the optimal blend ratio should be between 9:1 and 8:2, i.e. 10–20% OPBI cross-linker.

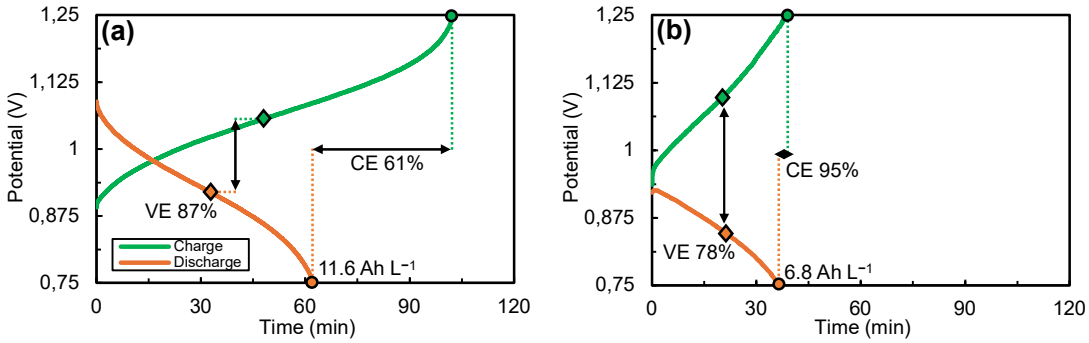

Figure 5.13: Cycle #1 charge and discharge curves illustrating VE, CE and discharge capacity of (a) SFS-OPBI 9:1 and (b) SFS-OPBI 8:2.

Accordingly, the amount of cross-linker was adjusted to prepare CEMs with blend ratios of 86:14 and 84:16 SFS-OPBI (Table 5.5 and Table B1). A summary of the efficiencies (CE, VE and EE), peak discharge capacities, imbalance and self-discharge for the four SFS-OPBI membranes (9:1, 86:14, 84:16 and 8:1) over 30 cycles is presented in **Figure 5.14**, illustrating the effect of increasing cross-linker on the selectivity and conductivity by changing the degree of molecular pore swelling and electrolyte absorption. The results from both the N-212 and the non-cross-linked SFS blend membrane (SFS-PVDF – Section 5.3.1.3) were included for comparison.

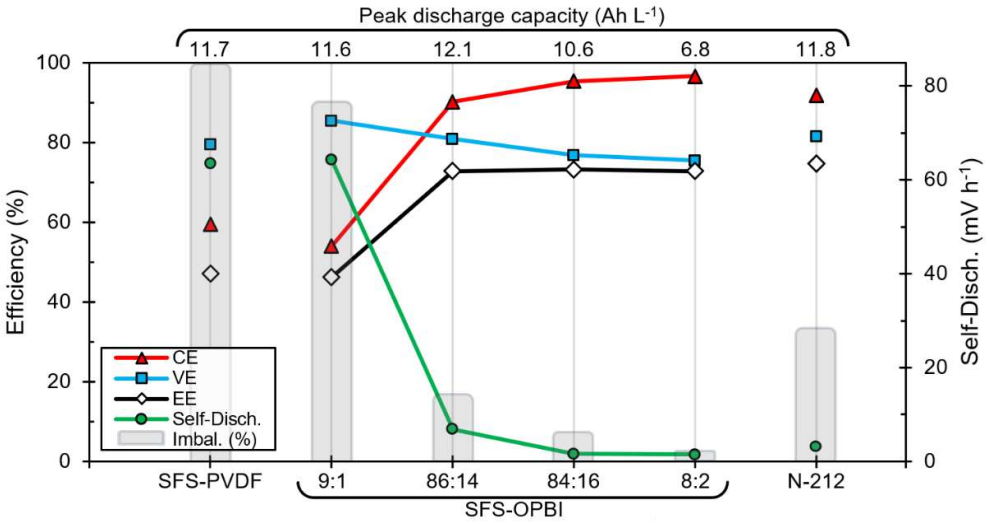

Figure 5.14: Peak discharge capacities, self-discharge rates, electrolyte imbalance and 30-cycle avg. efficiencies of various SFS-based membranes compared to N-212.

The transition from a non-cross-linked SFS-PVDF blend (Section 3.2.3) to an ionically cross-linked 9:1 SFS-OPBI blend slightly reduced electro-osmosis, but more of the OPBI cross-linker was required to effectively lower operational imbalance by reducing excessive swelling from the highly conductive SFS ionomer. The swelling, i.e., molecular pore size and cation conduction channels, was reduced by increasing the degree of cross-linking by increasing the OPBI content, which in turn increased the ionic selectivity, as supported by the decrease in WU% (Table 5.5), CE gains and reduced self-discharge rates (Figure 5.14). The optimal trade-off between selectivity and conductivity was obtained at a blend ratio of 84:16 SFS-OPBI, achieving the highest 30-cycle avg. EE of 73.2% of all CEM (Nafion alternatives) tested up to this point. While the highest CE (96.6%) was obtained by the 8:2 blend, the additional membrane resistance from too much positively charged imidazolium groups resulted in a significantly lower discharge capacity (6.8 Ah L^{-1}) compared to SFS-OPBI 84:16 (10.6 Ah L^{-1}) and N-212 (11.8 Ah L^{-1}). While the avg. EE of the 84:16 blend was slightly lower (1.6%) than the N-212 benchmark, the cation repulsion from the positively charged imidazolium groups resulted in an improved selectivity, obtaining a 3.5% higher CE and a lower self-discharge rate of 1.60 mV h^{-1} vs the 3.19 mV h^{-1} of N-212. Most importantly, narrower charge carrier conduction channels due to the cross-linking significantly reduced the electrolyte volume imbalance (4% of SFS-OPBI 84:16 vs 33% of N-212) after cycling (from supporting electrolyte crossover) by supressing electro-osmotic effects and water permeability.[23, 79, 80] All these properties contributed to SFS-OPBI 84:16 being more suitable for long-term operation in scaled-up systems than N-212.

All SFS-OPBI membranes exhibited excellent short-term chemical stability as no loss in IEC or tensile strength was measured after cycling (Table B1). **Figure B9** shows no staining or visible changes in SFS-OPBI 84:16 during ICFB cycling. However, the 3–8% increase in tensile strength for the four SFS-OPBI membranes and the operational increase in ASR, accompanied by thickness and weight decreases (up to ~5%) implied dimensional shrinking from water/swelling losses during cycling as had been observed with the SPEEK-95-OPBI (Section 5.3.2.1). Thickness measurements of the 84:16 blend after cycling revealed a decrease from 59.0 µm to 57.5 µm accompanied by a 4.5% weight loss (wetted). Shrinking was further implied by an operational increase in ASR (resulting in a 30-cycle avg. of 3.241 Ω cm^2). This effect was likely caused by the systematic and partial loss of the initial swelling gained from the pre-cycling procedure of protonation followed by extended 65 °C DI water washing (see Chapter 4 – Section 4.2.2.). It is possible that during cycling, anionic ferric complexes (such as $FeCl_4^-$) [81, 82] replaced coordinated water surrounding the anion exchange imidazolium sites, effectively reducing WU and swelling. This effect was also apparent in the 8:2 blend, since the discharge polarisation test before cycling displayed an ASR of only 2.137 Ω cm^2 that increased to a 30-cycle average of 3.443 Ω cm^2. The per-cycle average and normalised hourly capacity decay of cross-linked membranes were increased by this effect, as increasing the resistance shortened cycling times when using a constant current cycling with cut off-potentials of 0.75 V and 1.25 V.

5.3.2.3 Ionically & covalently cross-linked SFS-OPBI

Using ionically cross-linked CEMs of SFS with OPBI produced comparable performances to the benchmark N-212, while lowering electro-osmotic crossover. However, the dimensional changes observed between pre- and post-cycling in the heated (65 °C) electrolyte, did result in a reduced capacity retention. While a higher degree of cross-linking could reduce this effect, increasing the OPBI content seems to worsen conductivity, lowering the VE by polarising the membrane and consuming ion-exchange sites by the cross-linking, lowering the IEC.

The observed dimensional swelling and shrinking of SFS-based membranes can be further reduced by also covalently cross-linking the SFS, for example using 3,6-dioxa-1,8-octanedithiol in conjunction with a strong base, which induces fast click-like reactions.[30] To determine the effect of additional covalent cross-linking, three ionically cross-linked SFS-OBI membranes with varying thicknesses were also covalently cross-linked using [1,1'-biphenyl]-4,4'-dithiol (see **Figure 5.15**), which is a highly aromatic cross-linker with no ether groups, resulting in an increased oxidative stability.[83, 84] Due to the additional interconnectivity of the polymer and swelling inhibition, four percent more SFS ionomer was added (SFS:OPBI = 88:10) compared to the previously optimised blend (Section 5.3.2.2).

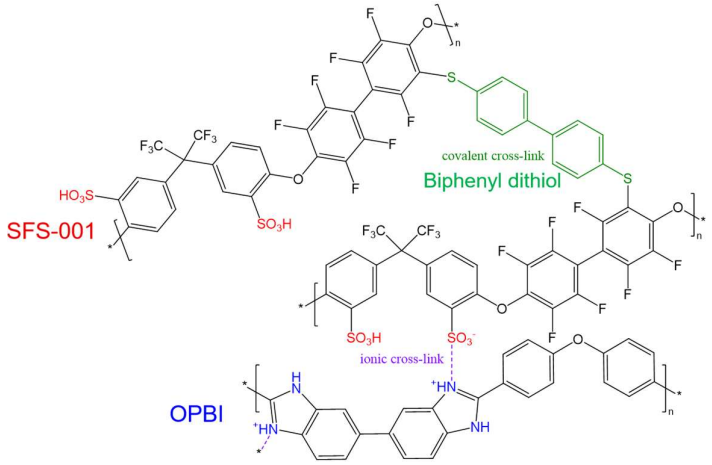

Figure 5.15: Ionic and covalent cross-linking of SFS-OPBI blends.

Initially two membranes with different membrane thicknesses (SA-210a = 26 µm and SA-210b = 50 µm) were prepared and tested in the ICFB (30 cycles). **Figure B10** confirms that no observable colour changes in the active area of the membranes had occurred during cycling. **Figure 5.16** (a, b) shows the ICFB performance (efficiencies and discharge capacity) of both membranes over 30 cycles. When using the thin SA-210a variant (Figure 5.16 (a)), the discharge capacity of the electrolyte rapidly decayed reaching half of its initial capacity at a plateau after only 12 cycles. The 50% decay despite a > 90% electrolyte imbalance after 12 cycles implied that mostly the supporting electrolyte, through osmotic drag, had migrated between catholyte and anolyte, thereby significantly changing the active metal salt concentrations.

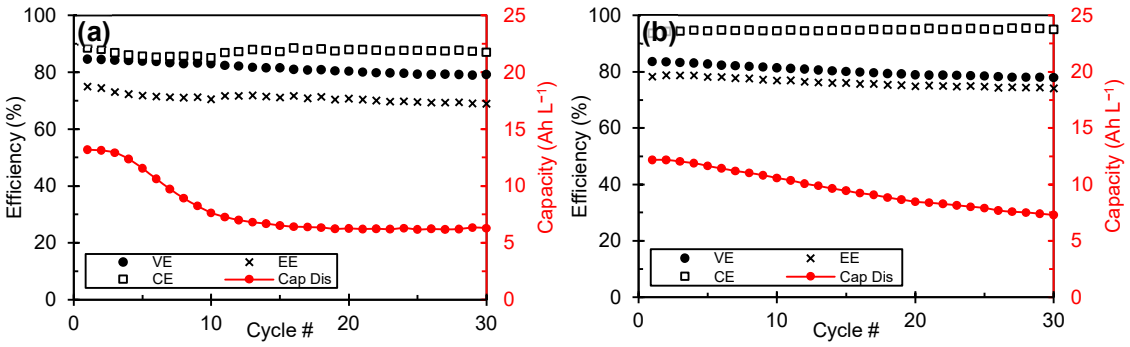

Figure 5.16: 30-Cycle performance parameters for (a) SA-210a and (b) SA-210b.

Using a thicker SA-210b variant (Figure 5.16 (b)) resulted in a reduction of i) the capacity decay, normalised for time, from 1.15% h^{-1} to 0.70% h^{-1}, ii) the electrolyte imbalance from ~100% to ~1%, and iii) the self-discharge rate from 9.73 mV to 2.44 mV h^{-1}. Together with the increased discharge capacity of 12.2 Ah L^{-1} vs 11.8 Ah L^{-1} (see Table B1 and **Figure 5.17**), these values were all improvements on the N-212 benchmark, with the exception of the capacity decay. The increased separation

efficiency, resulting in a CE of 94.8%, together with the higher discharge voltage, contributed to a 1.4% higher 30-cycle avg. EE than the N-212.

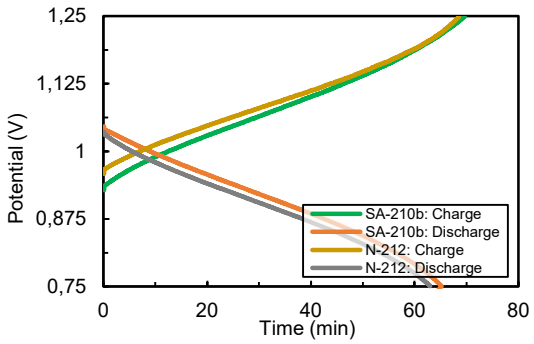

Figure 5.17: Cycle #1 charge and discharge curves of ionically & covalently cross-linked SFS-OPBI (SA-210b) compared to N-212.

In comparison to the ionically cross-linked SFS-OPBI (Section 5.3.2.2), it was clear that the additional covalent cross-linking reduced the contraction of the membrane polymer lattice and the operationally increasing ASR that both decrease VE during cycling. For example, the ASR measured between the discharge polarisation curves before cycling and the 30-cycle average ASR for SFS-OPBI 84:16 was 1.60–3.24 Ω cm² (Section 5.3.2.2) vs 2.04–2.72 Ω cm² for the covalently cross-linked SA-210b. The additional covalent cross-linking also reduced the contraction during cycling in terms of a decrease in thickness (SFS-OPBI 84:16 = 2.5% vs SA-210b = 1.5%) and weight (from 4.9% to 2.7%). The ASR, however, still increased during cycling, which was likely also influenced by other contributing factors (which were not measured) such as an Fe(II)/Fe(III) and Cr(II)/Cr(III) imbalance caused by H_2 side-reactions, oxygen intrusion and ageing electrolyte reducing the kinetics of the Cr couple in HCl when using electrolyte without substituting ligand additives.[8, 85-89]

To determine whether the EE could be further optimised by increasing the conductivity, a CEM with the same composition, but slightly thinner (46 µm) than SA-210b was prepared and tested. A slight improvement was attained with SA-262a-1100 (see Table B1). The slight (8%) thickness reduction lowered the path length of charge carriers, resulting in an increased VE (84.4%), which marginally increased the EE from 76.2% to 77.5%. However, this increased VE was accompanied by an anticipated increase in self-discharge rate (3.36 mV h^{-1}) and a notably higher electrolyte volume imbalance (28%). Hence, when considering a low-maintenance long-term operation, the 50 µm membrane (SA-210b) provided the best trade-off for this series of ionically and covalently cross-linked membranes tested.

Due to the high efficiencies and excellent selectivity of SA-210b, a longer cycling test was done. During the initial cycles of the long-term cycling, the effect of varying current densities (20 mA cm^{-2}, 40 mA cm^{-2} and 60 mA cm^{-2}) on the performance where investigated (see **Figure 5.18**). Reusing the same membrane from Figure 5.16 (a),

stable cycling was achieved without any signs of brittleness or fouling after an additional 113 cycles. However, long-term cycling was constrained by the discharge capacity, ASR and voltage efficiency that quickly worsened, resulting in an EE of 69.0% at Cycle 105, without a rebalancing cell to regenerate accumulated Fe^{3+} in the catholyte.[86, 88]. Increasing the current density had a significant increase in the charge-transfer resistance, resulting in EEs of 82.5%, 75.5% and 66.9% for 20 mA cm^{-2}, 40 mA cm^{-2} and 60 mA cm^{-2}, respectively, with an increasing CE of 93.2%, 95.8% and 97.2%, respectively. While an increased CE for both CEMs and AEMs is characteristic of an increasing current density in VFBs, the membrane-related capacity decay is clouded by the Fe^{3+} buildup during cycling.[40, 90, 91] While OPBI polarisation could play a role in the increasing ASR, these performance reductions were not due to membrane degradation, as confirmed by reverting all efficiencies and discharge capacity to their initial values by rinsing the membrane in 0.25 M HCl and exchanging the electrolyte in the system at Cycle 106 (see Figure 5.18). The prolonged cycling did not show (see **Figure B11**) or measure any change in electrolyte levels, showing that this ionically and covalently cross-linked CEM was effective at mitigating electro-osmosis.

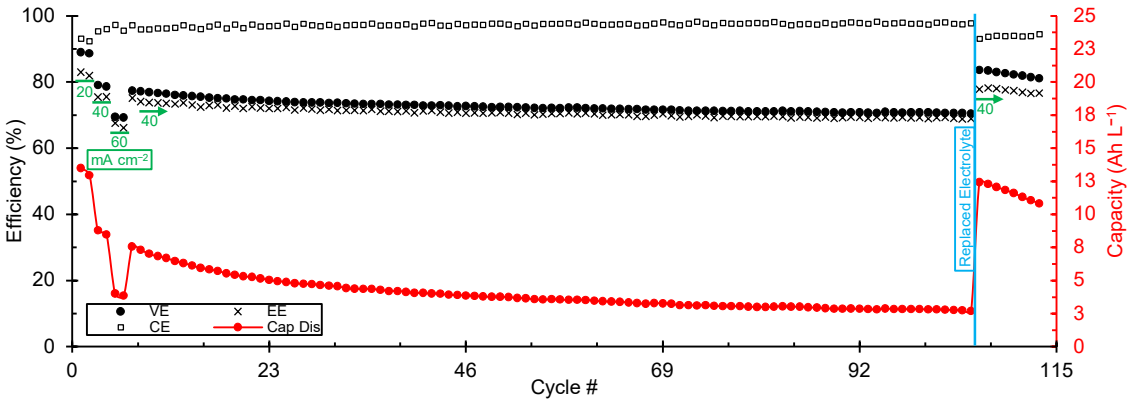

Figure 5.18: Performance parameters for SA-210b at 20, 40 and 60 mA cm^{-2} over 113 cycles, including electrolyte replacement after Cycle 105.

To further confirm the chemical stability of this membrane, a piece of fresh and the multiply cycled (totalling 176 cycles) SA-210b were analysed with SEM-EDX after washing in 1 M HCl at 65 °C for 24 h. **Figure 5.19** (a, b) shows the surface (100 µm scale) of both pieces with an overlay of elemental mapping, with no notable morphology changes apart from surface cracking of the cycled sample that likely occurred from the drying before SEM analysis. Interestingly, S analysis showed inhomogeneity in $–SO_3H$ clusters as large as 5.1 µm in diameter on the surface, while the benzyl and alkyl F was evenly distributed. Comparing the C to S ratios of both samples showed that no notable loss of cation exchange groups occurred after multiple ICFB testing. No Fe or Cr was registered, unlike the membranes analysed that contained $–PO_3H_2$ groups (see Section 5.3.1.3), which again confirms the

complexing observed for $–PO_3H_2$-containing membranes. Additionally, given the previously mentioned possibility of ferric anions bonding to OPBI during cycling (see Section 5.3.2.2), the lack of Fe in Figure 5.19 (b) implies that any iron-based anions would have had weak enough ionic interactions with OPBI to be removed by acid washing.

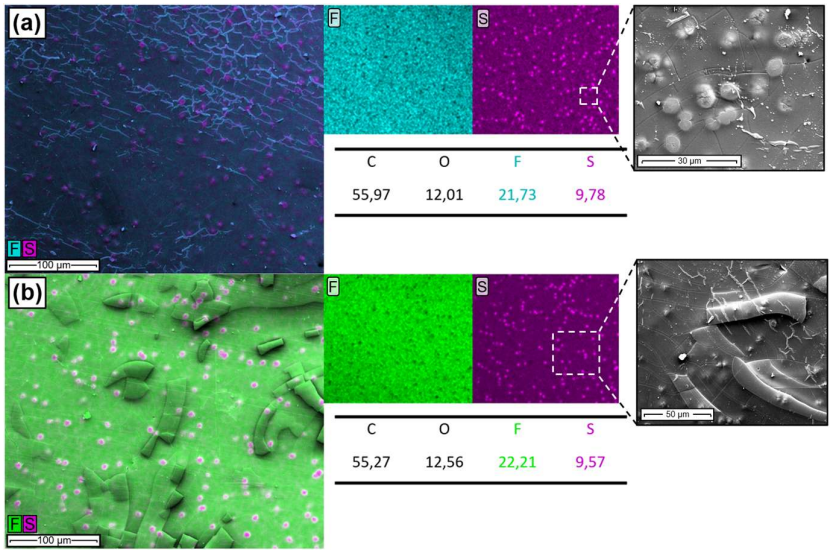

Figure 5.19: Surface SEM imaging and EDX elemental mapping of the SA-210b blend membrane (a) pristine and (b) after cycling in the ICFB.

5.4 Conclusion

Initially, a range of existing and novel blended and nanofibre-reinforced composite membranes were benchmarked against N-212 in terms of stability and ICFB performance. Only the sulfonic acid functional group-based membranes yielded satisfactory stability with maintained VEs in the ICFB, where the best performing ionomer (SFS) yielded VEs of 79.4% when blended with PVDF and 83.9% when used as a nanofibre mat with Nafion. In contrast, the phosphonic acid functional group-containing CEMs were chemically incompatible due to brittleness and the deactivation of the ion-exchange sites by irreversible covalent cross-linking with Fe/Cr. The Nafion- and piperidine/piperidinium-containing fibre mat PPFS-Pip-D showed the lowest electro-osmosis rates when compared to N-212, lowering the electrolyte imbalance levels to 2% and self-discharge rates to 2.038 mV h^{-1}, which came at the cost of its conductivity, lowering the EE from 74.8% to 68.2%.

Based on the screening results, sulfonated ionomers were further developed focussing on two acid-excess (SPEEK and SFS) membranes cross-linked with OPBI as acid-base cross-linked membranes are known for their enhanced stability and modifiable selectivity vs conductivity. Highly sulfonated and ionically cross-linked SPEEK-95-OPBI membranes yielded an optimal WU and highest performance at a blend ratio of

89:11 (55 μm) with a 1.1% higher EE than SPEEK-57 and 3.3% lower EE than N-212 at substantially reduced electrolyte imbalance levels (4% vs 50% of SPEEK-57 and 33% of N-212). The best ionically cross-linked SFS-OPBI membrane (59 μm) with a blend ratio of 84:16 yielded an increased CE (95.3% vs 91.8%) and reduced electrolyte imbalance (4%) and self-discharge rate (1.60 mV h^{-1} vs the 3.19 mV h^{-1}) compared to N-212. The ionically and covalently cross-linked SFS OPBI blend SA-210b displayed the least electro-osmosis (electrolyte imbalance = 1%), with an IEC of 1.54 mmol g^{-1}, outperforming the benchmark N-212 and ionically cross-linked CEMs with an EE of 76.2%. This study has clearly demonstrated that cost-effective aromatic backbone-based membranes can be optimised to overcome the selectivity and operational electrolyte imbalance challenges faced by the benchmark N-212 in an ICFB.

References

[1] S. Ahmad, T. Nawaz, A. Ali, M.F. Orhan, A. Samreen, A.M. Kannan, An overview of proton exchange membranes for fuel cells: Materials and manufacturing, International Journal of Hydrogen Energy, 47 (2022) 19086-19131. https://doi.org/10.1016/j.ijhydene.2022.04.099.

[2] N. Esmaeili, E.M. Gray, C.J. Webb, Non-Fluorinated Polymer Composite Proton Exchange Membranes for Fuel Cell Applications – A Review, ChemPhysChem, 20 (2019) 2016-2053. https://doi.org/10.1002/cphc.201900191.

[3] B.G. Thiam, S. Vaudreuil, Review—Recent Membranes for Vanadium Redox Flow Batteries, Journal of The Electrochemical Society, 168 (2021) 070553. 10.1149/1945-7111/ac163c.

[4] T.T.K. Huynh, T. Yang, P.S. Nayanthara, Y. Yang, J. Ye, H. Wang, Construction of High-Performance Membranes for Vanadium Redox Flow Batteries: Challenges, Development, and Perspectives, Nano-Micro Letters, 17 (2025) 260. 10.1007/s40820-025-01736-x.

[5] Y.K. Zeng, T.S. Zhao, L. An, X.L. Zhou, L. Wei, A comparative study of all-vanadium and iron-chromium redox flow batteries for large-scale energy storage, Journal of Power Sources, 300 (2015) 438-443. https://doi.org/10.1016/j.jpowsour.2015.09.100.

[6] B. Li, J. Liu, Progress and directions in low-cost redox-flow batteries for large-scale energy storage, National Science Review, 4 (2017) 91-105. 10.1093/nsr/nww098.

[7] L. Qiao, S. Liu, M. Fang, M. Yang, X. Ma, A Composite Membrane with High Stability and Low Cost Specifically for Iron–Chromium Flow Battery, Journal, 14 (2022). 10.3390/polym14112245.

[8] C. Sun, H. Zhang, Review of the Development of First-Generation Redox Flow Batteries: Iron-Chromium System, ChemSusChem, 15 (2021) 15. 10.1002/cssc.202101798.

[9] D. Düerkop, H. Widdecke, C. Schilde, U. Kunz, A. Schmiemann, Polymer membranes for all-vanadium redox flow batteries: a review, Membranes, 11 (2021) 214.

[10] Y. Zhou, L. Yu, J. Wang, L. Liu, F. Liang, J. Xi, Rational use and reuse of Nafion 212 membrane in vanadium flow batteries, RSC Advances, 7 (2017) 19425-19433. 10.1039/C7RA00294G.

[11] N. Mans, D.J. van der Westhuizen, H.M. Krieg, Membrane Screening for Iron–Chrome Redox Flow Batteries, Advanced Energy and Sustainability Research, 5 (2024) 2300195. https://doi.org/10.1002/aesr.202300195.

[12] S. Ebner, S. Spirk, T. Stern, C. Mair-Bauernfeind, How Green are Redox Flow Batteries?, ChemSusChem, 16 (2023) e202201818. https://doi.org/10.1002/cssc.202201818.

[13] S. Maurya, S.-H. Shin, Y. Kim, S.-H. Moon, A review on recent developments of anion exchange membranes for fuel cells and redox flow batteries, RSC Advances, 5 (2015) 37206-37230. 10.1039/C5RA04741B.

[14] H. Cho, H.M. Krieg, J.A. Kerres, Application of Novel Anion-Exchange Blend Membranes (AEBMs) to Vanadium Redox Flow Batteries, Journal, 8 (2018). 10.3390/membranes8020033.

[15] R.S. Raja Rafidah, W. Rashmi, M. Khalid, W.Y. Wong, J. Priyanka, Recent Progress in the Development of Aromatic Polymer-Based Proton Exchange Membranes for Fuel Cell Applications, Polymers, 12 (2020) 1061.

[16] Y. Yang, Q. Wang, S. Xiong, Z. Song, Research progress on optimized membranes for vanadium redox flow batteries, Inorganic Chemistry Frontiers, 11 (2024) 4049-4079. 10.1039/D4QI00520A.

[17] E. Bai, H. Zhu, C. Sun, G. Liu, X. Xie, C. Xu, S. Wu, A Comparative Study of Nafion 212 and Sulfonated Poly(Ether Ether Ketone) Membranes with Different Degrees of Sulfonation on the Performance of Iron-Chromium Redox Flow Battery, Journal, 13 (2023). 10.3390/membranes13100820.

[18] Y. Wang, K. Geng, Q. Tan, T. Guo, X. Hu, H. Tang, L. Liu, N. Li, Highly Ion Selective Proton Exchange Membrane Based on Sulfonated Polybenzimidazoles for Iron–Chromium Redox Flow Battery, ACS Applied Energy Materials, 5 (2022) 15918-15927. 10.1021/acsaem.2c03471.

[19] Stability of Conjugated Dienes- Molecular Orbital Theory.

[20] C. Sun, Z. Huan, X.-D. Luo, N. Chen, A comparative study of Nafion and sulfonated poly(ether ether ketone) membrane performance for iron-chromium redox flow battery, Ionics, 25 (2019). 10.1007/s11581-019-02971-0.

[21] A. Chromik, A.R. dos Santos, T. Turek, U. Kunz, T. Häring, J. Kerres, Stability of acid-excess acid–base blend membranes in all-vanadium redox-flow batteries, Journal of Membrane Science, 476 (2015) 148-155. https://doi.org/10.1016/j.memsci.2014.11.036.

[22] Q. Dai, Z. Liu, L. Huang, C. Wang, Y. Zhao, Q. Fu, A. Zheng, H. Zhang, X. Li, Thin-film composite membrane breaking the trade-off between conductivity and selectivity for a flow battery, Nature Communications, 11 (2020) 13. 10.1038/s41467-019-13704-2.

[23] J. Molina, J.J. de Pablo, J.P. Hernández-Ortiz, Structure and proton conduction in sulfonated poly(ether ether ketone) semi-permeable membranes: a multi-scale computational approach, Physical Chemistry Chemical Physics, 21 (2019) 9362-9375. 10.1039/C9CP00598F.
[24] D. Chen, M.A. Hickner, E. Agar, E.C. Kumbur, Optimizing membrane thickness for vanadium redox flow batteries, Journal of Membrane Science, 437 (2013) 108-113. https://doi.org/10.1016/j.memsci.2013.02.007.
[25] T. Mu, W. Tang, Y. Jin, X. Che, J. Liu, J. Yang, Ether-Free Poly(p-terphenyl-co-acetylpyridine) Membranes with Different Thicknesses for Vanadium Redox Flow Batteries, ACS Applied Energy Materials, 5 (2022) 11713-11722. 10.1021/acsaem.2c02216.
[26] L. Ding, X. Song, L. Wang, Z. Zhao, G. He, Preparation of dense polybenzimidazole proton exchange membranes with different basicity and flexibility for vanadium redox flow battery applications, Electrochimica Acta, 292 (2018) 10-19. https://doi.org/10.1016/j.electacta.2018.08.128.
[27] S. He, S. Zhai, C. Zhang, Y. Xue, W. Yang, J. Lin, Effect of Sulfonation Degree and PVDF Content on the Structure and Transport Properties of SPEEK/PVDF Blend Membranes, Journal, 11 (2019). 10.3390/polym11040676.
[28] D. Chen, X. Chen, L. Ding, X. Li, Advanced acid-base blend ion exchange membranes with high performance for vanadium flow battery application, Journal of Membrane Science, 553 (2018) 25-31. https://doi.org/10.1016/j.memsci.2018.02.039.
[29] Y. Zheng, W. Xu, Y. Wu, J. Ding, H. Yu, X. You, Y. Wang, Z. Xu, A cross-linked sulfonated polyimide membrane with regulated acid-base interaction and high-performance for vanadium redox flow battery, Journal of Membrane Science, 718 (2025) 123651. https://doi.org/10.1016/j.memsci.2024.123651.
[30] S. Auffarth, W. Dafinger, J. Mehler, V. Ardizzon, P. Preuster, P. Wasserscheid, S. Thiele, J. Kerres, Cross-linked proton-exchange membranes with strongly reduced fuel crossover and increased chemical stability for direct-isopropanol fuel cells, Journal of Materials Chemistry A, 10 (2022) 17208-17216. 10.1039/D2TA03832C.
[31] A. Katzfuß, K. Krajinovic, A. Chromik, J. Kerres, Partially fluorinated sulfonated poly(arylene sulfone)s blended with polybenzimidazole, J. Polym. Sci., Part A: Polym. Chem., 49 (2011) 1919-1927. https://doi.org/10.1002/pola.24624.
[32] M.S. Mu'min, A. Krieger, M. Wagner, S. Thiele, J. Kerres, High-Throughput Electrospinning of Unmodified and Aminated Poly(Pentafluorostyrene) for Fiber-Reinforced Proton Exchange Membranes, Macromolecular Materials and Engineering, 310 (2025) 2400078. https://doi.org/10.1002/mame.202400078.
[33] E. Bülbül, V. Atanasov, M. Mehlhorn, M. Bürger, A. Chromik, T. Häring, J. Kerres, Highly phosphonated polypentafluorostyrene blended with polybenzimidazole: Application in vanadium redox flow battery, Journal of Membrane Science, 570-571 (2019) 194-203. https://doi.org/10.1016/j.memsci.2018.10.027.
[34] V. Atanasov, A.S. Lee, E.J. Park, S. Maurya, E.D. Baca, C. Fujimoto, M. Hibbs, I. Matanovic, J. Kerres, Y.S. Kim, Synergistically integrated phosphonated poly(pentafluorostyrene) for fuel cells, Nature Materials, 20 (2021) 370-377. 10.1038/s41563-020-00841-z.
[35] F. Mack, V. Gogel, L. Jörissen, J. Kerres, High performance anode based on a partially fluorinated sulfonated polyether for direct methanol fuel cells operating at 130 °C, Journal of Power Sources, 255 (2014) 223-229. https://doi.org/10.1016/j.jpowsour.2014.01.029.
[36] T. Stigler, M. Wagner, S. Thiele, J. Kerres, Modification of Phosphonated Poly(pentafluorostyrene) toward Ductile Membranes for Electrochemical Applications, Macromolecules, 57 (2024) 364-372. 10.1021/acs.macromol.3c01193.
[37] C.A. Machado, G.O. Brown, R. Yang, T.E. Hopkins, J.G. Pribyl, T.H. Epps, III, Redox Flow Battery Membranes: Improving Battery Performance by Leveraging Structure–Property Relationships, ACS Energy Letters, 6 (2021) 158-176. 10.1021/acsenergylett.0c02205.
[38] P. Knauth, M.L. Di Vona, Sulfonated aromatic ionomers: Analysis of proton conductivity and proton mobility, Solid State Ionics, 225 (2012) 255-259. https://doi.org/10.1016/j.ssi.2012.01.043.
[39] M. Jung, W. Lee, N. Nambi Krishnan, S. Kim, G. Gupta, L. Komsiyska, C. Harms, Y. Kwon, D. Henkensmeier, Porous-Nafion/PBI composite membranes and Nafion/PBI blend membranes for vanadium redox flow batteries, Appl. Surf. Sci., 450 (2018) 301-311. https://doi.org/10.1016/j.apsusc.2018.04.198.
[40] H. Cho, V. Atanasov, H.M. Krieg, J.A. Kerres, Novel Anion Exchange Membrane Based on Poly(Pentafluorostyrene) Substituted with Mercaptotetrazole Pendant Groups and Its Blend with Polybenzimidazole for Vanadium Redox Flow Battery Applications, Journal, 12 (2020). 10.3390/polym12040915.

[41] H.-L. Wu, C.-C.M. Ma, C.-H. Li, C.-Y. Chen, Swelling behavior and solubility parameter of sulfonated poly(ether ether ketone), Journal of Polymer Science Part B: Polymer Physics, 44 (2006) 3128-3134. https://doi.org/10.1002/polb.20964.
[42] M. Eikerling, Y. Kornyshev, A.M. Kuznetsov, J. Ulstrup, S. Walbran, Mechanisms of Proton Conductance in Polymer Electrolyte Membranes, Journal of Physical Chemistry B, 105 (2001). 10.1021/jp003182s.
[43] N. Mans, H.M. Krieg, D.J. van der Westhuizen, The Effect of Electrolyte Composition on the Performance of a Single-Cell Iron–Chromium Flow Battery, Advanced Energy and Sustainability Research, 5 (2024) 2300238. https://doi.org/10.1002/aesr.202300238.
[44] Y.K. Zeng, T.S. Zhao, X.L. Zhou, L. Zeng, L. Wei, The effects of design parameters on the charge-discharge performance of iron-chromium redox flow batteries, Applied Energy, 182 (2016) 204-209. https://doi.org/10.1016/j.apenergy.2016.08.135.
[45] J.A. Kerres, Development of ionomer membranes for fuel cells, Journal of Membrane Science, 185 (2001) 3-27. https://doi.org/10.1016/S0376-7388(00)00631-1.
[46] M.S. Mu'min, M. Komma, D. Abbas, M. Wagner, A. Krieger, S. Thiele, T. Böhm, J. Kerres, Electrospun phosphonated poly(pentafluorostyrene) nanofibers as a reinforcement of Nafion membranes for fuel cell application, Journal of Membrane Science, 685 (2023) 121915. https://doi.org/10.1016/j.memsci.2023.121915.
[47] H. Cho, A. Krastel, F. Arslan, T. Morawietz, J. Bender, J. Kerres, V. Atanasov, Novel guanidinium functionalized poly(pentafluorostyrene): Synthesis and application as ion-pair membrane in PA doped HT-PEMFC, Journal of Membrane Science, 717 (2025) 123560. https://doi.org/10.1016/j.memsci.2024.123560.
[48] R.Y.M. Huang, P. Shao, C.M. Burns, X. Feng, Sulfonation of poly(ether ether ketone)(PEEK): Kinetic study and characterization, Journal of Applied Polymer Science, 82 (2001) 2651-2660. https://doi.org/10.1002/app.2118.
[49] S.N.S.S. Daud, M.N.A.M. Norddin, J. Jaafar, R. Sudirman, M.H.D. Othman, A.F. Ismail, Highly Sulfonated Poly(Ether Ether Ketone) Blend with Hydrophobic Polyether Sulfone as an Alternative Electrolyte for Proton Exchange Membrane Fuel Cell, Arabian Journal for Science and Engineering, 46 (2021) 6189-6205. 10.1007/s13369-020-04898-5.
[50] S. Zaidi, S.D. Mikhailenko, G. Robertson, M. Guiver, S. Kaliaguine, Proton conducting composite membranes from polyether ether ketone and heteropolyacids for fuel cell applications, Journal of Membrane Science, 173 (2000) 17-34.
[51] D. Hughes, B.R. Clark, C.D. Murphy, Biodegradation of polyfluorinated biphenyl in bacteria, Biodegradation, 22 (2011) 741-749. 10.1007/s10532-010-9411-7.
[52] C. Vargas, B. Song, M. Camps, M.M. Häggblom, Anaerobic degradation of fluorinated aromatic compounds, Appl. Microbiol. Biotechnol., 53 (2000) 342-347. 10.1007/s002530050032.
[53] H. Brunn, G. Arnold, W. Körner, G. Rippen, K.G. Steinhäuser, I. Valentin, PFAS: forever chemicals—persistent, bioaccumulative and mobile. Reviewing the status and the need for their phase out and remediation of contaminated sites, Environmental Sciences Europe, 35 (2023) 20. 10.1186/s12302-023-00721-8.
[54] V. Atanasov, J. Kerres, Highly phosphonated polypentafluorostyrene, Macromolecules, 44 (2011) 6416-6423.
[55] G. Sych, J. Simokaitiene, R. Lygaitis, E. Jatautiene, R. Pashazadeh, G. Buika, J.V. Grazulevicius, Structure-properties relationship of tetrafluorostyrene-based monomers and polymers containing different donor moieties, React. Funct. Polym., 143 (2019) 104323.
[56] J. Chen, L. Dumas, J. Duchet-Rumeau, E. Fleury, A. Charlot, D. Portinha, Tuning h-bond capability of hydroxylated-poly (2, 3, 4, 5, 6-pentafluorostyrene) grafted copolymers prepared by chemoselective and versatile thiol-para-fluoro “click-type” coupling with mercaptoalcohols, J. Polym. Sci., Part A: Polym. Chem., 50 (2012) 3452-3460.
[57] J.-M. Noy, Y. Li, W. Smolan, P.J. Roth, Azide–para-Fluoro Substitution on Polymers: Multipurpose Precursors for Efficient Sequential Postpolymerization Modification, Macromolecules, 52 (2019) 3083-3091.
[58] L.P. Wackett, Strategies for the Biodegradation of Polyfluorinated Compounds, Microorganisms, 10 (2022) 1664.
[59] L. Wang, Y. Zhang, N. Sun, W. Sun, Y. Hu, H. Tang, Precipitation Methods Using Calcium-Containing Ores for Fluoride Removal in Wastewater, Minerals, 9 (2019) 511.
[60] V. Atanasov, M. Bürger, S. Lyonnard, L. Porcar, J. Kerres, Sulfonated poly(pentafluorostyrene): Synthesis & characterization, Solid State Ionics, 252 (2013) 75-83. https://doi.org/10.1016/j.ssi.2013.06.010.

[61] J.A. Kerres, A. Katzfuß, A. Chromik, Sulfonated Low-Cost Ionomers as Acidic Cross-Linkers for High-Temperature PBIOO Membranes, ECS Transactions, 33 (2010) 797. 10.1149/1.3484574.
[62] B. Maria Mahimai, G. Sivasubramanian, K. Sekar, D. Kannaiyan, P. Deivanayagam, Sulfonated poly(ether ether ketone): efficient ion-exchange polymer electrolytes for fuel cell applications–a versatile review, Materials Advances, 3 (2022) 6085-6095. 10.1039/D2MA00562J.
[63] Z. Mai, H. Zhang, X. Li, S. Xiao, H. Zhang, Nafion/polyvinylidene fluoride blend membranes with improved ion selectivity for vanadium redox flow battery application, Journal of Power Sources, 196 (2011) 5737-5741.
[64] R. Devanathan, Recent developments in proton exchange membranes for fuel cells, Energy & Environmental Science, 1 (2008) 101-119. 10.1039/B808149M.
[65] J. Kerres, W. Zhang, W. Cui, New sulfonated engineering polymers via the metalation route. II. Sulfinated/sulfonated poly(ether sulfone) PSU Udel and its crosslinking, J. Polym. Sci., Part A: Polym. Chem., 36 (1998) 1441-1448. https://doi.org/10.1002/(SICI)1099-0518(19980715)36:9<1441::AID-POLA12>3.0.CO;2-4.
[66] Y. Zhang, L. Zheng, B. Liu, H. Wang, H. Shi, Sulfonated polysulfone proton exchange membrane influenced by a varied sulfonation degree for vanadium redox flow battery, Journal of Membrane Science, 584 (2019) 173-180. https://doi.org/10.1016/j.memsci.2019.04.073.
[67] Chromium(III) phosphate, 2024/12, © 2023 ChemicalBook https://www.chemicalbook.com/ChemicalProductProperty_EN_CB0406705.htm (accessed: 2025/09).
[68] S. Auffarth, M. Maier, P. Martschin, T. Stigler, M. Wagner, T. Böhm, A. Hutzler, S. Thiele, J. Kerres, Nanostructured proton-exchange membranes from self-cross-linking perfluoroalkyl-free block-co-polymers, Materials Today Advances, 23 (2024) 100521. https://doi.org/10.1016/j.mtadv.2024.100521.
[69] R. Souzy, B. Ameduri, Functional fluoropolymers for fuel cell membranes, Prog. Polym. Sci., 30 (2005) 644-687. https://doi.org/10.1016/j.progpolymsci.2005.03.004.
[70] Z. Huang, S.M. Oh, K.I. Winey, M.A. Hickner, Water Dynamics of Superacid Aromatic Proton Exchange Membranes for Fuel Cell Applications, Macromolecules, 58 (2025) 2630-2639. 10.1021/acs.macromol.4c02925.
[71] J. Xi, B. Jiang, L. Yu, L. Liu, Membrane evaluation for vanadium flow batteries in a temperature range of −20–50°C, Journal of Membrane Science, 522 (2017) 45-55. https://doi.org/10.1016/j.memsci.2016.09.012.
[72] I. Salmeron-Sanchez, P. Mansouri Bakvand, A. Shirole, J. Ramón Avilés-Moreno, P. Ocón, P. Jannasch, R. Wreland Lindström, A. Khataee, Zwitterionic poly(terphenylene piperidinium) membranes for vanadium redox flow batteries, Chem. Eng. J., 474 (2023) 145879. https://doi.org/10.1016/j.cej.2023.145879.
[73] N.H. Hagedorn, NASA Redox Storage System Development Project. Final Report, (1984).
[74] S.N. Oreiro, A. Bentien, J. Sloth, M. Rahimi, M.B. Madsen, T. Drechsler, Crossover analysis in a commercial 6 kW/43kAh vanadium redox flow battery utilizing anion exchange membrane, Chem. Eng. J., 490 (2024) 151947. https://doi.org/10.1016/j.cej.2024.151947.
[75] A. Bhattarai, P.C. Ghimire, A. Whitehead, R. Schweiss, G.G. Scherer, N. Wai, H.H. Hng, Novel Approaches for Solving the Capacity Fade Problem during Operation of a Vanadium Redox Flow Battery, Batteries, 4 (2018). 10.3390/batteries4040048.
[76] T. Sukkar, M. Skyllas-Kazacos, Water transfer behaviour across cation exchange membranes in the vanadium redox battery, Journal of Membrane Science, 222 (2003) 235-247. https://doi.org/10.1016/S0376-7388(03)00309-0.
[77] H. Opperman, J. Kerres, H. Krieg, SO2 crossover flux of Nafion® and sFS-PBI membranes using a chronocoulometric (CC) monitoring technique, Journal of Membrane Science, 415-416 (2012) 842-849. https://doi.org/10.1016/j.memsci.2012.06.002.
[78] R. Peach, H.M. Krieg, A.J. Krüger, D. Bessarabov, J. Kerres, Novel cross-linked PBI-blended membranes evaluated for high temperature fuel cell application and SO2 electrolysis, Materials Today: Proceedings, 5 (2018) 10524-10532. https://doi.org/10.1016/j.matpr.2017.12.384.
[79] S. Sreenath, N. P S, M. Krebsz, J. Andrews, R.K. Nagarale, Ion Exchange Membranes: Latest Developments toward High-Performance Vanadium Redox Flow Batteries, ACS Applied Energy Materials, 7 (2024) 10846-10876. 10.1021/acsaem.4c01714.
[80] P. Qian, H. Wang, L. Zhang, Y. Zhou, H. Shi, An enhanced stability and efficiency of SPEEK-based composite membrane influenced by amphoteric side-chain polymer for vanadium redox flow battery, Journal of Membrane Science, 643 (2022) 120011. https://doi.org/10.1016/j.memsci.2021.120011.

[81] J.S. Ling, J. Charleston, Advances in Membrane Technology for the NASA Redox Energy Storage System, (1980).
[82] R. Assink, Fouling mechanism of separator membranes for the iron/chromium redox battery, Journal of membrane science, 17 (1984) 205-217.
[83] F. Xu, Y. Li, J. Ding, B. Lin, Current Challenges on the Alkaline Stability of Anion Exchange Membranes for Fuel Cells, ChemElectroChem, 10 (2023) e202300445. https://doi.org/10.1002/celc.202300445.
[84] S. Zhang, X. Zhu, C. Jin, Development of a high-performance anion exchange membrane using poly(isatin biphenylene) with flexible heterocyclic quaternary ammonium cations for alkaline fuel cells, Journal of Materials Chemistry A, 7 (2019) 6883-6893. 10.1039/C8TA11291F.
[85] Y. Ye, M. Wu, M. Nan, M. Fang, M. Yang, L. Qiao, X. Ma, The Influence of Inorganic Salt Additives in the Electrolyte on Iron–Chromium Flow Batteries at Room Temperature, ACS Applied Energy Materials, 7 (2024) 4200-4206. 10.1021/acsaem.4c00542.
[86] T. Herbert, N. Mans, D.J. van der Westhuizen, H.M. Krieg, Investigation of ICRFB hybrid rebalancing systems, Journal of Power Sources, 594 (2024) 234029. https://doi.org/10.1016/j.jpowsour.2023.234029.
[87] J.P. du Toit, H. Krieg, N. Mans, D.J. van der Westhuizen, Purification and analysis of ferrous chloride for an Fe/Cr flow battery application, Masters Dissertation (2022).
[88] Y.K. Zeng, T.S. Zhao, X.L. Zhou, J. Zou, Y.X. Ren, A hydrogen-ferric ion rebalance cell operating at low hydrogen concentrations for capacity restoration of iron-chromium redox flow batteries, Journal of Power Sources, 352 (2017) 77-82. https://doi.org/10.1016/j.jpowsour.2017.03.125.
[89] N. Poli, M. Schäffer, A. Trovo, J. Noack, M. Guarnieri, P. Fischer, Novel electrolyte rebalancing method for vanadium redox flow batteries, Chem. Eng. J., 405 (2021) 126583.
[90] M.R. Mohamed, P.K. Leung, M.H. Sulaiman, Performance characterization of a vanadium redox flow battery at different operating parameters under a standardized test-bed system, Applied Energy, 137 (2015) 402-412. https://doi.org/10.1016/j.apenergy.2014.10.042.
[91] M. Zarei-Jelyani, M.M. Loghavi, M. Babaiee, R. Eqra, The significance of charge and discharge current densities in the performance of vanadium redox flow battery, Electrochimica Acta, 443 (2023) 141922. https://doi.org/10.1016/j.electacta.2023.141922.

CHAPTER 6: Evaluation and Recommendations

Chapter table of contents

6.1 Evaluation

The overarching aim of this thesis was to advance the ICFB by developing membrane alternatives to Nafion. With the focus on advancing the up-scaling potential of the ICFB, membrane materials and chemistries should be developed that substantially reduce cost and the use of polyfluoroalkyl substances, while increasing the performance and selectivity. **Table 6.1** provides an overview of how the four different objectives, established at the outset of this study (see Section 1.3), were addressed in the experimental Chapters 3−5. Although Objective 1 was completed during the experimental work of Chapters 3 and 4, construction of an optimised and consistent ICFB was required before measuring any membrane performance, allowing fair comparison. Accordingly, the test station development, with its challenges, are separately discussed in Section 6.1.1, before focussing more on the membrane (MPS, AEM and CEM) developments in Section 6.1.2.

Table 6.1: Experimental result chapters with corresponding objectives.

Chapter	Content of chapter	Objective	Sub objectives
3	**MPS:** Testing of commercially available MPSs in the ICFB followed by crossover mitigation.	1	(i) Construct a lab-scale ICFB test station. (ii) Optimise various parameters of the test station. (iii) Ensure repeatability.
		2	(i) Test commercial MPSs. (ii) Identify and address challenges. (iii) Identify parameters to optimise MPSs.
4	**AEM:** Testing of different polymers and chemistries in the ICFB.	1	(i) Fully addressed in MPS objective 1 (i). (ii) Optimise various parameters of test station. (iii) Ensure repeatability.
		3	(i) Test novel AEM chemistries adopted from VFB. (ii) Investigate AEM incompatibility. (iii) Develop AEM alternative to N-212 with higher selectivity.
5	**CEM:** Screening different polymers and chemistries for further development of the ICFB.	4	(i) Further develop SPEEK for newer electrolyte configuration. (ii) Screen CEM polymer materials adopted from VFB and FC. (iii) Identify promising materials and investigate challenges. (iv) Develop promising materials for ICFB up scaling and long-term cycling.

6.1.1 ICFB test station

In line with Objective 1, repeatable testing of membrane performance in a single-cell ICFB setup was required as a foundation of this membrane screening and development study. As mentioned in the literature review (Section 2.5.1), both the electrolyte and electrodes significantly affect performance measurements of a FB. Accordingly, a test station was constructed with an in-house designed and manufactured single-cell FB (in collaboration with NWU instrument-making, see Appendix A – Figure A3 (b). The first setup (V1 – **Figure 6.1**) skewed the results obtained with the benchmark N-212 significantly, necessitating further setup optimisations before testing MPSs, AEMs and CEMs. The challenges encountered with the V1 setup were as follows.

i) The electrolyte required two hours to reach the equilibrium temperature (65 °C), which was ascribed to the slow heating of the aluminium FB cell which acted as a radiator, cooling the electrolyte during circulation. The cell did not have a probe for measuring the cell temperature.

ii) The precipitation of solid Fe_2O_3 in the catholyte vessel confirmed the oxidation of Fe through air intrusion at the electrolyte holders.

iii) The piping of the peristaltic pump occasionally shifted, which resulted in pipes tearing, requiring severe tightening.

iv) The results obtained from the Biologic potentiostat showed higher internal cell resistances than those setups using a Gamry potentiostat.

Figure 6.1: Initial ICFB test station (V1) design.

ICFB test station V2 (see **Figure 6.2**) was developed to address the above challenges:

i) The long heating time was reduced to one hour by directly heating the FB cell with a hot plate.

ii) The ingress of oxygen was prevented by equipping the electrolyte holders' caps and pipe connections with Viton™ O-rings.

iii) Although pipes would frequently tear, a Watson Marlow peristaltic pump using pump heads with clamping capabilities solved the shifting of pipes.

iv) A Gamry 5000E potentiostat was procured.

Figure 6.2: ICFB test station V2.

After further significant optimisations, discussed in Sections 6.1.1.1–6.1.1.6 and summarised in Section 6.1.1.7, a third and final version (V3 – see Figure A3 (a)) was developed.

6.1.1.1 Electrolyte

An equimolar and optimal electrolyte composition (1.3 M Fe/Cr in 1.0 M HCl) was chosen in line with literature [1-6], to minimise differences between experiments that could originate from impurities, the hydrogen evolution reaction (HER) and capacity decay rates from Fe or Cr favoured crossover. The chosen 1.0 M HCl also favoured a capacity retention, which was required for 30-cycle tests (using 100 mL) without any form of capacity regeneration or rebalancing.

After more specialised (mass-transfer and ionic conductivity) resistance measurements using electrical impedance spectroscopy (EIS) (see Appendix B – **Figure B12**), further electrolyte optimisation was deemed necessary. While increasing the electrolyte flow rate through the cell would result in a decreased resistance, the chosen experimental flow rate was only reasonably increased since large-scale applications will have a point of diminishing performance benefits from pumping losses.[7] While increasing the flow rate did result in a decreased resistance in V1, various challenges were encountered that inhibited accurate interpretation and equivalent circuit model fitting of the EIS experimental results without undesired assumptions. Some of these challenges included equipment constraints, the varying state of charge (SOC) during testing and the need for method development (like distribution of relaxation time, DRT, studies).[8, 9]. The further work required to continue the optimisation fell outside the scope of this membrane development study. Based on the preliminary optimisation, a flow rate of 65 mL min^{-1} (30% increase from the 50 mL min^{-1} in literature [10]) was chosen for all MPSs, AEMs and CEMs tested.

6.1.1.2 Temperature control

When using V2, the cell temperature varied up to 10 °C in line with room temperature changes (day and night). This was reduced to less than 1 °C by introducing the following changes:

i) The system heating time was reduced by switching to a smaller and more responsive water circulator (Julabo CORIO CD-BC4).
ii) To ensure an optimal amount of the redox active specie $Cr(H_2O)_5Cl^{2+}$ [11], temperature regulation of the cell (probe) and electrodes was introduced.
iii) To reduce temperature loss between the electrolytes (> 5 °C), the piping and connections from the water circulator were replaced with shorter and equal length piping with dual split Y-connections, thereby introducing parallel instead of in series heating.

6.1.1.3 Pressure buildup

While the new seals reduced oxygen ingress, hydrogen generation at the anolyte side caused a pressure buildup. By connecting the anolyte and catholyte headspaces, equal outlet pressures and a positive pressure at all seals were attained further mitigating oxygen-based oxidation of Fe^{2+} and Cr^{2+}.

6.1.1.4 Pipes

To reduce the frequent pipe tearing, the large peristaltic pump was replaced with a smaller Watson Marlow 323S pump, and the tubing (Masterflex™ L/S™ Viton™) was replaced with Marprene tubing.

6.1.1.5 Carbon felt

During V2 testing, hydrogen evolution was observed in the pipes at the negative side of the cell, forming gas cavities in the felt that caused anomalies in charge and discharge curves due to active electrode area fluctuations. From VFB literature, it was possible that the GFA 6 SGL carbon felts had contributed to this by either deteriorating into CO_2 and/or by catalysing H_2 formation at the negative electrode surface.[12] This was confirmed when replacing these with PAN felts (CT GF065 graphite felt from CeTech) which eliminated the gas formation while resulting in an increased capacity retention.

To activate the surface, increasing hydrophilicity and surface area thereby generating hydrophilic and increasing redox active sites, the felts were initially pretreated at 400 °C for 6 hours.[13] In alignment with recent literature, this pretreatment was changed to 650 °C for 30 minutes.[14] It was shown that the heat treatment increased the hydrophilicity (Figure A4) by decreasing the contact angle (θ) from 126° before treatment to < 90° after treatment (no droplet visible). To ensure repeatability in felt compression and to minimise dead zones in electrolyte flow, a die cutter was used. In addition, 0.50 mm thicker felts (thickness = 6.50 mm) were introduced in V3, resulting in an increased compression ratio (from 20.0% to 32.6%), which is known to improve cell performance by increasing electrode area and reducing the ASR.[15] While there have been ample developments regarding doping or coating carbon-based electrodes for the ICFB [13, 16, 17] and VFB [18-22], the uncomplicated electrodes used in this study were chosen as such, to ensure a constant variable when testing membranes.

6.1.1.6 Current collector

The contact area between the BPPs and the current collectors, which is influenced by the materials used, can contribute significantly to an increased overall resistance, for example caused by uneven current distributions and electrochemical reactions at the electrodes of FBs.[23] On the copper plates (see **Figure 6.3**), a thin oxidised layer formed after each experimental run which contributed to the resistance. This was reduced by routinely cleaning these surfaces using 600 grit sandpaper. Since abrasion typically lowers surface area against flat surfaces, carbon paper (Toray Paper – 110

µm) was inserted between the current collectors and the bipolar plates (BPPs), which further reduced the overpotential.

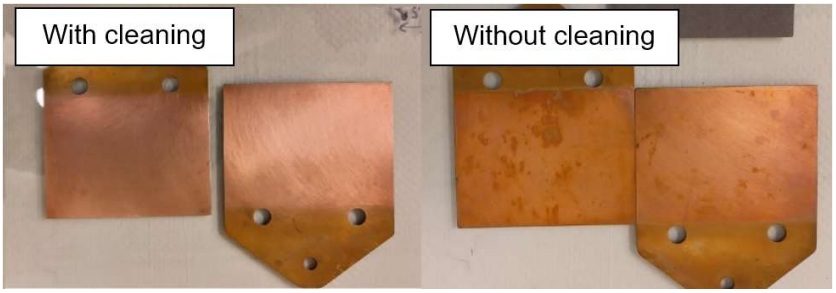

Figure 6.3: Copper current collectors with and without routine surface cleaning.

6.1.1.7 Summary

Table 6.2 summarises the most important performance indicators after 30 cycles for the three versions (V1–V3) of the testing station (for V3* the results after 10 cycles are also given) using Nafion® 212.

Table 6.2: Performance improvements of FB test station alterations/optimisations, using N-212 for 30 cycles (V1–V3) and 10 cycles (V3*).

	Cap Dis avg. (Ah L^{-1})	Cap Decay (%)	CE (%)	VE (%)	EE (%)	ASR (Ω CM^2)
V1	9.30	$^{\#}$2.09/^{H}1.39 h^{-1}	89.3	75.1	67.0	3.559
V2	9.37	$^{\#}$1.79/^{H}0.90 h^{-1}	90.9	75.5	68.7	3.486
V3	10.63	$^{\#}$1.00/^{H}0.42 h^{-1}	91.8	81.5	74.8	2.497
V3*	11.71	$^{\#}$0.23/^{H}0.09 h^{-1}	92.0	82.3	75.7	2.416

$^{\#}$ Average capacity decay per cycle
^{H} Hourly capacity decay (from electrolyte run time)
* 10-cycle average

The most observable changes between V1 and V2 was a slight overall efficiency increase and reduction in capacity decay, which was most likely due to the reduction in air intrusion (Fe^{2+} oxidation). The changes from V2 to V3 resulted in a 12.5% increased peak discharge capacity (in Ah L^{-1}), by reducing the area specific resistance (ASR) by 27.3%. This led to an increased capacity retention, with an average of 0.91% over 30 cycles (0.42% per hour of electrolyte runtime). From V1 to V3, the CE and VE increased by 2.5% and 6.4% respectively, resulting in a 7.8% increase in EE when using the same electrolyte composition and supplier, confirming that the optimisation improved performance.

The 10-cycle averages for (V3*) were included in Table 6.2 to illustrate the initial capacity gain observed, which can be ascribed to the Cr migrating from the catholyte to the anolyte and the Fe from the anolyte to the catholyte, effectively increasing the capacity. In cases without MPSs that had lower capacity decays, as observed with V3, such an initial capacity gain can overshadow the capacity loss caused by the imbalance. Comparing the performance results obtained with V3 after 10 and 30 cycles, Figure 3.2 (a), it is clear that this effect faded away after 10 cycles. Based on these results 30 cycles were introduced for the dense membranes (AEMs and CEMs), to ensure a fair comparison. The long-term cycling tests with the most developed CEM (see Section 5.3.2.3 – Figure 5.18), proved challenging due to the lack of a rebalancing cell.

In conclusion, the electrode material, compression and treatment method (see Section 3.2.2.2) was selected according to the simplest and most repeatable methods from literature [14, 15], yielding relatively optimal performance enhancements without catalyst coating requirements. The method validation, method development, as well as electrolyte and electrode selection and replacement for each experiment, resulted in adequate repeatability for the physico-chemical properties (Sections 3.2.1, 3.2.2, 4.2.2.2, 4.2.2.4, 4.2.2.6 & 5.2) and the performance parameters (Section 4.2.2.6 – Figure 4.1 & Section 3.2.2.4 – Figure A5) of the membranes tested.

6.1.2 Membranes

6.1.2.1 MPS

After the setup optimisation (Objective 1), Objective 2 entailed the investigation of the feasibility of commercially available hydrocarbon-based microporous separators (MPSs). MPSs were the cheapest membranes investigated in this study, being able to reduce membrane cost by 99% when produced at the same scale as lithium-ion batteries (see Section 2.3.1 – Figure 2.6).[24, 25] While selectivity challenges were expected when introducing a porous membrane, the cost reduction benefits of using cheap materials that are already available on a large scale warranted an investigation into MPS behaviour and their requirements specifically for an ICFB. Accordingly, 10 commercially available MPSs were sourced, followed by an evaluation of each in the ICFB of each as discussed in Chapter 3.

While the diversity in MPS materials (PE, PP, phenolic resins and a PFSA coated composite) and manufacturing methods (extruded and stretched) from four different suppliers enabled an extensive investigation into their application potentials. However, the diversity between the MPSs resulted in too many variable changes at a time, which complicated extrapolation of clear correlations between physical properties (porosity, pore size, thickness, tortuosity and WU) and the performance indicators. While only one commercially available MPS with a CEM coating could be sourced at the time, the cost and selectivity benefits from convection mitigation using such composites were apparent in literature [26-30] and confirmed by the experimental results (see Section 3.3.2.7).

The expected selectivity challenges with MPSs were confirmed by the CEs (ranging from 45–90%) and rapid volumetric crossover of electrolyte towards the anolyte tank for the thinnest MPSs (see Section 3.3.2.5). As a result, the EEs for most MPSs remained below 70%. However, while the convection of electrolyte made cycling tests challenging, the results did produce valuable information. For example, comparing Gurley number measurements (measurement of air/fluid transport resistance by pore size, pore length and tortuosity – Figure 2.23) to cycling performance and behaviour was useful, showing that MPSs with low Gurley numbers (> 15 000 s) could still yield higher convection rates and lower CEs than the thicker MPSs with significantly lower permeabilities (1135 s). Understanding that thickness and transmembrane pressures had the largest impact on convection allowed further investigation into reducing these effects without the need to further investigate variables such as pore size or porosity. Several extrapolations for future optimisation studies were made using the physical properties and ICFB performance (see Figure 3.7), reinforcing the fact that thickness strongly determines the capacity decay, self-discharge rates and ionic selectivity. However, convection cannot simply be eliminated by using thick separators, as the excessive thickness required results in high ASRs, hence, alternative mitigation was explored.

Since pressure-driven convection was found to be the leading cause for low efficiencies of the commercial MPSs tested (that had been optimised for lithium-ion and lead-acid batteries) the viscosity changes of the electrolyte were investigated to determine its influence on the convection rate. One breakthrough entailed finding a direct correlation between catholyte viscosity and SOC. These viscosity changes influenced hydraulic backpressures in the ICFB flow fields depending on the type of pump used in an ICFB. Preliminary method development of hydraulic balancing (see Section 3.3.3.2) mitigated convection (at least for the duration 30 cycles) by using an uncomplicated pulse dampening system and increasing the anolyte pumping rate. These adjustments, which reduced capacity decay of a permeable MPS 16-fold and notably increased the EE from 57.3% to 62.3%, can be adapted and applied to large-scale systems paving the way for the use of thinner and highly economical MPSs. However, the SOC changes constantly during battery use and only a static asymmetric flow rate has been implemented, without measuring the exact fluid pressures at the inlet or outlets. Lastly, while short-term ex-situ and ICFB testing of these hydrocarbon polymers in the 1.0 M HCl environment (at elevated temperatures of 65 °C) did suggest physico-chemical stability, long-term testing would be required for verification.

6.1.2.2 AEM

Since AEMs should act as a positively charged barrier repelling metal cations, thus reducing crossover, they theoretically could be more selective than the benchmark CEM N-212. However, except for the work done on tertiary amine AEMs by Ionics Inc. for NASA in the 1970s and 1980s, charge/discharge cycling in an ICFB using AEMs has been unsuccessful as literature ascribes it to a membrane fouling phenomena.[10, 31] Accordingly, Objective 3 also entailed the investigation of the charging and

discharging challenges associated with AEMs, the results of which are presented in Chapter 4, where AEMs with novel materials and combinations, including cost-effective PBIs, were investigated.

The incompatibility between AEMs and the ICFB chemistry, reported in literature [10, 31], was confirmed (Section 4.3.1) when the novel tetramethylimidazolium-quaternized polystyrene (TMImQPS – see Table 4.1) AEM blended with F_6PBI, failed to charge or discharge despite the success of similar membrane blends in the VFB.[32] Further investigation confirmed a high membrane resistance, which theoretically could be overcome by supplying higher overpotentials than the normal voltage window (0.75 V to 1.25 V) of operation (see Figure 4.3 (a)). Since ferric chloride complexes (Section 2.3.2.1.1) form in the catholyte with an increasing SOC, the increase in resistance was usually more dominant when attempting to discharge, which was in line with literature.[10, 31, 33] Attempting to reduce the membrane fouling by lowering the chloride concentrations in the electrolyte (by incorporating sulfates as sulfuric acid), unfortunately resulted in an increased ASR.

However, the MIG membranes containing *m*PBI cross-linked with ≤ 3 wt.% of the acidic cross-linker PWN, successfully discharged the ICFB electrolyte (see Table 4.1), yielding higher CEs than N-212 with lower self-discharge rates (in line with VFB literature), with no measurable solvent crossover.[34-36] MIG-15 (see Figure 4.5), specifically, had the 3rd highest overall 30-cycle avg. EE (76.1%) of all the membranes tested in this study. This is particularly promising for large-scale applications since *m*PBI-based membranes are significantly cheaper to produce than N-212, especially at a mature production level, as is the case for the VFB (**Figure 6.4**).[34] While the aromaticity and lack of hetero-atoms of the *m*PBI polymer chain make it chemically stable in the acidic environments of FBs, long-term in-situ degradation tests are required to confirm its stability in an ICFB.[27, 37]

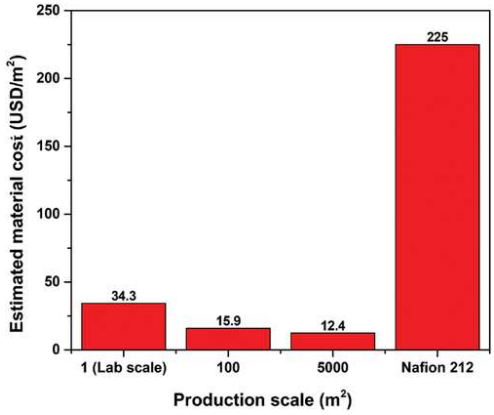

Figure 6.4: Estimated cost of *m*PBI-based membrane assemblies at different production scales, compared to the lowest literature value for N-212.[34, 38]

(Reproduced with permission from [34] under CC BY)

While the AEM results obtained in Chapter 3 met Objective 3 (Section 1.3), the successful charging and discharging of electrolyte with *m*PBI-based AEMs contrasted with the rest of the experimental AEM results obtained in this study and in literature [3, 54], warranting further testing. Additionally, the *m*PBI AEMs exhibited an abnormal gold discolouration, as well as increases in IEC and thickness (see Figure 4.6) after cycling. Assuming that larger intermolecular spaces from an amorphous and swollen polymer matrix could allow cation and anion conduction [39, 40], the effect of the type of PBI (OPBI instead of *m*PBI) and different cross-linkers (PWN & SPEEK) was investigated (Section 4.3.3).

While no gold coloration was observed with the OPBI-based AEMs, they again prevented the discharge of the ICFB, confirming that the prevention of discharge was linked to the type of PBI used. Interestingly, the OPBI-based AEMs that had been cross-linked showed both an increase in IEC (larger than the experimental error) and a non-linear increase in discharge resistance vs current density. This pointed towards additional mass-transfer limitations that could have been caused by membrane polarisation, contraction or ion-exchange site clogging (from ferric chloride complexes). The increased IEC could have resulted from the detaching of ionic cross-links during cycling, freeing up imidazole nitrogen sites and acidic functional groups to be protonated and titrated. However, regardless of the exact ion-exchange mechanism and the cause of the colour changes observed for the *m*PBI-based AEMs, their enhanced selectivity and capabilities to discharge was a novel finding.

In the literature review (Section 2.3.2.1.2) it was mentioned that PBIs and novel quaternary imidazolium-based AEMs had superior chemical stability over ammonium-based AEMs in VFBs. While the interactions of these materials with the ICFB electrolyte were investigated, AEMs based primarily of pyrrolidinium, pyridinium and piperidinium, that could have different interactions including possible immunity to fouling from the ferric chloride complexes, were not tested. While the aim of this study was to find alternative AEMs to fluorinated alkyls, testing the performance of an unblended F_6PBI (without TMImQPS) could have contributed to a better understanding of why the *m*PBI based AEMs outperformed the OPBI based AEMs.

6.1.2.3 CEM

Chapter 5 presents the results of the testing of novel CEM materials for the ICFB in line with Objective 4. The chemistries and compositions were mostly chosen based on promising developments from VFB and FC literature (see Literature Review – Section 2.3.2.2). Screening and development were aimed at finding alternative materials that maintain the benchmark efficiencies of N-212 while both minimising electrolyte imbalance from electro-osmotic crossover of the electrolyte and reducing the cost. Both sulfonated and phosphonated CEMs were tested that had been ionically, or ionically and covalently cross-linked to improve the dimensional and chemical stability of these cost-effective aromatic backbone-based membranes, while allowing the modification of the selectivity vs conductivity trade-off.

i) Phosphonated CEMs

The in-situ and ex-situ tests revealed that all phosphonic acid functional group-based CEMs, had an inherent chemical incompatibility due to the irreversible covalent bonding of Fe/Cr, thereby deactivating the phosphonic acid ion-exchange sites. This was further confirmed by SEM EDX, their poor mechanical stability and elevated ASRs, showing the unsuitability of these CEMs for the ICFB.

ii) Nanofibre reinforced Nafion composites

Due to the well-known excellent chemical stability of Nafion, nanofibre reinforced Nafion composites with a lower Nafion content (reduced cost) were also investigated. From the various nanofibre materials investigated, a piperidine/piperidinium fibre mat showed the highest potential to improve the selectivity of Nafion by nearly eliminating electrolyte imbalance levels and reducing self-discharge rates. However, the polarisation of the basic ionomer came at the cost of conductivity, which lowered the EEs.

iii) Sulfonated CEMs

Since literature showed that sulfonated PEEK (SPEEK) could potentially overcome the selectivity and cost limitations of N-212 in an ICFB [41, 42], SPEEK was also the first sulfonated polymer investigated in this study. Due to the inaccuracies caused by the second-order sulfonation reaction at the elevated temperatures used in literature (Section 5.2.1.2), a new synthesis procedure with a simplistic DS prediction model (Section 5.2.2 – Equation 5.2 and Figure 5.3) was developed. Subsequently, a SPEEK-57 membrane (DS = 56.6%, 25 µm) was synthesised and compared to an in-house manufactured highly sulfonated SPEEK-95 that had been acid-base cross-linked with OPBI. The trade-off optimisations allowed the 55 µm SPEEK-95-OPBI to outperform both the thin 26 µm SPEEK-57 and the 58 µm N-212 in terms of CE (93.5%) and volumetric electrolyte imbalance (4%), while it's EE (71.5%) outperformed only that of SPEEK-57 due to dimensional contractions increasing resistance. The improved performance and selectivity of the provided a low-cost workaround for the DS, solubility and thickness limitations of pure SPEEK-based CEMs in the ICFB. Additionally, the non-linear change in swelling, at a certain threshold, when adjusting blend ratios is a new and practically relevant finding for future CEM optimisations, as it was shown that the specific DS and/or IEC can further complicate experimental optimisation efforts of membrane blend ratios.

The higher EE reported for the SPEEK-57 CEM in literature, can most notably be ascribed to the different electrolyte compositions used in both studies, where the electrolyte used in this study (1.3 M Fe/Cr in 1 M HCl) had been optimised for capacity retention (Section 5.3.2.1).[4] While the highly sulfonated SPEEK-95-OPBI CEM mitigated electro-osmosis while yielding EEs similar to N-212, its long-term stability could be a concern. Literature reports that strong acidic conditions can cause protonation of the ethereal oxygen atoms in SPEEK, producing an additional electron-withdrawing group next to the $–SO_3H$ groups present in SPEEK (see **Figure 6.5)**.[43]

As a result, increasing the DS of SPEEK can accelerate degradation in VFBs, since lone pair electrons easily attack the nucleophilic sites of SPEEK exposed to the acidic and oxidising environment (highly oxidative VO_2^+). There is a similar concern with the ether hetero-atom (–O–) in OPBI, which could undergo a similar degradation in an acidic environment. However, VFB studies have demonstrated the stability of PBIs with ethereal oxygens when exposed to VO_2^+ in acidic environments, which was ascribed to the repulsion from the polarised OPBI containing imidazolium.[44, 45] In addition, this specific mechanism of degradation via a cationic attack is unlikely in the ICFB, which to our knowledge lacks the nucleophilic oxide species found in VFB electrolyte.

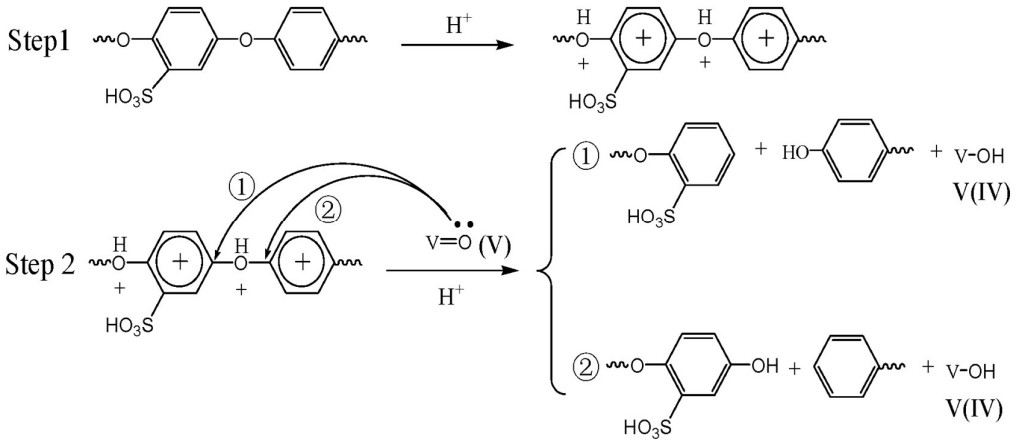

Figure 6.5: The degradation mechanism proposed for a 91% DS SPEEK membrane in a VO_2^+ solution.
(Reprint with permission from [43]. © 2014 Royal Society of Chemistry, license ID: 1662176-1)

In the next step, the SPEEK was replaced by SFS, a partially fluorinated sulfonated poly(arylene sulfone) that showed promise both in PEMFCs [46] and the screening results (Section 5.3.1). To reduce the excessive water uptake (WU) observed, the SFS was ionically cross-linked with OPBI. While having a slightly lower VE, the CEM with the optimal blend-ratio (SFS:OPBI = 84:16; thickness = 59 µm) had a higher CE and EE while having a lower electro-osmosis and self-discharge rate than the N-212 benchmark. Subsequently, an ionically and covalently ([1,1'-biphenyl]-4,4'-dithiol) cross-linked SFS-OPBI membrane was developed. The additional swelling suppression allowed the use of more SFS ionomer SFS:OPBI (88:12), resulting in a further increase in EE with negligible electro-osmosis. While longer cycling tests (Figure 5.18) showed performance degradations, these were unrelated to the membrane since electrolyte replacement fully restored both the efficiencies and the discharge capacity. The partially fluorinated alkyl chain of SFS added stability and enhanced the pKa of the sulfonic acids. However, the search for perfluorinated alkyl-free CEM alternatives should continue.

The promising results obtained (Chapter 5) for the SPEEK-95-OPBI and SFS-OPBI CEMs clearly contributed to the development of ICFBs. However, it is worth mentioning that all the ionically cross-linked CEMs displayed higher capacity decay rates than the benchmark N-212 (likely due to dimensional contractions and OPBI polarisation during cycling). Although this effect, which systematically increased ASRs, was reduced by a prior water treatment at 65 °C and covalent cross-linking, a better understanding of the increase in ASR could be valuable, as it would enable further optimisation of cross-linked CEMs that retain a low ASR. Since long term in-situ tests were not possible in this study (absence of rebalancer), the ex-situ weight change over 190 days in an ICFB electrolyte @ 65 °C was measured for the most promising (and one chemically incompatible phosphonated) CEMs (**Figure 6.6**). The results confirmed the chemical incompatibility of the phosphonated terphenyl-based SA-104-c (glass-like brittleness and a significant increase in weight confirming irreversible Fe/Cr cross-linking – see Figure B7), as well as the stability of all the sulfonated CEMs tested.

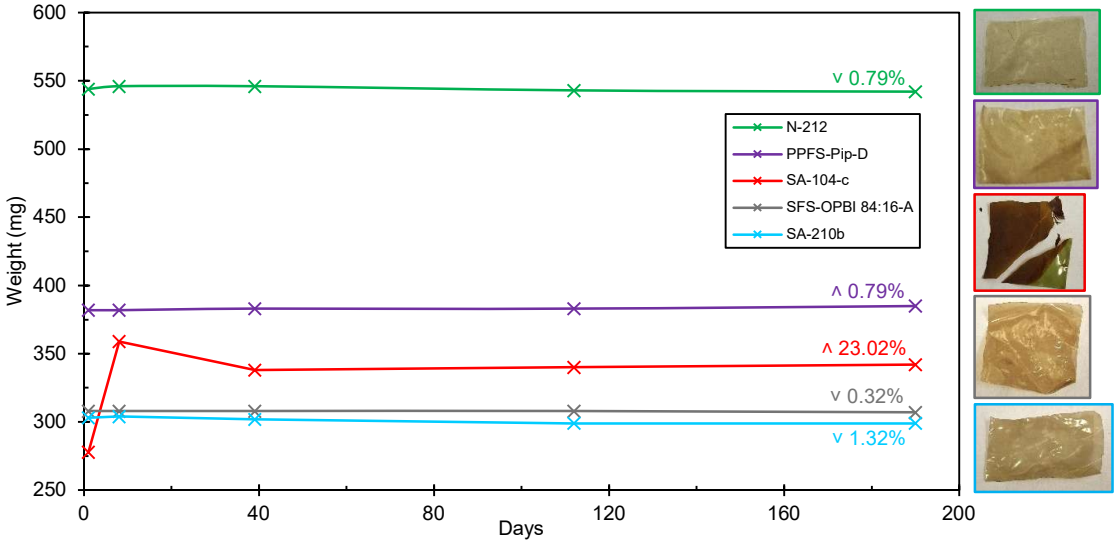

Figure 6.6: Long-term ex-situ chemical stability tests (in ICFB electrolyte @ 65 °C) of phosphonic acid-containing SA-104-c, PPFS-piperidinium nanofibre mat composite and sulfonated CEMs (N-212 and 2x SFS-OPBIs) by monitoring weight changes over 190 days.

6.1.2.4 Comparative analysis of MPS, AEM & CEM

Contributions to the identified research gap of different membrane chemistries and materials were made by improving the cost, ionic selectivity, and imbalance from electro-osmotic crossover (essential for up-scaling of low-maintenance systems) compared to the benchmark perfluorinated Nafion. In **Figure 6.7** the performance of the most optimised membranes from Chapters 3–5 is compared. Notably none of these membranes have previously been applied in, or optimised for, the ICFB. All the

novel membranes outperformed N-212 in terms of cost, imbalance and CE (excluding MPS), while an AEM and CEM had higher EEs.

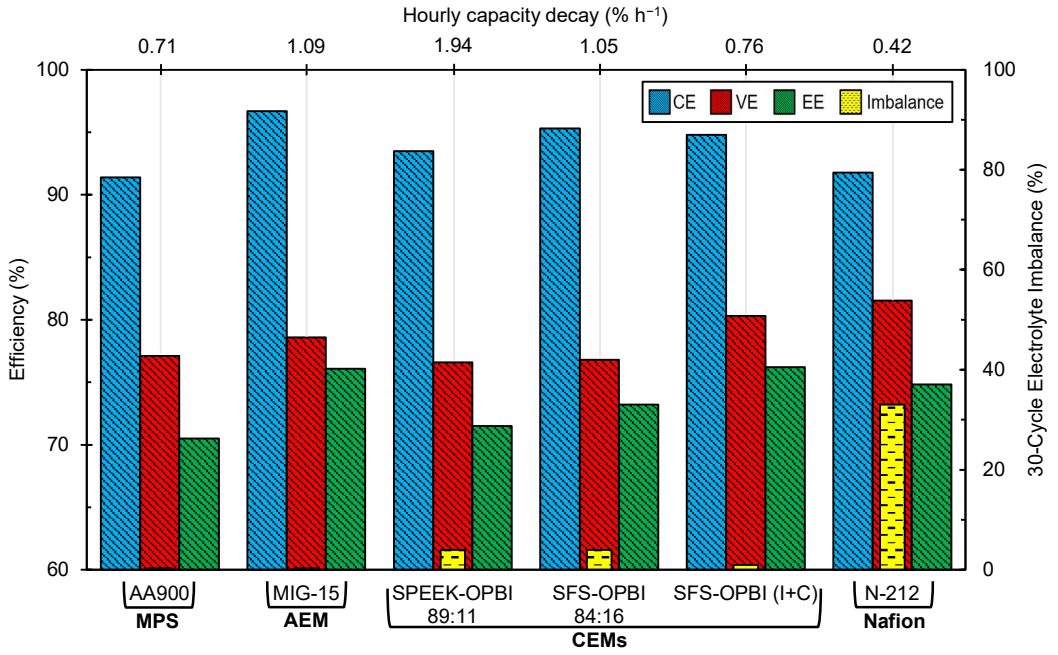

Figure 6.7: Comparison of performance parameters, electro-osmotic imbalances and hourly capacity decay rates between the most promising MPS, AEM and CEMs and N-212.

One of the biggest unresolved challenges NASA faced during up-scaling (see Section 2.2.2 [47]), which is still encountered in upscaled FBs during long-term cycling today, is high electro-osmotic crossover rates.[48-51] It is therefore disconcerting that most membrane related ICFB literature fails to mention electro-osmotic crossover rates. This study has demonstrated that while focussing on this important variable, MPSs, AEMs and CEMs alternative to PFSA was delivered that could address this challenge.

According to Figure 6.7, the membranes presented from this study had higher capacity decay rates than N-212. Contributing factors (see Section 5.3.2.3) that could have increased ASRs and capacity decay rates include oxygen intrusion, electrolyte ageing and side reactions (see Section 6.1.1). One possible solution to reduce the capacity decay could entail attaching alternative ligands (than Cl^- and H_2O) to Cr in the electrolyte, effectively thereby reducing ageing by increasing reaction kinetics without heating requirements.[52] Since the capacity decay rates were related to ASR changes, it could be possible that the higher $Cr^{2+/3+}$ migration rates of N-212 lowered its resistance by acting as a charge balancer (see Section 3.3.2.1 and Figure 3.2).

Despite the elevated capacity decay rates, the MPS, AEM and CEMs presented in Figure 6.7 are still considered to be competitive cost-effective alternatives to N-212 for long-term operation in up-scaled ICFBs due to their ionic selectivity, low fluorine

content, stability and most importantly, substantially reduced volumetric electrolyte imbalance rates. In summary, **Table 6.3** provides an overview of the key advantages and disadvantages of the preferential materials for the cheapest and most ion selective MPSs (hydrocarbons), AEMs (*m*PBI-PWN) and CEMs (SPEEK- and SFS-OBPI) obtained.

Table 6.3: Key advantages and disadvantages of different membrane types and materials based on literature [42, 53-55] and results from Chapters 3–5 and Figure 6.7.

Type	Material	Advantages	Disadvantages
MPS	Hydro carbons (i.e., PE)	• PFAS-free • Low cost • Chemical and mechanical stability (lack of ion-exchange groups) • Highly modifiable • High material variety • VE benefits from simplified ion transport mechanism • Lower capacity decay vs AEM and CEMs	• Lowest EE • Convection of electrolyte requires thick membranes (reducing VE), or controlled transmembrane pressures • Poor ionic selectivity (lowest CE), requiring accurate pore size control • Hydrophobic materials require additives (e.g., silica) • Higher capacity decay than N-212
AEM	*m*PBI-PWN	• PFAS-free • Low cost • Highest ionic selectivity (CE) and lowest self-discharge rates • No electro-osmotic crossover • Higher EE than N-212 • Immune to cationic attack degradation mechanisms	• Relatively high ASR, likely from polarisation of membrane • Inherent incompatibility with ICFB related to ferric chloride complexes, requiring high molecular pore sizes
CEM	SPEEK-OPBI	• PFAS-free • Low cost • Higher ionic selectivity than N-212 • Lower electro-osmotic crossover than N-212 • Similar efficiencies than N-212 • Environmentally friendly synthesis	• Solubility of high IEC SPEEK requires modification and optimisation • Low ionic conductivity requires high water uptake, complicated by IEC limitations in aqueous systems, resulting in thin membranes in ICFB • Chemical stability concerns from protonation of ether-groups in acidic environment

	SFS-OPBI	• Highest EE when covalently cross-linked • Negligible electro-osmotic crossover • High ionic conductivity for an aromatic polymer • Proven ex-situ long-term chemical stability	• High swelling of ionomer requires modification and optimisation efforts • Potentially high cost • Partially fluorinated • Moderately complicated synthesis

The ICFB could potentially benefit from a combination of various materials and chemistries (composites), similar to the VFB.[26, 56] For example, thin acid-base blend CEM (optimised to be highly selective) coatings on porous substrates such as PE, PP, SPEEK (low DS), PEEK or AEM PBIs could have excellent intramolecular interactions, no electro-osmosis and even benefit from the Donnan exclusion principle without fouling.

6.2 Recommendations

Based on the overview and evaluation of this study (Section 6.1), this section concludes the thesis by providing suggestions for follow-up studies and methodological improvements for the test station, MPSs, AEMs and CEMs (Sections 6.2.1–6.2.4).

6.2.1 ICFB test station

While the test station was optimised over three iterations (Section 6.1.1), the focus of the study was on the development of suitable membranes for the ICFB. As a result, electrode materials and electrolyte flow rates were not investigated to the same extent as membranes. In addition, in the absence of a rebalancer, the long-term (> 30 cycles) testing of membranes is clouded by electrolyte ageing and varying membrane specific crossover mechanisms. Prolonged in-situ testing is however vital considering that literature describes the sudden failure of supposedly chemically stable CEMs after 250 [57] or even 500 [58] cycles. Accordingly, the following recommendations are made.

- More intricate BBPs with built-in flow fields should be investigated and optimised for ICFB efficiency. Electrolyte distribution can significantly reduce the overall cell resistance, seeing that only normal flat BPPs in a flow through configuration was used for simplicity, repeatability and availability of materials during this study.[59, 60]
- Optimise electrolyte flow rate: After electrode optimisation, determine EIS changes as a function of flow rate to establish the optimum trade-off between round-trip efficiencies and pumping losses.
- Long-term testing on more membrane materials and stacks (5–10 cells), after development and implementation of a rebalance cell, would make this study

more impactful by demonstrating the durability of the technology with low maintenance, high capacity retention and membrane chemical stability.[61] Long-term tests could better quantify Fe/Cr imbalance and measurement errors, while performance data would aid the ICFB by demonstrating feasibility to researchers/investors.

- The EEs for membranes obtained during this study could possibly be elevated further using electrodes with, e.g., catalysts that enhance the sluggish $Cr^{2+/3+}$ kinetics.[16, 62]
- Develop industry standards for success criteria/benchmarks for the ICFB regarding imbalance, ii) EE , and iii) current density, as none currently exist.

6.2.2 MPS

According to the evaluation of Objective 2 (Section 6.1.2.1 and Chapter 3), there were novel findings that could significantly aid future research towards the feasible application of MPSs in an ICFB. However, most of the commercially available separators were manufactured for optimal performance in battery technologies excluding the ICFB. To develop an ICFB specific MPS, the following recommendations are made.

- Evaluate new and commercial MPSs with a high wettability and void space.
- When assessing MPSs, change and optimise one parameter at a time which should include thicknesses (300-800 µm) and permeabilities (Gurley number: 1500-1000). Obtain more data points to build on the current data sets to create trends for optimisation.
- Investigate the usefulness of using thickness normalised Gurley numbers, seeing that thickness was identified as the most significant variable.
- Investigate the cause for the inverse relationship between the hourly capacity decay and the permeability and porosity.
- Investigate cost-effective modifications (e.g., wettability, thickness, and permeability) of commercial MPSs to reduce resistance and capacity decay (increase conductivity), while increasing selectivity and separation.
- Synthesise a variety of cost-effective CEM ionomers and use as thin coatings to enhance selectivity and mitigate convection of MPSs in the ICFB.
- Investigate and confirm the inverse relationship observed between hourly capacity decay and permeability (Figure 3.7 (e)).
- Since VFB literature reports good separation and conductivity by applying the size exclusion principle, investigate porous separators with a reduced pore size (such as nanofiltration (NF) membranes).[63] Speciation studies of the ICFB electrolyte should be included with the NF membrane developments, since pore sizes could be fine-tuned with knowledge of the exact speciation and Stokes radius of the metallic species present.
- Further develop the static hydraulic balancing method (from Section 3.3.3), using both computational fluid dynamics (CFD) modelling and experimental

measurements to incorporate different designs of dynamic asymmetric pumping and transport channels for electrolytes.

- Viscosity changes (only measured in this work at 25 °C) are tied directly to the dynamic SOC. Development of a dynamic control process can be introduced to eliminate, and possibly reverse, crossover-induced capacity decay. This concept has already been proven in literature for a Fe/V FB (see **Figure 6.8**).

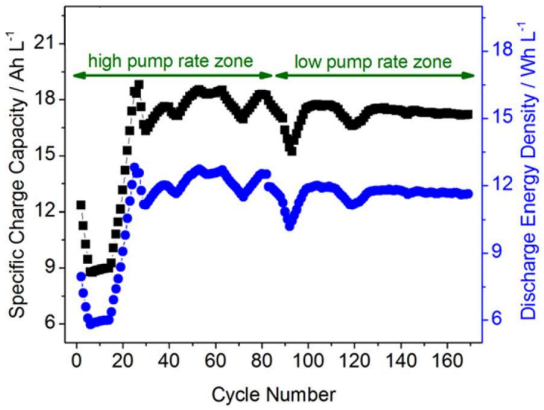

Figure 6.8: Capacity stabilisation by adjusting the electrolyte flow rate for an MPS, with specific charge capacity and discharge energy density as a function of the cycle number.[64]

6.2.3 AEM

In line with Objective 3, Chapter 4 delivered a cost-effective and PFAS-free membrane alternative to N-212. However, based on the evaluation of experimental contributions, the following recommendations are made that can further contribute to the development of AEMs for the ICFB.

- Conduct an in-depth investigation into the specific swelling effects of PWN to optimise the MIG membranes (*m*PBI with low amount of PWN cross-linker) focussing on thickness reductions to increase the VE.
- Since swelling and electrolyte absorption was the most likely explanation as to why *m*PBI-based membranes could charge and discharge ICFB electrolyte, by allowing proton conduction, a study into further reduction of intermolecular forces could enable a conductivity vs selectivity trade-off optimisation.
- Investigate the long term in-situ degradation tests, with a rebalance cell, to confirm the stability of *m*PBI in an ICFB.
- Manufacture ultrathin (≤ 25 µm) OPBI membranes and test discharge ability.
- Manufacture base-excess AEMs and blends from additional novel ionomers, such as pyrrolidinium, pyridinium and piperidinium, as well as other promising materials from VFBs and water electrolysers.

- Manufacture a pristine F_6PBI membrane and investigate ICFB cycling resistance to further elucidate the different behaviours of *m*PBI vs HT-3.
- Due to $FeCl_4$ fouling membranes (shown in previous studies [10], but should be verified by SEM EDX), basic polymers (PBIs) and anion exchange ionomers could benefit from the replacement of chlorides (Cl^-) by alternative anionic ligands in the ICFB electrolyte. Replacing the water in the hydration sphere of Cr ($Cr(H_2O)_6^{3+}$ and $Cr(H_2O)_5Cl^{2+}$) with anionic ligands could increase the redox kinetics without requiring elevated temperatures, while enlarging complexes to reduce the metallic-ion crossover.[52]

6.2.4 CEM

It is apparent from Chapter 5 and Section 6.1.2.3 that Objective 4 was fulfilled, resulting in the development of multiple alternatives CEMs to N-212 that retained similar EEs while lowering electro-osmosis and increasing selectivity. From the critical evaluation of the scientific contributions, the following recommendations can be made to benefit the development of the ICFB.

- Since a fibre mat of low-cost polystyrene-based PPFS-Pip increased the selectivity of N-212, further investigation of composite membranes with very conductive ionomers incorporated into PPFS-Pip fibre mats could be considered. In addition, the selectivity of the ionomers could be increased by this weak base.
- Further investigate the dimensional contractions of acid-excess acid-base blends with OPBI to allow a higher sustained capacity while increasing the EE.
- Conduct an in-depth investigation into the long-term chemical stability of cross-linked SPEEK-95-OPBI in the ICFB, since literature supports accelerated degradation of highly sulfonated PEEK in the highly oxidative and acidic environment of the VFB.[43] This should include investigating different pathways for degradation of pristine vs cross-linked membranes.
- Based on the positive results when using sulfonated ionomers and the multiple reaction pathways of cost-effective PPFST (see Figure 5.4), it is highly recommended to manufacture and test a sulfonated variant.
- In view of the environmental concern of fluorinated alkyls, the possible development of SFS-like ionomers that do not contain CF_3, could be considered. Groups such as $–SO_2–$ could provide similar main chain flexibility while retaining chemical stability.
- Considering the results obtained with the CEMs tested in this study, cost-effective CEM materials could also be coated on porous substrates of PE, PP, SPEEK (low DS), PEEK or AEM PBIs and tested in an ICFB.
- Seeing that the cost of materials is usually reduced when production is upscaled, a theoretical investigation of the cost of lab-scale vs roll-to-roll production of membranes should be conducted.

References

[1] Y.K. Zeng, T.S. Zhao, X.L. Zhou, L. Zeng, L. Wei, The effects of design parameters on the charge-discharge performance of iron-chromium redox flow batteries, Applied Energy, 182 (2016) 204-209. https://doi.org/10.1016/j.apenergy.2016.08.135.

[2] Y.S. Kim, S.H. Oh, E. Kim, D. Kim, S. Kim, C.H. Chu, K. Park, Iron-chrome crossover through nafion membrane in iron-chrome redox flow battery, Korean Chemical Engineering Research, 56 (2018) 24-28. 10.9713/kcer.2018.56.1.24.

[3] Y. Wang, K. Geng, Q. Tan, T. Guo, X. Hu, H. Tang, L. Liu, N. Li, Highly Ion Selective Proton Exchange Membrane Based on Sulfonated Polybenzimidazoles for Iron–Chromium Redox Flow Battery, ACS Applied Energy Materials, 5 (2022) 15918-15927. 10.1021/acsaem.2c03471.

[4] N. Mans, H.M. Krieg, D.J. van der Westhuizen, The Effect of Electrolyte Composition on the Performance of a Single-Cell Iron–Chromium Flow Battery, Advanced Energy and Sustainability Research, 5 (2024) 2300238. https://doi.org/10.1002/aesr.202300238.

[5] N. Mans, D.J. van der Westhuizen, H.M. Krieg, The effect of common metallic impurities on the performance of a single-cell iron-chromium redox flow battery, Electrochimica Acta, 526 (2025) 146167. https://doi.org/10.1016/j.electacta.2025.146167.

[6] L. Cao, M. Skyllas-Kazacos, C. Menictas, J. Noack, A review of electrolyte additives and impurities in vanadium redox flow batteries, Journal of Energy Chemistry, 27 (2018) 1269-1291. https://doi.org/10.1016/j.jechem.2018.04.007.

[7] C.-N. Sun, F.M. Delnick, D.S. Aaron, A.B. Papandrew, M.M. Mench, T.A. Zawodzinski, Resolving Losses at the Negative Electrode in All-Vanadium Redox Flow Batteries Using Electrochemical Impedance Spectroscopy, Journal of The Electrochemical Society, 161 (2014) A981. 10.1149/2.045406jes.

[8] M.A. Danzer, Generalized Distribution of Relaxation Times Analysis for the Characterization of Impedance Spectra, Journal, 5 (2019). 10.3390/batteries5030053.

[9] D. Vivona, M. Messaggi, A. Baricci, A. Casalegno, M. Zago, Unravelling the Contribution of Kinetics and Mass Transport Phenomena to Impedance Spectra in Vanadium Redox Flow Batteries: Development and Validation of a 1D Physics-Based Analytical Model, Journal of The Electrochemical Society, 167 (2020) 110534. 10.1149/1945-7111/aba36b.

[10] N. Mans, D.J. van der Westhuizen, H.M. Krieg, Membrane Screening for Iron–Chrome Redox Flow Batteries, Advanced Energy and Sustainability Research, 5 (2024) 2300195. https://doi.org/10.1002/aesr.202300195.

[11] D.A. Johnson, M.A. Reid, Chemical and Electrochemical Behaviour of the Cr(III)/Cr(II) Half Cell in the NASA Redox Energy Storage System, (1982).

[12] L. Eifert, Z. Jusys, R. Banerjee, R.J. Behm, R. Zeis, Differential Electrochemical Mass Spectrometry of Carbon Felt Electrodes for Vanadium Redox Flow Batteries, ACS Applied Energy Materials, 1 (2018) 6714-6718. 10.1021/acsaem.8b01550.

[13] H. Zhang, Y. Tan, J. Li, B. Xue, Studies on properties of rayon- and polyacrylonitrile-based graphite felt electrodes affecting Fe/Cr redox flow battery performance, Electrochimica Acta, 248 (2017) 603-613. https://doi.org/10.1016/j.electacta.2017.08.016.

[14] A. Kaur, K. Il Jeong, S. Su Kim, J. Woo Lim, Optimization of thermal treatment of carbon felt electrode based on the mechanical properties for high-efficiency vanadium redox flow batteries, Composite Structures, 290 (2022) 115546. https://doi.org/10.1016/j.compstruct.2022.115546.

[15] J. Charvát, P. Mazúr, J. Dundálek, J. Pocedič, J. Vrána, J. Mrlík, J. Kosek, S. Dinter, Performance enhancement of vanadium redox flow battery by optimized electrode compression and operational conditions, Journal of Energy Storage, 30 (2020) 101468. https://doi.org/10.1016/j.est.2020.101468.

[16] Y. Niu, S. Zeng, G. Wu, Q. Gao, R. Zhou, C. Li, Y. Zhou, Q. Xu, Preparation of N-B doped composite electrode for iron-chromium redox flow battery, Green Energy and Intelligent Transportation, 3 (2024) 100158. https://doi.org/10.1016/j.geits.2024.100158.

[17] M. Wu, M. Nan, S. Liu, C. Zhong, L. Qiao, H. Zhang, X. Ma, Multi-dimensional Bi@C electrocatalyst for Cr3+/Cr2+ redox reaction boosting high-performance iron-chromium flow batteries, Science China Chemistry, 68 (2025) 2735-2743. 10.1007/s11426-024-2375-6.

[18] B. Sun, M. Skyllas-Kazacos, Modification of graphite electrode materials for vanadium redox flow battery application—I. Thermal treatment, Electrochimica acta, 37 (1992) 1253-1260.

[19] B. Sun, M. Skyllas-Kazacos, Chemical modification of graphite electrode materials for vanadium redox flow battery application—part II. Acid treatments, Electrochimica Acta, 37 (1992) 2459-2465.

[20] B. Li, M. Gu, Z. Nie, Y. Shao, Q. Luo, X. Wei, X. Li, J. Xiao, C. Wang, V. Sprenkle, Bismuth nanoparticle decorating graphite felt as a high-performance electrode for an all-vanadium redox flow battery, Nano Lett., 13 (2013) 1330-1335.
[21] P. Huang, W. Ling, H. Sheng, Y. Zhou, X. Wu, X.-X. Zeng, X. Wu, Y.-G. Guo, Heteroatom-doped electrodes for all-vanadium redox flow batteries with ultralong lifespan, Journal of Materials Chemistry A, 6 (2018) 41-44.
[22] K. Kim, M.-S. Park, Y. Kim, J.H. Kim, S. Dou, M. Skyllas-Kazacos, A technology review of electrodes and reaction mechanisms in vanadium redox flow batteries, Journal of Materials Chemistry A, (2015).
[23] K.I. Jeong, J.-M. Jeong, J. Oh, J.W. Lim, S.S. Kim, An integrated composite structure with reduced electrode / bipolar plate contact resistance for vanadium redox flow battery, Composites Part B: Engineering, 233 (2022) 109657. https://doi.org/10.1016/j.compositesb.2022.109657.
[24] S. Ha, K.G. Gallagher, Estimating the system price of redox flow batteries for grid storage, Journal of Power Sources, 296 (2015) 122-132. https://doi.org/10.1016/j.jpowsour.2015.07.004.
[25] Y.K. Zeng, T.S. Zhao, L. An, X.L. Zhou, L. Wei, A comparative study of all-vanadium and iron-chromium redox flow batteries for large-scale energy storage, Journal of Power Sources, 300 (2015) 438-443. https://doi.org/10.1016/j.jpowsour.2015.09.100.
[26] Q. Dai, Z. Liu, L. Huang, C. Wang, Y. Zhao, Q. Fu, A. Zheng, H. Zhang, X. Li, Thin-film composite membrane breaking the trade-off between conductivity and selectivity for a flow battery, Nature Communications, 11 (2020) 13. 10.1038/s41467-019-13704-2.
[27] J.C. Duburg, K. Azizi, S. Primdahl, H.A. Hjuler, E. Zanzola, T.J. Schmidt, L. Gubler, Composite Polybenzimidazole Membrane with High Capacity Retention for Vanadium Redox Flow Batteries, Journal, 26 (2021). 10.3390/molecules26061679.
[28] M. Jung, W. Lee, N. Nambi Krishnan, S. Kim, G. Gupta, L. Komsiyska, C. Harms, Y. Kwon, D. Henkensmeier, Porous-Nafion/PBI composite membranes and Nafion/PBI blend membranes for vanadium redox flow batteries, Appl. Surf. Sci., 450 (2018) 301-311. https://doi.org/10.1016/j.apsusc.2018.04.198.
[29] W. Lee, M. Jung, D. Serhiichuk, C. Noh, G. Gupta, C. Harms, Y. Kwon, D. Henkensmeier, Layered composite membranes based on porous PVDF coated with a thin, dense PBI layer for vanadium redox flow batteries, Journal of Membrane Science, 591 (2019) 117333. https://doi.org/10.1016/j.memsci.2019.117333.
[30] X.L. Zhou, T.S. Zhao, L. An, Y.K. Zeng, X.B. Zhu, Performance of a vanadium redox flow battery with a VANADion membrane, Applied Energy, 180 (2016) 353-359. https://doi.org/10.1016/j.apenergy.2016.08.001.
[31] R. Assink, Fouling mechanism of separator membranes for the iron/chromium redox battery, Journal of membrane science, 17 (1984) 205-217.
[32] H. Cho, H.M. Krieg, J.A. Kerres, Application of Novel Anion-Exchange Blend Membranes (AEBMs) to Vanadium Redox Flow Batteries, Journal, 8 (2018). 10.3390/membranes8020033.
[33] J. S. Ling, J. Charleston, Advances in Membrane Technology for the NASA Redox Energy Storage System, (1980).
[34] X.H. Do, S. Abbas, M.M. Ikhsan, S.-Y. Choi, H.Y. Ha, K. Azizi, H.A. Hjuler, D. Henkensmeier, Membrane Assemblies with Soft Protective Layers: Dense and Gel-Type Polybenzimidazole Membranes and Their Use in Vanadium Redox Flow Batteries, Small, 18 (2022) 2206284. https://doi.org/10.1002/smll.202206284.
[35] C. Noh, M. Jung, D. Henkensmeier, S.W. Nam, Y. Kwon, Vanadium Redox Flow Batteries Using meta-Polybenzimidazole-Based Membranes of Different Thicknesses, ACS Applied Materials & Interfaces, 9 (2017) 36799-36809. 10.1021/acsami.7b10598.
[36] X.L. Zhou, T.S. Zhao, L. An, L. Wei, C. Zhang, The use of polybenzimidazole membranes in vanadium redox flow batteries leading to increased coulombic efficiency and cycling performance, Electrochimica Acta, 153 (2015) 492-498. https://doi.org/10.1016/j.electacta.2014.11.185.
[37] M. Jung, W. Lee, C. Noh, A. Konovalova, G.S. Yi, S. Kim, Y. Kwon, D. Henkensmeier, Blending polybenzimidazole with an anion exchange polymer increases the efficiency of vanadium redox flow batteries, Journal of Membrane Science, 580 (2019) 110-116. https://doi.org/10.1016/j.memsci.2019.03.014.
[38] D. Düerkop, H. Widdecke, C. Schilde, U. Kunz, A. Schmiemann, Polymer membranes for all-vanadium redox flow batteries: a review, Membranes, 11 (2021) 214.
[39] L. Zeng, T.S. Zhao, L. Wei, H.R. Jiang, M.C. Wu, Anion exchange membranes for aqueous acid-based redox flow batteries: Current status and challenges, Applied Energy, 233-234 (2019) 622-643. https://doi.org/10.1016/j.apenergy.2018.10.063.

[40] D. Chen, M.A. Hickner, E. Agar, E.C. Kumbur, Selective anion exchange membranes for high coulombic efficiency vanadium redox flow batteries, Electrochemistry Communications, 26 (2013) 37-40. https://doi.org/10.1016/j.elecom.2012.10.007.
[41] C. Sun, Z. Huan, X.-D. Luo, N. Chen, A comparative study of Nafion and sulfonated poly(ether ether ketone) membrane performance for iron-chromium redox flow battery, Ionics, 25 (2019). 10.1007/s11581-019-02971-0.
[42] E. Bai, H. Zhu, C. Sun, G. Liu, X. Xie, C. Xu, S. Wu, A Comparative Study of Nafion 212 and Sulfonated Poly(Ether Ether Ketone) Membranes with Different Degrees of Sulfonation on the Performance of Iron-Chromium Redox Flow Battery, Journal, 13 (2023). 10.3390/membranes13100820.
[43] Z. Yuan, X. Li, J. Hu, W. Xu, J. Cao, H. Zhang, Degradation mechanism of sulfonated poly(ether ether ketone) (SPEEK) ion exchange membranes under vanadium flow battery medium, Physical Chemistry Chemical Physics, 16 (2014) 19841-19847. 10.1039/C4CP03329A.
[44] T.T. Bui, M. Shin, M. Rahimi, A. Bentien, Y. Kwon, D. Henkensmeier, Highly efficient vanadium redox flow batteries enabled by a trilayer polybenzimidazole membrane assembly, Carbon Energy, 6 (2024) e473.
[45] T.T. Bui, S. Park, M. Shin, M.M. Ikhsan, Y. Kwon, D. Henkensmeier, Sulfonated Polybenzimidazole Membranes: How Sulfonation Affects Properties, Stability, and Performance in Vanadium Redox Flow Batteries, Advanced Energy Materials, 15 (2025) 2500440. https://doi.org/10.1002/aenm.202500440.
[46] A. Katzfuß, K. Krajinovic, A. Chromik, J. Kerres, Partially fluorinated sulfonated poly(arylene sulfone)s blended with polybenzimidazole, J. Polym. Sci., Part A: Polym. Chem., 49 (2011) 1919-1927. https://doi.org/10.1002/pola.24624.
[47] N.H. Hagedorn, NASA Redox Storage System Development Project. Final Report, (1984).
[48] K. Knehr, E. Kumbur, Role of convection and related effects on species crossover and capacity loss in vanadium redox flow batteries, Electrochemistry Communications, 23 (2012) 76-79.
[49] K. Oh, M. Moazzam, G. Gwak, H. Ju, Water crossover phenomena in all-vanadium redox flow batteries, Electrochimica Acta, 297 (2019) 101-111. https://doi.org/10.1016/j.electacta.2018.11.151.
[50] L. Yan, D. Li, S. Li, Z. Xu, J. Dong, W. Jing, W. Xing, Balancing osmotic pressure of electrolytes for nanoporous membrane vanadium redox flow battery with a draw solute, ACS Applied Materials & Interfaces, 8 (2016) 35289-35297.
[51] K.P. Smith, C.W. Monroe, Image-based mechanical balancing of reservoir volumes during benchtop flow battery operation, Frontiers in Chemical Engineering, 3 (2021) 748865.
[52] Y. Ye, M. Wu, M. Nan, M. Fang, M. Yang, L. Qiao, X. Ma, The Influence of Inorganic Salt Additives in the Electrolyte on Iron–Chromium Flow Batteries at Room Temperature, ACS Applied Energy Materials, 7 (2024) 4200-4206. 10.1021/acsaem.4c00542.
[53] T.T.K. Huynh, T. Yang, P.S. Nayanthara, Y. Yang, J. Ye, H. Wang, Construction of High-Performance Membranes for Vanadium Redox Flow Batteries: Challenges, Development, and Perspectives, Nano-Micro Letters, 17 (2025) 260. 10.1007/s40820-025-01736-x.
[54] J.P. du Toit, H.M. Krieg, The feasibility of microporous separators in iron-chromium flow batteries, Journal of Energy Storage, 107 (2025) 115008. https://doi.org/10.1016/j.est.2024.115008.
[55] T.N.L. Doan, T.K.A. Hoang, P. Chen, Recent development of polymer membranes as separators for all-vanadium redox flow batteries, RSC Advances, 5 (2015) 72805-72815. 10.1039/C5RA05914C.
[56] J. Chu, Q. Liu, W. Ji, J. Li, X. Ma, Novel microporous sulfonated polyimide membranes with high energy efficiency under low ion exchange capacity for all vanadium flow battery, Electrochimica Acta, 446 (2023) 142080. https://doi.org/10.1016/j.electacta.2023.142080.
[57] Q. Chen, L. Ding, L. Wang, H. Yang, X. Yu, High Proton Selectivity Sulfonated Polyimides Ion Exchange Membranes for Vanadium Flow Batteries, Journal, 10 (2018). 10.3390/polym10121315.
[58] W. Liang, E. Ghasemiestahbanati, N.T. Eden, D. Acharya, C.M. Doherty, M. Majumder, M.R. Hill, Flow Battery with Remarkably Stable Performance at High Current Density: Development of A Nonfluorinated Separator with Concurrent Rejection and Conductivity, Angew. Chem. Int. Ed., 64 (2025) e202505383. https://doi.org/10.1002/anie.202505383.
[59] S. Kumar, S. Jayanti, Effect of flow field on the performance of an all-vanadium redox flow battery, Journal of Power Sources, 307 (2016) 782-787. https://doi.org/10.1016/j.jpowsour.2016.01.048.
[60] Y.K. Zeng, X.L. Zhou, L. An, L. Wei, T.S. Zhao, A high-performance flow-field structured iron-chromium redox flow battery, Journal of Power Sources, 324 (2016) 738-744. https://doi.org/10.1016/j.jpowsour.2016.05.138.

[61] Y.K. Zeng, T.S. Zhao, X.L. Zhou, J. Zou, Y.X. Ren, A hydrogen-ferric ion rebalance cell operating at low hydrogen concentrations for capacity restoration of iron-chromium redox flow batteries, Journal of Power Sources, 352 (2017) 77-82. https://doi.org/10.1016/j.jpowsour.2017.03.125.
[62] D.A. Johnson, M.A. Reid, Chemical and Electrochemical Behavior of the Cr(III)/Cr(II) Half-Cell in the Iron-Chromium Redox Energy Storage System, Journal of The Electrochemical Society, 132 (1985) 1058-1062. 10.1149/1.2114015.
[63] R. Tan, A. Wang, R. Malpass-Evans, R. Williams, E.W. Zhao, T. Liu, C. Ye, X. Zhou, B.P. Darwich, Z. Fan, L. Turcani, E. Jackson, L. Chen, S.Y. Chong, T. Li, K.E. Jelfs, A.I. Cooper, N.P. Brandon, C.P. Grey, N.B. McKeown, Q. Song, Hydrophilic microporous membranes for selective ion separation and flow-battery energy storage, Nature Materials, 19 (2020) 195-202. 10.1038/s41563-019-0536-8.
[64] X. Wei, L. Li, Q. Luo, Z. Nie, W. Wang, B. Li, G.-G. Xia, E. Miller, J. Chambers, Z. Yang, Microporous separators for Fe/V redox flow batteries, Journal of Power Sources, 218 (2012) 39-45. https://doi.org/10.1016/j.jpowsour.2012.06.073.

APPENDIX A

Figure A1: Photographs of new cut MPS samples: (1) EW-200, (2) EW-200 Gen 2.2, (3) C-5550, (4) C-3401, (5) C-2340, (6) Breathtech, (7) DARAK 2000, (8) VANADion-20, (9) AA175 and (10) AA900.

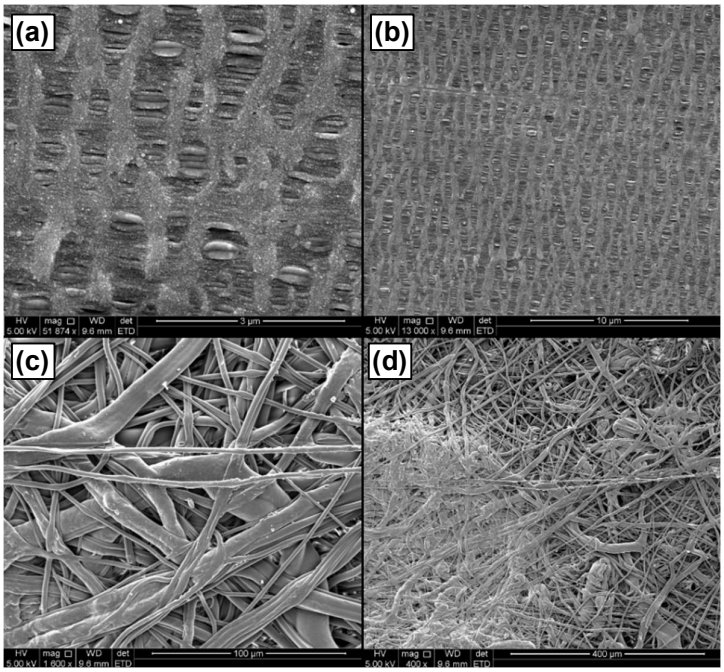

Figure A2: C-5550: Surface SEM imaging with 400x -52 000x magnification of the (a, b) smooth front, and (c, d) more amorphous side with fibres.

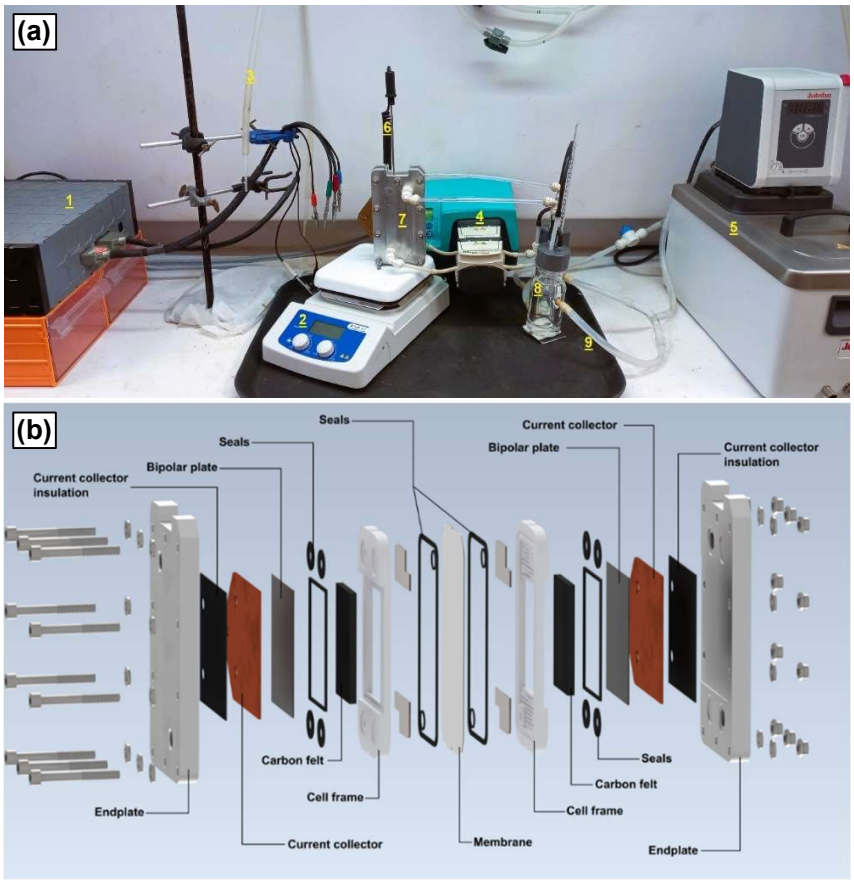

Figure A3: (a) Experimental FB test station used for testing MPSs, AEMs & CEMs. Potentiostat (1), hot plate (2), N_2 line (3), peristaltic pump (4), water heating circulator (5), temperature probe (6), lab-scale cell (7) and parallel water pipes and double walled glass electrolyte tanks (8, 9). (b) Single-cell illustration.

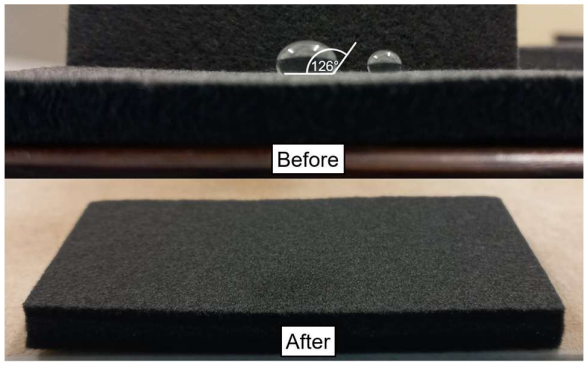

Figure A4: Wettability of CT GF065 graphite felt electrodes before and after thermal treatment.

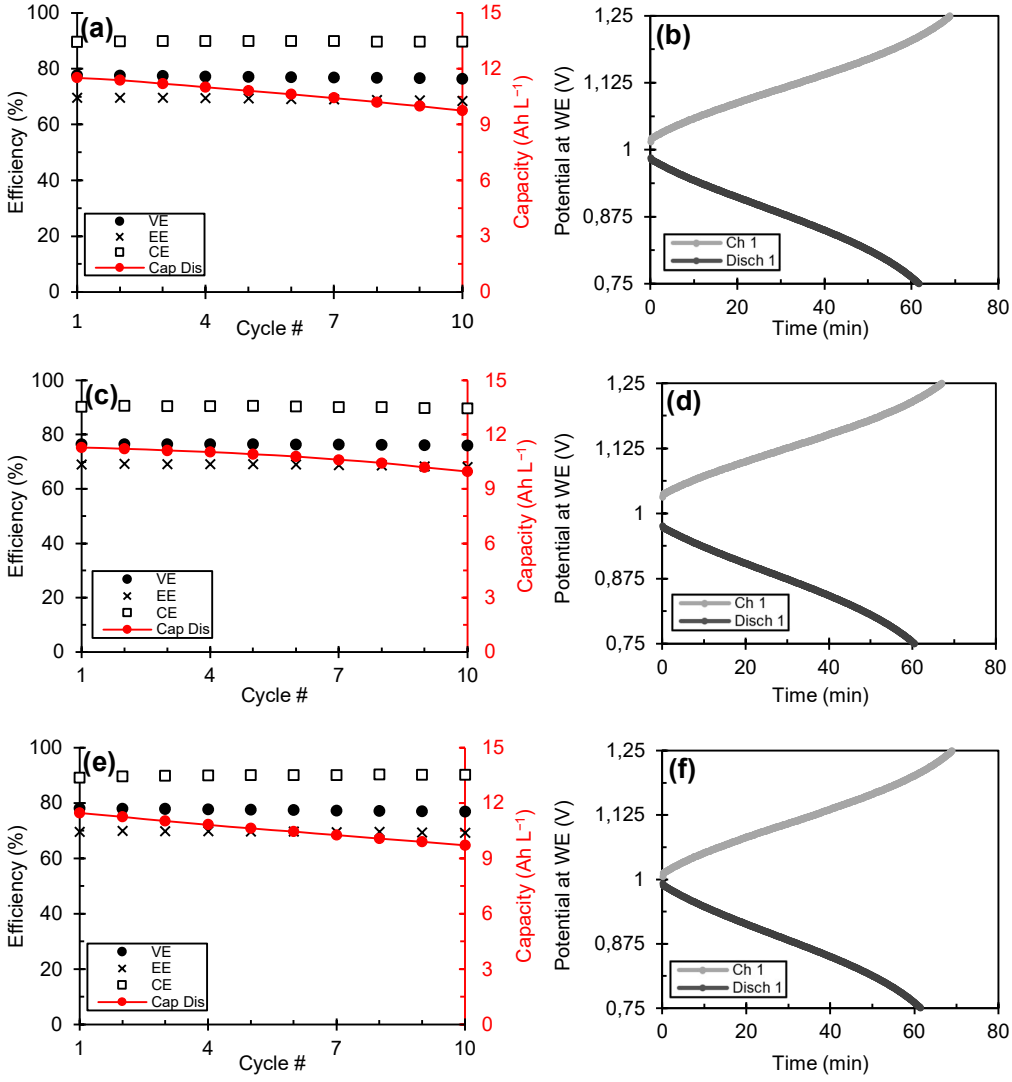

Figure A5: Repeatability tests with different AA900 pieces: (a, c & e) 10 cycle performance, (b, d & f) first-cycle charge and discharge curves.

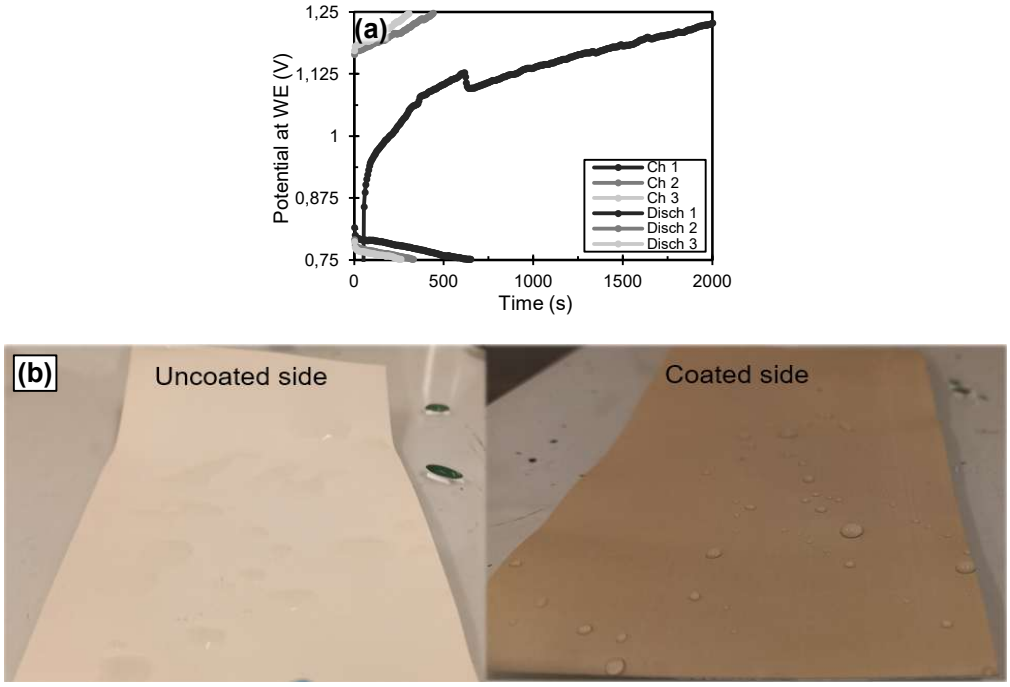

Figure A6: EW-200 Gen 2.2: (a) charge and discharge curves and (b) wetting of uncoated and coated sides.

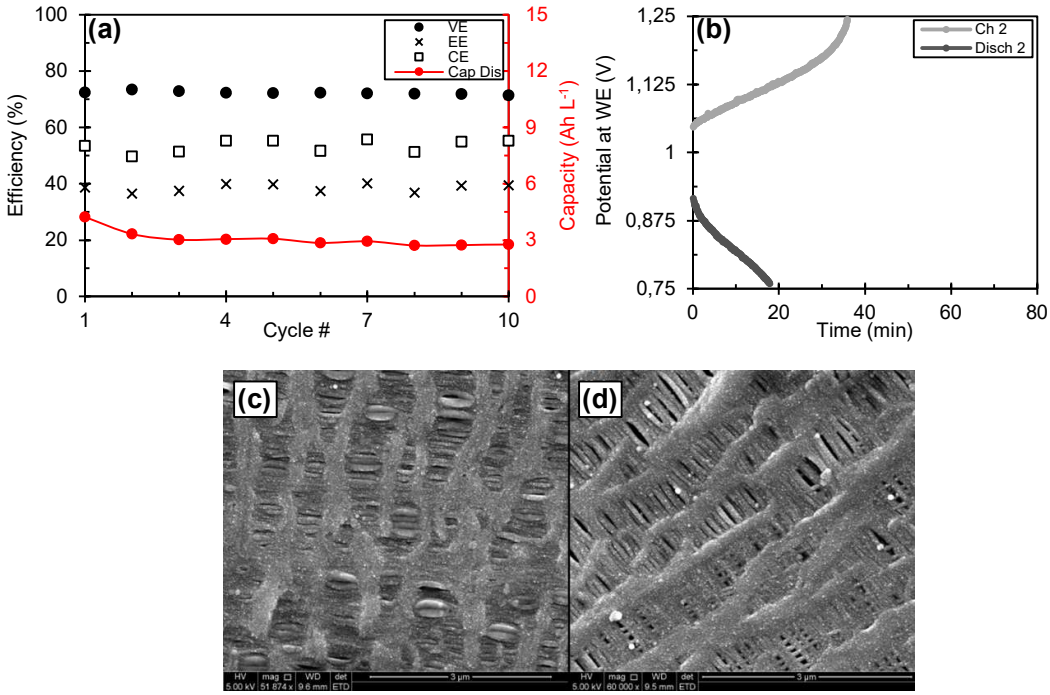

Figure A7: C-5550: (a) 10-cycle performance, (b) first-cycle charge and discharge curves and (c, d) SEM imaging of surface before (at 51 874x) and after cycling (at 60 000x), respectively.

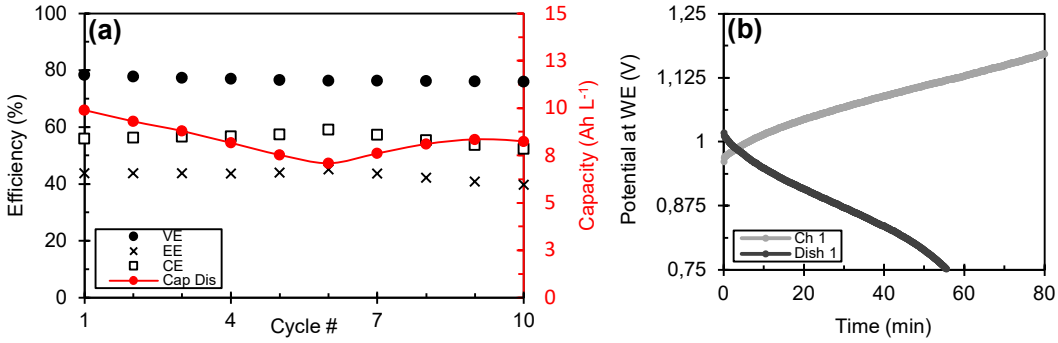

Figure A8: AA175: (a) 10-cycle performance and (b) first-cycle charge and discharge curves.

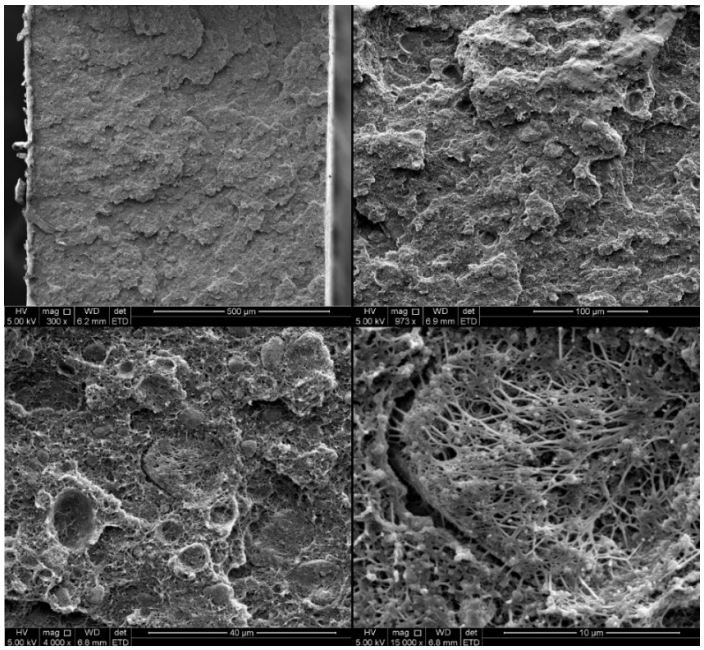

Figure A9: Cross-section SEM imaging with 300x -15 000x magnification of a used AA900 MPS.

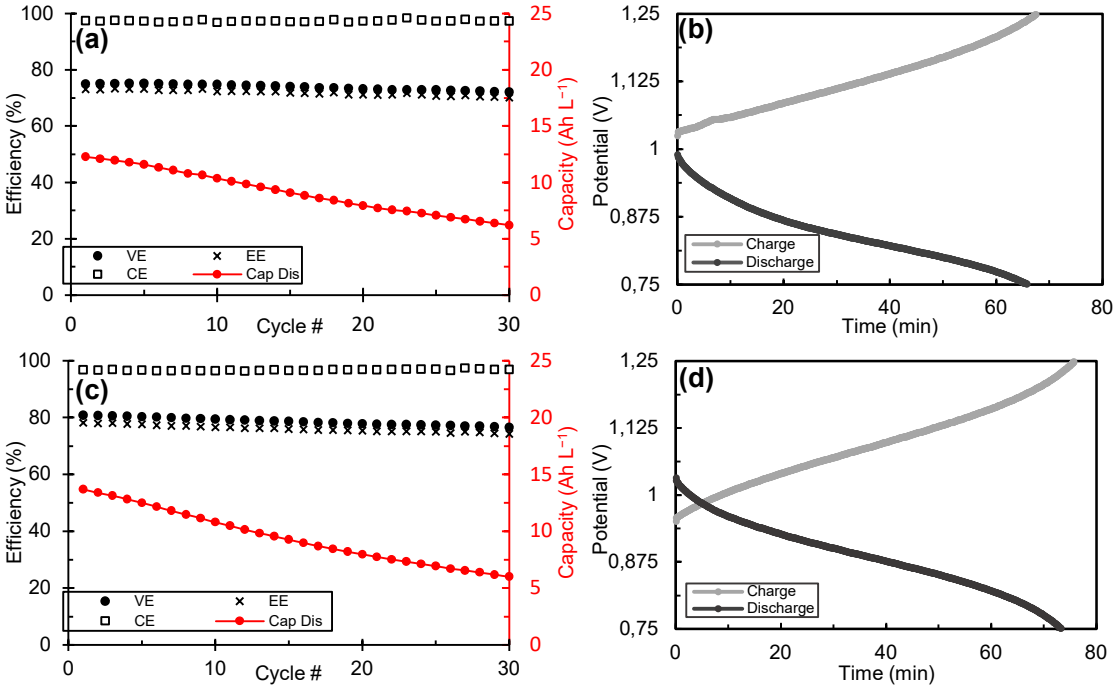

Figure A10: 30-Cycle performance parameters and cycle #1 charge and discharge curves and of AEMs: (a, b) MIG-11 and (c, d) MIG-15.

APPENDIX B

Table B1: Summary of discharge capacity, capacity decay (per cycle and normalised hourly), performance parameters, operational electrolyte imbalance, self-discharge values and losses (IEC & tensile strength) for all CEMs tested.

Membrane	Peak Dis. Cap. (Ah L^{-1})	Cap. Decay (%, % h^{-1})	CE (%)	VE (%)	EE (%)	ASR (Ω cm^2)	Imbal. (%)	Self-Disch. (mV h^{-1})	Δ IEC (%)	Δ Tensile strength (%)
N-212	11.8	*1.00/^{H}0.42	91.8	81.5	74.8	$^{\#}$2.38/$^{\Delta}$2.50	33	3.187	0	−16
SPEEK-57	12.5	*1.77/^{H}0.70	84.8	83.0	70.4	$^{\#}$2.00/$^{\Delta}$2.34	50	6.711	−7	21
Screening										
SPEEK-PBIOO-a	0	--	--	--	--	$^{\#}$18.59	n.m.	--	−6	10
SPEEK-PBIOO-b	0	--	--	--	--	$^{--}$	n.m.	--	−5	17
SA-99T-a (1 cycle)	3.03	--	61.5	66.1	40.6	$^{\#}$4.00/$^{\Delta}$5.27	99	91.66	−58	n.m.
SA-99T-ab	9.39	*3.64/^{H}3.86	95.5	68.8	65.9	$^{\#}$3.50/$^{\Delta}$4.62	7	3.106	−38	−80
SA-104-c	11.7	*2.29/^{H}1.03	90.5	73.3	66.3	$^{\#}$3.20/$^{\Delta}$3.87	93	6.266	−80	−64
PWN-PVDF	--	--	--	--	--	--	--	--	−77	−69
SFS-PVDF	11.7	*4.40/^{H}1.81	59.4	79.4	47.1	$^{\#}$1.90/$^{\Delta}$2.70	100	63.50	−5	−3
Ionically cross-linked blends										
SPEEK-95-OPBI 90:10	9.31	2.10/1.36	71.6	86.1	61.6	$^{\#}$1.93/$^{\Delta}$1.79	80	47.51	0	7
SPEEK-95-OPBI 89:11	12.4	5.22/1.94	93.5	76.6	71.5	$^{\#}$2.18/$^{\Delta}$4.40	4	2.532	0	4
SPEEK-95-OPBI 88:12	11.8	4.95/1.92	90.9	74.8	67.9	$^{\#}$2.36/$^{\Delta}$3.62	0	4.530	0	10

SPEEK-95-OPBI 87:13	11.2	9.98/4.74	91.9	72.2	66.3	$^{\#}$2.38/$^{\Delta}$4.62	0	2.691	0	7
SFS-OPBI 9:1	11.6	*2.69/^{H}0.98	54.0	85.4	46.2	$^{\#}$1.80/$^{\Delta}$2.02	91	64.29	0	8
SFS-OPBI 86:14-A	12.1	*2.00/^{H}0.89	90.2	80.8	72.8	$^{\#}$2.34/$^{\Delta}$2.64	18	6.872	0	5
SFS-OPBI 84:16-A	10.64	*2.15/^{H}1.05	95.3	76.8	73.2	$^{\#}$2.38/$^{\Delta}$3.24	4	1.604	0	8
SFS-OPBI 8:2	6.81	*1.54/^{H}1.15	96.6	75.4	72.8	$^{\#}$2.14/$^{\Delta}$3.44	1	1.465	0	3
Covalently & Ionically cross-linked SFS-OPBI										
SA-210a	13.2	*2.47/^{H}1.15	87.2	81.5	71.1	$^{\#}$2.01/$^{\Delta}$2.56	100	9.730	0	3
SA-210b	12.2	*1.75/^{H}0.76	94.8	80.3	76.2	$^{\#}$2.04/$^{\Delta}$2.72	1	2.439	0	4
SA-262a-1100	12.8	*1.52/^{H}0.60	92.3	84.0	77.5	$^{\#}$2.07/$^{\Delta}$2.69	28	3.359	0	5
Fibre-spun composites										
PWN-OPBI	--	--	--	--	--	--	n.m.	--	n.m.	n.m.
PWN-D	--	--	--	--	--	--	n.m.	--	n.m.	n.m.
PWN-OPBI-D	11.9	*1.06/^{H}0.44	82.2	79.3	65.2	$^{\#}$2.58/$^{\Delta}$2.93	93	11.95	−14	−14
PPFS-D	11.6	*3.24/^{H}1.40	86.5	74.8	64.7	$^{\#}$2.44/$^{\Delta}$3.59	11	11.35	0	5
SFS-PVDF-D	12.6	*2.90/^{H}0.95	73.0	83.9	61.2	$^{\#}$2.07/$^{\Delta}$2.22	96	20.97	DO	24
PPFS-Pip-D	10.5	*1.02/^{H}0.65	91.3	74.7	68.2	$^{\#}$2.77/$^{\Delta}$3.61	2	2.038	0	−10

* Average capacity decay per cycle using charge/discharge average voltages

^{H} Hourly capacity decay (from electrolyte run time)

$^{\#}$ Area specific resistance calculated from the slope of discharge polarisation curve before cycling

$^{\Delta}$ 30-cycle Area specific resistance from charge/discharge curves

n.m. – not measurable

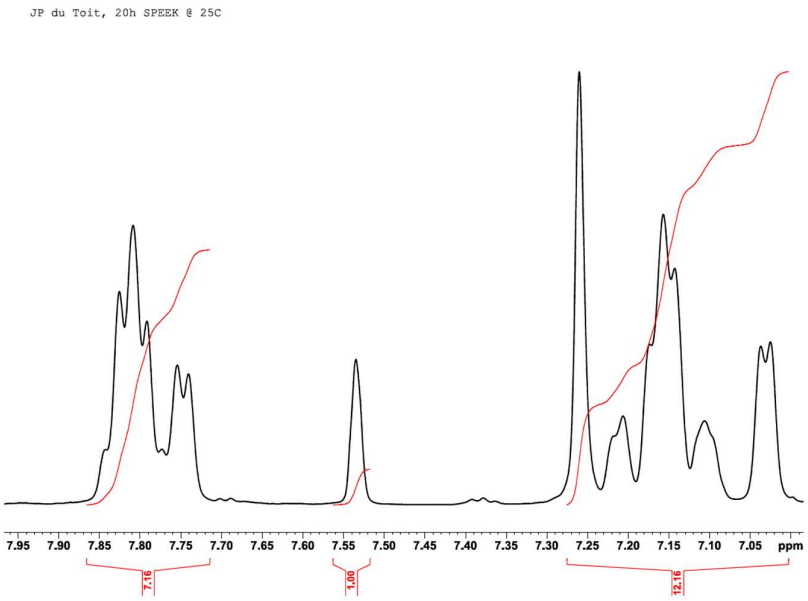

Figure B1: Processed NMR spectra for 20-hour sulfonation of PEEK at 25 °C.

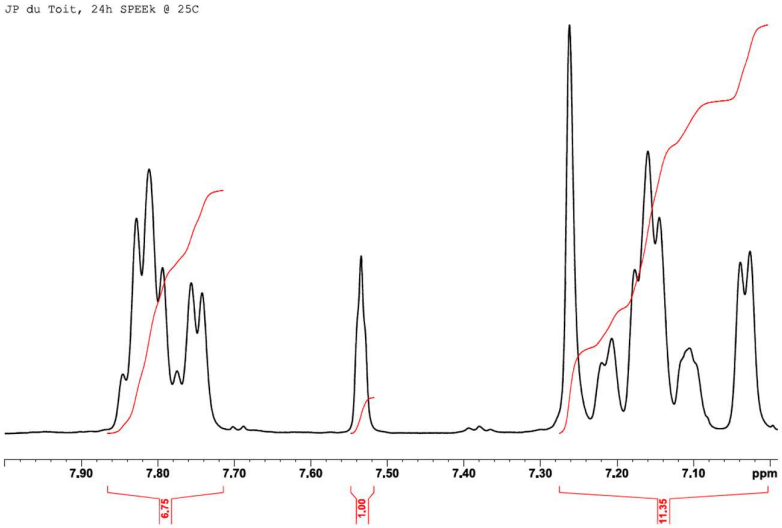

Figure B2: Processed NMR spectra for 24-hour sulfonation of PEEK at 25 °C.

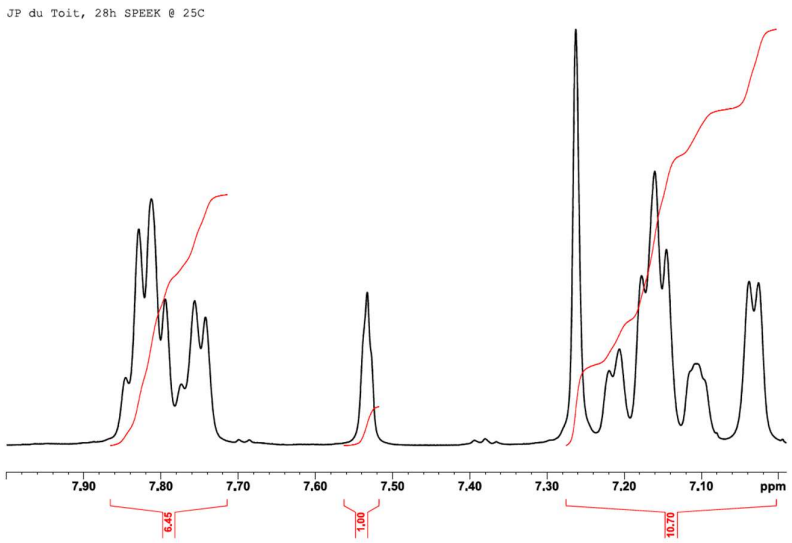

Figure B3: Processed NMR spectra for 28-hour sulfonation of PEEK at 25 °C.

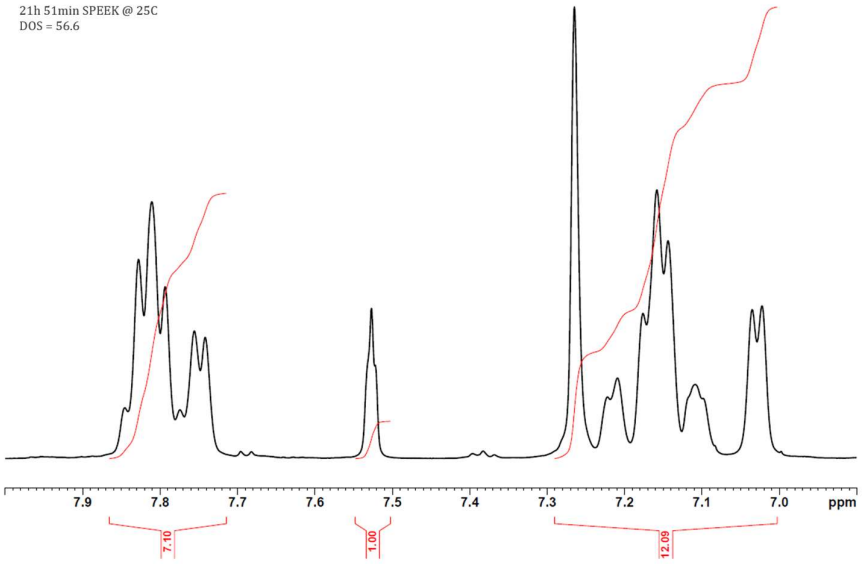

Figure B4: Processed NMR spectra of SPEEK-57: 22-hour sulfonation of PEEK at 25 °C.

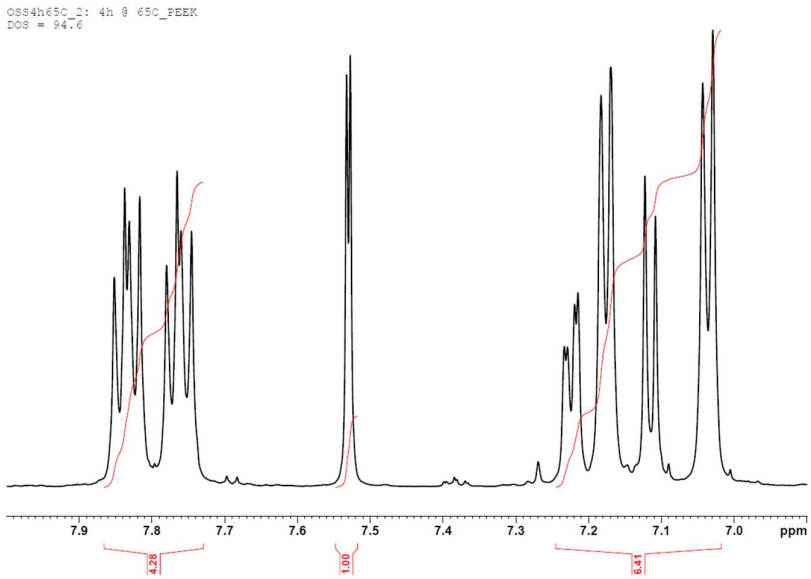

Figure B5: Processed NMR spectra of SPEEK-95: 4-hour sulfonation of PEEK at 65 °C.

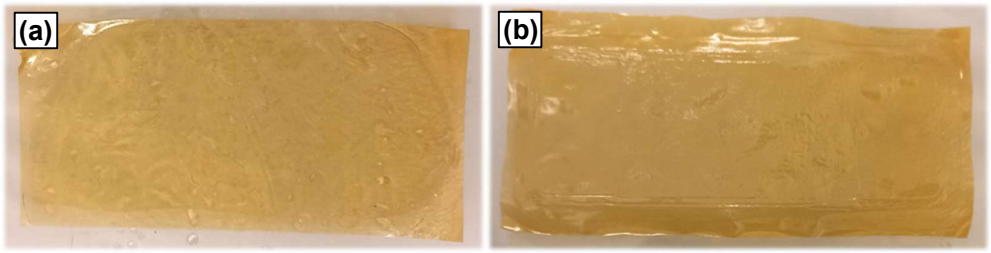

Figure B6: Photographic images of SPEEK-PBIOO-b (a) before and (b) after cycling.

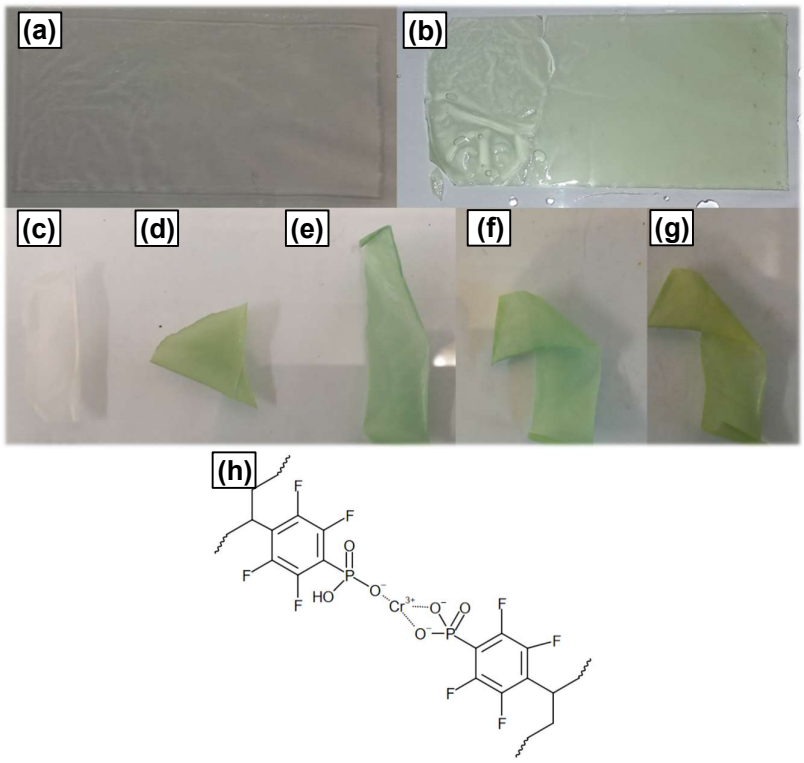

Figure B7: Photographic images of PWN-PVDF (a, c) before and (b, d) after electrolyte preconditioning and after washing at 65 °C using (e) 1 M HCl, (f) 1 M $AlCl_3$ and (g) V_2O_5 in 2 M H_2SO_4. (h) Proposed cross-linking between Cr^{3+} and PWN.

Figure B8: Photograph of fibre mat composite membrane PPFS-D with electrolyte trapped in-between delaminated polymer layers.

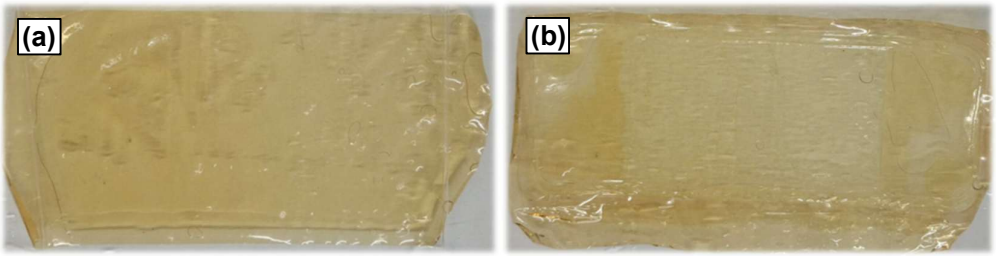

Figure B9: Photographic images of SFS-OPBI 84:16 (a) before and (b) after cycling.

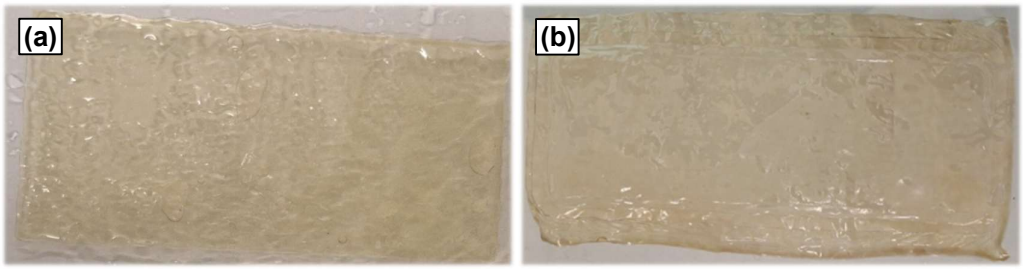

Figure B10: (a, b) Photographic images of SA-210b before and after cycling.

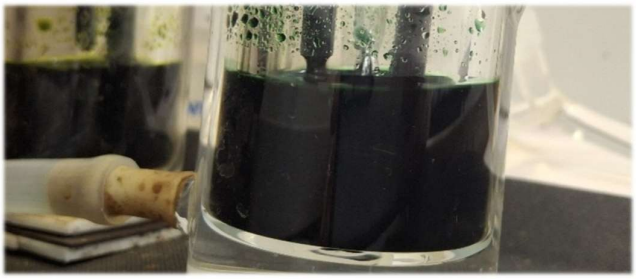

Figure B11: Electrolyte levels at cycle 105 using SA-210b.

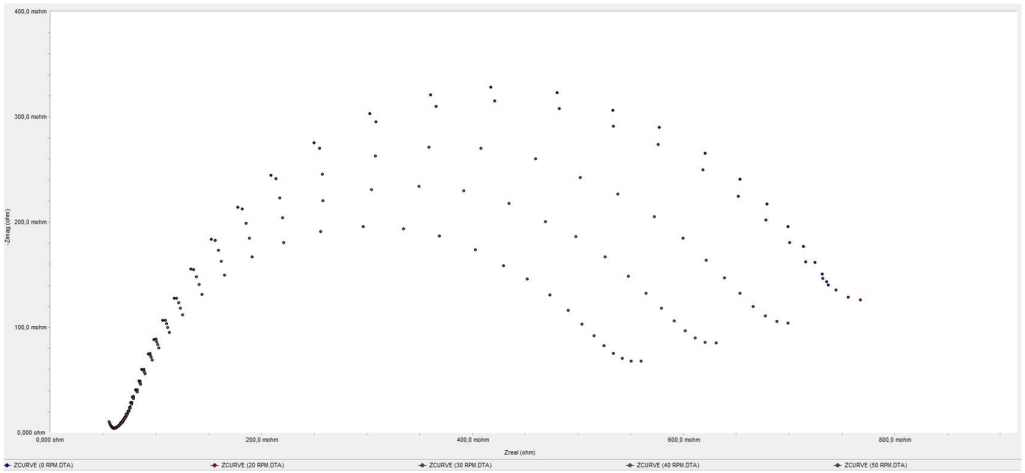

Figure B12: Nyquist plots showing the impedance of a single-cell test station with varying electrolyte pumping rates (0, 20, 30, 40 & 50 RPM) at 0% SOC, 0 A DC and 100 mA AC.